

การสังเคราะห์และการประเมินความเป็นพิษต่อเซลล์ของอนุภาคระดับนาโนเมตรของทองคำ/อนุพันธ์  
พอลิแลนสำหรับการรักษาโรคมะเร็ง



นายศักดิ์ชัย หลักสี

จุฬาลงกรณ์มหาวิทยาลัย

บทคัดย่อและแฟ้มข้อมูลฉบับเต็มของวิทยานิพนธ์ตั้งแต่ปีการศึกษา 2554 ที่ให้บริการในคลังปัญญาจุฬาฯ (CUIR)  
เป็นแฟ้มข้อมูลของนิสิตเจ้าของวิทยานิพนธ์ ที่ส่งผ่านทางบัณฑิตวิทยาลัย

The abstract and full text of theses from the academic year 2011 in Chulalongkorn University Intellectual Repository (CUIR)  
are the thesis authors' files submitted through the University Graduate School.

วิทยานิพนธ์นี้เป็นส่วนหนึ่งของการศึกษาตามหลักสูตรปริญญาวิทยาศาสตรดุษฎีบัณฑิต

สาขาวิชาเคมี ภาควิชาเคมี

คณะวิทยาศาสตร์ จุฬาลงกรณ์มหาวิทยาลัย

ปีการศึกษา 2560

ลิขสิทธิ์ของจุฬาลงกรณ์มหาวิทยาลัย

SYNTHESIS AND CYTOTOXICITY EVALUATION OF GOLD NANOPARTICLES/PULLULAN  
DERIVATIVES FOR CANCER TREATMENT



A Dissertation Submitted in Partial Fulfillment of the Requirements  
for the Degree of Doctor of Philosophy Program in Chemistry

Department of Chemistry

Faculty of Science

Chulalongkorn University

Academic Year 2017

Copyright of Chulalongkorn University

Thesis Title	SYNTHESIS AND CYTOTOXICITY EVALUATION OF GOLD NANOPARTICLES/PULLULAN DERIVATIVES FOR CANCER TREATMENT
By	Mr. Sakchai Laksee
Field of Study	Chemistry
Thesis Advisor	Professor Nongnuj Muangsin, Ph.D.

---

Accepted by the Faculty of Science, Chulalongkorn University in Partial  
Fulfillment of the Requirements for the Doctoral Degree

.....Dean of the Faculty of Science  
(Professor Polkit Sangvanich, Ph.D.)

THESIS COMMITTEE

.....Chairman  
(Associate Professor Vudhichai Parasuk, Ph.D.)

.....Thesis Advisor  
(Professor Nongnuj Muangsin, Ph.D.)

.....Examiner  
(Professor Thawatchai Tuntulani, Ph.D.)

.....Examiner  
(Associate Professor Nuanphun Chantarasiri, Ph.D.)

.....External Examiner  
(Assistant Professor Thitiphan Chimsook, Ph.D.)

CHULALONGKORN UNIVERSITY

ศักดิ์ชัย หลักสี : การสังเคราะห์และการประเมินความเป็นพิษต่อเซลล์ของอนุภาคระดับนาโนเมตรของทองคำ/อนุพันธ์พุลลูแลนสำหรับการรักษาโรคมะเร็ง (SYNTHESIS AND CYTOTOXICITY EVALUATION OF GOLD NANOPARTICLES/PULLULAN DERIVATIVES FOR CANCER TREATMENT) อ.ที่ปรึกษาวิทยานิพนธ์หลัก: ศ. ดร.นงนุช เหมืองสิน, 165 หน้า.

งานนี้มุ่งเน้นการพัฒนาอนุภาคระดับนาโนเมตรของทองคำที่ทำงานหลายฟังก์ชันโดยใช้อนุพันธ์พุลลูแลนทำหน้าที่สามอย่างทั้งเป็นตัวรีดิวซ์ ตัวเพิ่มความเสถียร ตัวช่วยปกคลุม สำหรับนำส่งยา Camptothecin (CPT) หรือ Doxorubicin (DOX) สู่ตำแหน่งเป้าหมายเพื่อเพิ่มประสิทธิภาพและลดผลข้างเคียงของตัวยา โดยอนุภาคระดับนาโนเมตรของทองคำถูกดัดแปลงพื้นผิวประกอบด้วย 3 ส่วนที่สำคัญบนพุลลูแลนคือ (i) ควอท188 ทำหน้าที่เป็นประจวบควเพื่อเพิ่มการเข้าสู่เซลล์และการออกฤทธิ์ (ii) กรดพาราอะมิโนเบนโซอิก (PABA) ทำหน้าที่เป็นโมเลกุลไฮโดรโฟบิกเพื่อช่วยการเข้ากันกับเซลล์และ (iii) กรดโฟลิก (FA) ทำหน้าที่เป็นลิแกนด์เป้าหมายช่วยเข้าจับกับตัวรับโฟเลตบนเยื่อหุ้มเซลล์และเพิ่มการเข้าสู่เซลล์มะเร็ง อนุภาคทรงกลมของ AuNPs@FA-PABA-QP ซึ่งสังเคราะห์ด้วยกระบวนการสีเขียวและง่ายภายใต้สภาวะที่เหมาะสม ทำหน้าที่เป็นอนุภาคนำส่งยาระดับนาโนเมตร พิสูจน์เอกลักษณ์ด้วยเทคนิคทางสเปกโตรสโกปีและกล้องจุลทรรศน์พบว่ามีความเสถียรสูงและมีขนาดเฉลี่ย  $12.6 \pm 1.5$  นาโนเมตร จากการศึกษาความเป็นพิษต่อเซลล์พบว่า CPT-AuNPs@FA-PABA-QP และ DOX-AuNPs@FA-PABA-QP สามารถเพิ่มฤทธิ์ในการยับยั้งเซลล์มะเร็ง Chago-k1 ของยา CPT และ DOX ได้ประมาณ 2.80 และ 4.82 เท่าเมื่อเทียบกับตัวยาเพียงอย่างเดียว ขณะที่อนุภาคนำส่งยาระดับนาโนเมตรของทองคำทั้งสองลดความเป็นพิษต่อเซลล์ปกติ และ Drug-AuNPs@FA-PABA-QP สามารถควบคุมการปลดปล่อยตัวยาทั้งสองที่ pH 5.0 ได้ดีกว่าใน pH 7.4 ขณะที่ระบบเหล่านี้มีการเข้าสู่เซลล์มะเร็งสูงผ่าน folate receptor-mediated endocytosis นอกจากนี้ CPT-AuNPs@FA-PABA-QP และ DOX-AuNPs@FA-PABA-QP ยังช่วยเพิ่มผลรวมการตายของเซลล์มะเร็งแบบอะพอโทซิสอย่างมีนัยสำคัญที่ 14% และ 26% และยังเพิ่มการเหนี่ยวรั้งเซลล์มะเร็งในวัฏจักรของเซลล์ระยะ G0-G1 (11%) และ S/G2-M (31%) ตามลำดับ จากผลการวิจัยเหล่านี้ชี้ให้เห็นว่าการรวมตัวกันแบบใหม่ของ CPT-AuNPs@FA-PABA-QP และ DOX-AuNPs@FA-PABA-QP ทำหน้าที่เป็นรูปแบบนำส่งยาสู่ตำแหน่งเป้าหมายแบบใหม่ที่มีศักยภาพในการพัฒนาต่อเพื่อรักษาโรคมะเร็ง

ภาควิชา เคมี ปลายมือชื่อนิสิต .....

สาขาวิชา เคมี ปลายมือชื่อ อ.ที่ปรึกษาหลัก .....

ปีการศึกษา 2560

# # 5772846523 : MAJOR CHEMISTRY

KEYWORDS: GOLD NANOPARTICLES / PULLULAN DERIVATIVES / DOXORUBICIN / CAMPTOTHECIN / CYTOTOXICITY / CANCER TREATMENT / ANTICANCER ACTIVITY

SAKCHAI LAKSEE: SYNTHESIS AND CYTOTOXICITY EVALUATION OF GOLD NANOPARTICLES/PULLULAN DERIVATIVES FOR CANCER TREATMENT.

ADVISOR: PROF. NONGNUJ MUANGSIN, Ph.D., 165 pp.

This study focused on the development of multifunctional gold nanoparticles (AuNPs) using pullulan derivatives as a trifunctional reducing, stabilizing and capping agent for targeted delivery of camptothecin (CPT) or doxorubicin (DOX) in order to enhance their efficacy and reduce side effects. The surface of AuNPs was functionalized to contain 3 beneficial components on pullulan as followed: (i) quat188 as a positive charge to increase cellular uptake and activities, (ii) *para*-aminobenzoic acid (PABA) as a hydrophobic molecule to enhance biocompatibility, and (iii) folic acid (FA) as a targeting ligand to bind with folate receptor on cancerous cell membranes and enhance intracellular uptake. Facile and green synthesis of spherical AuNPs@FA-PABA-QP as nanocarriers under optimum condition were characterized by various spectroscopic and microscopic techniques with high stability and an average size of  $12.6 \pm 1.5$  nm. The cytotoxicity of CPT-AuNPs@FA-PABA-QP and DOX-AuNPs@FA-PABA-QP were evaluated and found to enhance anticancer activity against Chago-k1 cancer cells of CPT and DOX by approximately 2.80 and 4.82-time comparing with Drug-alone, respectively, whereas they exhibited less toxic to normal cells. The release of both drugs from Drug-AuNPs@FA-PABA-QP in pH 5.0 was higher than pH 7.4, when they were highly taken up into cells by folate receptor-mediated endocytosis. Moreover, CPT-AuNPs@FA-PABA-QP and DOX-AuNPs@FA-PABA-QP increased significantly total-apoptosis (14% and 26%) and then enhanced G0-G1 (11%) and S/G2-M (31%) arrest, inducing cell death, respectively. These results suggested that the novel combinations of CPT-AuNPs@FA-PABA-QP and DOX-AuNPs@FA-PABA-QP as new targeted platforms have the potential to be developed for cancer treatments.

Department: Chemistry Student's Signature .....

Field of Study: Chemistry Advisor's Signature .....

Academic Year: 2017

## ACKNOWLEDGEMENTS

I would like to thank you from deep in my heart to my thesis advisor, Professor Dr. Nongnuj Muangsin, for long time of teaching practice and valuable comments and suggestions in every part of my research in this dissertation. I would like to thank my thesis advisor for her kindness for support and encouragement to give me the good opportunities during this research.

Moreover, I would like to extend to Associate Professor Dr. Vudhichai Parasuk as the chairman, Professor Dr. Thawatchai Tuntulani, Associate Professor Dr. Nuanphun Chantarasiri and Assistant Professor Dr. Thitiphon Chimsook as the examiner for their kindness and valuable suggestions throughout my dissertation.

Additionally, I am also thankful to Associate Professor Dr. Tanapat Palaga and Songchan Puthong for all experiments of biological activities. I am strongly grateful for my financial support from Department of Chemistry, Faculty of Science, Chulalongkorn University, funding from the Ratchadapisak Sompoch Endowment Fund (2016), Chulalongkorn University to NM (CU-59-037-AM), and funding from National Nanotechnology Center (NANOTEC), NSTDA, Ministry of Science and Technology, Thailand, through its program of Center of Excellence Network, Nanotec-CU Center of Excellence on Food and Agriculture. I am strongly grateful for my scholarship support by Science Achievement Scholarship of Thailand (SAST) to SL (Grant No. CU-06-2555 and CU-02-2557). I would like to thank all those people and the members of my laboratory who provide happiness and supporting for me to complete this dissertation.

Finally, I am also thankful to my family and my nice friends for their assistance and encouragement throughout my research period.

## CONTENTS

	Page
THAI ABSTRACT .....	iv
ENGLISH ABSTRACT .....	v
ACKNOWLEDGEMENTS .....	vi
CONTENTS .....	vii
LIST OF TABLES .....	xiv
LIST OF FIGURES.....	xv
LIST OF ABBREVIATIONS AND SYMBOLS.....	xxii
CHAPTER I INTRODUCTION .....	1
1.1 Introduction.....	1
1.2 Scope of this research.....	3
1.3 Objectives of this research.....	6
CHAPTER II BACKGROUND AND LITERATURE REVIEWS .....	7
2.1 Cancer.....	7
2.2 Chemotherapeutic drugs.....	8
2.3 Nanotechnologies.....	10
2.4 Gold nanoparticle (AuNPs) .....	12
2.4.1 AuNPs for anticancer drug delivery.....	13
2.4.2 Active and passive targeted nanocarriers for drug delivery .....	17
2.4.3 Shape and particle size of AuNPs for drug delivery .....	18
2.4.4 Surface functionalization of AuNPs for drug delivery.....	22
2.4.5 Localized surface plasmon resonance (LSPR) .....	23
2.5 Cytotoxicity by MTT assay.....	24

	Page
2.6 Apoptosis assay .....	25
2.7 Cell death: apoptosis and necrosis pathways.....	27
2.8 The cell cycle .....	28
CHAPTER III EXPERIMENTAL .....	29
3.1 Analytical instruments.....	29
3.1.1 Nuclear magnetic resonance spectroscopy (NMR).....	29
3.1.2 Attenuated total reflectance fourier transform infrared spectroscopy (ATR-FTIR) .....	29
3.1.3 Thermogravimetric analysis (TGA).....	29
3.1.4 Ultraviolet and visible spectrophotometry (UV-VIS).....	30
3.1.5 X-ray diffraction (XRD).....	30
3.1.6 Transmission electron microscopy (TEM) .....	30
3.1.7 X-ray photoelectron spectroscopy (XPS).....	30
3.1.8 Zeta-potential analysis .....	31
3.1.9 Fluorescence spectroscopy .....	31
3.1.10 Inductively coupled plasma optical emission spectroscopy (ICP- OES).....	31
3.1.11 Confocal laser scanning microscopy (CLSM).....	32
3.1.12 Flow cytometry.....	32
3.2 Materials and chemicals .....	32
3.3 The experimental methods .....	33
Part I: Design, synthesis and characterization of pullulan and its derivatives as a trifunctional reducing, stabilizing and capping agent for synthesis of gold nanoparticles (AuNPs). .....	35



	Page
3.3.1 General procedure for synthesis of pullulan and its derivatives.....	35
3.3.2 Synthesis of quat188-pullulan (QP) by etherification.....	36
3.3.3 Synthesis of <i>para</i> -aminobenzoic acid-quat188-pullulan (PABA-QP) by esterification .....	37
3.3.4 Synthesis of folic acid- <i>para</i> -aminobenzoic acid-quat188-pullulan (FA- PABA-QP) by esterification .....	38
3.3.5 Calculation of degree of quaternization (%DQ) and substitution (%DS).....	39
3.3.6 Determination of PABA and FA content in pullulan derivatives.....	39
3.3.7 Characterization of pullulan and its derivatives.....	40
Part II: Synthesis and characterization of pullulan derivatives reduced/stabilized/ capped gold nanoparticles (AuNPs@pullulan derivatives) as targeted nanocarriers for anticancer drug delivery systems.	41
3.3.8 Synthesis of AuNPs@pullulan derivatives.....	41
3.3.9 Characterization of AuNPs@pullulan derivatives.....	42
Part III: Preparation and characterization of anticancer drugs loaded on AuNPs@pullulan derivatives for enhancing anticancer activities. ....	43
3.3.10 Preparation of anticancer drugs (DOX or CPT) loaded on AuNPs.....	43
3.3.11 Characterization of anticancer drugs (DOX or CPT) loaded on AuNPs.....	44
Part IV: Evaluation of their cytotoxicity against human cancer and normal cells, intracellular uptake, drug release, and anticancer mechanism (cell cycle and apoptosis assay) of AuNPs@pullulan derivatives. ....	45
3.3.12 Cell culture and reagents .....	45
3.3.13 Cytotoxicity studies by MTT assay .....	45

	Page
3.3.14 Cell morphology study.....	46
3.3.15 Colony formation assay.....	46
3.3.16 Intracellular uptake study.....	47
3.3.17 Confocal study.....	47
3.3.18 <i>In vitro</i> drug release profiles.....	48
3.3.19 Cell cycle assay.....	48
3.3.20 Apoptosis assay.....	49
CHAPTER IV RESULTS AND DISCUSSION.....	50
Part I: Design, synthesis and characterization of pullulan and its derivatives as a trifunctional reducing, stabilizing and capping agent for synthesis of gold nanoparticles (AuNPs).....	51
4.1 Synthesis and characterization of pullulan (P) and its derivatives (QP, PABA- QP and FA-PABA-QP).....	52
4.1.1 <sup>1</sup> H NMR spectra of P, QP, PABA-QP and FA-PABA-QP.....	54
4.1.2 ATR-FTIR spectra of P, QP, PABA-QP and FA-PABA-QP.....	56
4.1.3 TG and DTG curves of P, QP, PABA-QP and FA-PABA-QP.....	58
4.1.4 The determination of PABA and FA content in PABA-QP and FA-PABA- QP.....	61
Part II: Synthesis and characterization of pullulan derivatives reduced/stabilized/ capped gold nanoparticles (AuNPs@pullulan derivatives) as targeted nanocarriers for anticancer drug delivery systems.	62
4.2 Synthesis of AuNPs using PABA-QP (AuNPs@PABA-QP) as a passive targeted nanocarriers.....	62
4.2.1 Effect of pH.....	63
4.2.2 Effect of PABA-QP concentration.....	65

4.3 Synthesis of AuNPs using FA-PABA-QP (AuNPs@FA-PABA-QP) as an active targeted nanocarriers .....	67
4.3.1 Effect of pH .....	68
4.3.2 Effect of temperature .....	69
4.3.3 Effect of FA-PABA-QP concentration.....	70
4.3.4 Effect of types of a reducing/stabilizing/capping agent.....	72
4.4 Characterization of AuNPs using pullulan derivatives (AuNPs@ pullulan derivatives) as targeted nanocarriers for anticancer drug delivery.....	75
4.4.1 Transmission electron microscopy (TEM) and the histograms of AuNPs@pullulan derivatives.....	75
4.4.2 X-ray diffraction (XRD) and selected area of electron diffraction (SAED) patterns of AuNPs@pullulan derivatives .....	78
4.4.3 Zeta-potential analysis of AuNPs@pullulan derivatives .....	81
4.4.4 Energy Dispersive Spectroscopy (EDS) for TEM of AuNPs@pullulan derivatives .....	83
4.4.5 X-ray photoelectron spectroscopy (XPS) and ATR-FTIR of AuNPs@FA-PABA-QP .....	85
Part III: Preparation and characterization of anticancer drugs loaded on AuNPs@pullulan derivatives for enhancing anticancer activities. ....	87
4.5 Preparation and characterization of DOX-loaded on AuNPs@PABA-QP .....	87
4.5.1 UV-Vis and zeta-potential analysis of DOX-AuNPs@PABA-QP.....	87
4.5.2 ATR-FTIR and fluorescence spectroscopy of DOX-AuNPs@PABA-QP ...	89
4.6 Preparation and characterization of DOX-loaded and CPT-loaded on AuNPs@FA-PABA-QP .....	90

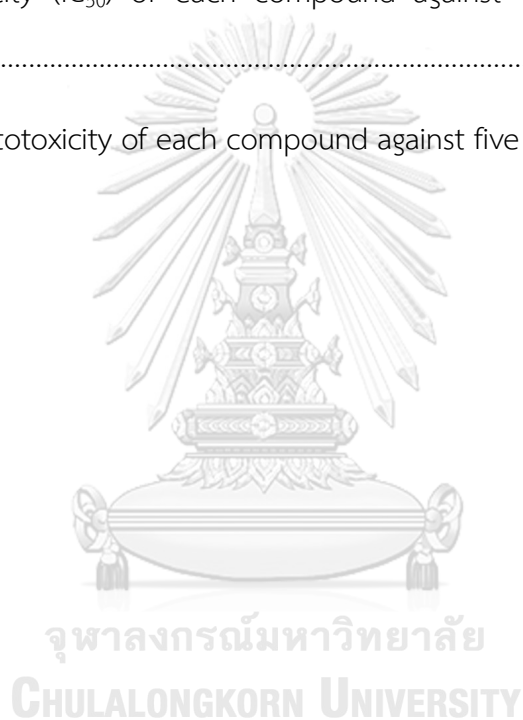
	Page
4.6.1 UV-Vis and zeta-potential analysis of DOX-AuNPs@FA-PABA-QP and CPT-AuNPs@FA-PABA-QP.....	91
4.6.2 ATR-FTIR and fluorescence spectroscopy of DOX-AuNPs@FA-PABA-QP and CPT-AuNPs@FA-PABA-QP .....	92
Part IV: Evaluation of their cytotoxicity against human cancer and normal cells, intracellular uptake, drug release, and anticancer mechanism (cell cycle and apoptosis assay) of AuNPs@pullulan derivatives. ....	95
4.7 Biological activities of DOX-AuNPs@PABA-QP.....	95
4.7.1 Cytotoxicity study of DOX-AuNPs@PABA-QP .....	95
4.7.2 Intracellular uptake study by TEM of AuNPs@PABA-QP .....	99
4.7.3 Confocal study of DOX-AuNPs@PABA-QP.....	100
4.7.4 Cell cycle assay of DOX-AuNPs@PABA-QP.....	102
4.7.5 Apoptosis assay of DOX-AuNPs@PABA-QP.....	103
4.8 Biological activities of DOX-AuNPs@FA-PABA-QP and CPT-AuNPs@FA-PABA-QP.....	105
4.8.1 Cytotoxicity study of Drug-AuNPs@FA-PABA-QP .....	105
4.8.2 Colony formation assay of Drug-AuNPs@FA-PABA-QP .....	108
4.8.3 Cell morphology study of Drug-AuNPs@FA-PABA-QP.....	109
4.8.4 Intracellular uptake study by TEM of AuNPs@FA-PABA-QP .....	111
4.8.5 Confocal study of Drug-AuNPs@FA-PABA-QP .....	112
4.8.6 <i>In vitro</i> release profiles of Drug-AuNPs@FA-PABA-QP.....	114
4.8.7 Cell cycle assay of Drug-AuNPs@FA-PABA-QP.....	116
4.8.8 Apoptosis assay of Drug-AuNPs@FA-PABA-QP.....	118
CHAPTER V CONCLUSION.....	120

	Page
REFERENCES .....	122
APPENDICES.....	135
APPENDIX A .....	136
APPENDIX B .....	160
VITA.....	165



## LIST OF TABLES

Table 1 XRD data showing $2\theta$ ( $^{\circ}$ ) and d-spacing ( $\text{\AA}$ ) of $\text{HAuCl}_4$ ( $\text{Au}^{3+}$ ), $\text{AuNPs@P}$ , $\text{AuNPs@QP}$ , $\text{AuNPs@PABA-QP}$ and $\text{AuNPs@FA-PABA-QP}$ ( $\text{Au}^0$ ).....	80
Table 2 The zeta potential of $\text{AuNPs@pullulan}$ derivatives under optimal condition. .....	81
Table 3 Cytotoxicity ( $\text{IC}_{50}$ ) of each compound against Chago-k1 and KATO-III cells. ....	98
Table 4 <i>In vitro</i> cytotoxicity of each compound against five cancer cells.....	107



## LIST OF FIGURES

Figure 1 Scope of this research and the proposed scheme of FA-targeted delivery of the chemodrugs using AuNPs@pullulan derivatives as nanocarriers. ....	5
Figure 2 Cell divisions of cancer and normal cells [19]. ....	8
Figure 3 Chemical structure and action mode of cisplatin to crosslink with purine bases on the DNA [21]. ....	9
Figure 4 Chemical structure and action mode of camptothecin to bind with topoisomerase I and DNA [5]. ....	9
Figure 5 Chemical structure and action mode of doxorubicin to bind with DNA [22]. .....	10
Figure 6 Several different types of nanocarriers for delivery systems: polymeric, lipid-based, and inorganic nanocarriers [24]. ....	11
Figure 7 Chemical structure of pullulan [31]. ....	13
Figure 8 Summary of antitumor drugs conjugated with AuNPs [32]. ....	14
Figure 9 (a) Design illustration of doxorubicin-tethered responsive AuNPs. (b) The cooperation between increased DOX cellular entry and an intracellular release of DOX in cancer cells for overcome drug resistance [33]. ....	15
Figure 10 Structure of platinum tethered AuNPs [34]. ....	16
Figure 11 Preparation of TAM-PEG-SH attachments to AuNPs [36]. ....	16
Figure 12 Intracellular uptake of AuNPs functionalized via thiolated DOX (Au-PEG-SS-DOX) to MDR HepG2-R cells as observed by confocal scanning microscopy [37]. .....	17

Figure 13 A schematic illustration of by active and passive targeting drug delivery systems [38].	18
Figure 14 Effect of gold nanoparticle shapes for drug delivery [39].	19
Figure 15 Quantification of AuNPs uptake per cell is presented. The different surface modifications are named by the coding ((A) ethanediamine, (B) glucosamine, (C) hydroxypropylamine, (D) taurine, and (E) PEG based on three different core sizes (18, 35 and 65 nm) [40].	20
Figure 16 Accumulation of AuNPs (15, 50 and 100 nm) within the intestinal epithelium: change in the amount of gold measured in the Caco-2 monolayers [41].	21
Figure 17 The targeted drug delivery system of 5-Fu-AuNPs@pullulan-FA [47].	23
Figure 18 Localized surface plasmon resonance (LSPR) of AuNPs [48].	23
Figure 19 Reduction of MTT into formazan dye in living cells.	24
Figure 20 Diagram showing healthy and apoptotic cells with markers for detection of apoptosis [52].	26
Figure 21 Flow cytometric quadrant dot plot of apoptotic cancer cells after 24 h treatment with drug. Apoptosis of cancer cells as detected by Annexin-V-FITC/PI dual staining method [52].	26
Figure 22 Cell death process including apoptosis and necrosis pathways [57].	27
Figure 23 The cell cycle consists of four distinct phases [58].	28
Figure 24 The materials and methods in experimental procedures are divided into four parts.	34
Figure 25 Schematic representation of pullulan and its derivatives (QP, PABA and FA-PABA-QP).	35



Figure 26 Synthetic pathway of quat188-pullulan (QP) by etherification.....	36
Figure 27 Synthetic pathway of para-aminobenzoic acid-quat188-pullulan (PABA-QP) by esterification.....	37
Figure 28 Synthetic pathway of folic acid-para-aminobenzoic acid-quat188-pullulan (FA-PABA-QP) by esterification.....	38
Figure 29 Synthetic pathway of AuNPs formations using pullulan and its derivatives under optimal conditions.....	41
Figure 30 Preparations and proposed chemical structure of DOX-loaded and CPT-loaded onto AuNPs using pullulan and its derivatives.....	44
Figure 31 Chemical and molecular structure of pullulan derivatives (FA-PABA-QP).....	52
Figure 32 Synthetic pathway of (a) pullulan (P), (b) quat188-pullulan (QP), (c) para-aminobenzoic acid-quat188-pullulan (PABA-QP), and (d) folic acid-para-aminobenzoic acid-quat188-pullulan (FA-PABA-QP).....	53
Figure 33 <sup>1</sup> H NMR spectra of (a) pullulan (P), (b) QP, (c) PABA-QP, and (d) FA-PABA-QP.....	55
Figure 34 ATR-FTIR spectra of (a) pullulan (P), (b) QP, (c) PABA-QP, and (d) FA-PABA-QP.....	57
Figure 35 Representative TG and DTG curves of (a) pullulan (P), (b) QP, (c) PABA-QP, and (d) FA-PABA-QP.....	60
Figure 36 Design and synthetic pathways of AuNPs@PABA-QP as a passive targeted nanocarriers by green reduction.....	62

Figure 37 (a) UV-vis spectra, (b) corresponding photographic images and (c) plot of intensity ratio between $\lambda_{\text{max}}$ at 520 and 650 nm of AuNPs@PABA-QP after synthesis at different pH.....	65
Figure 38 (a) UV-vis spectra, (b) corresponding photographic images and (c) plot of intensity ratio between $\lambda_{\text{max}}$ at 520 and 650 nm of AuNPs@PABA-QP after synthesis at different PABA-QP concentrations.....	66
Figure 39 Design and green synthetic method of AuNPs@FA-PABA-QP as an active targeted nanocarriers by green reduction.....	67
Figure 40 (a) UV-vis spectra, (b) corresponding photographic images and (c) plot of intensity ratio between $\lambda_{\text{max}}$ at 520 and 650 nm of AuNPs@FA-PABA-QP as an active targeted nanocarriers after synthesis at different pH.....	69
Figure 41 (a) UV-vis spectra, (b) corresponding photographic images and (c) plot of intensity ratio between $\lambda_{\text{max}}$ at 520 and 650 nm of AuNPs@FA-PABA-QP as an active targeted nanocarriers after synthesis at different reaction temperature.....	70
Figure 42 (a) UV-vis spectra, (b) corresponding photographic images and (c) plot of intensity ratio between $\lambda_{\text{max}}$ at 520 and 650 nm of AuNPs@FA-PABA-QP as an active targeted nanocarriers after synthesis at different FA-PABA-QP concentrations.....	71
Figure 43 (a) UV-vis spectra and (b) corresponding photographic images of AuNPs@FA-PABA-QP as an active targeted nanocarriers after synthesis at different types of a reducing/stabilizing/capping agent. ....	74
Figure 44 Characterizations of AuNPs formation: (a) TEM images and (b) histograms of (i) AuNPs@P, (ii) AuNPs@QP, (iii) AuNPs@PABA-QP, and (iv) AuNPs@FA-PABA-QP under optimal conditions. ....	77
Figure 45 XRD patterns of (a) HAuCl <sub>4</sub> , (b) AuNPs@P, (c) AuNPs@QP, (d) AuNPs@PABA-QP and (e) AuNPs@FA-PABA-QP. ....	79

Figure 46 The selected area of electron diffraction (SAED) patterns XRD patterns of (a) AuNPs@PABA-QP and (b) AuNPs@FA-PABA-QP.....	80
Figure 47 Zeta-potential analysis of (a) AuNPs@P, (b) AuNPs@QP, (c) AuNPs@PABA-QP and (d) AuNPs@FA-PABA-QP.....	82
Figure 48 (a) EDS spectrum, (b) dark-field TEM micrograph, (c-e) the elemental mapping in the same AuNPs region and (f) the elemental composition of AuNPs@FA-PABA-QP under optimal condition.....	84
Figure 49 (a) XPS survey spectrum and (b) XPS spectrum of the Au (4f) core level region for AuNPs@FA-PABA-QP film.....	86
Figure 50 Preparation and chemical structure of DOX-loaded on AuNPs@PABA-QP.....	87
Figure 51 (a) UV-vis spectra and (b) zeta-potentials of (i) AuNPs@PABA-QP and (ii) DOX-AuNPs@PABA-QP.....	88
Figure 52 ATR-FTIR spectra of (a) AuNPs@PABA-QP, (b) DOX and (c) DOX-AuNPs@PABA-QP.....	90
Figure 53 Preparation and chemical structure of DOX-loaded and CPT-loaded on AuNPs@FA-PABA-QP.....	91
Figure 54 (a) UV-vis spectra and (b) zeta-potentials of (i) AuNPs@FA-PABA-QP, (ii) DOX-AuNPs@FA-PABA-QP and (iii) CPT-AuNPs@FA-PABA-QP.....	92
Figure 55 ATR-FTIR spectra of (a) AuNPs@FA-PABA-QP, (b) DOX, (c) DOX-AuNPs@FA-PABA-QP, (d) CPT and (e) CPT-AuNPs@FA-PABA-QP.....	94
Figure 56 Schematic representation showing intracellular releasing of DOX on AuNPs@PABA-QP as a passive targeted nanocarriers in Chago-k1 cells.....	95

Figure 57 Cytotoxicity of DOX and DOX-AuNPs@PABA-QP against normal cells (Wi-38) compared with PABA-QP, AuNPs@P and AuNPs@PABA-QP. ....	99
Figure 58 Intracellular uptake by TEM images of (a) untreated and treated Chago-k1 cells with 40 $\mu$ M (b) AuNPs@P, (c) AuNPs@QP and (d) AuNPs@PABA-QP after 72 h (N=nucleus; Nu=nucleolus; C=cytoplasm; V=vacuole).....	100
Figure 59 Confocal microscopy images showing intracellular uptake of (a) control group and Chago-k1 cells incubated with (b) AuNPs@PABA-QP, (c) DOX and (d) DOX-AuNPs@PABA-QP at 37°C for 12 h (DOX and AuNPs@PABA-QP at 0.3 and 40 $\mu$ M, respectively).....	101
Figure 60 Cell cycle analysis of Chago-k1 cells after 24 h treatment with (a) control, (b) AuNPs@PABA-QP, (c) DOX and (d-f) DOX-AuNPs@PABA-QP as detected by Annexin V-FITC/PI dual staining method. ....	103
Figure 61 Flow cytometric analysis of Chago-k1 cells after 12 h treatment with (a) control, (b) AuNPs@PABA-QP, (c) DOX and (d) DOX-AuNPs@PABA-QP as detected by Annexin V-FITC/PI dual staining method. ....	104
Figure 62 Schematic representation showing intracellular releasing of DOX and CPT on AuNPs@FA-PABA-QP as an active targeted nanocarriers in Chago-k1 cells. ....	105
Figure 63 Cytotoxicity of AuNPs@FA-PABA-QP against (a) cancer (Hep-G2 and Chago-k1), and (b) normal cells (Wi-38) for 72 h.....	107
Figure 64 Colony formation assay in Chago-k1 cells treated with DOX-AuNPs@FA-PABA-QP, CPT-AuNPs@FA-PABA-QP and compared with other groups.....	108
Figure 65 Phase contrast micrographs showed cytotoxic effect exerted by DMSO, AuNPs@P, AuNPs@QP, AuNPs@PABA-QP, AuNPs@FA-PABA-QP, DOX, CPT, and the combination of DOX-AuNPs@FA-PABA-QP and CPT-AuNPs@FA-PABA-QP against	

Chago-k1 after 72 h. Treated cells were photographed under a light microscope at a magnification of 20x (scale bare: 100 $\mu$ m).....	110
Figure 66 Intracellular uptake by TEM images of Chago-k1 cells after culturing with or without AuNPs@FA-PABA-QP as an active targeted nanocarriers for 72h (N=nucleus; Nu=nucleolus; C=cytoplasm; V=vacuole). .....	111
Figure 67 Confocal laser scanning microscope images of (a) control and Chago-k1 cells incubated with (b) 40 $\mu$ M AuNPs@FA-PABA-QP, (c) DOX, (d) DOX-AuNPs@FA-PABA-QP, (e) CPT, (d) CPT-AuNPs@FA-PABA-QP at 37°C for 12 h. ....	113
Figure 68 Release profiles of (a) CPT-AuNPs@FA-PABA-QP and (b) DOX-AuNPs@FA-PABA-QP in PBS (pH 7.4) and acetate buffer (pH 5.0). .....	115
Figure 69 (a-b) Cell cycle analysis and (c-d) cell populations of Chago-k1 cells after 24h treatment with (i) control, (ii) AuNPs@FA-PABA-QP, (iii-iv) CPT or DOX, and (v-vi) CPT-AuNPs@FA-PABA-QP or DOX-AuNPs@FA-PABA-QP as detected by PI. ....	117
Figure 70 (a-b) Flow cytometric analysis of Chago-k1 cells after 12h treatment with (i) control, (ii) AuNPs@FA-PABA-QP, (iii-iv) CPT or DOX, and (v-vi) CPT-AuNPs@FA-PABA-QP or DOX-AuNPs@FA-PABA-QP as detected by Annexin V-FITC/PI staining.....	119

## LIST OF ABBREVIATIONS AND SYMBOLS

$^1\text{H}$ NMR	$^1\text{H}$ nuclear magnetic resonance spectroscopy
ATR-FTIR	Attenuated total reflectance fourier transform infrared spectroscopy
TGA	Thermogravimetric analysis
TEM	Transmission electron microscopy
EDS	Energy dispersive X-ray spectroscopy
SAED	Selected area electron diffraction
UV-vis	UV-vis spectroscopy
LSPR	Localized surface plasmon resonance
XRD	X-ray diffractometer
XPS	X-ray photoelectron spectroscopy
CLSM	Confocal laser scanning microscopy
DCC	<i>N,N'</i> -dicyclohexylcarbodiimide
DMAP	4-Dimethyl aminopyridine
$\text{HAuCl}_4$	Tetrachloroauric acid or hydrogen tetrachloroaurate (III)
DOX	Doxorubicin hydrochloride
CPT	Camptothecin
MTT	3-(4,5-Dimethylthiazol-2-yl)-2,5-diphenyltetrazolium bromide
PI	Propidium Iodide
DAPI	4',6-Diamidino-2-phenylindole
Annexin V-FITC	Annexin V-fluorescein isothiocyanate
PBS	Phosphate-buffered saline
P	Pullulan
QP	Quat188-pullulan

PABA-QP	<i>para</i> -Aminobenzoic acid-quat188-pullulan
FA-PABA-QP	Folic acid- <i>para</i> -aminobenzoic acid-quat188-pullulan
AuNPs	Gold nanoparticles
AuNPs@pullulan derivatives	Gold nanoparticles reduced/stabilized/capped with pullulan derivatives
AuNPs@P	Gold nanoparticles reduced/stabilized/capped with pullulan
AuNPs@QP	Gold nanoparticles reduced/stabilized/capped with quat188-pullulan
AuNPs@PABA-QP	Gold nanoparticles reduced/stabilized/capped with <i>para</i> -aminobenzoic acid-quat188-pullulan
AuNPs@FA-PABA-QP	Gold nanoparticles reduced/stabilized/capped with folic acid- <i>para</i> -aminobenzoic acid-quat188-pullulan
DOX-AuNPs@P	Doxorubicin hydrochloride loaded gold nanoparticles reduced/stabilized/capped with pullulan
DOX-AuNPs@PABA-QP	Doxorubicin hydrochloride loaded gold nanoparticles reduced/stabilized/capped with <i>para</i> -aminobenzoic acid-quat188-pullulan
DOX-AuNPs@FA-PABA-QP	Doxorubicin hydrochloride loaded gold nanoparticles reduced/stabilized/capped with folic acid- <i>para</i> -aminobenzoic acid-quat188-pullulan
CPT-AuNPs@FA-PABA-QP	Camptothecin loaded gold nanoparticles reduced/stabilized/capped with folic acid- <i>para</i> -aminobenzoic acid-quat188-pullulan
DQ	Degree of quaternization
DS	Degree of substitution
IC <sub>50</sub>	The half maximal inhibitory concentration

$\zeta$	Zeta potential
%	Percentage
°C	Celsius degree
mL	Milliliter
$\mu$ L	Microliter
mmol	Millimole
$\mu$ M	Micromolar
nm	Nanometer
MHz	Megahertz
$\delta$	Chemical shift
aq	Aqueous
$\text{cm}^{-1}$	Wavenumber
d	Doublet
D <sub>2</sub> O	Deuterium oxide
DMSO-d <sub>6</sub>	Deuterated dimethylsulfoxide
g	Gram
mg	Milligram
h	Hour
m/z	Mass per charge ratio
min	Minute
ppm	Part per million
mV	Millivolt
rt	Room temperature
v/v	Volume/Volume
w/v	Weight/Volume



# CHAPTER I

## INTRODUCTION

### 1.1 Introduction

Cancer is a major leading cause and the second reason of death worldwide in developing countries, and it is rapidly increasing [1]. The number of cancer cases is increasing with 10.9 million new cases and 6.7 million deaths in 2002, compared with 14.1 million new cancer cases and 8.2 million deaths in 2012 [2, 3]. In spite of all available methods for cancer treatments, chemotherapy is a main therapeutic approach. Major impediments to effective cancer treatments are related to high toxicity on normal cells and acquisition of multidrug resistance (MDR) against chemotherapeutic agents to inhibit cancer cells. Thus, the selective accumulations of high concentration of drugs in only cancerous cells remain an important challenge to improve safety and efficacy of conventional anticancer drugs [4]. The considerable efforts have been made to solve MDR problem but only constrained successes have been accomplished by using in difficult clinics. The most common chemotherapeutic agents have been used to treat different types of cancer and different ways for cancer treatments such as doxorubicin (DOX), camptothecin (CPT), cisplatin and etc. CPT, a cytotoxic quinolone alkaloid, was used as a cancer treatment in traditional Chinese medicine because their planar pentacyclic ring is considered as one of the most major factor to inhibit cancer by topoisomerase inhibition and DNA binding [5, 6]. DOX is a chemotherapy medication used to kill various cancer, which destroys the DNA strand during replication, causes DNA damage, and shows a significant anticancer activity in wide spectrum of cancer by intercalation with DNA and topoisomerase II inhibition. Although DOX and CPT show extreme anticancer activities and they can kill the cancer cells by various ways [7], the main problems are encountered with DOX which shows

non-specificity and high toxicity to normal cells showing dangerous side effect, short life-time in the body. Additionally, the number of poor characteristics of CPT has limited its clinical applications including low solubility, low stability at physical pH and severe systemic toxicities which results in a narrow therapeutic index [6]. To overcome these problems of drugs, many researchers have used nanotechnology as nanocarriers to delivery drugs into targeted site of cancer cells by non-covalent loading and covalent conjugation for reducing toxicity and sustaining the therapeutic efficacy [8].

Therefore, nanotechnologies are speedily growing area of scientific research and are aimed to overcome these problems of all drugs for chemotherapy [4]. Several nanocarriers systems including dendrimers, solid lipid nanoparticles, polymersomes, nanospheres, carbon nanotubes, polymeric nanoparticles, peptide nanoparticles, and metallic nanoparticles have provide a new platforms for drug delivery, bio-sensing, bio-imaging and chemotherapy [9]. Among the board diversity of nanoparticles, gold nanoparticles (AuNPs) have recently emerged as a promising drugs delivery systems for efficient delivery and release of drugs into diverse cell types [10]. AuNPs have advantages more than other metallic nanoparticles as potential nanocarriers for targeted drug delivery due to inert material, non-cytotoxicity, high biocompatibility, and unique physicochemical properties. Furthermore, the surface fabrications of AuNPs can be highly tunable properties with the diversity to incorporate multiple drugs by non-covalent or covalent functionalization on the modified surface of AuNPs and their size can be easily fabricated by controlling synthetic approaches [11].

Most of synthetic methods of AuNPs have been synthesized by chemical approaches using toxic chemicals that may affect to human health and environment and may not suitable for drug delivery [12, 13]. To overcome these problems, green synthesis has attracted considerable attention to decrease the use of toxic chemicals and methods. Our study focused on the use of eco-friendly agents for fabrications of AuNPs by using carbohydrate polymers-coated AuNPs to provide effective therapeutic

agents improving biocompatibility and increasing ability in chemodrugs delivery, including chitosan, cellulose, hyaluronic acid, gellan gum, pullulan and etc. [13, 14]. Among the board diversity of polysaccharides, pullulan has attracted considerable attention to use as green agents for AuNPs synthesis owing to its high soluble, non-toxic, non-carcinogenic, non-mutagenic, biocompatible, biodegradable and natural biopolymer [15]. For example, Laksee and co-workers [14] developed a simple, green and efficient approach to synthesis of AuNPs using pullulan as a reducing/stabilizing/capping agent for anticancer drug delivery to improve safety and efficacy of these systems. AuNPs could be selectively delivered to cancer cells by passive or active targeting pathways. Currently, many researchers have studied multifunctional AuNPs to targeted drug delivery by surface modification with hydrophobic, hydrophilic and targeted molecules to enhance specificity and intracellular uptake into only cancer cells to reduce toxicity, protect drugs from human environmental effects and sustain efficacy of drugs [16]. In previous reports, general synthesis method of AuNPs involved using toxic chemicals that are not suitable for drug delivery. In consequence, we focus on the development of folate-amphiphilic pullulan stabilized AuNPs as nanocarriers for drug delivery in order to increase their performance and reduce their side effects.

## 1.2 Scope of this research

In this research, we focused on the development of gold nanoparticles (AuNPs) using pullulan derivatives as both reducing and stabilizing agents for cancer targeted drug delivery system in order to enhance their anticancer efficacy and reduce side effects. Gold nanoparticles were designed to contain three structural components of pullulan derivatives as followed: (i) quat188 as a positive charge to increase cellular uptake and anticancer activities, (ii) *para*-aminobenzoic acid (PABA) as a hydrophobic molecule to enhance cell permeability and compatibility with hydrophobic drug, and

(iii) folic acid (FA) as a targeting ligand to bind to folate receptor protein (FR) overexpressed on the surface of many human cancer cells as shown in Figure 1. The pullulan derivatives stabilized gold nanoparticles (AuNPs@pullulan derivatives) were synthesized and characterized by UV-VIS, FTIR, TEM and DLS techniques. Moreover, the anticancer activities of AuNPs@pullulan derivatives with or without anticancer drug against cancer and normal cell lines were evaluated by using MTT assay. Finally, the cellular uptake and biological activities of AuNPs@pullulan derivatives were characterized by TEM techniques. The scope of this research and the proposed scheme of FA-targeted delivery of the chemodrugs using AuNPs@pullulan derivatives as nanocarriers are divided into four parts as shown in Figure 1:

**Part I:** Synthesis of pullulan derivatives as a trifunctional reducing, stabilizing and capping agent for synthesis of AuNPs.

**Part II:** Preparation of AuNPs@pullulan derivatives as targeted nanocarriers for anticancer drug delivery systems.

**Part III:** Fabrication of anticancer drugs loaded on AuNPs@pullulan derivatives for enhancing anticancer activities.

**Part IV:** Evaluation of their cytotoxicity, intracellular uptake, drug release, cell cycle and apoptosis assay.

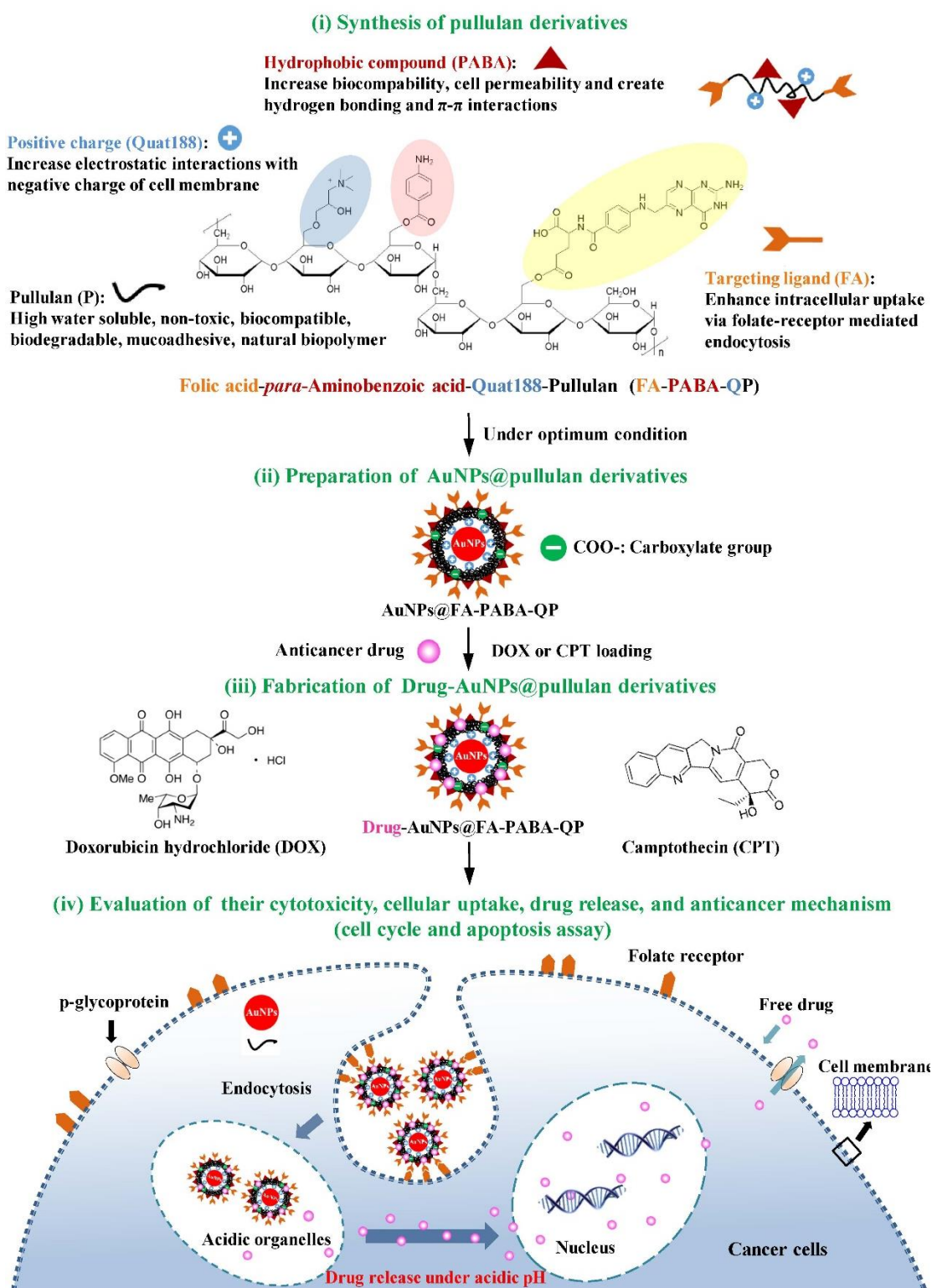


**Figure 1** Scope of this research and the proposed scheme of FA-targeted delivery of the chemodrugs using AuNPs@pullulan derivatives as nanocarriers.

### 1.3 Objectives of this research

1. To design, synthesize and characterize pullulan and its derivatives as a trifunctional reducing, stabilizing and capping agent for synthesis of gold nanoparticles (AuNPs).
2. To synthesize and characterize pullulan derivatives reduced/stabilized/capped gold nanoparticles (AuNPs@pullulan derivatives) as targeted nanocarriers for anticancer drug delivery systems.
3. To prepare and characterize anticancer drugs loaded on AuNPs@pullulan derivatives for enhancing anticancer activities.
4. To evaluate their cytotoxicity against human cancer and normal cells, intracellular uptake, drug release, and anticancer mechanism (cell cycle and apoptosis assay) of AuNPs@pullulan derivatives.

## CHAPTER II

### BACKGROUND AND LITERATURE REVIEWS

#### 2.1 Cancer

Cancer is a major leading cause and the second reason of death worldwide in developing countries, and it is rapidly increasing [1]. The number of cancer cases is increasing with 10.9 million new cases and 6.7 million deaths in 2002, compared with 14.1 million new cancer cases and 8.2 million deaths in 2012 [2, 3]. The number of cancer cases is increasing because of the growth aging of the population, as well as prevalence of established risk factor [17-19]. The cancerous cells is a large group of diseases involving unregulated proliferation of cells and uncontrolled cancer cell divisions as shown in Figure 2.

The cancer is treated several ways, such as surgical removal, chemotherapy, radiation and combination of these treatments, depending on the stage and type of cancer cells. In spite of all available methods for cancer treatments, chemotherapy is a main therapeutic approach. Major impediments to effective cancer treatments are related to high toxicity on normal cells and acquisition of multidrug resistance (MDR) against chemotherapeutic agents to inhibit cancer cells. Thus, the selective accumulations of high concentration of drugs in only cancerous cells remain an important challenge to improve safety and efficacy of conventional anticancer drugs [4]. The considerable efforts have been made to solve MDR problem but only constrained successes have been accomplished by using in difficult clinics.

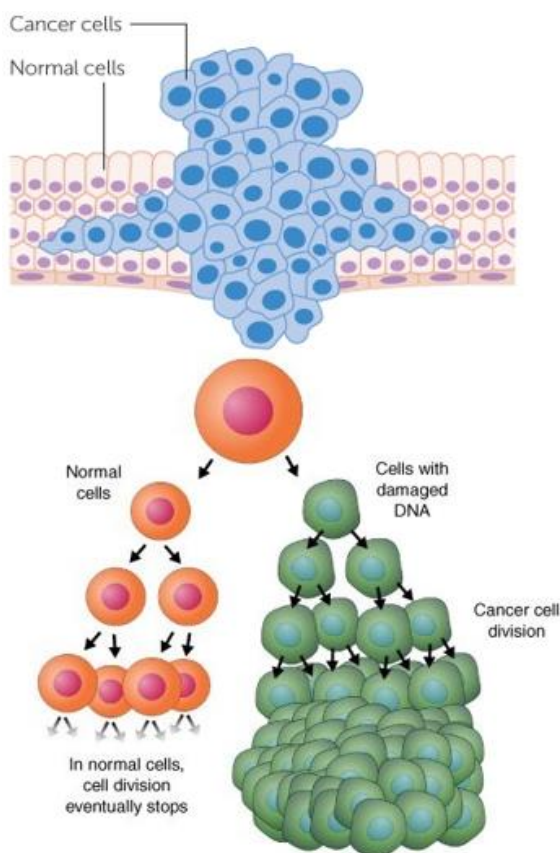


Figure 2 Cell divisions of cancer and normal cells [19].

## 2.2 Chemotherapeutic drugs

Chemotherapy is the most common cancer treatment but its effectiveness is limited by its high toxicity towards normal cells and causes significant adverse side effects [20]. The most common chemotherapeutic agents have been used to treat different types of cancer and different ways for cancer treatments such as cisplatin, doxorubicin (DOX), camptothecin (CPT) and the other drugs.

In mid-1960s, cisplatin (cis-dichloridodiammineplatinum (II),  $\text{cis-}[\text{PtCl}_2(\text{NH}_3)_2]$ ) has been used to treat a worldwide variety of cancer. Its mode of *action* has been linked to its ability to crosslink with purine bases on the DNA and interferes with DNA replication, which inhibit proliferating cancer cells as shown in Figure 3. However, its effectiveness is limited by its very high toxicity and incidence of drug resistance [21].



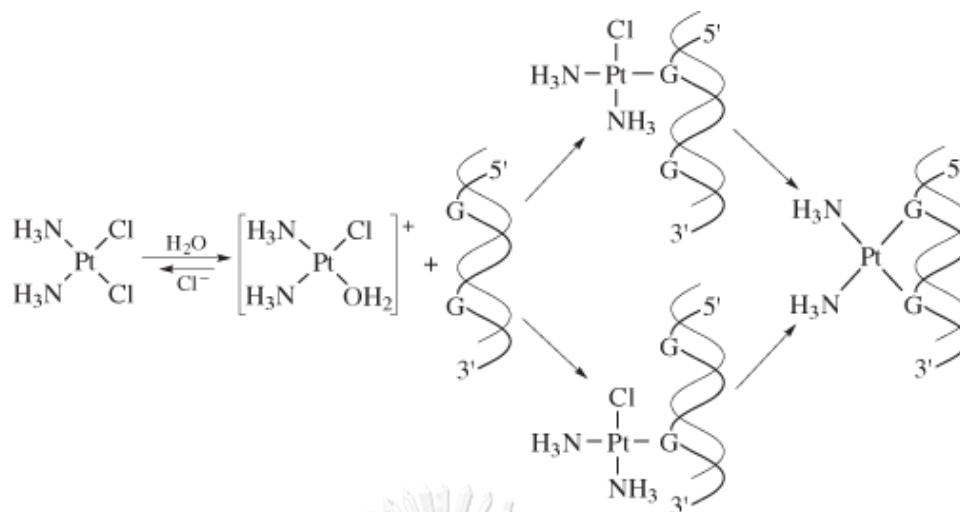


**Figure 3** Chemical structure and action mode of cisplatin to crosslink with purine bases on the DNA [21].

Camptothecin (CPT), a cytotoxic quinolone alkaloid, was used as a cancer treatment in traditional Chinese medicine because their planar pentacyclic ring is considered as one of the most major factor to inhibit cancer by topoisomerase inhibition and DNA binding (Figure 4) [5, 6]. Additionally, although CPT show high anticancer activities and the number of poor characteristics of CPT has limited its clinical applications including low solubility, low stability at physical pH and severe systemic toxicities which results in a narrow therapeutic index [6].

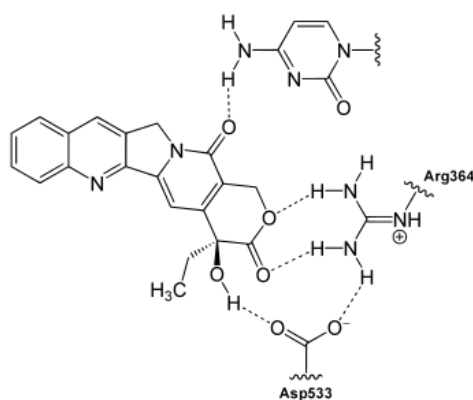


**Figure 4** Chemical structure and action mode of camptothecin to bind with topoisomerase I and DNA [5].

Doxorubicin (DOX) is a chemotherapy medication used to kill various cancer, which destroys the DNA strand during replication, causes DNA damage, and shows a significant anticancer activity in wide spectrum of cancer by intercalation with DNA and topoisomerase II inhibition (Figure 5) [22]. Although DOX show extreme anticancer activities and they can kill the cancer cells by various ways [7], the main problems are encountered with DOX which shows non-specificity and high toxicity to normal cells showing dangerous side effect, short life-time in the body. To overcome these problems of drugs, many researchers have used nanotechnology as nanocarriers to deliver drugs into targeted site of cancer cells by non-covalent loading and covalent conjugation for reducing toxicity and sustaining the therapeutic efficacy [8].

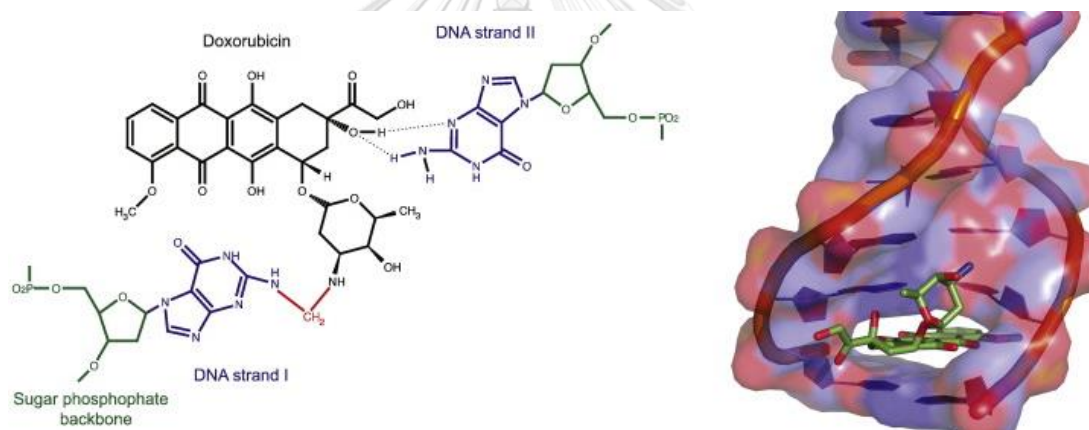


**Figure 5** Chemical structure and action mode of doxorubicin to bind with DNA [22].

### 2.3 Nanotechnologies

Nanotechnologies are speedily growing area of scientific research and are aimed to overcome these problems of all drugs for chemotherapy [4]. Several different types of nanocarriers applied in the design of smart nanocarriers can be classified as polymeric (e.g. polymeric nanoparticles, polymeric micelles, dendimers, polymeric hydrogels and polymer-drug conjugates), lipid-based (e.g. liposomes, solid lipid nanoparticles, phospholipid micelles, nanoemulsions and self-emulsifying drug

delivery), and inorganic nanocarriers (e.g. quantum dot, gold nanoparticles, magnetic nanoparticles, silica nanoparticles and carbon nanotubes), as shown in Figure 6 [23]. Several nanocarriers systems have provide a new platforms for drug delivery, bio-sensing, bio-imaging and chemotherapy [9]. Nanocarriers based delivery of all compounds for cancer prevention and other treatments provide more flexibility in terms of chemistry and structure for synthesis, whereas inorganic nanocarriers have interesting chemical and physical properties including specific optical and other properties [24, 25] Among the board diversity of nanoparticles, gold nanoparticles (AuNPs) have recently emerged as a promising drugs delivery systems for efficient delivery and release of drugs into diverse cell types [10].

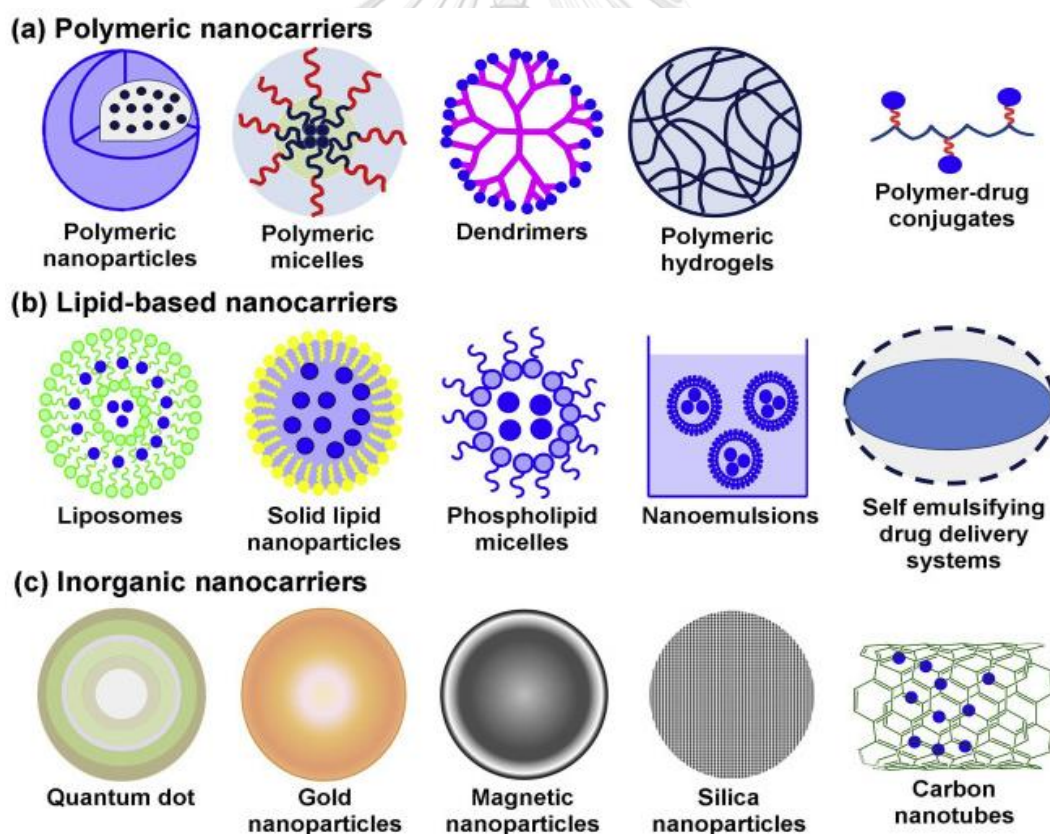


**Figure 6** Several different types of nanocarriers for delivery systems: polymeric, lipid-based, and inorganic nanocarriers [24].

## 2.4 Gold nanoparticle (AuNPs)

Currently, gold nanoparticles (AuNPs) have advantages more than other metallic nanoparticles as potential nanocarriers for targeted drug delivery due to inert material, and unique physicochemical properties. Furthermore, the surface fabrications of AuNPs can be highly tunable properties with the diversity to incorporate multiple drugs by non-covalent or covalent functionalization on the modified surface of AuNPs and their size can be easily fabricated by controlling synthetic approaches [11].

Gold nanoparticles (AuNPs) have generally been synthesized by various methods: (i) physical methods such as laser ablation, UV-irradiations and ultrasonolysis; (ii) chemical methods using chemical reagents such as sodium borohydride, citric acid, and hydrazine; (iii) the supercritical fluid method; (iv) biological methods such as using fungi and bacteria; and (v) utilization of plant extracts. Existing physical and chemical syntheses have successfully generated well-defined nanoparticles. Nevertheless, the reducing reagents and physical methods are quite expensive and hazardous and are not suitable for anticancer drug delivery systems [26, 27]. To overcome these problems, green synthesis of AuNPs is now carried out by using biopolymer-coated AuNPs for cancer therapy, including heparin, chitosan, dextran, cellulose, guar gum and xanthan gum, to provide different shape and size of AuNPs [16]. Nevertheless, these biopolymers have fundamental problems such as low solubility and high viscosity, and they require derivatization with some compounds to the biopolymer backbone with specific applications. Pullulan is a nonionic polysaccharide that shows superior properties such as high water solubility, nontoxicity, biocompatibility and low cost.

Pullulan can be easily modified in order to extend its biomedical applications by grafting different chemical structures onto its backbone (Figure 7) [14]. Moreover, pullulan is generally used in numerous biomedical applications and food industries due to its high solubility and low viscosity [14]. Pullulan is produced from starch by

the growing yeast-like fungus *Aureobasidium pullulans* [28]. In addition, pullulan is a water soluble polysaccharide polymer that is comprised of maltotriose in which the three glucose units are linked by an  $\alpha$ -(1,4) glycosidic bond and the maltotriose units are linked by an  $\alpha$ -(1,6) glycosidic bond [29]. Pullulan has a wide range of commercial and industrial applications in many fields, including pharmaceuticals, food science, biotechnology and health care [30]. The use of a polymeric system as a drug carrier offers several advantages as it protects the payload drugs from the biological environment, improves their water solubility and reduces the side effect.

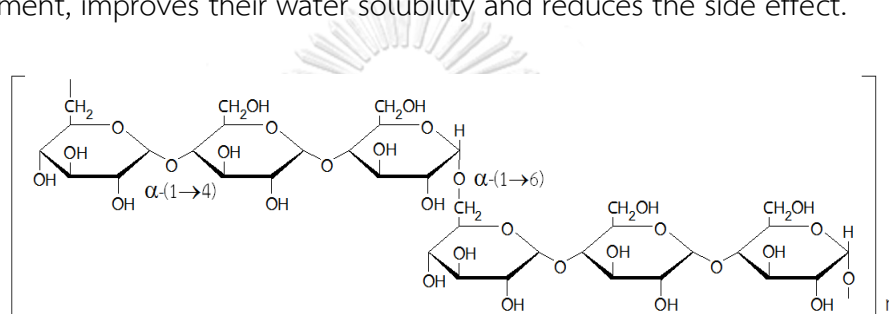


**Figure 7** Chemical structure of pullulan [31].

#### 2.4.1 AuNPs for anticancer drug delivery

Accordingly, current research has focused on the development of novel biomedical nanotechnologies with aim of obtaining treatment with a higher effectiveness, decreased toxicity to normal cells, reduced dose requirement, a wider spectrum of activities to overcome multidrug resistance (MDR), and better selectivity of delivery systems for the drugs to the target cancer cells [20, 32-34]. Today, AuNPs have drawn increasing attention due to their inert, non-toxic and biocompatible potential carriers for payload drug delivery applications [10, 32, 33]. The attachment of the payload anticancer drug to the AuNPs can lead to an enhanced cytotoxicity compared to the free drug because it can accumulate in the targeted cancer cells by endocytosis and enhanced permeability and retention (EPR) effect [32].

Gold nanoparticles (AuNPs) carrying anticancer payloads represent another important class of covalent conjugates (Figure 8). Cancer is a major target of new therapeutics because of the drawbacks associated with current treatment strategies which include large systemic side effects due to the non-specificity of many cancer drugs such as cisplatin, paclitaxel, tamoxifen, and doxorubicin. AuNPs can lead to increased toxicity compared to free anticancer drug and increased specificity of the drug conjugate to cancer cells must be combined with drug [35].

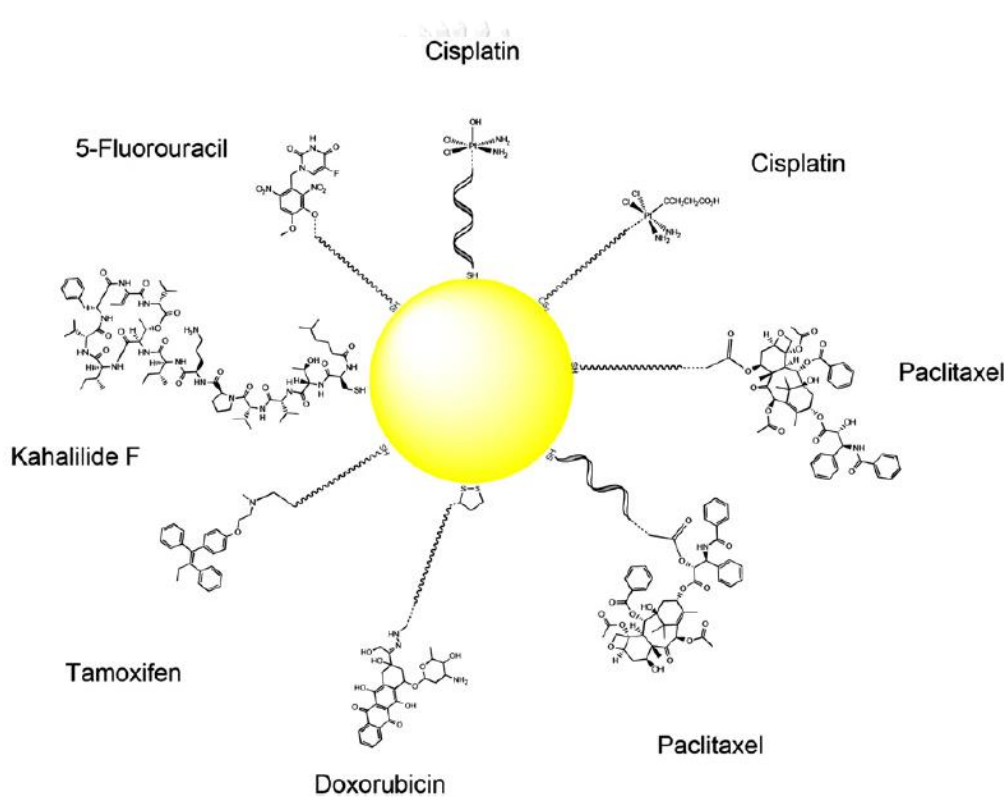


**Figure 8** Summary of antitumor drugs conjugated with AuNPs [32].

In 2011, Wang et al. [33] developed a drug delivery system via tethers doxorubicin (DOX) conjugated with polyethylene glycol (PEG) as a spacer by an acid-labile linkage on the surface of 30 nm gold nanoparticles (AuNPs) for overcoming multidrug resistance (MDR) in cancer cells (Figure 9). The results showed that DOX-Hyd@AuNPs can enhance cytotoxicity, apoptosis, drug accumulation, and inhibit the

growth of multidrug resistant MCF-7/ADR cancer cells by endocytosis and subsequent acid responsive drug release in cells when compared with the direct incubation of cancer cells with free doxorubicin. Moreover, in MCF-7/ADR cells, the  $IC_{50}$  of DOX-Hyd@AuNPs ( $IC_{50} = 1.82 \mu\text{g/mL}$ ) was nearly six times less than that of free DOX ( $IC_{50} = 10.12 \mu\text{g/mL}$ ).

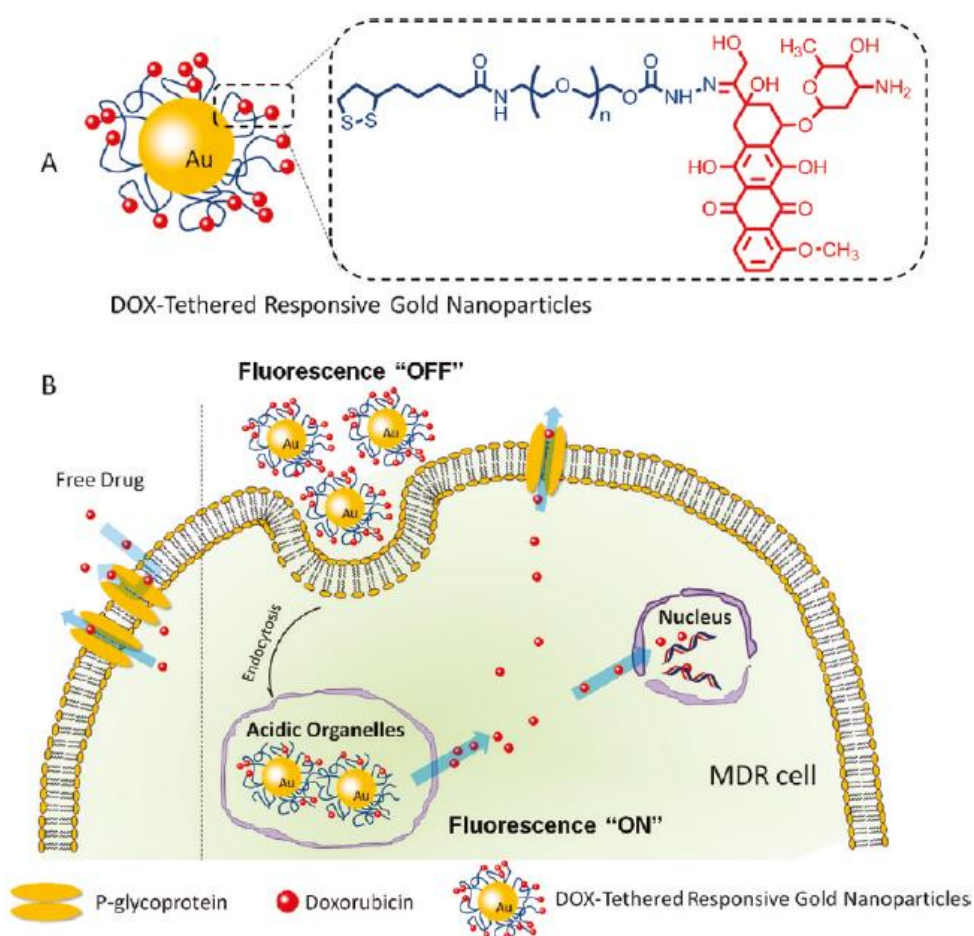


**Figure 9** (a) Design illustration of doxorubicin-tethered responsive AuNPs. (b) The cooperation between increased DOX cellular entry and an intracellular release of DOX in cancer cells for overcome drug resistance [33].

In 2010, Brown et al. [34] improved anticancer agent delivery of the oxaliplatin with AuNPs (Figure 10). The platinum-tethered AuNPs showed significantly higher

cytotoxicity than free oxaliplatin against A549 lung cancer cell lines, and the PEGylated AuNPs exhibited cellular uptake by endocytosis.

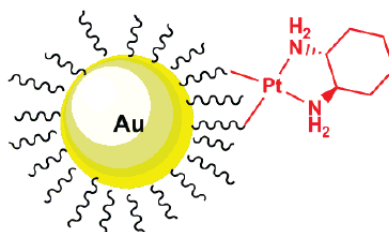


**Figure 10** Structure of platinum tethered AuNPs [34].

In 2009, Dreaden et al. [36] synthesized tamoxifen-PEG-SH (TAM-PEG-SH) attachments to AuNPs conjugates (Figure 11) that can be applied to selectively deliver plasmonic AuNPs onto an estrogen receptor bearing cell line. The synthesized conjugates were found to have an up to 2.7-fold enhanced anticancer potency against breast cancer cells with a high estrogen receptor expression level.

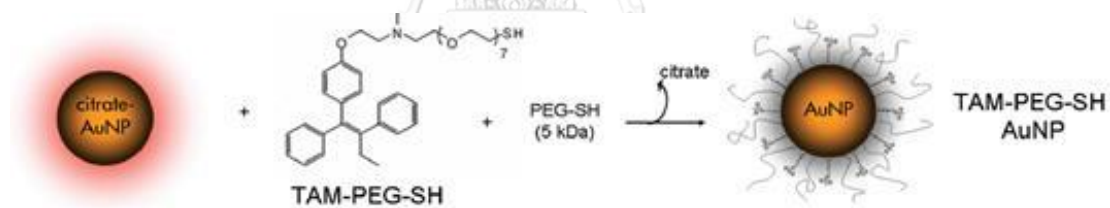


**Figure 11** Preparation of TAM-PEG-SH attachments to AuNPs [36].

In 2012, Gu et al. [37] developed a gold nanoparticles functionalized via thiolated DOX-drug molecule (DOX-SH) with disulfide bond (Au-PEG-SS-DOX) for overcoming MDR (Figure 4). The result showed that the enhanced cytotoxicity and intracellular uptake by endocytosis of Au-PEG-SS-DOX was greater than the free DOX in MDR HepG2-R liver cancer cell line at a nanoparticles dose greater than 15  $\mu\text{M}$  and its conjugated can be cleaved via thiol-reducing enzymes aided from an acidic pH into the lysosome.



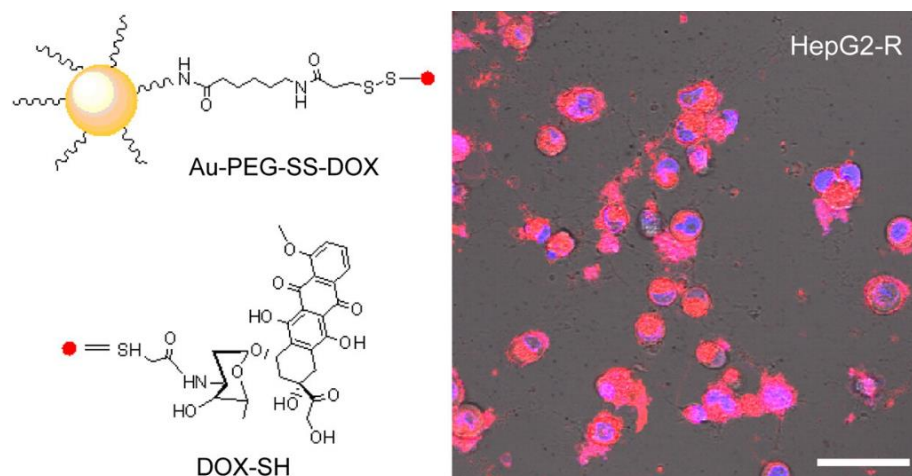


**Figure 12** Intracellular uptake of AuNPs functionalized via thiolated DOX (Au-PEG-SS-DOX) to MDR HepG2-R cells as observed by confocal scanning microscopy [37].

#### 2.4.2 Active and passive targeted nanocarriers for drug delivery

For anticancer drug applications, the goals of nanocarriers are to arrive at the diseased tissues after administration into circulatory systems. Two systems have been developed for targeting including passive and active targeted nanocarriers (Figure 13). Passive targeted nanocarriers depends on homing of the vectors in cancer cells owing to extravasation through leaky blood vessel (gaps by approximately 600 nm). An important aspect of carrier systems in the 5-20 nm is their efficacy to take advantage of the enhanced permeation and retention (EPR) effect. Moreover, active targeted nanocarriers presents targeting ligands on nanocarriers surface for specific recognition by cell surface receptors. The targeting ligands could be small molecules, peptides or proteins. Combination of both types of targeting will render an ideal carrier for drug delivery systems [38].

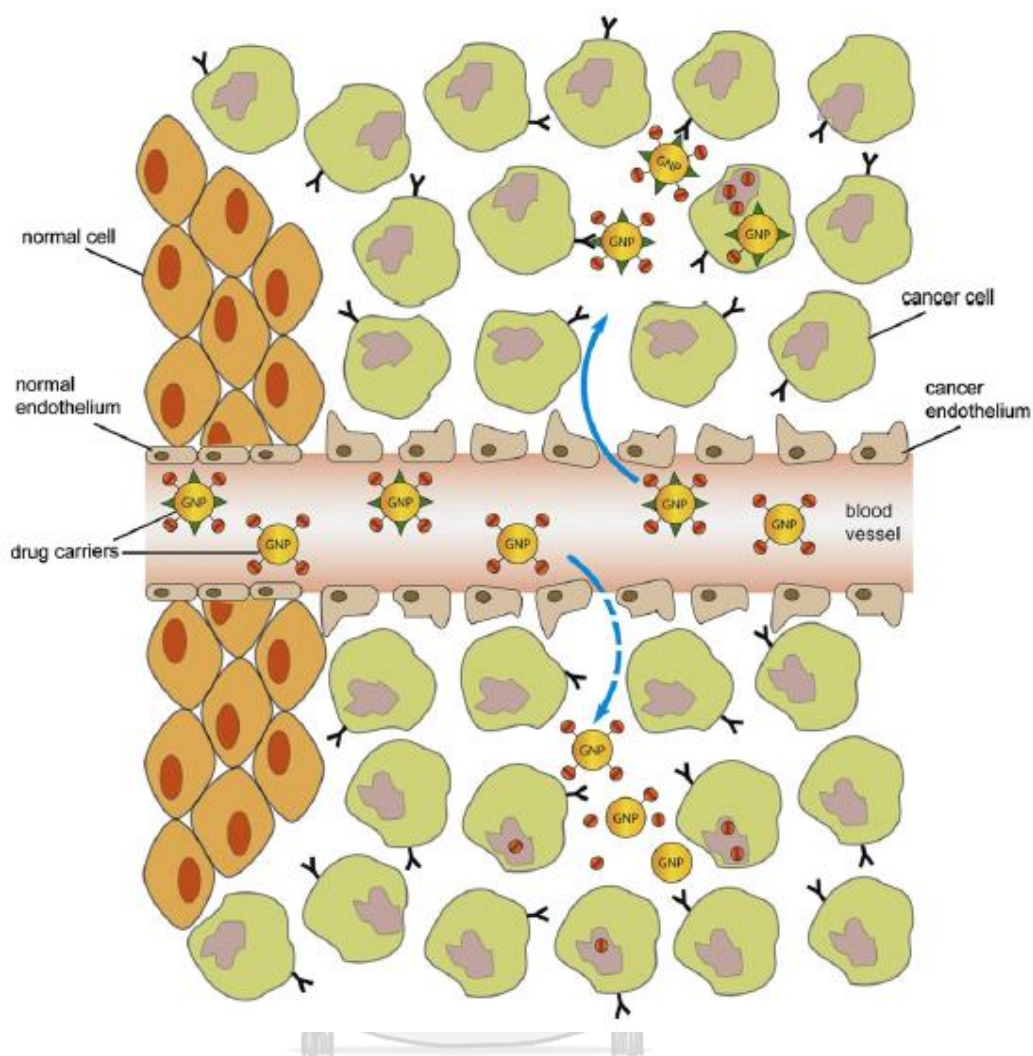


**Figure 13** A schematic illustration of by active and passive targeting drug delivery systems [38].

CHULALONGKORN UNIVERSITY

### 2.4.3 Shape and particle size of AuNPs for drug delivery

AuNPs are widely accepted that physicochemical properties of nanoparticles, predominantly size and surface characteristics, inherently study their behavior in biological activity and systems, and their intracellular uptake. There is mounting evidence that shape and size of AuNPs also plays a main role both *in vitro* and *in vivo* cytotoxicity [39].

For example, In 2016, Adnan and co-worker [39] compared three different AuNPs shapes (spherical, rod and star) for delivery of doxorubicin. The resulting grafting density was compared between the three different AuNPs. Spherical AuNPs exhibited the highest grafting density of the drug conjugated polymer on AuNPs (Figure 14).

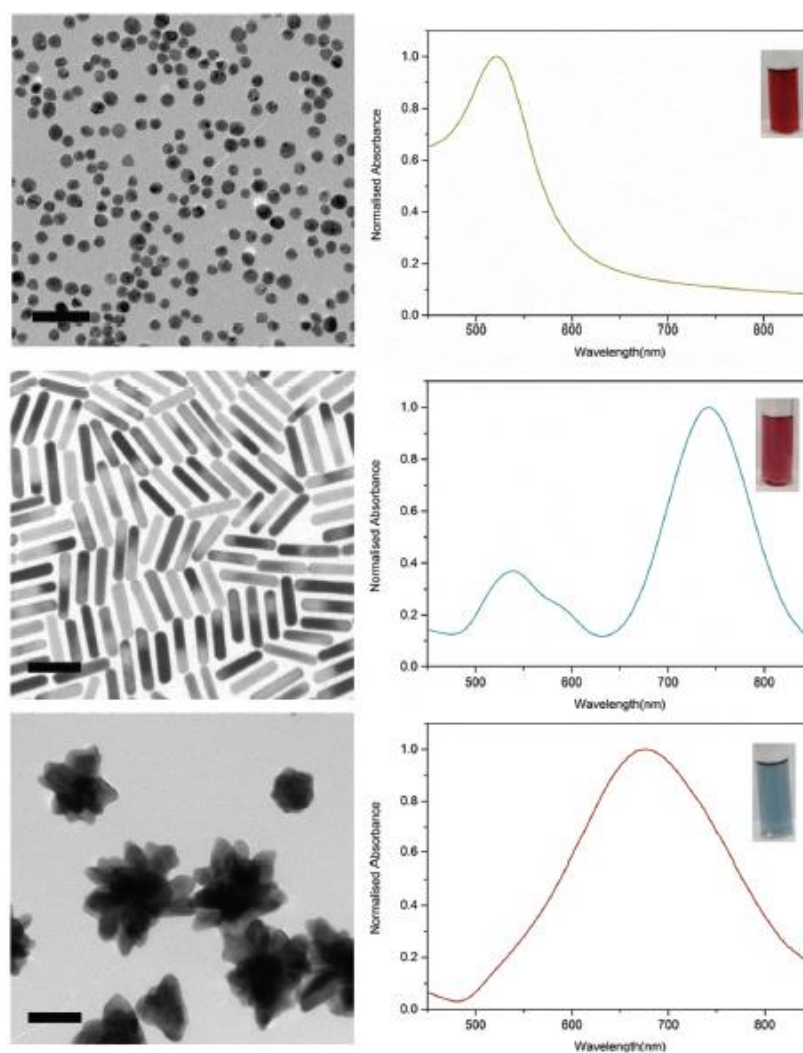


**Figure 14** Effect of gold nanoparticle shapes for drug delivery [39].

In 2012, Freese and co-worker [40] prepared fifteen sequentially modified AuNPs based on three different core sizes (18, 35 and 65 nm). In general, the smallest AuNPs (18 nm) were internalized in the highest amount compared with 35 and 65 nm-sized, respectively, by ICP-AES technique (Figure 15). Similarly, Yao and co-workers [41]

studied the influence of particle size and concentration of AuNPs on their absorption, accumulation, and cytotoxicity in model intestinal epithelial cells. As the mean particle size of the AuNPs decreased (from 100 to 50 to 15 nm), their rate of absorption by the intestinal epithelium cells increased (Figure 16). Also, the small particle size of AuNPs showed better than bigger particle size.

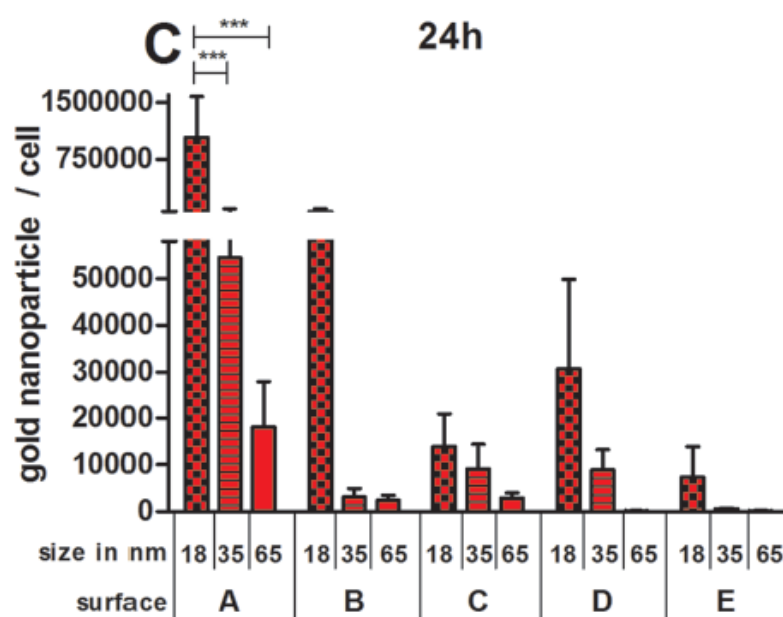


**Figure 15** Quantification of AuNPs uptake per cell is presented. The different surface modifications are named by the coding ((A) ethanediamine, (B) glucosamine, (C) hydroxypropylamine, (D) taurine, and (E) PEG based on three different core sizes (18, 35 and 65 nm) [40].

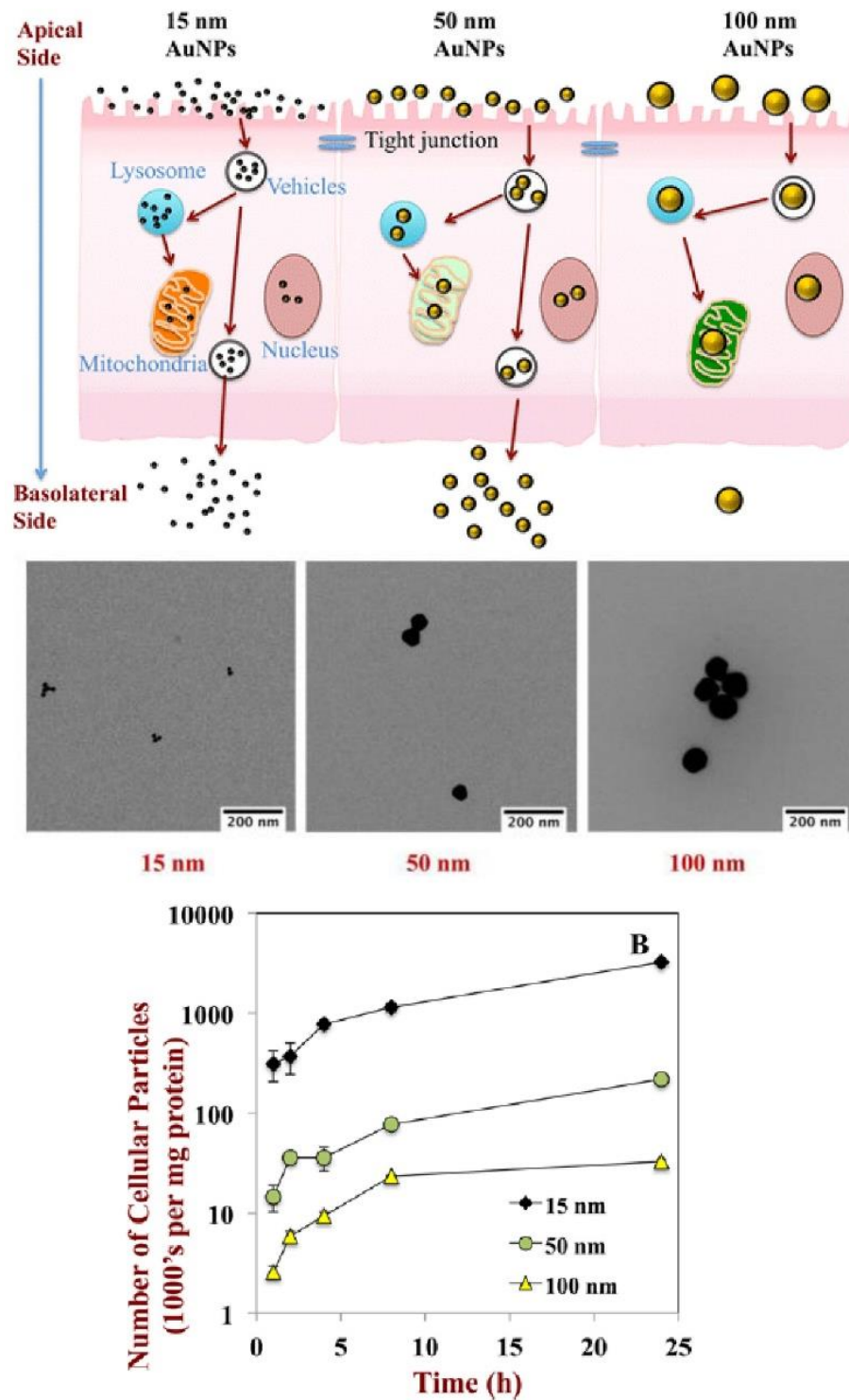


**Figure 16** Accumulation of AuNPs (15, 50 and 100 nm) within the intestinal epithelium: change in the amount of gold measured in the Caco-2 monolayers [41].

#### 2.4.4 Surface functionalization of AuNPs for drug delivery

Surface functional compound is one of the important factors influencing the properties of nanoparticles. Previous reports have been developed the activity of AuNPs through their surface functionalization. The modification with positive charge, hydrophobic part and targeting ligand in order to enhanced selective intracellular uptake and ability of these systems. To enhance the cellular uptake of AuNPs as an anticancer drug delivery system, the modifications of polysaccharide with positive charge, hydrophobic molecule, and targeting ligand were carried out [42].

For instance, Noh and co-worker [43] exhibited high enhanced cellular delivery and transfection of plasmid DNA into cells by using cationic modified AuNPs due to strong electrostatic interactions with the negative charge of cells. The cytotoxicity and uptake of cationic AuNPs depend on their size, shape, morphology and surface grating, which are related to their enhanced activity relative to that of anionic nanoparticles [44]. Hydrophobic modified chitosan were used to reduce and coat onto AuNPs which help enhance efficacy and intracellular uptake of hydrophobic anticancer drugs [45]. Furthermore, folate targeting attached PEGylated AuNPs showed targeting of cancer cells efficiently. Doxorubicin-loaded nanocarriers were produced using folate-modified PEG-functionalized AuNPs for targeted delivery to positive folate-receptor cancer cells which showed high delivery, cellular uptake and cytotoxicity of DOX in KB cells [46].

In 2014, Ganeshkumar et al. [47] found that FA-targeted 5-Fluorouracil-loaded AuNPs@pullulan (Figure 17) could significantly decrease  $IC_{50}$  when treated with Hep-G2 liver cancer cells. These 5-Fu-AuNPs@pullulan-FA had higher concentrations in liver of zebrafish embryo compared to non-targeted AuNPs@pullulan. The FA as targeting ligand increases cellular uptake after accumulation in cancer cells through binding and endocytosis.

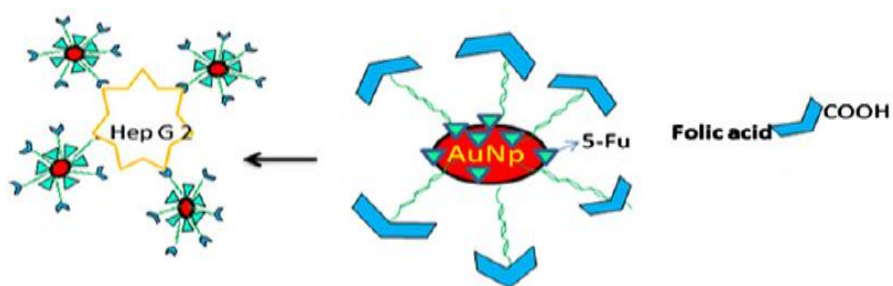


**Figure 17** The targeted drug delivery system of 5-Fu-AuNPs@pullulan-FA [47].

#### 2.4.5 Localized surface plasmon resonance (LSPR)

Localized surface plasmon resonance (LSPR) is a unique photophysical phenomenon for metal nanoparticles. It is a collective electron oscillation of metal particles where upon excitation by incident light at the same frequency as surface electron oscillation at the interface and the surrounding the metal particles, as shown in Figure 18. The photon energy is changed to thermal energy, which is known as an absorption phenomenon. Moreover, plasmon can be also accelerated, it can radiate energy in any directions and which is a scattering process. Therefore, the light extinction is sum of the absorption and the scattering. The frequency and intensity of LSPR band is characteristic of the type of metal nanoparticles, size and shape of nanostructures. For spherical gold nanoparticles (AuNPs) with 5-20 nm size has the light extinction maxima at 520 nm in the visible range and to give red color solutions [48, 49].

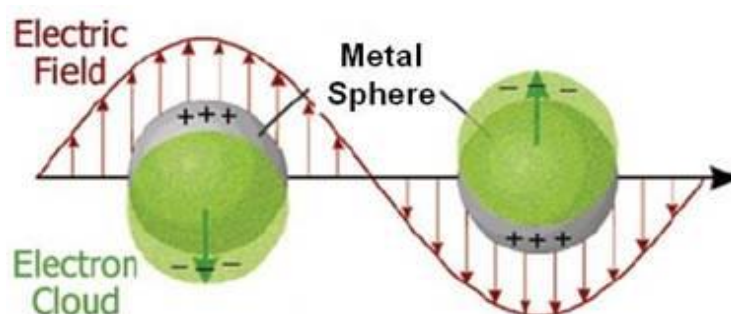


**Figure 18** Localized surface plasmon resonance (LSPR) of AuNPs [48].

## 2.5 Cytotoxicity by MTT assay

MTT assay is a colorimetric assay for assessing cell viability. The yellow tetrazolium MTT dye is reduced by metabolically active cells, in part by the action of mitochondrial reductase enzymes as shown in Figure 19. The enzymes are capable of reducing the MTT dye into purple formazan can be solubilized and quantified by spectrophotometric means.

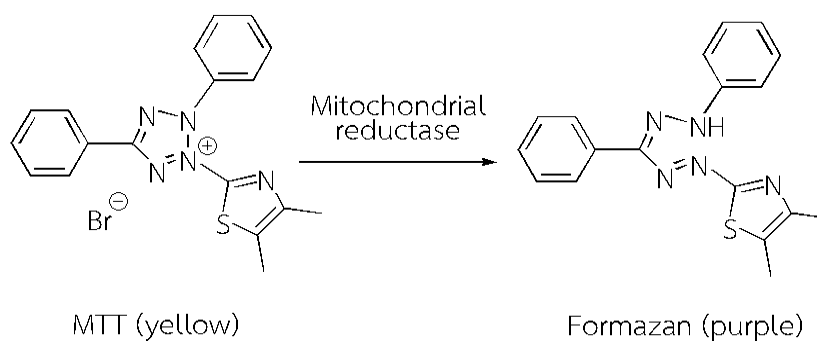


**Figure 19** Reduction of MTT into formazan dye in living cells.

MTT [3-(4,5-dimethylthiazol-2-yl)-2,5-diphenyltetrazolium bromide], a yellow tetrazole, is reduced to purple formazan in living cells [50]. The solution of dimethyl sulfoxide (DMSO) is added to dissolve the insoluble purple formazan crystal product into a colored solution. The absorbance of this colored solution can be quantified by measuring at a certain 540 nm by a spectrophotometer. The absorption maximum is dependent on the solvent employed. When the absorbance of purple formazan which produce by living cells treated with a drugs is compared with cells untreated or control cells.



## 2.6 Apoptosis assay

Apoptosis is a normal genetically programmed process that occurs during embryonic development, as well as in maintenance of tissue homeostasis, under pathological conditions, and in aging. The term apoptosis, from the Greek word for “falling off” of leaves from a tree, is used to describe a phenomenon in which a cell actively participates in its own destructive processes [51]. The process is characterized by specific morphologic features, including loss of plasma membrane asymmetry and attachment, plasma membrane blebbing, condensation of the cytoplasm and nucleus, and internucleosomal cleavage of DNA. Loss of plasma membrane asymmetry is one of the earliest features of apoptosis [52-54]. In apoptotic cells, the membrane phospholipid phosphatidylserine (PS) is translocated from the inner to the outer leaflet of the plasma membrane, thereby exposing PS to the external cellular environment. Annexin V is a 35-36 kDa  $\text{Ca}^{2+}$ -dependent phospholipid-binding protein with high affinity for PS, and binds to exposed apoptotic cell surface PS [55]. Annexin V can be conjugated to fluorochromes while retaining its high affinity for PS and thus serves as a sensitive probe for flow cytometric analysis of cells undergoing apoptosis [56] as shown in Figure 20.

PS translocation precedes the loss of membrane integrity, which accompanies the later stages of cell death resulting from either apoptotic or necrotic processes. Therefore, staining with Annexin V is typically used in conjunction with a vital dye such as propidium iodide (PI) for identification of early and late apoptotic cells. Viable cells with intact membranes exclude PI, whereas the membranes of dead and damaged cells are permeable to PI. Therefore, cells that are considered viable are both Annexin V<sup>-</sup>PI<sup>-</sup>, while cells that are in early apoptosis are Annexin V<sup>+</sup>PI<sup>-</sup>, and cells that are in late apoptosis or already dead are both Annexin V<sup>+</sup>PI<sup>+</sup>. This assay does not distinguish between cells that have undergone apoptotic death versus those that have died as a

result of a necrotic pathway because they will also stain with both Annexin V and PI. However, when apoptosis is measured over time, cells can often be tracked from Annexin V<sup>-</sup>PI<sup>-</sup> (viable, or no measurable apoptosis), to Annexin V<sup>+</sup>PI<sup>-</sup> (early apoptosis with intact membranes), and finally to Annexin V<sup>+</sup>PI<sup>+</sup> (end stage apoptosis and death). This process is summarized in Figure 21.

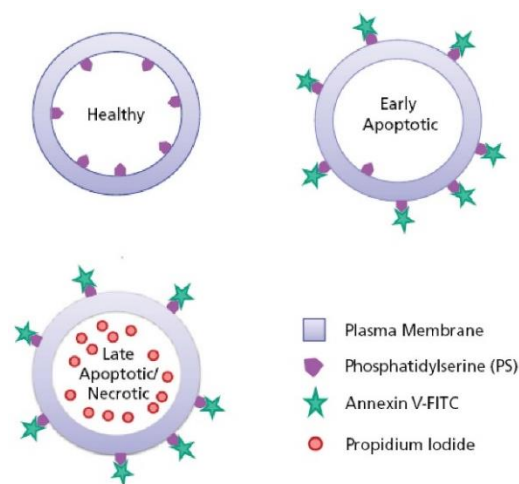


**Figure 20** Diagram showing healthy and apoptotic cells with markers for detection of apoptosis [52].

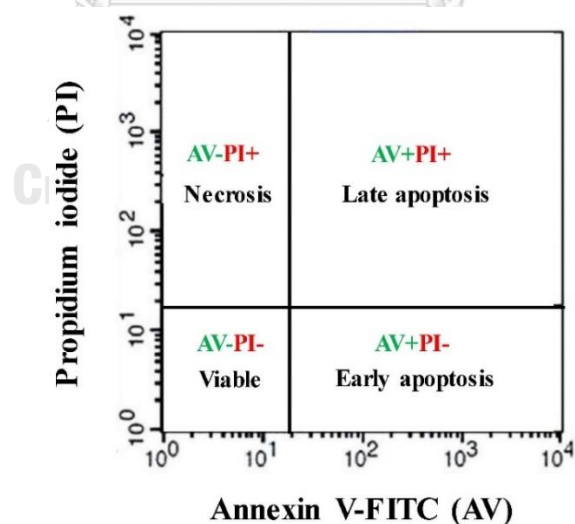


**Figure 21** Flow cytometric quadrant dot plot of apoptotic cancer cells after 24 h treatment with drug. Apoptosis of cancer cells as detected by Annexin-V-FITC/PI dual staining method [52].

## 2.7 Cell death: apoptosis and necrosis pathways

Cell death process can be divided into two classes: apoptosis and necrosis [57].

(i) Apoptosis (programmed cell death) is generally occurred by normal, healthy processes in the body and targeted cause of cellular death. This causes cells to shrink, develop blebs on the cells, undergo genetic and protein degradation in nucleus, and have their mitochondria collapse. The fragments are each wrapped in their own membrane, with other chemicals released. These chemicals lead macrophages to eliminate the fragments and dead cells. The macrophages in turn release cytokines that inhibit inflammatory responses.

(ii) Necrosis (unplanned cell death) is generated by external factors such as trauma or infection which result in the unregulated digestion of cell components. Necrosis begins with cell swelling, the chromatin gets digested, the plasma and organelle membranes are disrupted, the organelles break down completely and finally the cell lyses, spewing its intracellular content and eliciting an immune response (inflammation).

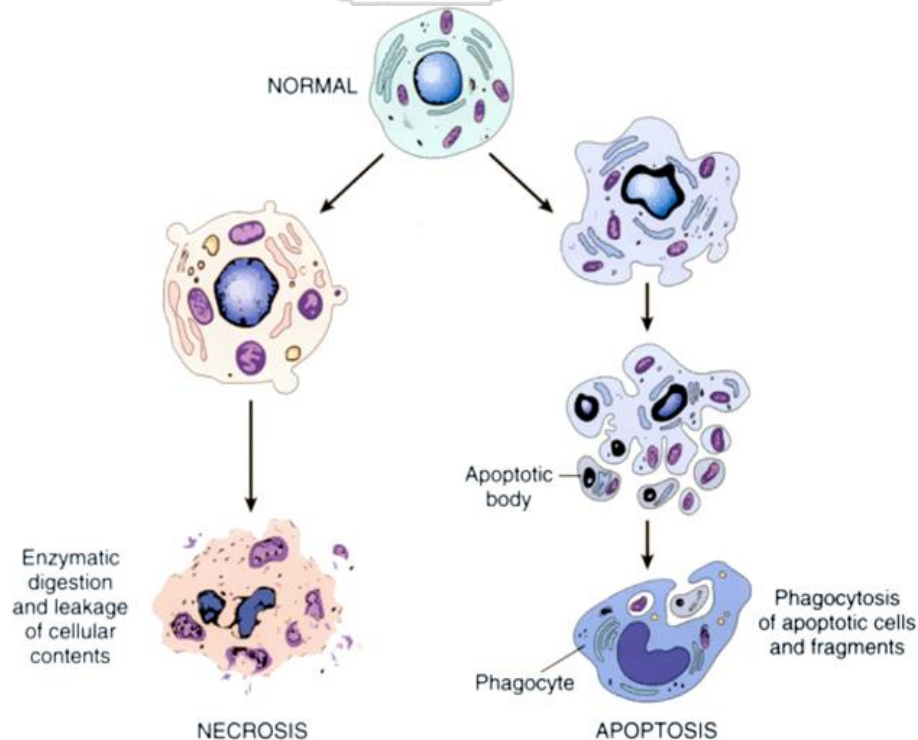


**Figure 22** Cell death process including apoptosis and necrosis pathways [57].

## 2.8 The cell cycle

The cell cycle consists of five distinct phases:  $G_0$ ,  $G_1$ , S (synthesis),  $G_2$  (interphase) and M phase (mitosis) as follows (Figure 23).

- (i)  $G_0$  phase: Cells have left the cycle and has stopped dividing.
- (ii)  $G_1$  phase:  $G_1$  checkpoint control mechanism ensures that is ready for DNA synthesis and Cells increase in size.
- (iii) S phase: DNA replication occurs.
- (iv)  $G_2$  phase: Cells continue to grow.  $G_2$  checkpoint control mechanism ensures that is ready to enter M phase and divide.
- (v) M phase: Cell growth stops at this stage and cellular energy is focused on the orderly division into two daughter cells. A checkpoint in the middle of mitosis ensures that the cell is ready to complete cell division [58].

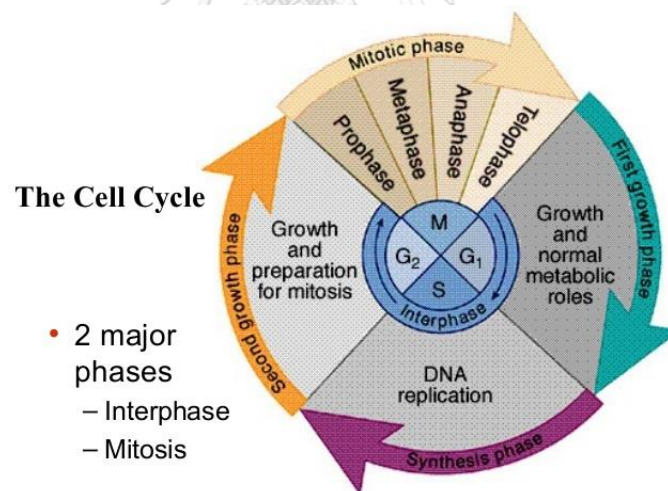


**Figure 23** The cell cycle consists of four distinct phases [58].

## CHAPTER III

### EXPERIMENTAL

#### 3.1 Analytical instruments

##### 3.1.1 Nuclear magnetic resonance spectroscopy (NMR)

The  $^1\text{H}$  NMR and  $^{13}\text{C}$  NMR data at 400 MHz and 101 MHz were recorded on a Varian Mercury plus spectrometer and a Bruker model ACF200 spectrometer at Chulalongkorn University, respectively. All chemical shifts ( $\delta$ ) of all samples (pullulan and pullulan derivatives) were reported in part per million (ppm) relative to a residual proton or a carbon signal in deuterated solvents peak using  $\text{D}_2\text{O}$  solvent as internal reference. Coupling constants ( $J$ ) were reported in Hertz (Hz). The  $^1\text{H}$  NMR and  $^{13}\text{C}$  NMR spectra were processed with a MestReNova software.

##### 3.1.2 Attenuated total reflectance fourier transform infrared spectroscopy (ATR-FTIR)

The ATR-FTIR spectra were recorded on a Nicolet 6700 ATR-FTIR spectrophotometer at Chulalongkorn University. The ATR-FTIR spectra of all samples (pullulan and pullulan derivatives) were recorded in the region from  $4000\text{ cm}^{-1}$  to  $400\text{ cm}^{-1}$  in ATR transmittance mode. The solid samples prepared and spectra reported in wavenumber ( $\text{cm}^{-1}$ ).

##### 3.1.3 Thermogravimetric analysis (TGA)

The TGA has been widely used for characterization of polymeric materials. Thermal stability of each of pullulan and pullulan derivatives was evaluated by thermogravimetric analysis (TGA) using a PerkinElmer Pyris Diamond TG/DTA machine

under a nitrogen flow rate of 30 mL/min. Approximately 5 mg of samples were placed in the aluminum oxide pan, sealed and heated at 20°C /min from 50 to 600°C.

#### **3.1.4 Ultraviolet and visible spectrophotometry (UV-VIS)**

The UV-visible spectra of all samples were recorded on a UV-Visible spectrophotometer (HP-8453, Agilent) at Chulalongkorn University. The UV-visible spectra were recorded in the range from 200 nm to 800 nm and cell width is 1 cm.

#### **3.1.5 X-ray diffraction (XRD)**

The crystal phases of H<sub>2</sub>AuCl<sub>4</sub>, AuNPs@pullulan (AuNPs@P) and AuNPs@pullulan derivatives (AuNPs@QP, AuNPs@PABA-QP and AuNPs@FA-PABA-QP) were characterized using a D/AX 2200 X-ray diffractometer (Rigaku, Japan) with Cu (K $\alpha$ ) radiation at an accelerating voltage of 40 kV and an applied current of 30 mA. The XRD patterns of AuNPs@pullulan derivatives were recorded at  $2\theta$  in the range 30-80°.

#### **3.1.6 Transmission electron microscopy (TEM)**

TEM images were recorded on a transmission electron microscope (TEM, JEOL, JEM2001) an operating at 200 kV accelerating voltage. The morphologies of gold nanoparticles (AuNPs) were observed by TEM. The samples for TEM observations were obtained by dropping the reaction solution in dilutions of 5  $\mu$ L onto carbon coated copper grids without any purification in desiccators overnight.

#### **3.1.7 X-ray photoelectron spectroscopy (XPS)**

The X-ray photoelectron spectrometry (XPS) measurement was carried out using a Kratos Axis Ultra DLD spectrometer equipped with Al K $\alpha$  radiation. The residual pressure in the ion-pumped analysis chamber was below  $5 \times 10^{-7}$  torr. XPS spectra were record with pass energy of 160 eV for survey scan and 20 eV for narrow scan. The

spectra of Au (4f) were recorded in cycles at a binding energy range of 77-92 eV and calibrated by assigning the binding energy of C 1 s to 284.6 eV.

### 3.1.8 Zeta-potential analysis

The surface charge of AuNPs using pullulan and its derivatives before and after was determined by measurement of zeta potential. The zeta potential ( $\zeta$ ) was determined using a Malvern Zeta Potential Analyzer (Malvern instrument Ltd, Zetasizer version 7.01).

### 3.1.9 Fluorescence spectroscopy

The fluorescence spectra of samples were recorded on a fluorescence spectrophotometer (Cary Eclipse, Agilent Technologies) at Chulalongkorn University. The concentration of doxorubicin hydrochloride (DOX) and camptothecin (CPT) were determined by fluorescence maximum emission wavelength at 594 and 436 nm, with excitation at 490 and 390 nm using fluorescence spectroscopy, respectively. The fluorescence spectra of DOX and CPT loaded on AuNPs@pullulan derivatives were recorded in the range from 490-800 and 390-750 nm and cell width is 1 cm, respectively.

### 3.1.10 Inductively coupled plasma optical emission spectroscopy (ICP-OES)

The inductively coupled plasma optical emission spectrometer (iCAP 6500 ICP-OES, Thermo Scientific) was used to measure the mass fractions of Au element using calibration curves generated from standard solutions and AuNPs in all sample after synthesis and after intracellular uptake in cancer cells.

### 3.1.11 Confocal laser scanning microscopy (CLSM)

The coverslips of all sample after treatment in Chago-k1 cells were observed under the confocal laser scanning microscope (FLUOVIEW FV3000, Olympus Corporation., Tokyo, Japan) fitted with a camera, using computer-based programmable image analyzer (OLYMPUS FLUOVIEW FV30S-SW, Olympus Micro).

### 3.1.12 Flow cytometry

The intracellular fluorescence detections of all samples were performed on a fluorescence-activated cell sorting (FACS) flow cytometer (Cytomics FC500MPL, Bectan Coulter Inc., USA). At least  $10^6$  cells of each sample were measured. Then, FITC and PI dye emissions were detected in FL1 and FL3 channels, respectively. Acquired data were analyzed by FlowJo flow cytometry analysis software.

## 3.2 Materials and chemicals

Pullulan (P) with Mw of ~50-70 kDa and *N*-(3-chloro-2-hydroxypropyl) trimethylammonium chloride (Quat188) were purchased from TCL, Japan. *N,N'*-dicyclohexylcarbodiimide (DCC), 4-dimethyl aminopyridine (DMAP), *para*-aminobenzoic acid (PABA), folic acid (FA), 3-(4,5-dimethylthiazol-2-yl)-2,5-diphenyltetrazolium bromide (MTT) dye were obtained from Sigma-Aldrich, USA. Doxorubicin hydrochloride (DOX) and camptothecin (CPT) was obtained from Beijing Packbuy M&C Co., Ltd. Cellulose dialysis tubing (Membrane Filtration Products, USA) with a 12-14 kDa Mw cut-off was used to purify all modified pullulan derivatives. All other chemicals were purchased from Fluka, Merck and Sigma-Aldrich chemicals Co., Ltd. All solvents for reactions were AR grade and purified according to standard procedures.



### 3.3 The experimental methods

The materials and methods in experimental sections are divided into four parts as shown in Figure 24:

**Part I:** Design, synthesis and characterization of pullulan and its derivatives as a trifunctional reducing, stabilizing and capping agent for synthesis of gold nanoparticles (AuNPs).

**Part II:** Synthesis and characterization of pullulan derivatives reduced/stabilized/capped gold nanoparticles (AuNPs@pullulan derivatives) as targeted nanocarriers for anticancer drug delivery systems.

**Part III:** Preparation and characterization of anticancer drugs loaded on AuNPs@pullulan derivatives for enhancing anticancer activities.

**Part IV:** Evaluation of their cytotoxicity against human cancer and normal cells, intracellular uptake, drug release, and anticancer mechanism (cell cycle and apoptosis assay) of AuNPs@pullulan derivatives.

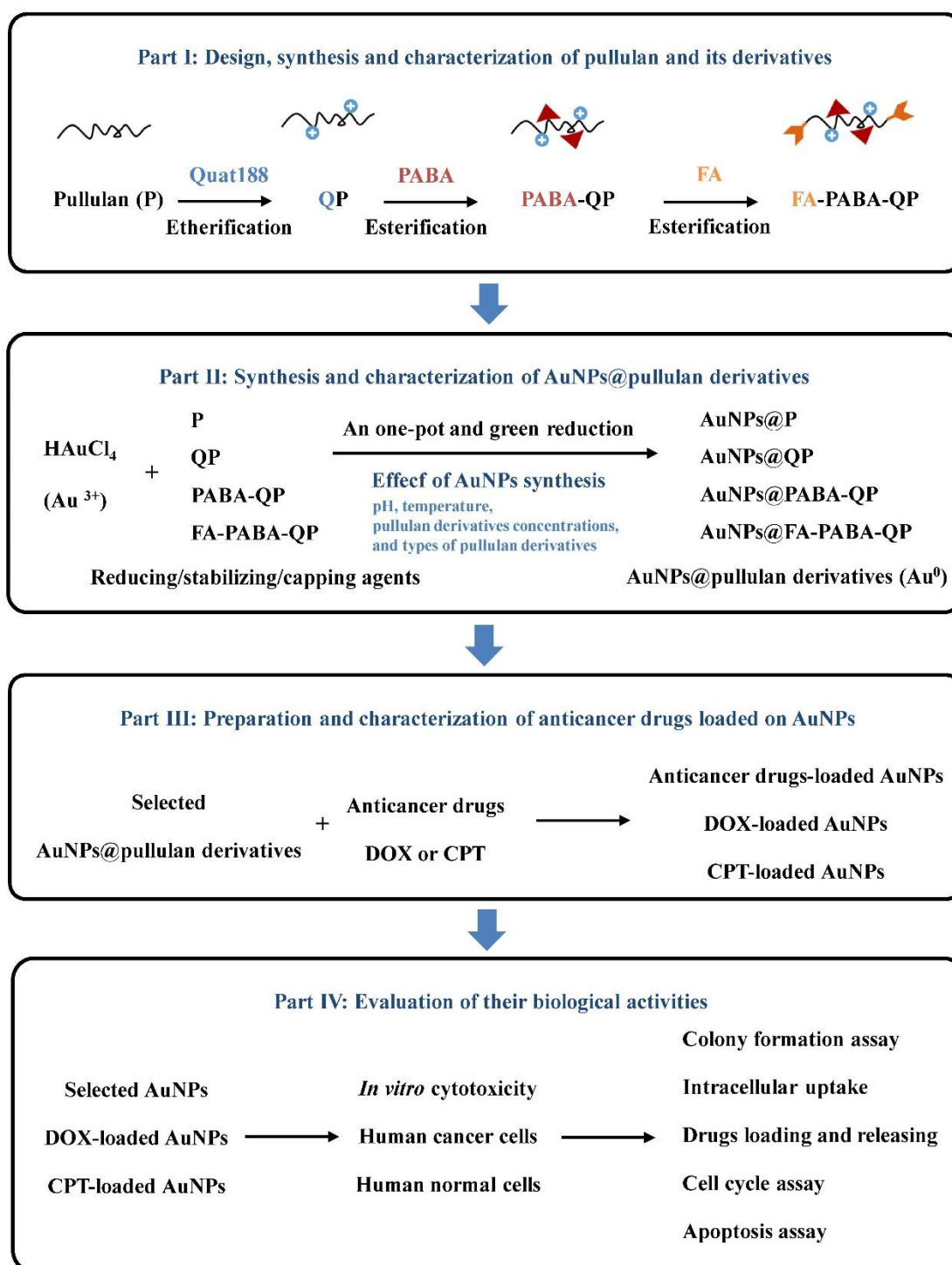


**Figure 24** The materials and methods in experimental procedures are divided into four parts.

Part I: Design, synthesis and characterization of pullulan and its derivatives as a trifunctional reducing, stabilizing and capping agent for synthesis of gold nanoparticles (AuNPs).

### 3.3.1 General procedure for synthesis of pullulan and its derivatives

Pullulan (P) was designed and synthesized to contain three components as follows. First, positive charge from quat188 by etherification of quaternized pullulan increases the electrostatic interactions between stabilizer and AuNPs and enhance the electrostatic interactions with negative charged cell membranes (QP). Second, hydrophobic part of *para*-aminobenzoic acid (PABA) creates intermolecular interactions for enhanced compatibility with drugs and hydrophobic parts of cells [16] (PABA-QP). Finally, folic acid (FA) as targeted ligand increases the receptor-mediated endocytosis pathway of AuNPs, which is overexpressed into human cancer cells (FA-PABA-QP) as shown in Figure 25.

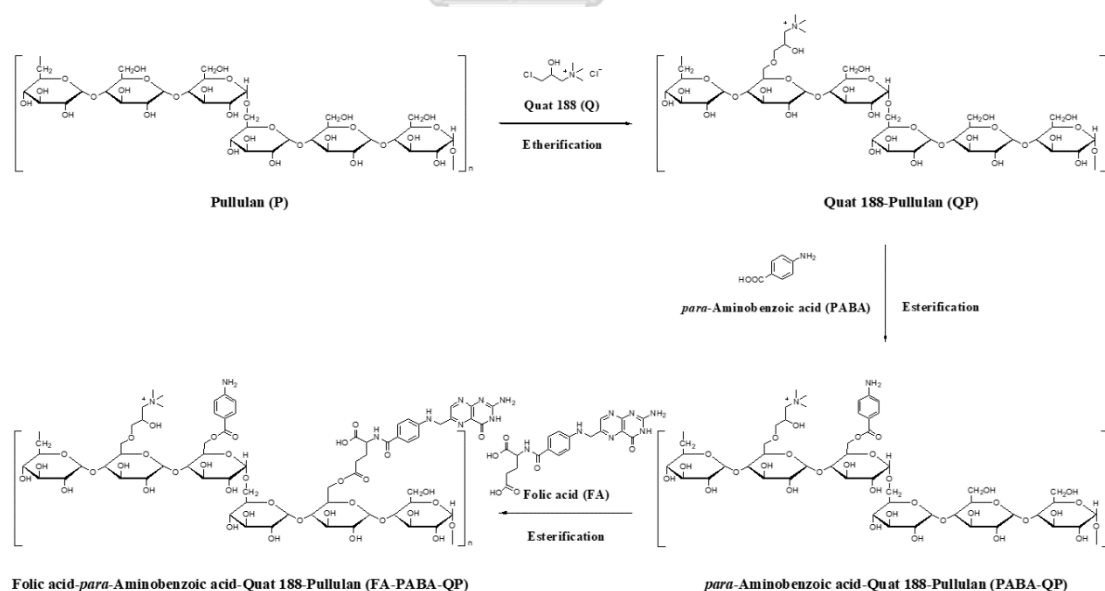


**Figure 25** Schematic representation of pullulan and its derivatives (QP, PABA and FA-PABA-QP).

### 3.3.2 Synthesis of quat188-pullulan (QP) by etherification

The etherification of pullulan was carried out using the epoxide form of *N*-(3-chloro-2-hydroxypropyl) trimethylammonium chloride (Quat188). Pullulan (P, 6 g) was dissolved in 45 mL of deionized (DI)-water, and then Quat188 (3.2 g) and NaOH (1.2 g) were dissolved in DI-water (15 mL). After adding Quat188/NaOH into the mixture, the reaction was continued at 60 °C for 24 h. Upon cooling, the mixture was neutralized to pH of 6-7 with concentrated hydrochloric acid (conc. HCl). The mixture was then precipitated in acetone, centrifuged, washed and dialyzed by DI-water for 3 days to remove the residual chemicals to obtain product. The QP sample was collected and dried at 60°C in an oven (yield 92% and white solid). The synthetic pathway and molecular structure of QP are shown in Figure 26.

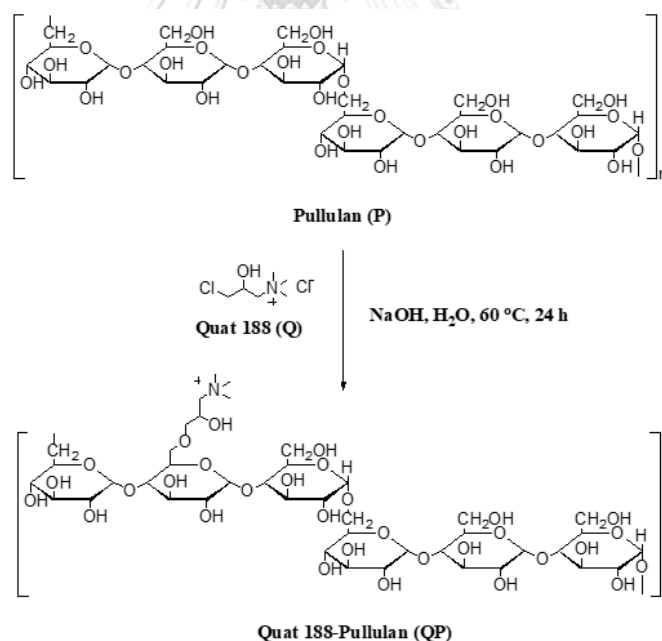


**Figure 26** Synthetic pathway of quat188-pullulan (QP) by etherification.

### 3.3.3 Synthesis of *para*-aminobenzoic acid-quat188-pullulan (PABA-QP) by esterification

PABA-QP conjugations via DMAP/DCC-mediated ester formations were used the modified method from previously studied [59]. The QP (5 g) was dissolved in 40 mL of DMSO by stirring at 60 °C for 0.5 h until a clear solution was produced. Then, 1100 mg of *para*-aminobenzoic acid (PABA) was activated in 20 mL of DMSO with 550 mg of DMAP at room temperature for 0.5 h. After adding 1100 mg of DCC in 10 mL of DMSO into the mixture solution, the reaction was continued at room temperature for 24 h. The mixture was then precipitated in acetone, centrifuged, washed and dialyzed by phosphate buffer (pH 7.4) for 3 days and DI-water for 2 days using a dialysis membrane. The product was collected and dried at 60°C in an oven (yield 89% and white solid). The synthetic pathway and molecular structure of PABA-QP are shown in Figure 27.

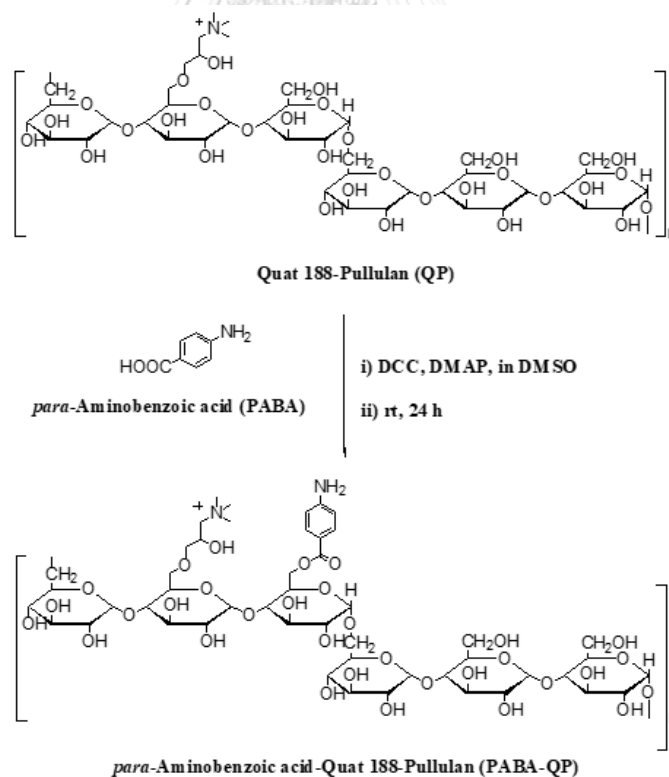


**Figure 27** Synthetic pathway of *para*-aminobenzoic acid-quat188-pullulan (PABA-QP) by esterification.

### 3.3.4 Synthesis of folic acid-*para*-aminobenzoic acid-quat188-pullulan (FA-PABA-QP) by esterification

FA-PABA-QP conjugations by esterification were used the modified method [59]. PABA-QP (3 g) was dissolved in 30 mL of DMSO by stirring at 60 °C for 0.5 h, after that 1350 mg of folic acid (FA) and 750 mg of DMAP were added. After adding 1350 mg of DCC into the mixture solution, the reaction was continued to proceed at room temperature for 24 h. The mixture was then precipitated using acetone, centrifuged and dialyzed by phosphate buffer (pH 7.4) for 3 days and distilled water for 2 days using a dialysis membrane. The FA-PABA-QP was collected and dried at 60 °C in an oven (yield 85% and yellow solid). The total PABA and FA contents were calculated with a linear equation based on the standard curve of PABA and FA. The synthetic pathway and molecular structure of FA-PABA-QP are shown in Figure 28.

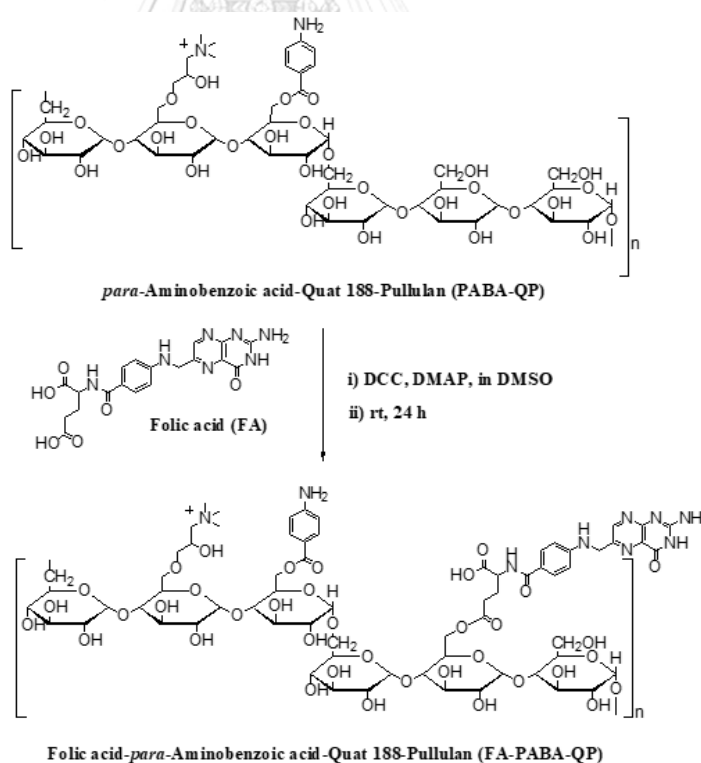


**Figure 28** Synthetic pathway of folic acid-*para*-aminobenzoic acid-quat188-pullulan (FA-PABA-QP) by esterification.

### 3.3.5 Calculation of degree of quaternization (%DQ) and substitution (%DS)

$^1\text{H}$  NMR spectra of pullulan (P), QP, PABA-QP, and FA-PABA-QP in  $\text{D}_2\text{O}$  were recorded on a 400 MHz NMR spectrometer. The degree of quaternization (%DQ) of quat188 and substitution (%DS) of PABA and FA on pullulan backbone were evaluated from  $^1\text{H}$  NMR by comparing the ratio of integral peaks using Eq.(1) for %DQ [60] and Eq.(2-3) for %DS<sub>PABA</sub> and %DS<sub>FA</sub> [61], respectively.

$$\%DQ = \left[ \frac{I_{[\text{Hb}]}}{I_{[\text{H1}]}} \times \frac{1}{9} \right] \times 100 \quad (1)$$

$$\%DS_{PABA} = \left[ \frac{I_{[\text{Hc-Hd}]}}{I_{[\text{H1}]}} \times \frac{1}{4} \right] \times 100 \quad (2)$$

$$\%DS_{FA} = \left[ \frac{I_{[\text{He-Hg}]}}{I_{[\text{H1}]}} \times \frac{1}{5} \right] \times 100 \quad (3)$$

Here,  $I_{[\text{Hb}]}$  is integration of trimethyl amino group's protons of quat188 at 3.24 ppm.

$I_{[\text{Hc-Hd}]}$  is the total integration of the protons of aromatic ring of PABA between 6.85 and 7.92 ppm.

$I_{[\text{He-Hg}]}$  is the total integration of the protons of aromatic ring of FA at 6.65, 7.65 and 8.67 ppm.

$I_{[\text{H1}]}$  is the total integration of H1 protons of pullulan between 4.95 and 5.37 ppm.

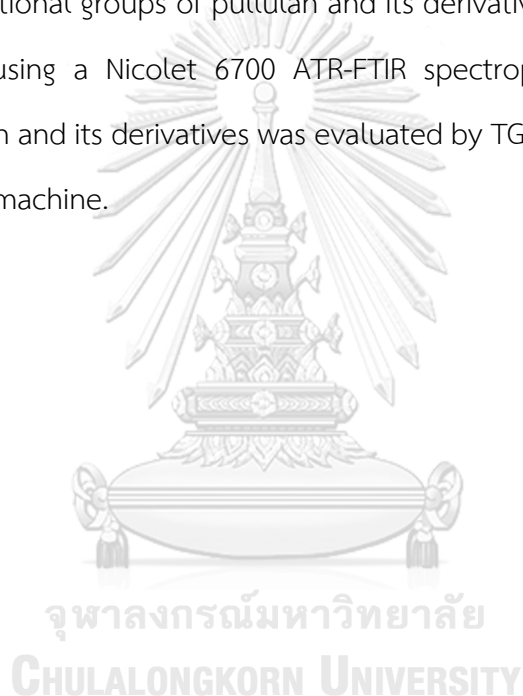
### 3.3.6 Determination of PABA and FA content in pullulan derivatives

The total PABA and FA contents that conjugated on pullulan backbone were calculated by determination of absorbance intensity at 295 and 360 nm using UV-vis spectrophotometer, respectively. Moreover, the linear equations based on the standard equation of PABA and FA from UV-vis spectra were prepared in the range of

0.1-5.0 and 10-70 ppm, respectively. The total PABA and FA contents of PABA-QP and FA-PABA-QP were expressed as mg of PABA and FA per g of PABA-QP and FA-PABA-QP.

### 3.3.7 Characterization of pullulan and its derivatives

The chemical structure of P, QP, PABA-QP and FA-PABA-QP and their degrees of quaternization of quat188, and degrees of substitution of PABA and FA were determined by  $^1\text{H}$  NMR using a Varian Mercury plus spectrometer. The chemical structure and functional groups of pullulan and its derivatives were analyzed by ATR-FTIR techniques using a Nicolet 6700 ATR-FTIR spectrophotometer. The thermal stability of pullulan and its derivatives was evaluated by TGA using a PerKinElmer Pyris Diamond TG/DTA machine.

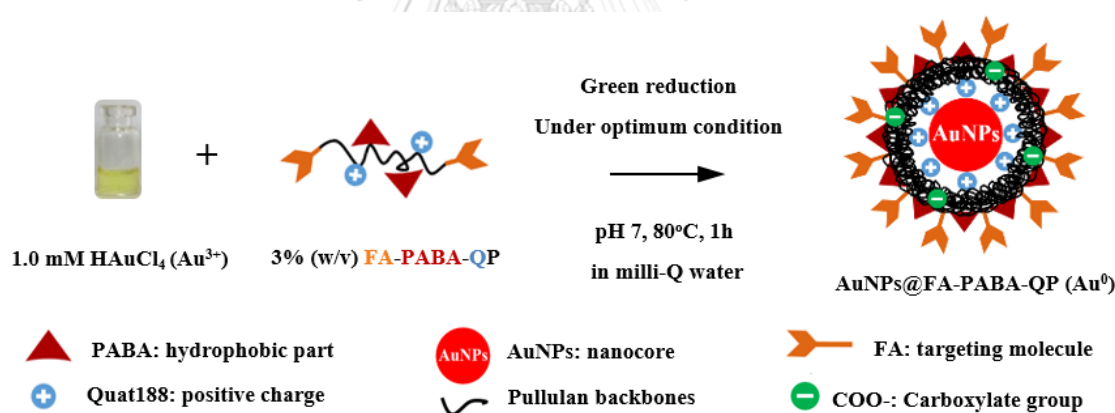




Part II: Synthesis and characterization of pullulan derivatives reduced/stabilized/capped gold nanoparticles (AuNPs@pullulan derivatives) as targeted nanocarriers for anticancer drug delivery systems.

### 3.3.8 Synthesis of AuNPs@pullulan derivatives

The synthesis process, AuNPs@pullulan derivatives were synthesized by green reduction and an efficient approach of using  $\text{HAuCl}_4$  with pullulan derivatives as a trifunctional reducing/stabilizing/capping agent. In this work, AuNPs were monitored with the color change and UV-vis spectroscopy. Moreover, the effects of pH, temperature, selected pullulan derivatives concentrations and types of reducing/stabilizing/capping agent were studied based on their ability to control the morphology and size of AuNPs as shown in Figure 29.



**To study their ability to control the morphology and particle size of AuNPs as follows:**

- The effects of pH (4, 7 and 10)
- The effects of temperature (RT, 60, 80, 100 °C)
- The effects of selected pullulan derivative concentration (1, 3, 5 and 7% w/v)
- The effects of type of pullulan derivatives (P, QP, PABA-QP and FA-PABA-QP)

**Figure 29** Synthetic pathway of AuNPs formations using pullulan and its derivatives under optimal conditions.

AuNPs@pullulan derivatives formations were used the modified method from previously studied [14]. Stock solutions of 5 mM HAuCl<sub>4</sub>, 6% (w/v) pullulan (P) and its derivatives (QP, PABA-QP and FA-PABA-QP) in milli-Q water and 5% (w/v) NaOH were prepared. In a typical reaction procedure, 700  $\mu$ L of 6% (w/v) pullulan and its derivatives were mixed with 40  $\mu$ L of 5% (w/v) NaOH solution at 80°C for 1 h. Then, the pH of the mixture solution was adjusted to 7 by using 0.1-1.0 M NaOH and HCl. Then, 280  $\mu$ L of 5 mM HAuCl<sub>4</sub> was added dropwise into the mixed solution and continued at 80°C for 1 h. The color changed from yellow to red, confirming the formation of gold nanoparticles (AuNPs) under optimal conditions. The mixed solution was reconstituted to the final volume of 1.4 mL with milli-Q water. After synthesis, the AuNPs solutions were kept at 0-5 °C. In this work, the effects of pH (4, 7 and 10), temperature (RT, 60, 80, 100 °C), selected pullulan derivatives (PABA-QP and FA-PABA-QP) concentration (1, 3, 5 and 7% w/v), and type of pullulan derivatives (P, QP, PABA-QP and FA-PABA-QP) were also evaluated to study their ability to control the morphology and particle size distributions of AuNPs under reactions of the same type to determine the role and ability of molecules modified on pullulan and its derivatives.

### 3.3.9 Characterization of AuNPs@pullulan derivatives

The formations and localized surface plasmon resonance (LSPR) bands of gold nanoparticles (AuNPs) using pullulan and its derivatives under optimal conditions were characterized by UV-vis (HP-8453 UV-Visible spectrophotometer) and photographs. The concentration of gold element was determined by ICP-OES (iCAP 6500 inductively coupled plasma optical emission spectrometer). The morphology, shape, and particle size distributions and particles charges of AuNPs under green reduction reactions of the same type were characterized by TEM (JEM2001 transmission electron microscope) and zeta-potential analysis (Malvern Zeta Potential Analyzer). The crystal phases and chemical compositions of HAuCl<sub>4</sub> and AuNPs were characterized by XRD (Rigaku X-ray

diffractometer), SAED-TEM, EDS-TEM, XPS (Kratos Axis Ultra DLD X-ray photoelectron spectrometer) and ATR-FTIR (Nicolet 6700 ATR-FTIR spectrophotometer).

**Part III: Preparation and characterization of anticancer drugs loaded on AuNPs@pullulan derivatives for enhancing anticancer activities.**

### 3.3.10 Preparation of anticancer drugs (DOX or CPT) loaded on AuNPs

A calculated amount of DOX and CPT was added to AuNPs@pullulan derivative dispersion, resulting in a final DOX and CPT of 100  $\mu$ M. The mixture of DOX and AuNPs using pullulan and its derivative dispersion was incubated for 12 hours at room temperature and then centrifuged at 12,000 rpm for 30 min. The obtained pellet after centrifugation was separated from the supernatant solution to further characterization. Drug loading was calculated by estimating DOX and CPT content of the supernatant in the AuNPs@pullulan derivatives. The amount of drug (DOX and CPT) concentration in supernatant was determined by the fluorescence maximum emission wavelength at 594 and 436 nm, with excitation at 480 and 380 nm using fluorescence spectroscopy (Cary Eclipse, Agilent Technologies), respectively. The percentage loading of DOX and CPT onto AuNPs@pullulan derivatives was calculated by using Eq. (4) [7, 62].

$$\% \text{ Drug loading efficiency} = (A-B/A) \times 100 \quad (4)$$

Where, A is the total amount of DOX or CPT added to AuNPs and B is the amount of DOX or CPT in supernatant after centrifugation. B was determined in the same detection procedure as mentioned above. The chemical structure of DOX-loaded and CPT-loaded onto AuNPs using pullulan and its derivatives as shown in Figure 30.

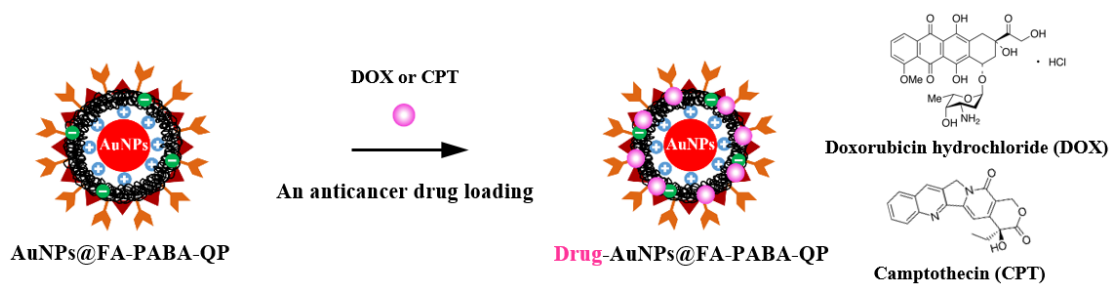


**Figure 30** Preparations and proposed chemical structure of DOX-loaded and CPT-loaded onto AuNPs using pullulan and its derivatives.

### 3.3.11 Characterization of anticancer drugs (DOX or CPT) loaded on AuNPs

The anticancer drugs (DOX and CPT) loading onto AuNPs using pullulan and its derivatives was also confirmed and characterized by UV-vis (HP-8453 UV-Visible spectrophotometer), ATR-FTIR (Nicolet 6700 ATR-FTIR spectrophotometer) and zeta potential analyses (Malvern Zeta Potential Analyzer). Additionally, the amount of drug (DOX and CPT) concentration in supernatant was determined by the fluorescence spectroscopy (Cary Eclipse, Agilent Technologies).

Part IV: Evaluation of their cytotoxicity against human cancer and normal cells, intracellular uptake, drug release, and anticancer mechanism (cell cycle and apoptosis assay) of AuNPs@pullulan derivatives.

### 3.3.12 Cell culture and reagents

The *in vitro* cytotoxic activity of all target samples was evaluated by using an MTT assay against seven human cancer cell lines of BT474 (breast cancer cells), SW620 (colon cancer cells), Hep-G2 (liver cancer cells), Chago-k1 (lung bronchogenic cancer cells), KATO-III (gastric cancer cells), KB (cervical cancer cells) and A549 (lung adenocarcinoma cells). All cancer cell lines were cultured in complete medium comprised of RPMI-1640 medium with 10% (v/v) fetal calf serum (FCS), while Wi-38 (human normal lung cell lines) was maintained in MEM medium with 10% (v/v) fetal calf serum, while CCD (normal skin fibroblast cell lines) was maintained in IBM medium with 10% (v/v) fetal calf serum and 2%(v/v) L-glutamine. Cultured cells were incubated at 37 °C in 5% carbon dioxide (CO<sub>2</sub>) and moisture-enriched atmosphere and it were passaged by trypsin. All cells were routinely passaged every three-four days.

### 3.3.13 Cytotoxicity studies by MTT assay

Determination of the cytotoxic activity of the compounds was based on the reduction of (3-(4,5-dimethylthiazol-2-yl)-2,5-diphenyltetrazolium bromide (MTT) dye by viable cells to generate a purple formazan product, whose absorbance was detected at 540 nm. Cancer cells were seeded at  $5 \times 10^3$  cells/well (200  $\mu$ L; 96-well plates) and incubated at 37°C for 24 h, after which 20  $\mu$ L/well of the test compound dissolved in DMSO and milli-Q water at various concentrations (0.001-1000  $\mu$ M) was added to triplicate wells per concentration per test compound and incubated for 72 h. Next, 10  $\mu$ L of MTT solution (5 mg/mL) was added into each well and incubated for 4 h prior to removal of the medium and the addition of 150  $\mu$ L of DMSO to each well

with aspiration to lyse the cells and dissolve the formazan. The  $A_{540}$  was then read using a 96-well plate reader, and the obtained value was assumed to represent the number of viable cells. The  $A_{540}$  of the control cells (only DMSO added) was taken as 100% and all other values were expressed as a percentage of the control as the %cell viability. The  $IC_{50}$  values, the concentration of an inhibitor that reduces the response by half, were calculated using the GraphPad Prism 5 software. The percent cell viability was calculate for each compound using the following Eq. (5) [14, 63]:

$$\% \text{ Cell viability} = (A/B) \times 100 \quad (5)$$

Where, A and B were the absorbance of the experimental and control cells, respectively.

#### **3.3.14 Cell morphology study**

Lung cancer cell line (Chago-k1) were plated in 96-well plates (5,000 cells/well) and incubated with all compounds and combinations at various concentrations for 72 h. Cells cultured in RPMI 1640 medium without the addition of the compounds and combinations were used as a non-treated control group. After treatment, the cell morphologies were imaged by using an optical microscope (Nikon DS-L3).

#### **3.3.15 Colony formation assay**

The colony formation assay that was also used to confirm the anticancer activity of all compounds and combinations after treatments. Selected Chago-k1 cancer cells were seeded in a 24-well plate in triplicate at a density of 1000 cells/well. After 24 h, serial dilutions of the combinations were added. After 10 days, the Chago-k1 cells were removed from the medium, washed in PBS, fixed with 0.5% glutaraldehyde, and then stained with 0.5% crystal violet for 30 min. After staining, the

Chago-k1 cells were thoroughly washed with DI-water. Colonies were imaged on an optical microscope (Nikon DS-L3) [14, 63].

### 3.3.16 Intracellular uptake study

Chago-k1 cancer cells were seeded at  $5 \times 10^3$  cells/well and incubated at 37 °C for 1 day, after which AuNPs@pullulan derivatives at the requisite final concentration (40  $\mu$ M) was added and incubated for 3 days. Next, the medium was removed and washed twice with 5 mL of PBS. The cells were then detached with trypsin, harvested and centrifuged at 1000 rpm for 5 min. The cells were fixed with 2.5% (w/v) glutaraldehyde in 0.1 M PBS and then with osmium tetroxide prior to being dehydrated in an ethanol series and then imbedded into resin (70°C, 9 h). Thin sections (90 nm) were taken using an ultramicrotome and stained with uranyl acetate and lead citrate. All samples were then characterized by TEM [14].

### 3.3.17 Confocal study

Confocal laser scanning microscope (CLSM) was used to investigate the intracellular uptake of DOX and CPT as an anticancer drug. Chago-k1 cells were seeded on glass-bottom dishes at a density of  $5 \times 10^3$  cells per dish in 0.5 mL of RPMI containing 10% FCS and incubated for 24 h at 37 °C. Cells were incubated with AuNPs@PABA-QP, AuNPs@FA-PABA-QP, DOX, CPT, DOX-AuNPs@PABA-QP, DOX-AuNPs@FA-PABA-QP and CPT-AuNPs@FA-PABA-QP at a final DOX, CPT and AuNPs using PABA-QP and FA-PABA-QP concentration of 0.3, 5.0 and 40  $\mu$ M for 12 h, respectively. The culture media was removed and the cells were rinsed with PBS for three times. After that, the nuclei were stained with 15  $\mu$ L of DAPI/Antifate solution (0.4 mg/mL) for 20 min. Then, the cells were washed three times with PBS. Fluorescence images of cells were obtained with an Olympus FV3000 confocal laser scanning microscope [64].

### 3.3.18 *In vitro* drug release profiles

Two samples of DOX-AuNPs@PABA-QP, DOX-AuNPs@FA-PABA-QP and CPT-AuNPs@FA-PABA-QP after loading at 100  $\mu\text{M}$  were suspended in 5 mL of PBS solution at pH 7.4, which represents the pH of the physiological blood and normal tissues in the human body, and acetate buffer at pH 5.0, which represents the average acidity of vesicles in intracellular endosomes and lysosomes (the range of pH=4.5-6.5), with constant shaking in the dark at 37 °C. At specific intervals, a certain volume of buffer was removed from the tubes and then also was returned to the same tubes. The concentrations of DOX and CPT in the released buffer were detected and determined by the fluorescence maximum emission wavelength at 594 and 436 nm, with excitation at 480 and 380 nm using fluorescence spectroscopy (Cary Eclipse, Agilent Technologies), respectively [65, 66]. The cumulative release of DOX and CPT into AuNPs@pullulan derivatives was calculated by using Eq. (6).

$$\% \text{ Cumulative drug release} = (\text{Released drug} / \text{Total drug}) \times 100 \quad (6)$$

### 3.3.19 Cell cycle assay

The analysis of cell cycle was analyzed by PI staining. Briefly, Chago-k1 cancer cells were treated with 40  $\mu\text{M}$  AuNPs@PABA-QP, 40  $\mu\text{M}$  AuNPs@FA-PABA-QP, DOX, CPT, DOX-AuNPs@PABA-QP, DOX-AuNPs@FA-PABA-QP and CPT-AuNPs@FA-PABA-QP at a final concentration of DOX (0.15 and 0.30  $\mu\text{M}$ ), and CPT (2.5 and 5.0  $\mu\text{M}$ ). After 24 h, Chago-k1 cells were harvested and washed with PBS after a gentle centrifugation at concentration of  $1 \times 10^6$  cells/mL. The cells were resuspended in PBS and fixed in 70% ethanol for at least 4 h at -20 °C. The fixed cells were washed twice in PBS and incubated for 30 min in the dark with DNase-free RNase A (0.5 mg/mL) and PI (0.02 mg/mL). Then, the data was analyzed by FACS analysis. Acquired data were analyzed by FlowJo V10 flow cytometry analysis software [63].



### 3.3.20 Apoptosis assay

Apoptosis/necrotic cells were detected by Annexin V-FITC/PI staining according to the manufacture's instruments (ImmunoTools, Germany). Chago-k1 cancer cells ( $2 \times 10^6$  cells/well) were treated with 40  $\mu\text{M}$  AuNPs@PABA-QP, 40  $\mu\text{M}$  AuNPs@FA-PABA-QP, DOX, CPT, DOX-AuNPs@PABA-QP, DOX-AuNPs@FA-PABA-QP and CPT-AuNPs@FA-PABA-QP at a final concentration of DOX (0.15 and 0.30  $\mu\text{M}$ ), and CPT (2.5 and 5.0  $\mu\text{M}$ ), respectively. After 12 h, Chago-k1 cells were harvested and washed twice with cold PBS followed by resuspension in 90  $\mu\text{L}$  of binding buffer and incubated with 5  $\mu\text{L}$  of Annexin V-FITC and 5  $\mu\text{L}$  of PI at 0-5  $^{\circ}\text{C}$  in dark for 20 min. Then, 400  $\mu\text{L}$  of binding buffer was added to each tube, mixed gently and kept the samples on ice. As soon as possible, samples were analyzed by FC500 flow cytometer (Beckman Coulter). FITC and PI emissions were detected in the FL1 and FL3 channels, respectively. Acquired data were analyzed by FlowJo V10 flow cytometry analysis software.

## CHAPTER IV

### RESULTS AND DISCUSSION

Currently, gold nanoparticles (AuNPs) in particular have continued to attract considerable attention for several decades due to their specific physical and chemical properties, such as optics, nanostructure fabrications, catalytic activity, sensing and bio-affinity, leading to a broad range of possible uses in pharmaceutical applications such as excellent drug delivery systems [27]. Moreover, AuNPs have been extensively studied as nanocarriers for enhanced therapeutic activity due to their inert, nontoxic nature and good biocompatibility, which not only provides biomedical benefits but also enables them to act as a tracer for diagnostic imaging. The advantages of these AuNPs are their easy monodispersed fabrication and their high surface area, which facilitates drug-loading [45]. In previous reports, the synthetic methods of AuNPs involved difficult approaches, long times, and the use of toxic and expensive chemicals that are not suitable for drug delivery applications. Moreover, there have been no reports of a facile and eco-friendly synthesis of AuNPs using novel pullulan and its derivatives as a reducing/stabilizing/capping agent without external toxic reagents. Therefore, we focus on the development of AuNPs using novel pullulan and its derivatives as a trifunctional reducing/stabilizing/capping agent for drug delivery systems in order to enhance their anticancer efficacy and reduce the side effects.

**Part I: Design, synthesis and characterization of pullulan and its derivatives as a trifunctional reducing, stabilizing and capping agent for synthesis of gold nanoparticles (AuNPs).**

The choice of conjugated functional molecules on pullulan backbone allowed the controlled fabrication of AuNPs and the surface functionalization of AuNPs with applications in cancer treatment. Pullulan (P) was synthesized to contain three structural components as shown in Figure 31:

- (i) The positive charge of quaternized pullulan from Quat188 of  $[+N(CH_3)_3]$  increases the electrostatic interactions between the positive charge of the stabilizer and the negative charge of the AuNPs surface.
- (ii) The hydrophobic compound of *para*-aminobenzoic acid (PABA) creates hydrogen bonding and  $\pi$ - $\pi$  stacking interactions for enhanced compatibility with anticancer drugs.
- (iii) Folic acid (FA) as targeted ligand creates intermolecular interactions for enhanced compatibility with anticancer drugs and increases the receptor-mediated endocytosis pathway of AuNPs, which is overexpressed into human cancer cells (FA-PABA-QP).

Another interesting point is that the functional groups modified onto pullulan derivative-capped AuNPs not only generate intermolecular interactions but are also beneficial for enhancing biological efficacy [67]. Another interesting point is that the functional groups modified onto pullulan derivative-capped AuNPs not only generate intermolecular interactions but are also beneficial for enhancing biological efficacy [16]. Subsequently, we characterized AuNPs and DOX-loaded AuNPs and evaluated their enhanced cytotoxicity with supporting cell cycle and apoptosis assay. In addition, Quat188, PABA and FA modified on pullulan backbone can increase cell uptake and cell permeability in biological processes as follows:

- (i) Quat188 can enhance the electrostatic interactions with the negative charge of cell membranes.
- (ii) PABA can increase the hydrophobic interactions with the hydrophobic parts of cell membranes and enhance biocompatibility with cells.
- (iii) FA can increase intracellular uptake via folate receptor-mediated endocytosis pathways to enhance efficacy of these systems.

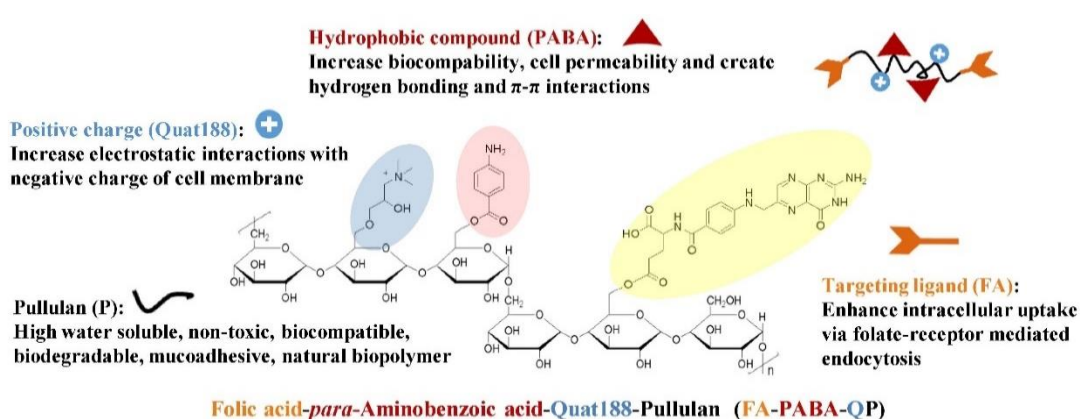


**Figure 31** Chemical and molecular structure of pullulan derivatives (FA-PABA-QP).

#### 4.1 Synthesis and characterization of pullulan (P) and its derivatives (QP, PABA-QP and FA-PABA-QP)

To synthesize pullulan derivatives (QP, PABA-QP and FA-PABA-QP), pullulan was modified by quaternization using *N*-(3-chloro-2-hydroxypropyl)-trimethylammonium chloride (Quat188) as a quaternizing agent, which reacted with the primary hydroxyl groups (etherification). Moreover, *para*-aminobenzoic acid (PABA) and folic acid (FA) were also attached by coupling of carboxylic groups to the primary hydroxyl groups of pullulan using DCC and DMAP as coupling agents, resulting in FA-PABA-QP (esterification) as shown in Figure 32. The modified pullulan samples were synthesized and characterized by  $^1\text{H}$  NMR, ATR-FTIR and TGA, as shown in Figure 32-34, respectively

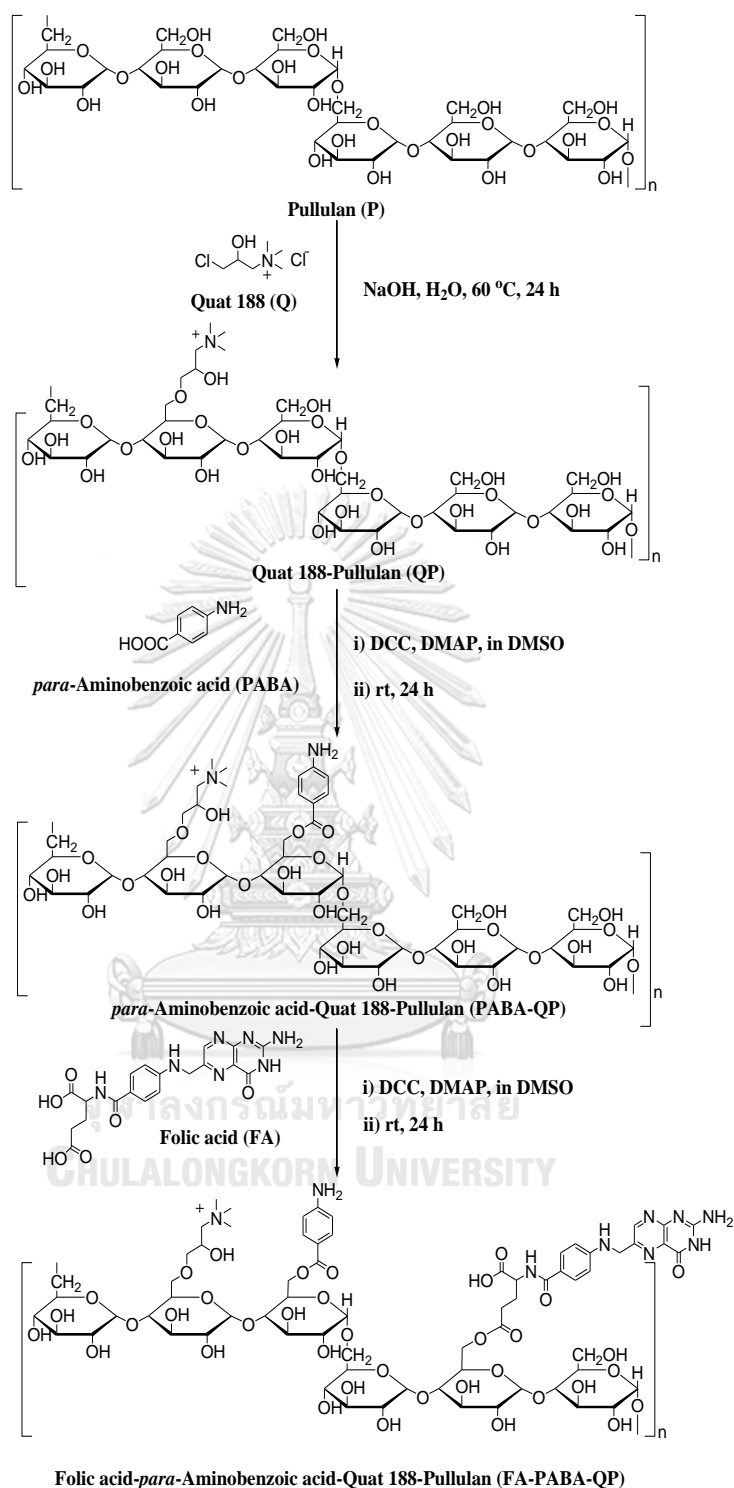


**Figure 32** Synthetic pathway of (a) pullulan (P), (b) quat188-pullulan (QP), (c) para-aminobenzoic acid-quat188-pullulan (PABA-QP), and (d) folic acid-para-aminobenzoic acid-quat188-pullulan (FA-PABA-QP).

#### 4.1.1 $^1\text{H}$ NMR spectra of P, QP, PABA-QP and FA-PABA-QP

The  $^1\text{H}$  NMR spectrum of the pullulan (P) showed the signals of the H1 protons at approximately 5.37 and 4.95 ppm, corresponding to  $\alpha$ -1,4- and  $\alpha$ -1,6-glycosidic bonds assigned to three anomeric protons of maltotriose units, respectively [68]. The H2-H6 protons at 4.07-3.36 ppm corresponded to methanediyl group ( $-\text{CH}_2-$ ) and methanediyl groups ( $>\text{CH}-$ ), as shown in Figure 33a. After quaternization, the quat188-pullulan (QP) exhibited new peaks appearing at 4.43 and 3.24 ppm and assigned to the  $\text{H}_a$  ( $>\text{CH}-\text{O}$ ) and  $\text{H}_b$  ( $+\text{N}(\text{CH}_3)_3$ ) protons of the Quat188 moiety, as shown in Figure 33b, respectively [69]. Compared with the QP spectrum, the  $^1\text{H}$  NMR spectrum of the *para*-aminobenzoic acid-quat188-pullulan (PABA-QP) showed new peaks of the aromatic protons of PABA at 6.85 and 7.92 ppm, assigned to  $\text{H}_c$  and  $\text{H}_d$ , as shown in Figure 33c. Moreover,  $^1\text{H}$  NMR analysis indicated that the degrees of quaternization (DQ) and substitution (DS) of Quat188 and PABA residues per 100 repeating glucose units for pullulan derivatives as calculated by the ratio of protons (Eq. 1-2) on PABA-QP were 15.6% and 5.8%, respectively. After substitution of FA, the folic acid-*para*-aminobenzoic acid-quat188-pullulan (FA-PABA-QP) demonstrated new peaks appearing at 4.43 and 3.24 ppm, which assigned to  $\text{H}_a$  and  $\text{H}_b$  of Quat188, respectively as shown in Figure 33d. The new peaks of PABA at 6.82 and 7.92 ppm and FA at 6.65, 7.65 and 8.67 ppm indicated to aromatic protons of  $\text{H}_c$ - $\text{H}_d$  and  $\text{H}_e$ - $\text{H}_g$ , respectively [69].  $^1\text{H}$  NMR analysis demonstrated the degree of quaternization (DQ) of Quat188 in FA-PABA-QP to be 15.5% (Eq. 1). The degree of substitution (DS) of PABA and FA modified onto FA-PABA-QP backbone was calculated by Eq. 2-3 to be 5.7% and 5.6%, respectively. Therefore,  $^1\text{H}$  NMR results confirmed that Quat188, PABA and FA were successfully conjugated onto pullulan to obtain new FA-PABA-QP.

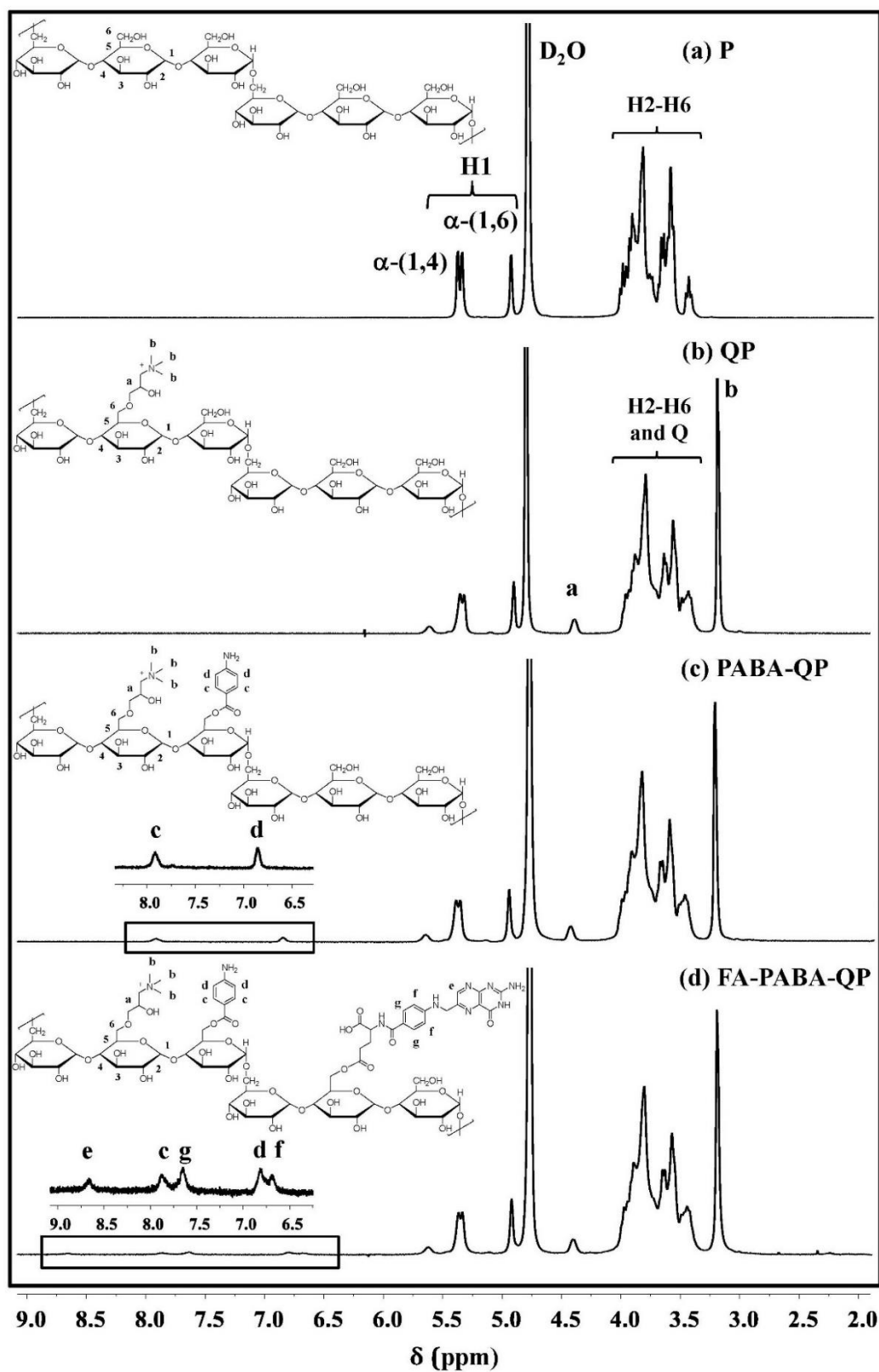


Figure 33  $^1\text{H}$  NMR spectra of (a) pullulan (P), (b) QP, (c) PABA-QP, and (d) FA-PABA-QP.

#### 4.1.2 ATR-FTIR spectra of P, QP, PABA-QP and FA-PABA-QP

The ATR-FTIR spectrum of pullulan (P) showed broad absorption at 3328 and 2930-2895  $\text{cm}^{-1}$ , attributed to O-H and stretching of  $sp^3$ -hybridized C-H. The absorption at 1643  $\text{cm}^{-1}$  corresponded to O-H bending, assigned to adsorbed water and C-O stretching. The characteristic peaks at 1352  $\text{cm}^{-1}$  were related to C-O-H bending, whereas that at 995 and 751  $\text{cm}^{-1}$  indicated the presence of  $\alpha$ -(1 $\rightarrow$ 6) and  $\alpha$ -(1 $\rightarrow$ 4)-D-glucosidic bonds, respectively, of the polysaccharide skeleton (C-O-C), as shown in Figure 34a [14]. The spectrum of the quat188-pullulan (QP) showed new peaks at 1577 and 1466  $\text{cm}^{-1}$ , which were attributed to O-H bending and C-H asymmetric stretching of methyl group [ $+N(\text{CH}_3)_3$ ] of Quat188, as shown in Figure 34b and Figure A1, respectively. After the modification of PABA, the new peak appearing at 1606  $\text{cm}^{-1}$  was assigned to the deformation of N-H in amino groups from PABA. In addition, the spectrum of the *para*-aminobenzoic acid-quat188-pullulan (PABA-QP) demonstrated a peak at 1463  $\text{cm}^{-1}$ , which is attributed to the C-H of the trimethylammonium groups, as shown in Figure 34c and Figure A2. After synthesis, the folic acid-*para*-aminobenzoic acid-quat188-pullulan (FA-PABA-QP) showed a new peak at 1452 and 1606  $\text{cm}^{-1}$ , which attributed to C-H stretching of Quat188 and N-H bending in amino groups of PABA and FA, respectively, as shown in Figure 34d and Figure A3. Then, the new characteristic peaks at 1696 and 1524  $\text{cm}^{-1}$  were attributed to C=O stretching and phenyl groups of FA. Therefore, ATR-FTIR results confirmed that Quat188, PABA and FA were successfully conjugated onto pullulan to obtain new FA-PABA-QP.



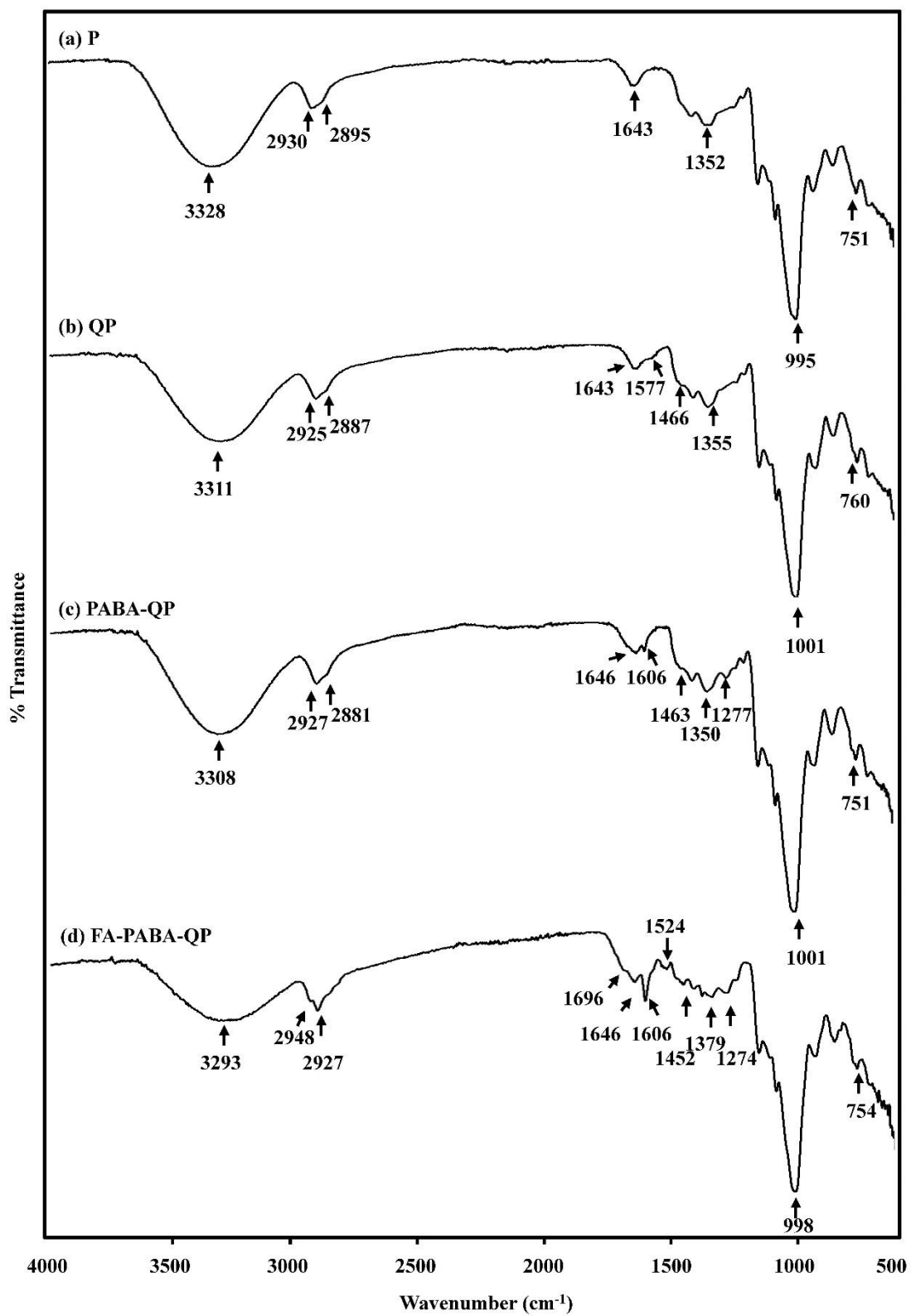
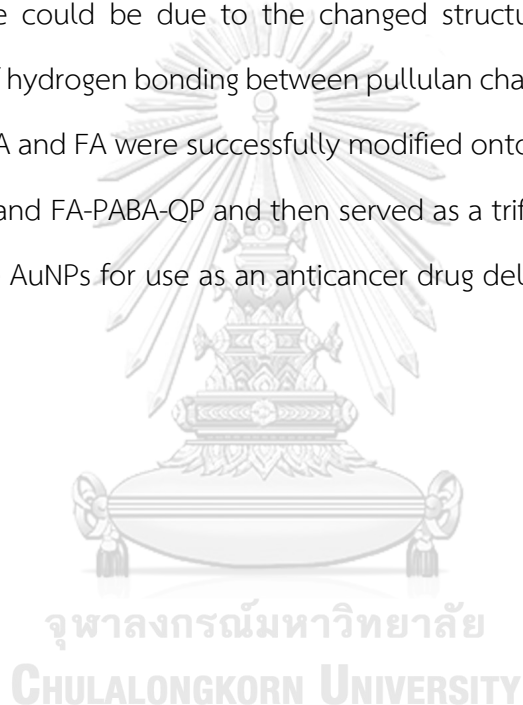


Figure 34 ATR-FTIR spectra of (a) pullulan (P), (b) QP, (c) PABA-QP, and (d) FA-PABA-QP.

#### 4.1.3 TG and DTG curves of P, QP, PABA-QP and FA-PABA-QP

The thermal properties of the pullulan and three modified-pullulan compounds were evaluated by TGA with two decomposition stages observed in their thermal degradation. During the first stage (50-150 °C) of the pullulan degradation, a slight loss of mass (7%) attributed to the volatilization of absorbed water is observed. The second stage, which was the highest thermal loss stage, occurred at 358 °C with a weight loss of 81% and is assigned to the degradation of the pullulan backbone as shown in Figure 35a. Thermoxidative degradation in an air atmosphere will also occur in addition to the thermal decomposition of the polysaccharide material. The TG and DTG curves of the quat188-pullulan (QP) exhibited 11% weight loss during the first stage from 50-210 °C, which is due to the greater hydrophilicity of Quat188 as shown in Figure 35b. This indicated a direct dependence of the residual water content on the number of charges on the polymer chains [70]. The stage of QP (335 °C) occurred at a lower temperature than that of pullulan and accounted for 73% weight loss due to the degradation of pullulan rings and the decomposition of the substituted sites of trimethylated derivatives. For the *para*-aminobenzoic acid-quat188-pullulan (PABA-QP), the first stage represented water loss (50-250 °C, 10%). PABA-QP started to degrade at lower temperature than pullulan, exhibiting their thermal decomposition at 342 °C, while a slightly lower weight loss at 69% corresponding to the cleavage of substituent groups possibly overlapped with the loss of Quat188 and PABA parts as shown in Figure 35c. The decreased thermal stability of PABA-QP, which indicated that conjugated groups may reduce the hydrogen bonding between the pullulan chain is consistent with the previous reports [71]. For the folic acid-*para*-aminobenzoic acid-quat188-pullulan (FA-PABA-QP), the first thermal decomposition stage represented the water loss occurring in the range of 50-240 °C with an 8% as shown in Figure 35d. The FA-PABA-QP started to degrade at lower temperature than pullulan, showing their

highest thermal decomposition at 337°C, while a slightly lower weight loss at 53%. This might be due to the cleavage of the substituent groups possibly overlapping with the loss of Quat188, PABA and FA parts. The decreased thermal stability of the FA-PABA-QP conjugated pullulan can explain by the fact that the PABA and FA groups might reduce the hydrogen bonding between pullulan chains. The three pullulan derivatives had a lower thermal stability compared to the unmodified pullulan. The loss of thermal stability upon the incorporation of Q188, PABA, and FA side chains onto the pullulan backbone could be due to the changed structure of pullulan, especially through the loss of hydrogen bonding between pullulan chains. These results indicated that Quat188, PABA and FA were successfully modified onto the pullulan backbone to give QP, PABA-QP and FA-PABA-QP and then served as a trifunctional agent to reduce, stabilize, and cap AuNPs for use as an anticancer drug delivery systems.



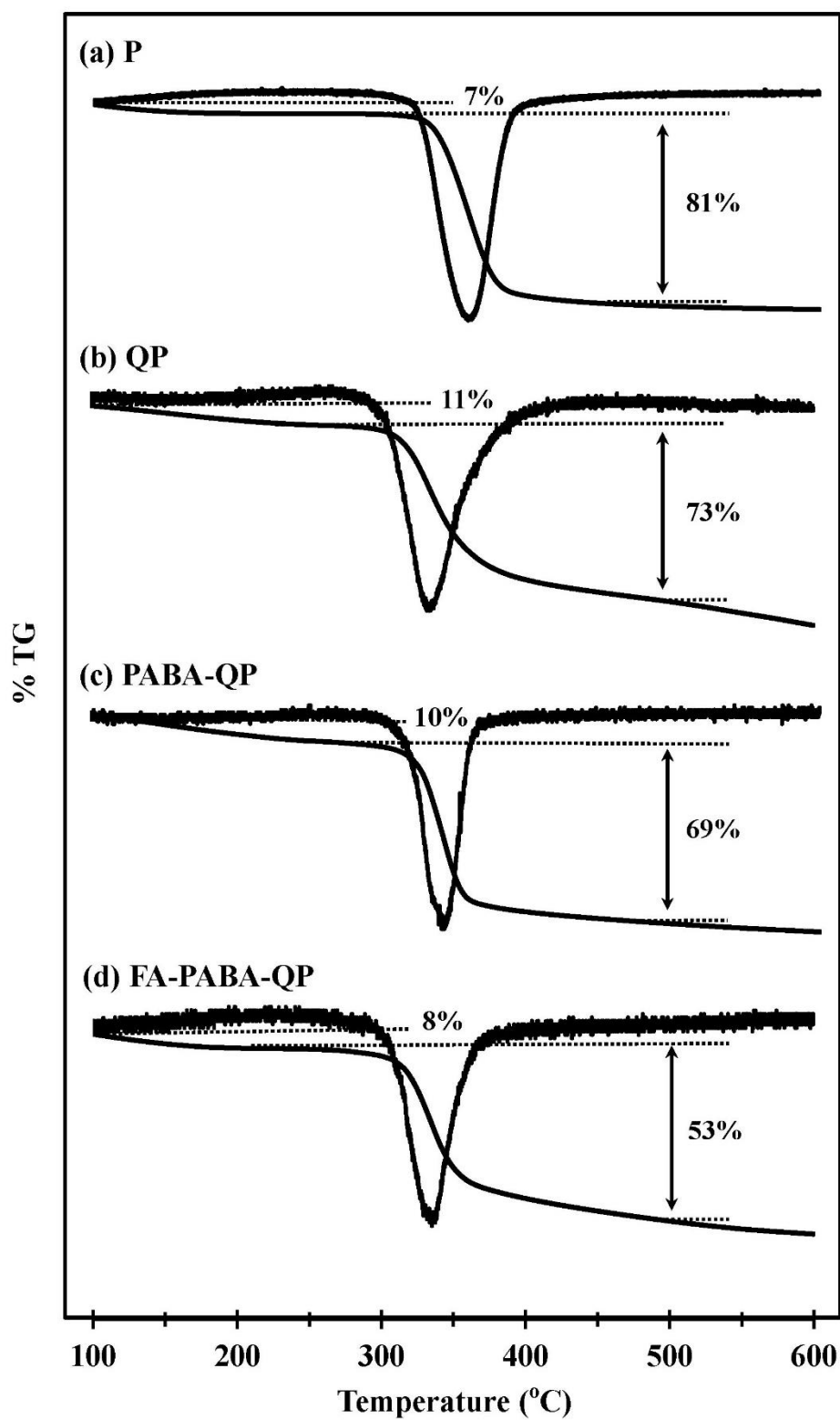


Figure 35 Representative TG and DTG curves of (a) pullulan (P), (b) QP, (c) PABA-QP, and (d) FA-PABA-QP.

#### 4.1.4 The determination of PABA and FA content in PABA-QP and FA-PABA-QP

The total PABA content in the *para*-aminobenzoic acid-quat188-pullulan (PABA-QP) was calculated with a linear equation based on the standard curve of PABA ( $y=0.2057x+0.0061$  and  $R^2=0.9995$ , as shown in Figure A4) from UV-vis analysis and was found to be 50.97 mg/g PABA-QP, as shown in Figure A6a. Moreover, the total PABA and FA contents in the folic acid-*para*-aminobenzoic acid-quat188-pullulan (FA-PABA-QP) were calculated with a linear equation based on the standard curve of PABA and FA ( $y=0.0171x-0.0166$  and  $R^2=0.9997$ , as shown in Figure A5) from UV-vis spectrum, which were 47 mg PABA/g FA-PABA-QP and 333 mg FA/g FA-PABA-QP, as shown in Figure A6b. These results confirmed that PABA and FA were successfully modified onto the pullulan backbone to obtain PABA-QP and FA-PABA-QP and then served as a trifunctional reducing, stabilizing and capping agents for AuNPs synthesis.

Part II: Synthesis and characterization of pullulan derivatives reduced/stabilized/capped gold nanoparticles (AuNPs@pullulan derivatives) as targeted nanocarriers for anticancer drug delivery systems.

#### 4.2 Synthesis of AuNPs using PABA-QP (AuNPs@PABA-QP) as a passive targeted nanocarriers

In the synthesis process, AuNPs@pullulan derivatives were synthesized by green reduction and an efficient approach of using  $\text{HAuCl}_4$  with pullulan derivatives as a trifunctional reducing, stabilizing and capping agent. They can create reducing species at the terminal groups of an open-chain form to reduce  $\text{HAuCl}_4$  to AuNPs and change into carboxylate groups as shown in Figure 36-37. The AuNPs is well-known that size, shape and surface morphology play a key role in controlling the chemical and physical properties. AuNPs with different morphologies appear in different colors that can be used as a visualized evidence to discuss the shape and size of AuNPs formed [26, 72]. In this work, AuNPs were monitored with the color change and UV-vis spectroscopy. Moreover, the effects of pH and PABA-QP concentrations as a reducing, stabilizing and capping agent were studied based on their ability to control the morphology and size of AuNPs as shown in Figure 37-38, respectively.

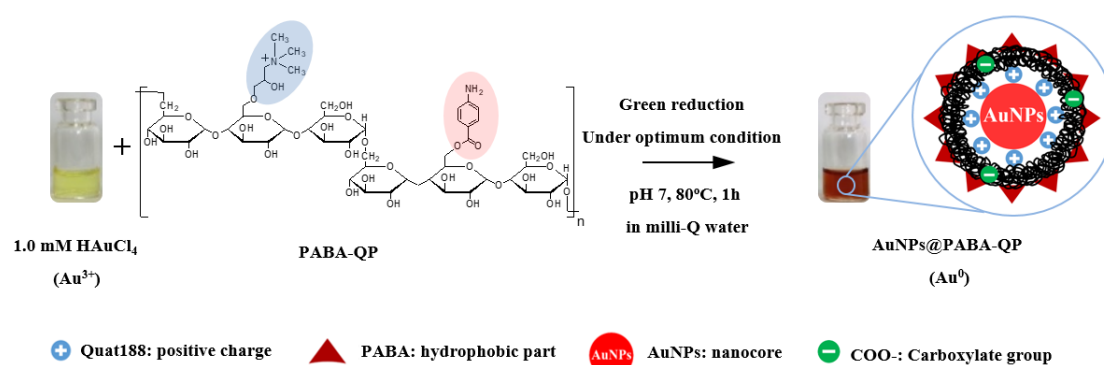


**Figure 36** Design and synthetic pathways of AuNPs@PABA-QP as a passive targeted nanocarriers by green reduction.

#### 4.2.1 Effect of pH

The reducing efficiency and mechanism of pullulan reducing  $\text{HAuCl}_4$  is associated with the pH of the system to open the ring at the end of modified pullulan chains, so the effect of pH was studied. Another interesting point is that the effect of pH to obtain AuNPs for drug delivery to gastrointestinal tracts which the performance and formation of AuNPs was evaluated at pH=4 and pH=7 as representative pH values of simulated duodenum and stimulated intestine fluid, respectively. PABA-QP and 1 mM  $\text{HAuCl}_4$  solution were colorless and yellow, respectively, while AuNPs@PABA-QP solution containing 3%(w/v) PABA-QP at pH 7 without any precipitation showed red color, indicating that  $\text{Au}^{3+}$  was reduced from  $\text{HAuCl}_4$  into AuNPs by PABA-QP as shown in Figure 37a-c. Furthermore, strong and narrow absorption peaks were observed at approximately 515 nm with no broad bands in the 600-850 nm range. The color change is attributed to the oscillation of free electrons induced by an interacting electromagnetic field in AuNPs, which is known as the localized surface plasmon resonance (LSPR) [73]. Given that the LSPR at 520 and 650 nm corresponded to smaller-sized and larger-sized AuNPs (Figure 37c), respectively, the  $A_{520}/A_{650}$  ratio was highest at pH 7. This indicated a narrow size distribution with no aggregations of AuNPs. By contrast, the solution at pH 4 showed orange color and a weak LSPR intensity of AuNPs formations because reducing species under acidic pH are generated very low that lead to obtaining low yield of AuNPs@PABA-QP. Furthermore, the solution at pH 10 became black and a broad band in the 600-850 nm range was observed, which may be due to the aggregations of AuNPs. According to our previous study, a generation mechanism of the negative AuNPs formations was proposed where pullulan creates reducing species under alkaline treatment to reduce  $\text{Au}^{3+}$  to  $\text{Au}^0$ , while the hydroxyl groups were oxidized to carboxylate groups [14]. In the preparation of AuNPs, NaOH may act as a catalyst to facilitate the formation of AuNPs, in which high NaOH may

generate more carboxylate groups on PABA-QP due to the higher reducing species and reducing ability. Although the high concentration of NaOH (pH 10) increases the reducing ability of PABA-QP, it also decreases the reduction potential of  $\text{Au}^{3+}$  complexes. This could be explained by the formation of gold complexes ( $\text{AuCl}_4^-$ ,  $\text{AuCl}_3(\text{OH})^-$ ,  $\text{AuCl}_2(\text{OH})_2^-$ ,  $\text{AuCl}(\text{OH})_3^-$  and  $\text{Au}(\text{OH})_4^-$ ) at various pH owing to different reduction potentials. The gold complexes change from  $\text{AuCl}_4^-$  into  $\text{Au}(\text{OH})_4^-$  when pH is enhanced, which  $\text{AuCl}_4^-$  and  $\text{Au}(\text{OH})_4^-$  have the highest and lowest reduction potential, respectively [74]. As the  $\text{Au}(\text{OH})_4^-$  with low reduction potential (hard to reduce) is formed and then bigger AuNPs@PABA-QP are produced under pH 10. In addition, this solution might also decrease efficacy of PABA-QP to stabilize AuNPs and then lead to agglomerations of AuNPs@PABA-QP. The aggregation could be ascribed to the electrostatic interactions between carboxylate anions and ammonium cations [75], which cover the gold nanoparticles as shown in Figure A7. Both pH values were not suitable for the use of AuNPs for drug delivery. Therefore, the best AuNPs solution at pH 7 was selected for further studies.



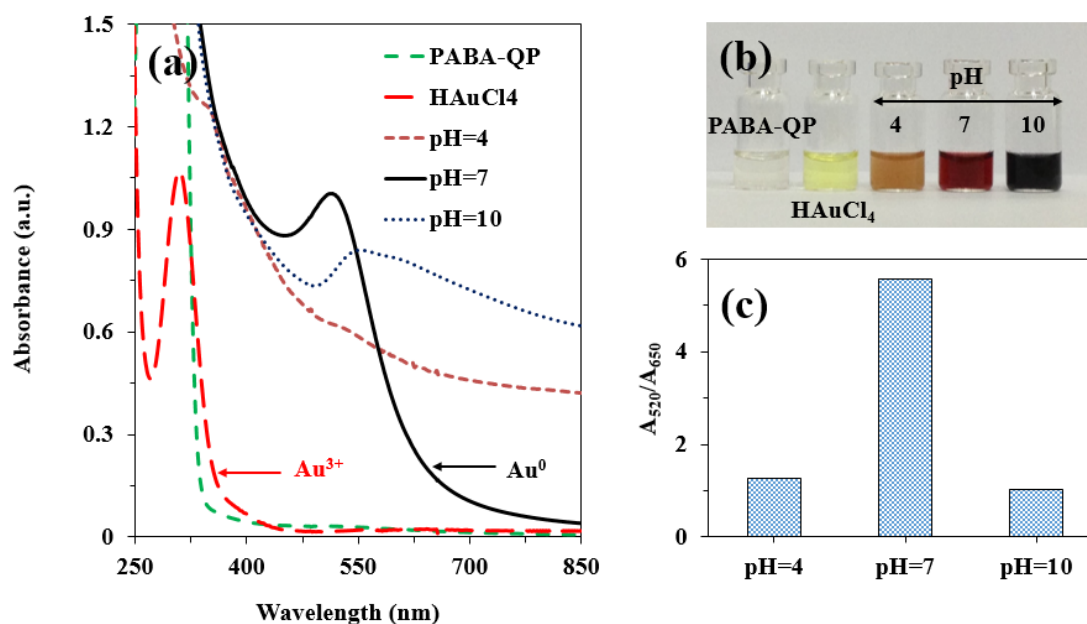


**Figure 37** (a) UV-vis spectra, (b) corresponding photographic images and (c) plot of intensity ratio between  $\lambda_{\max}$  at 520 and 650 nm of AuNPs@PABA-QP after synthesis at different pH.

#### 4.2.2 Effect of PABA-QP concentration

The effect of PABA-QP concentrations on the synthesis of AuNPs was studied in the range of 1-5% (w/v) at pH 7 and 80°C with 1 mM H<sub>AuCl</sub><sub>4</sub> for 1 h, as shown in Figure 38a-c. LSPR intensity increased rapidly with increased PABA concentrations due to the higher amount of PABA-QP as reducing agents, resulting in greater generation of AuNPs. As the PABA-QP concentration increasing from 1 to 3% (w/v) exhibited pink to red solution, respectively, the absorption maxima were observed at approximately 514-515 nm, and the LSPR intensity increased due to the higher reducing efficiency of PABA-QP. The  $A_{520}/A_{650}$  ratio was highest at a PABA-QP concentration of 3%, suggesting a narrow size distribution with no aggregation. In contrast, 5% of PABA-QP showed a purple solution with no significant change in the LSPR intensity and showed a slight redshift from 515 to 523 nm, which is related to the larger particle size of AuNPs

because the higher viscosity and steric effects of PABA-QP decreased its reducing efficiency [76, 77]. Therefore, 3% was found to be the optimal concentration of PABA-QP.

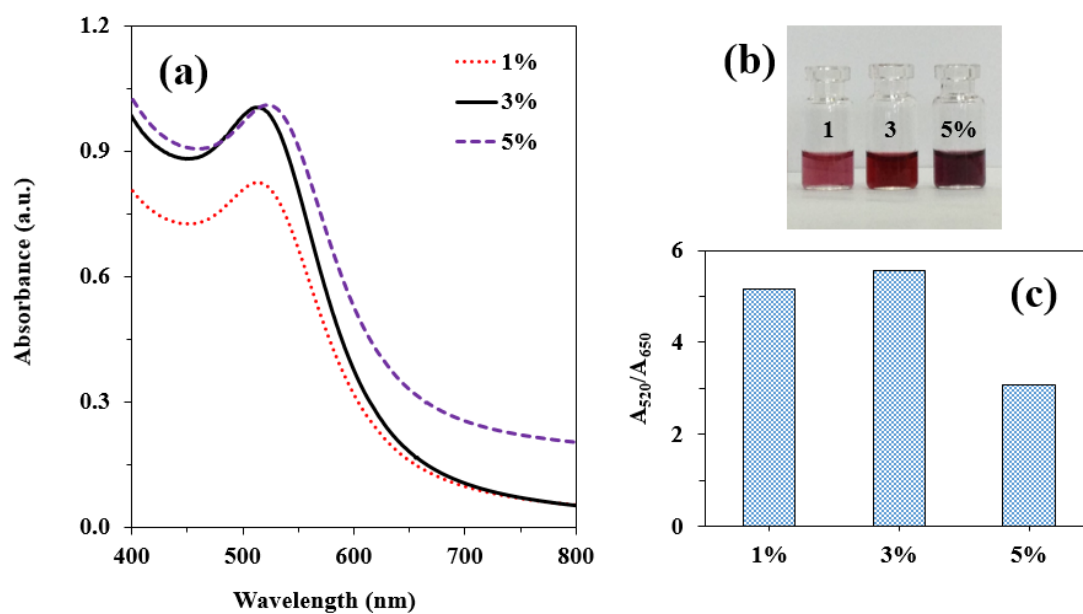


**Figure 38** (a) UV-vis spectra, (b) corresponding photographic images and (c) plot of intensity ratio between  $\lambda_{\max}$  at 520 and 650 nm of AuNPs@PABA-QP after synthesis at different PABA-QP concentrations.

### 4.3 Synthesis of AuNPs using FA-PABA-QP (AuNPs@FA-PABA-QP) as an active targeted nanocarriers

In this work, AuNPs@FA-PABA-QP were synthesized by the efficient method and one pot green reduction of  $\text{Au}^{3+}$  into  $\text{Au}^0$  with the addition of novel FA-PABA-QP as a trifunctional reducing, stabilizing and capping agent as shown in Figure 39. After synthesis, AuNPs@FA-PABA-QP formations were monitored by UV-vis spectroscopy and the change of solution color from yellow to orangish red. Moreover, the effects of pH, temperature, FA-PABA-QP concentrations and types of reducing, stabilizing and capping agents were studied based on their ability to control the particle size distribution and morphology and shape of AuNPs@FA-PABA-QP formations as shown in Figure 40-43.

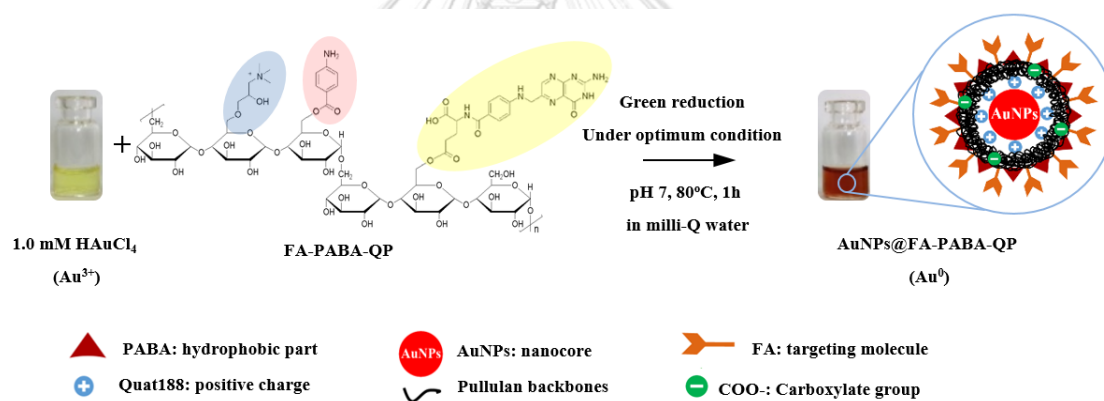


**Figure 39** Design and green synthetic method of AuNPs@FA-PABA-QP as an active targeted nanocarriers by green reduction.

### 4.3.1 Effect of pH

The reducing efficiency of FA-PABA-QP-reducing  $\text{Au}^{3+}$  is associated with pH of the solution to open at the terminal rings of FA-PABA-QP chains, then the effect of pH was studied. AuNPs@FA-PABA-QP formations were synthesized by the reduction of 1.0mM  $\text{HAuCl}_4$  using 3%(w/v) FA-PABA-QP into various pH (4, 7 and 10) of solution followed by heating at  $80^\circ\text{C}$  as shown in Figure 40. After synthesis, AuNPs@FA-PABA-QP absorbed radiation in the visible regions of 519-540 nm due to the strong LSPR transition, which confirmed the productions of AuNPs [78]. After adding NaOH and  $\text{HAuCl}_4$ , the solution color turned orangish-red and a strong LSPR peak around 519nm at neutral condition (pH 7). Moreover, given that LSPR at 520 and 650nm corresponded to smaller and bigger-sized AuNPs, respectively, the highest of  $A_{520}/A_{650}$  ratio was at pH 7 which indicated no aggregations with a narrow-size distribution of AuNPs@FA-PABA-QP( $\text{Au}^0$ ) [14]. Nevertheless, the solution color at pH 4 (acidic condition) presented orange and a weak LSPR intensity of AuNPs@FA-PABA-QP around 540nm, indicating that low reducing species are generated to obtaining low yield of AuNPs@FA-PABA-QP formations. Additionally, the solution at pH 10 (basic condition) became dark-blue color and observed a board LSPR within 600-800nm due to the aggregations of AuNPs. Although the solution at pH 10 increases the reducing efficacy of FA-PABA-QP, it also decreases the reduction potential of  $[\text{AuCl}_4]^-$  (high reduction potential) changing to  $[\text{Au}(\text{OH})_4]^-$  (low reduction potential) and then larger AuNPs@FA-PABA-QP started precipitating after 2 h as shown in Figure A7. In contrast at pH=7, the reducing and stabilizing efficiency of FA-PABA-QP under acidic and basic conditions showed lower reducing and lower stabilizing efficiency with incomplete reduction of AuNPs and not suitable AuNPs for drug delivery, respectively. Therefore, pH=7 was chosen as the optimal pH for synthesis of AuNPs@FA-PABA-QP.

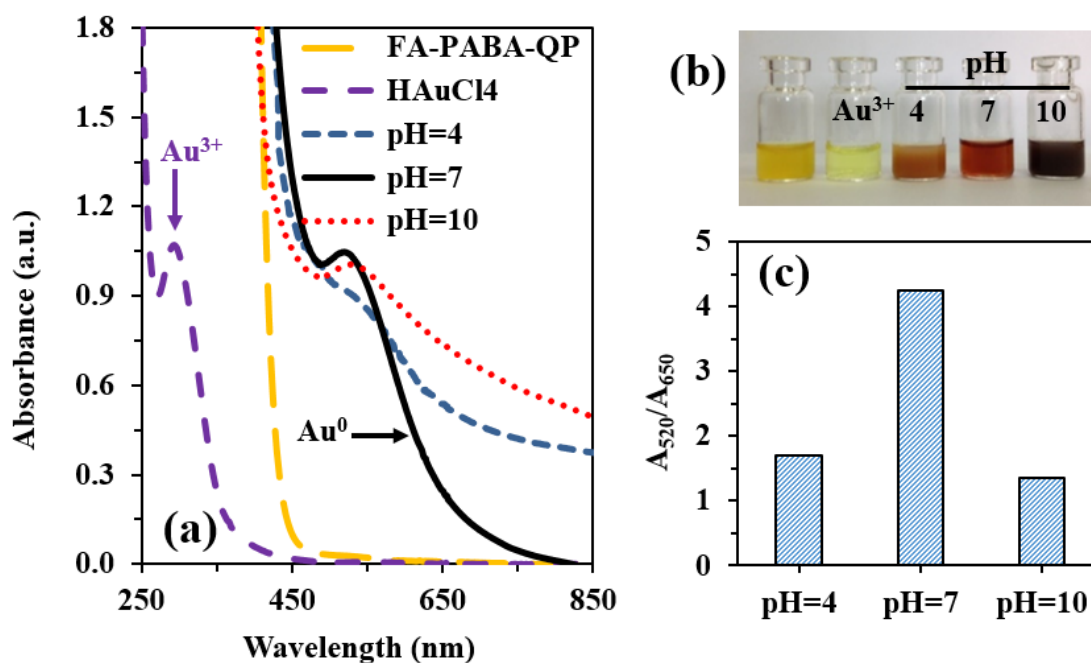


**Figure 40** (a) UV-vis spectra, (b) corresponding photographic images and (c) plot of intensity ratio between  $\lambda_{\max}$  at 520 and 650 nm of AuNPs@FA-PABA-QP as an active targeted nanocarriers after synthesis at different pH.

#### 4.3.2 Effect of temperature

In order to study the effect of temperature in the synthesis of AuNPs@FA-PABA-QP, the solution temperature was heated from room temperature (RT) to 60, 80 and 100 °C, as shown in Figure 41a-c. The fabrications of AuNPs@FA-PABA-QP at RT required an extended reaction time to complete the reduction reactions, while a LSPR intensity increased with increasing temperature. The heat-generation rate of AuNPs@FA-PABA-QP formations increased up to 80 °C and then the  $A_{520}/A_{650}$  ratio was the highest at 80°C which confirmed in complete reduction. The AuNPs generation could slow down the formation at a lower temperature which results in incomplete reductions, whereas the solution at temperature over 80 °C became black indicating the agglomerations of

AuNPs [76]. Thus, 80 °C was selected as the optimal temperature for AuNPs@FA-PABA-QP synthesis.

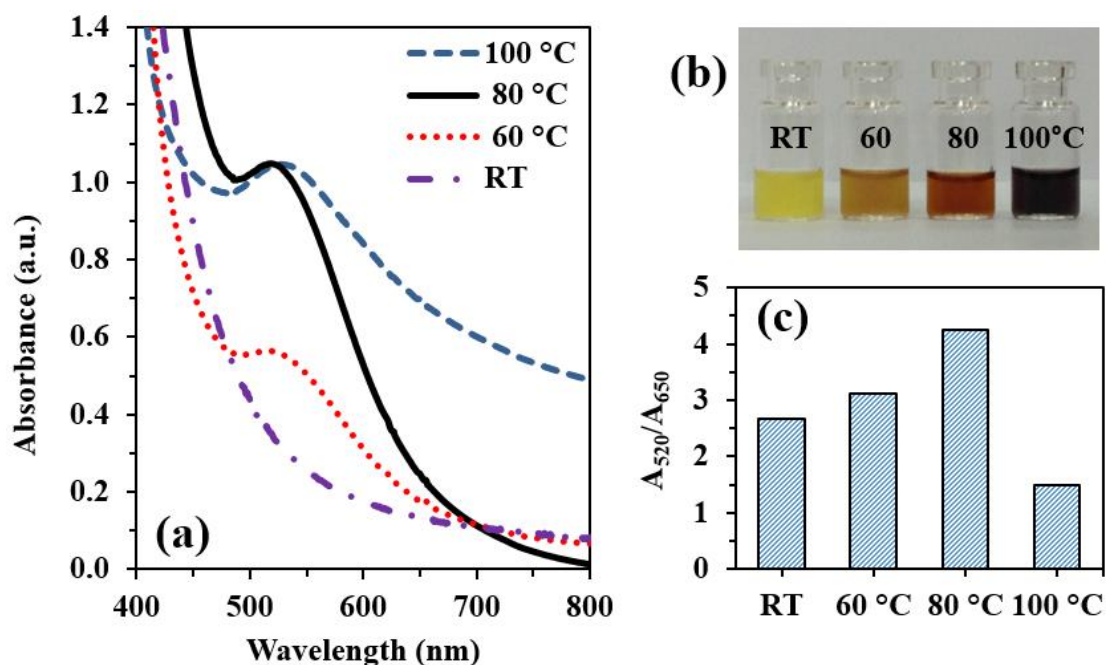


**Figure 41** (a) UV-vis spectra, (b) corresponding photographic images and (c) plot of intensity ratio between  $\lambda_{\max}$  at 520 and 650 nm of AuNPs@FA-PABA-QP as an active targeted nanocarriers after synthesis at different reaction temperature.

#### 4.3.3 Effect of FA-PABA-QP concentration

Bio-macromolecules are well known to generate and control the shape and size of metallic nanoparticles which serves as a stabilizers [79]. Then, to study the role and effect of FA-PABA-QP concentrations as a biopolymer in the reduction processes via green synthesis method to obtain AuNPs@FA-PABA-QP in the range of 1-7% (w/v) under pH7 at 80 °C for 1 h, as shown in Figure 42a-c. After adding various FA-PABA-QP into the mixed solution, substantial increase in LSPR intensity and absorption bands were observed when increasing FA-PABA-QP concentration was increased from 1 to 3%. The higher FA-PABA-QP could be attributed to enhance reducing efficacy,

stabilization and capping of synthesized AuNPs. Nevertheless, at FA-PABA-QP over 3%, the synthesized AuNPs did not show any significant change in the LSPR intensity and position of LSPR around 519-524 nm due to higher viscosities and steric effects of FA-PABA-QP decreased its reducing efficiency to generate AuNPs [76]. Hence, at 3% FA-PABA-QP was chosen for subsequent fabrications of AuNPs@FA-PABA-QP which  $A_{520}/A_{650}$  ratio was the highest. Moreover, the LSPR was observed a strong intensity around 519 nm and very narrow band which were well reduced, stabilized and capped by FA-PABA-QP without aggregation of AuNPs@FA-PABA-QP formations, and were colloidal stable for 0.5 months which showed suitable for drug delivery systems.

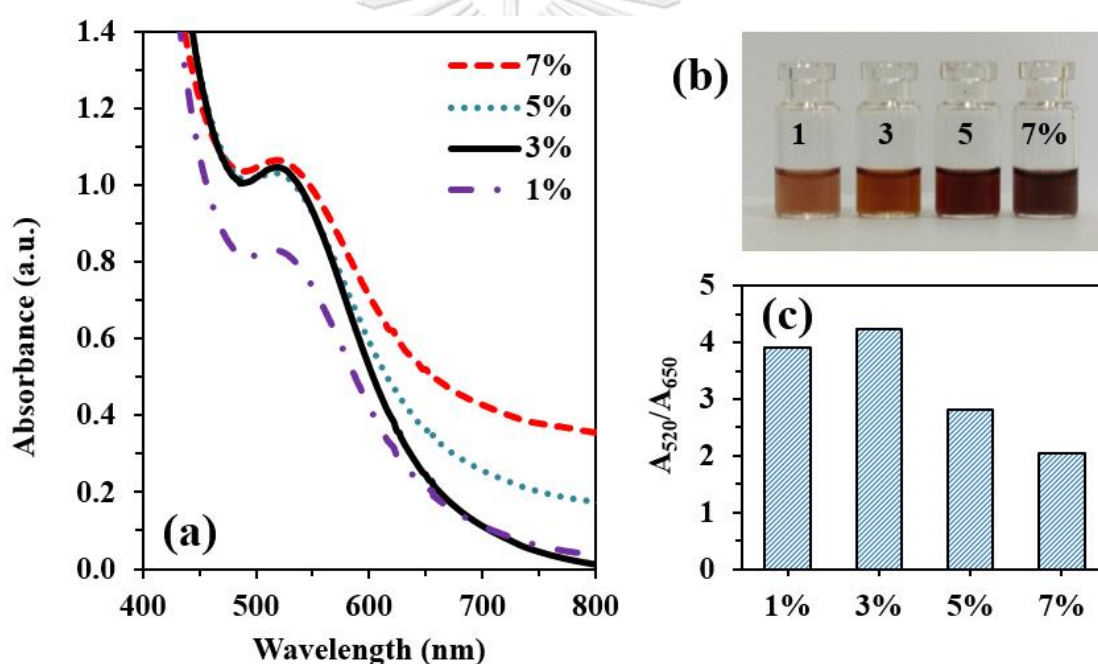


**Figure 42** (a) UV-vis spectra, (b) corresponding photographic images and (c) plot of intensity ratio between  $\lambda_{\max}$  at 520 and 650 nm of AuNPs@FA-PABA-QP as an active targeted nanocarriers after synthesis at different FA-PABA-QP concentrations.

#### 4.3.4 Effect of types of a reducing/stabilizing/capping agent

Biopolymers are well known to function as stabilizers to control nucleation, growth and self-assembly of AuNPs, and therefore, the effect of the type of reducing/stabilizing/capping agent was examined, as shown in Figure 43. The photographic images of AuNPs@P, AuNPs@QP, AuNPs@PABA-QP and AuNPs@FA-PABA-QP exhibited a slight change in solution color, namely, red-wine, soft-red, red and orangish-red solution, respectively, whereas characteristic LSPR changed slightly, and the absorption maxima were observed at approximately 514-519 nm. Moreover, AuNPs@P showed a second LSPR band in the approximately 600-800 nm range, indicating that AuNPs@P were produced with agglomeration after synthesis (red-wine solution) due to hydrogen bonding between hydroxyl groups covering on AuNPs@P more than AuNPs@FA-PABA-QP, AuNPs@QP and AuNPs@PABA-QP, respectively. Additionally, the solution color of AuNPs@QP showed soft-red solution as a consequence of lower LSPR intensity and lower yield of AuNPs@QP generations. In contrast, the LSPR spectra of AuNPs@PABA-QP and AuNPs@FA-PABA-QP were intense, strong, and had a narrow shape with no second peak at 650 nm, indicating a high yield of produced AuNPs (red and orangish-red solution) and good dispersion of AuNPs, which is in agreement with previous reported [80]. Furthermore, the color change of AuNPs@P was observed within 30 min after the addition of  $\text{HAuCl}_4$ , which was much faster than the color change observed for AuNPs@QP, AuNPs@PABA-QP and AuNPs@FA-PABA-QP, indicating that pullulan (P) may give rise to higher reaction rate than QP, PABA-QP and FA-PABA-QP to reduce  $\text{Au}^{3+}$  to  $\text{Au}^0$  than QP, PABA-QP and FA-PABA-QP, respectively. After storage for 15 days, the stability of AuNPs@P was lower than that of AuNPs@FA-PABA-QP, AuNPs@QP and AuNPs@PABA-QP, with the LSPR band of AuNPs@P showing a greater redshift than for AuNPs@FA-PABA-QP, AuNPs@QP and AuNPs@PABA-QP, indicating that AuNPs@P showed more aggregation to obtain larger



nanoparticles. This result indicated that AuNPs@P exhibited more self-aggregations to obtain bigger particles than AuNPs@FA-PABA-QP, AuNPs@QP and AuNPs@PABA-QP, respectively. This self-aggregations may be ascribed to hydrogen bonding between hydroxyl groups on pullulan backbone, which cover AuNPs@P more than AuNPs@FA-PABA-QP, AuNPs@QP and AuNPs@PABA-QP, respectively. On other hand, the conjugated molecules on pullulan covering onto AuNPs might reduce hydroxyl groups and hydrogen bonding, and then also increase electronic repulsion between ammonium cations and increase steric effect of aromatic parts leading to increase electrosteric stabilization of AuNPs [81]. These results confirmed that AuNPs@PABA-QP is more stable than AuNPs@QP, AuNPs@FA-PABA-QP and AuNPs@P because the stabilizing efficacy of PABA-QP capped onto AuNPs may be higher than QP, FA-PABA-QP, and P, respectively. Furthermore, the highest stability of AuNPs could be established by pullulan derivatives acting as not only a good reducing agent but also a stabilizer and capping agents to obtain highly stable AuNPs and good dispersion in aqueous solutions [26]. Moreover, the reduction of  $\text{HAuCl}_4$  was assumed to be completed after 1 h due to the absence of subsequent color and intensity changes. These results suggested that  $\text{Au}^{3+}$  ions were reduced in an eco-friendly manner to AuNPs by various types of a reducing/stabilizing/capping agents and were subsequently stabilized and capped by pullulan derivatives. This was achieved without the use of an external reducing/stabilizing/capping reagent, indicating that pullulan derivatives can be used as a tri-functional reducing/stabilizing/capping agent of AuNPs, as expected. Then, the pullulan derivative (PABA-QP and FA-PABA-QP) was selected for the synthesis of AuNPs synthesis for subsequent use as a passive and active targeted nanocarriers, respectively, in order to enhance their efficacy and reduce the side effects of anticancer drugs.

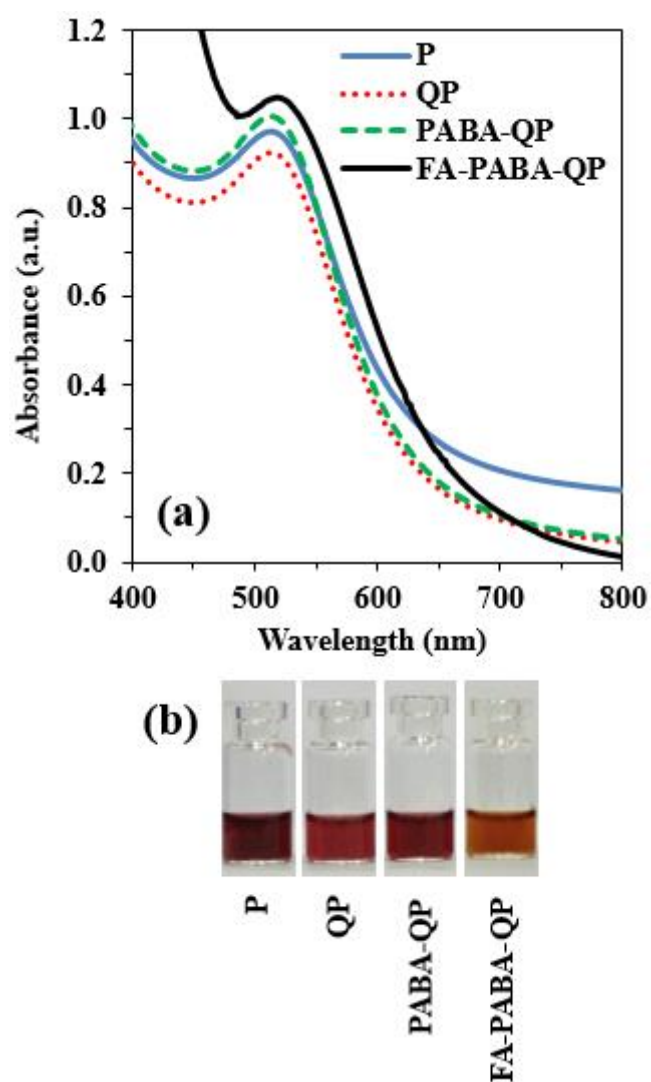


Figure 43 (a) UV-vis spectra and (b) corresponding photographic images of AuNPs@FA-PABA-QP as an active targeted nanocarriers after synthesis at different types of a reducing/stabilizing/capping agent.

#### 4.4 Characterization of AuNPs using pullulan derivatives (AuNPs@ pullulan derivatives) as targeted nanocarriers for anticancer drug delivery

The efficient, rapid and green synthesis for controlling the morphology, shape, and size distribution of suitable AuNPs@pullulan derivatives under optimal condition (1mM HAuCl<sub>4</sub>, 1h, pH7, 3% of pullulan derivatives and 80 °C) for anticancer drug delivery systems were characterized by TEM, XRD, zeta-potential, EDS, SAED, ATR-FTIR and XPS analyses. In this work, AuNPs@P, AuNPs@QP, AuNPs@PABA-QP and AuNPs@FA-PABA-QP were successfully synthesized by green reduction of HAuCl<sub>4</sub> with same condition in the presence of P, QP, PABA-QP and FA-PABA-QP as a reducing, stabilizing and capping agent.

##### 4.4.1 Transmission electron microscopy (TEM) and the histograms of AuNPs@pullulan derivatives

After eco-friendly and green synthesis, TEM images of AuNPs obtained under optimal conditions (pH 7, 3% pullulan derivatives, 1mM HAuCl<sub>4</sub>, 80°C and 1h) showed a dark sphere of AuNPs@pullulan derivatives without aggregations as shown in Figure 44. Histograms of the particle size distribution for AuNPs@P, AuNPs@QP, AuNPs@PABA-QP and AuNPs@FA-PABA-QP showed slightly change in the average size of approximately 15.2±2.5, 11.6±1.7, 13.7±1.9 and 12.6±1.5 nm, respectively. These results were consistent with the UV-vis spectra and photographs of AuNPs as shown in Figure 43, indicating that the particle size and shape of AuNPs@pullulan derivatives are suitable for anticancer drug delivery. Similarly, Freese and co-worker [40] prepared fifteen sequentially modified AuNPs based on three different core sizes (18, 35 and 65 nm). In general, the smallest AuNPs (18 nm) were internalized in the highest amount compared with 35 and 65 nm-sized, respectively, by ICP-AES technique. In particular, the red and orangish-red solution of monodispersed AuNPs@PABA-QP and AuNPs@FA-

PABA-QP showed an LSPR band that was intense and strong, indicating the lack of aggregation and a high yield of AuNPs@PABA-QP and AuNPs@FA-PABA-QP formations. Additionally, the average thicknesses of the PABA-QP and FA-PABA-QP shells on the AuNPs core studied from TEM images under dry conditions were  $2.0\pm 0.5$  nm and  $2.1\pm 0.5$  nm, respectively, as shown in Figure A8. Furthermore, the choice of conjugated molecules on the pullulan allowed for the achievement of two aims: the controlled synthesis of AuNPs and surface functionalization of AuNPs with application in cancer cells. Also, two and three structural features modified pullulan (PABA-QP and FA-PABA-QP) was selected for AuNPs synthesis, which is fully confirmed the suitability of AuNPs@pullulan derivatives for use as a passive and an active nanocarriers in good agreement with previous reports [16].



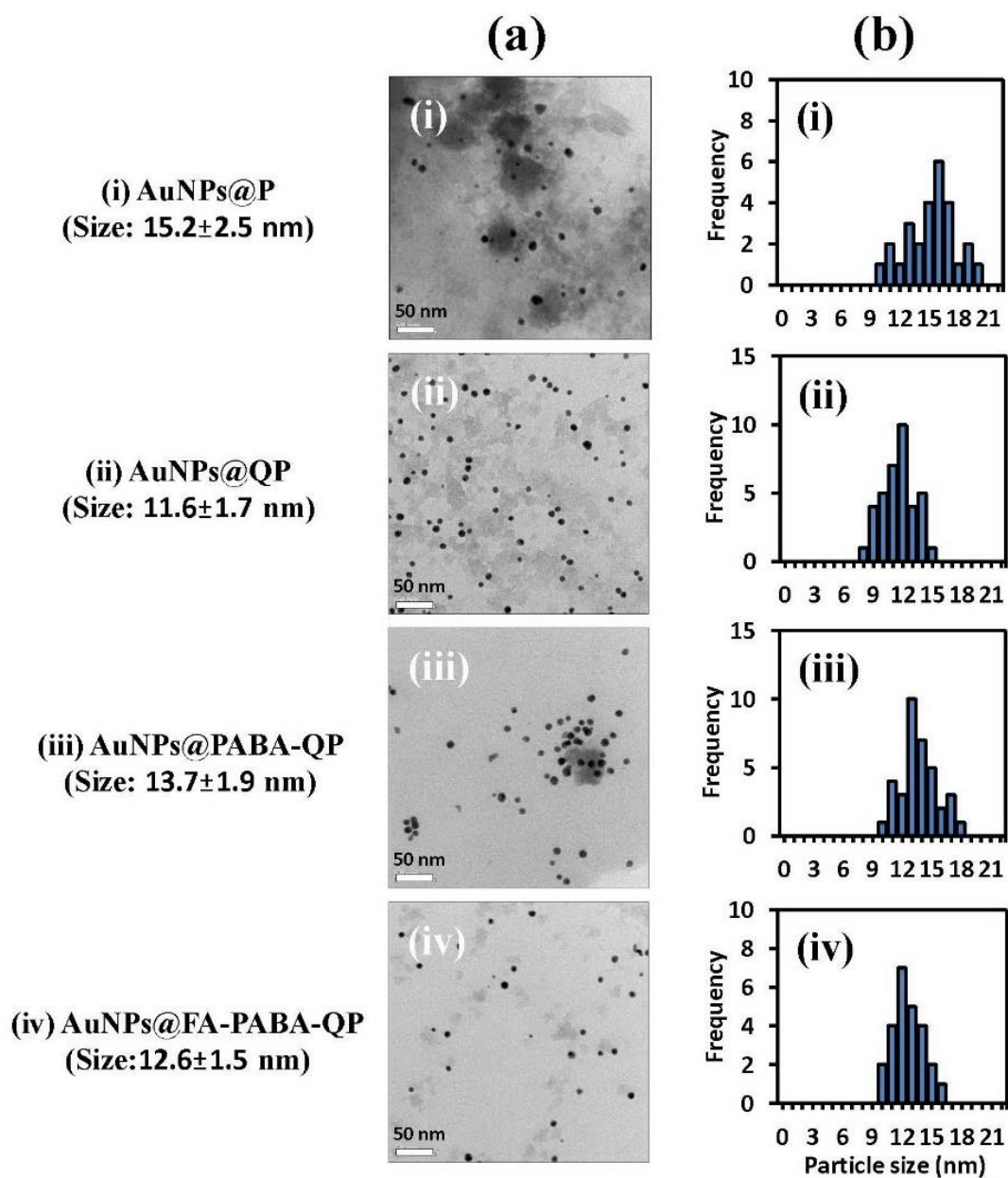


**Figure 44** Characterizations of AuNPs formation: (a) TEM images and (b) histograms of (i) AuNPs@P, (ii) AuNPs@QP, (iii) AuNPs@PABA-QP, and (iv) AuNPs@FA-PABA-QP under optimal conditions.

#### 4.4.2 X-ray diffraction (XRD) and selected area of electron diffraction (SAED) patterns of AuNPs@pullulan derivatives

XRD was used to characterize the crystal structure of AuNPs. Intense diffraction peaks of  $\text{HAuCl}_4$  were observed at  $2\theta$  values of 37.9, 44.2, 64.5 and 77.3°. Intense diffraction peaks of AuNPs@P, AuNPs@QP, AuNPs@PABA-QP and AuNPs@FA-PABA-QP were observed at  $2\theta$  ranges of 38.4-38.5, 44.3-44.8, 64.6-65.5 and 77.7-78.2°, corresponding to the (111), (200), (220) and (311) reflection planes of crystalline gold, respectively (JCPDS no.04-0784) as shown in Figure 45 and Table 1. Furthermore, XRD patterns of AuNPs@pullulan derivatives were shifted to higher  $2\theta$  and were more broad than the characteristic peaks for  $\text{HAuCl}_4$ , which is due to the smaller particle size and  $d$ -spacing of  $\text{Au}^0$  compared to those of  $\text{Au}^{3+}$  [82]. Similarly, SAED patterns of AuNPs@PABA-QP and AuNPs@FA-PABA-QP exhibits the rings of the reflections from the (111), (200), (220) and (311) planes which related to  $d$ -spacing of spherical AuNPs of 2.35, 2.04, 1.44, and 1.23 Å, respectively, as shown in Figure 46 and consistent with XRD patterns [80]. The lattice plane with the  $d$ -spacing of 2.35 Å related to Au (111) was measured in both AuNPs@PABA-QP and AuNPs@FA-PABA-QP, as shown in Figure A8 [7].

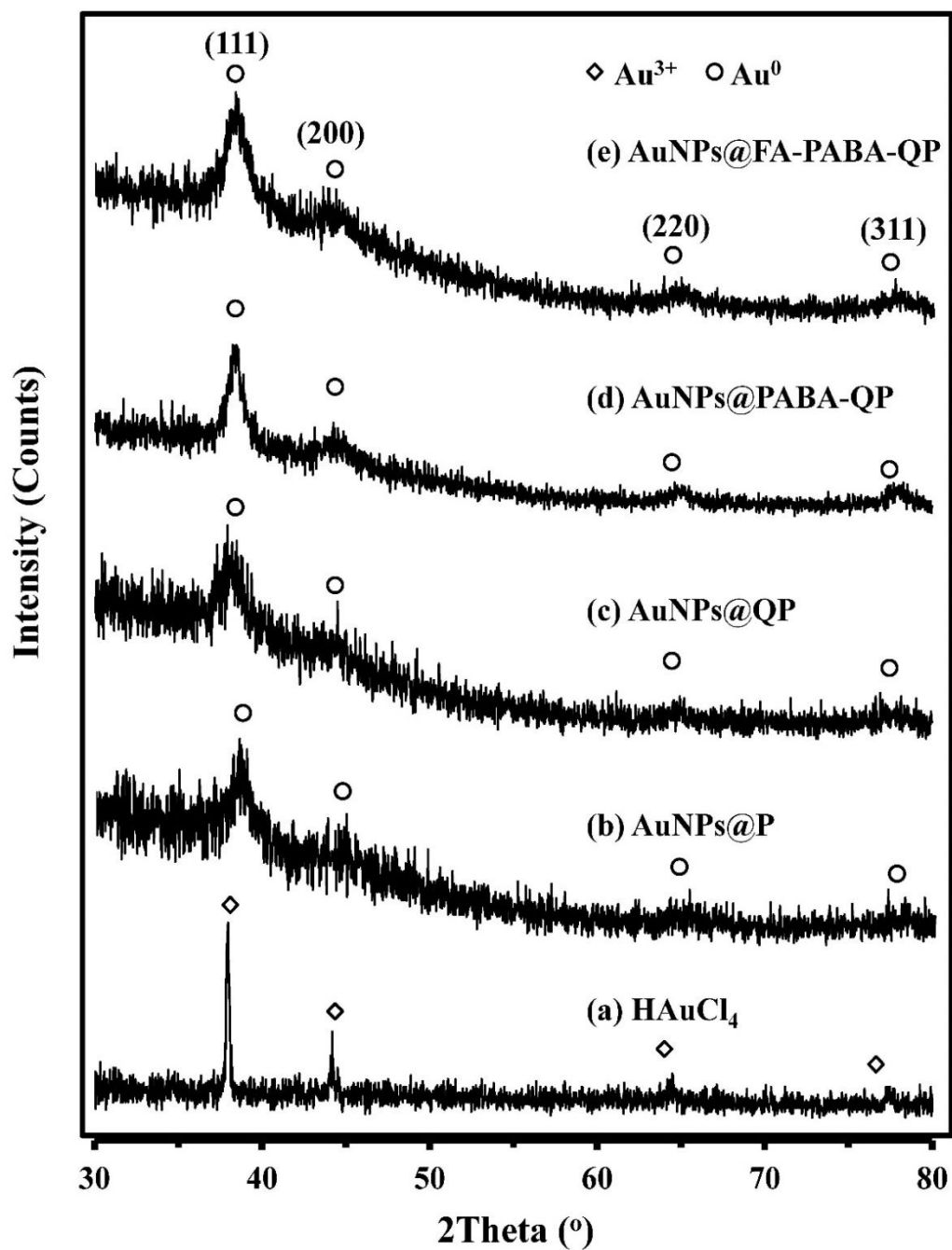
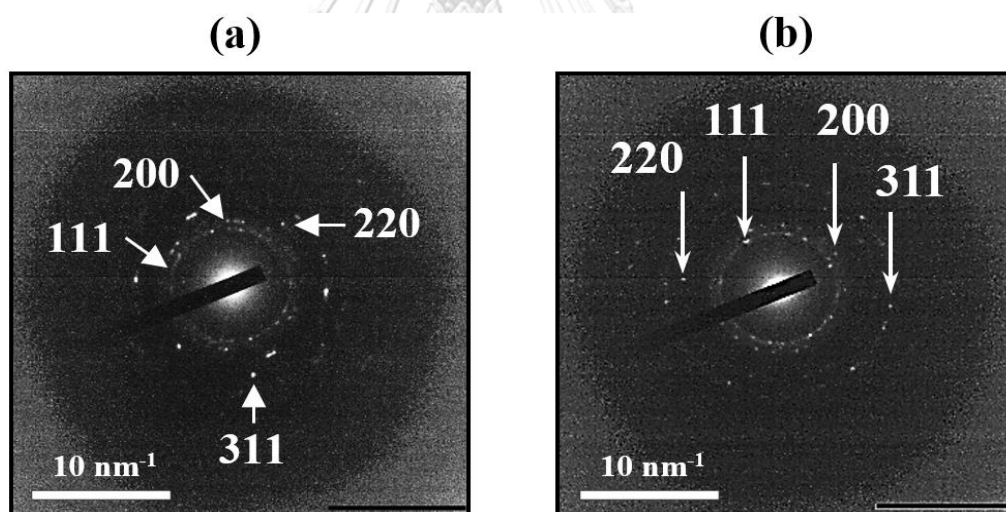


Figure 45 XRD patterns of (a) HAuCl<sub>4</sub>, (b) AuNPs@P, (c) AuNPs@QP, (d) AuNPs@PABA-QP and (e) AuNPs@FA-PABA-QP.

**Table 1** XRD data showing  $2\theta$  ( $^\circ$ ) and d-spacing ( $\text{\AA}$ ) of  $\text{HAuCl}_4$  ( $\text{Au}^{3+}$ ),  $\text{AuNPs@P}$ ,  $\text{AuNPs@QP}$ ,  $\text{AuNPs@PABA-QP}$  and  $\text{AuNPs@FA-PABA-QP}$  ( $\text{Au}^0$ ).

Sample	$2\theta$ value of crystalline gold ( $^\circ$ ), d-spacing ( $\text{\AA}$ )			
	(111), 2.36	(200), 2.04	(220), 1.44	(311), 1.23
$\text{HAuCl}_4$ ( $\text{Au}^{3+}$ )	37.9	44.2	64.5	77.3
$\text{AuNPs@P}$	38.5	44.8	65.5	78.2
$\text{AuNPs@QP}$	38.5	44.4	65.0	78.0
$\text{AuNPs@PABA-QP}$	38.5	44.3	64.6	77.9
$\text{AuNPs@FA-PABA-QP}$	38.4	44.5	65.0	77.7



**Figure 46** The selected area of electron diffraction (SAED) patterns XRD patterns of (a)  $\text{AuNPs@PABA-QP}$  and (b)  $\text{AuNPs@FA-PABA-QP}$ .



#### 4.4.3 Zeta-potential analysis of AuNPs@pullulan derivatives

The surface charge of AuNPs were determined by zeta-potential analysis, which evaluated the electric potential at the boundary of the double layer of AuNPs [83]. The zeta potential values of AuNPs@P were found to be  $-14.20 \pm 5.32$  mV, suggesting the presence of free negatively charged carboxylate groups (COO<sup>-</sup>) on the surface of AuNPs as shown in Figure 47 and Table 2. This results was consistent with our previous study [14]. Zeta potential values of AuNPs@QP, AuNPs@PABA-QP and AuNPs@FA-PABA-QP were  $-0.74 \pm 4.73$ ,  $0.49 \pm 5.63$  and  $1.74 \pm 5.49$  mV, respectively. This increase in the zeta potential was attributed to the presence of the positive charge of the quaternary ammonium groups of the pullulan-backbone shells surrounding the AuNPs core by electrostatic interactions so that the aromatic rings of substituted PABA and FA were directed toward the outside of the AuNPs structure [84]. These results confirmed that AuNPs@pullulan derivatives were successfully synthesized and then served as universal nanocarriers to deliver and enhance cytotoxicity of the anticancer drugs.

**Table 2** The zeta potential of AuNPs@pullulan derivatives under optimal condition.

Compound	Zeta Potential ( $\zeta$ , mV)
AuNPs@P	$-14.20 \pm 5.32$
AuNPs@QP	$-0.74 \pm 4.73$
AuNPs@PABA-QP	$0.49 \pm 5.63$
AuNPs@FA-PABA-QP	$1.74 \pm 5.49$

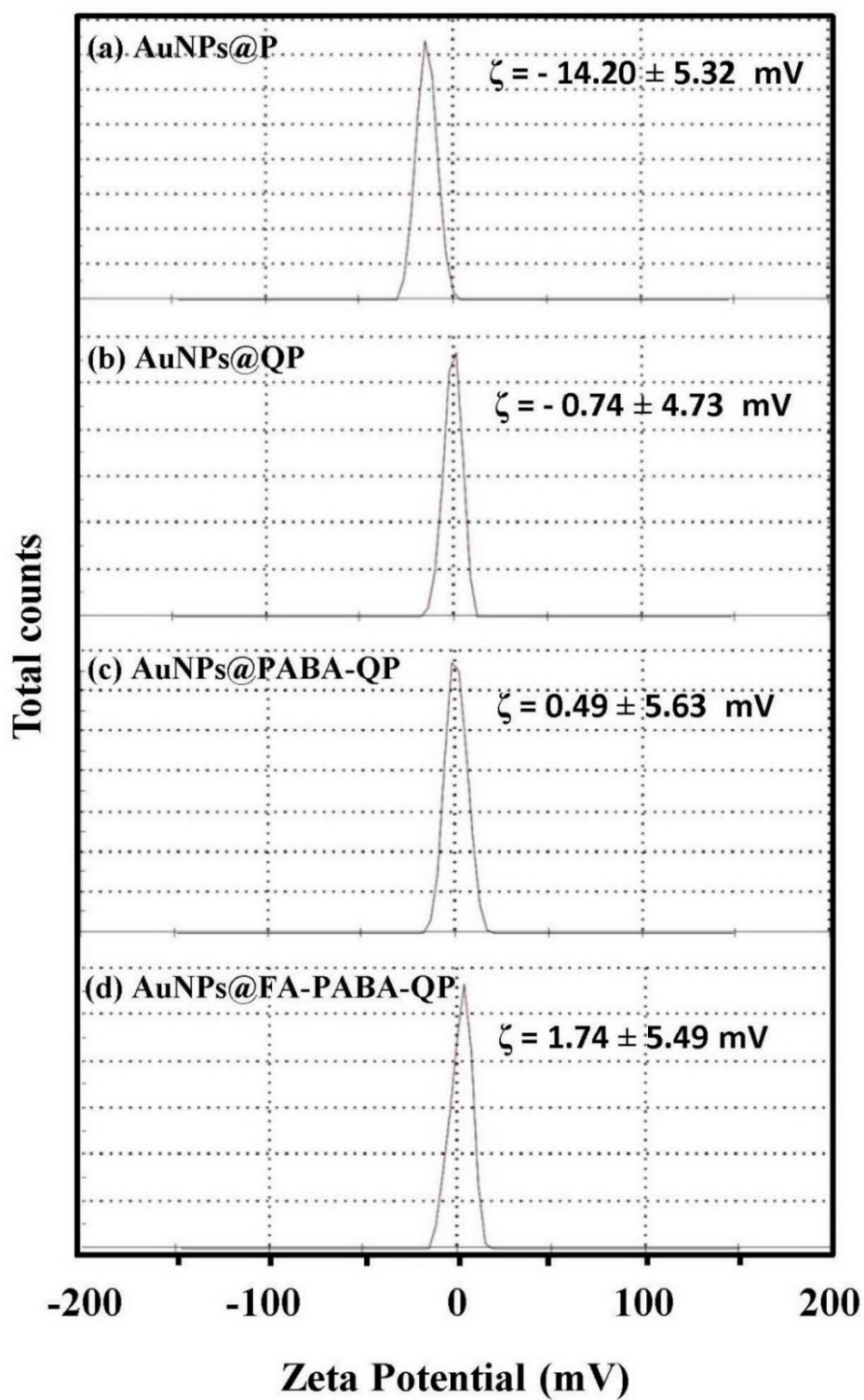
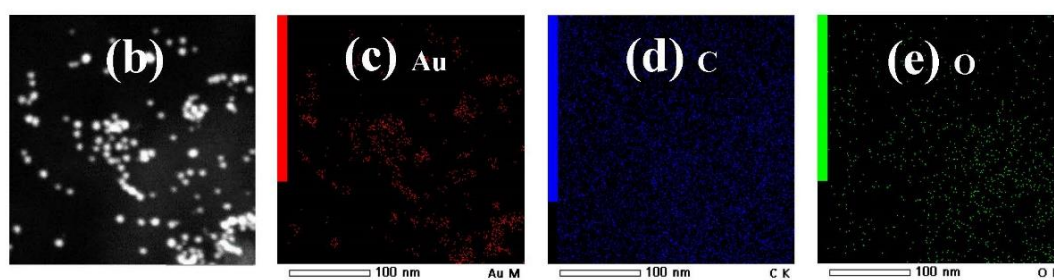
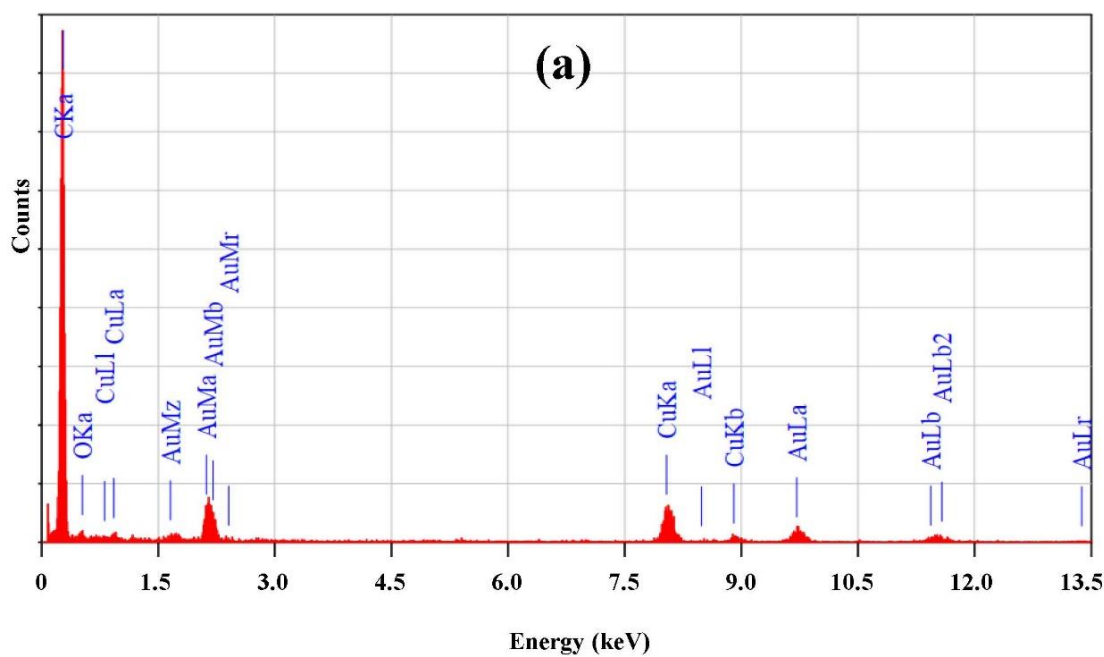


Figure 47 Zeta-potential analysis of (a) AuNPs@P, (b) AuNPs@QP, (c) AuNPs@PABA-QP and (d) AuNPs@FA-PABA-QP.

#### 4.4.4 Energy Dispersive Spectroscopy (EDS) for TEM of AuNPs@pullulan derivatives

The elements of AuNPs@FA-PABA-QP from TEM-EDS spectrum showed characteristic peaks of carbon, oxygen, copper and gold, which gave 10.1% by mass at 2.1 keV of a strong signal from Au atoms as shown in Figure 48a-f. This result confirmed that AuNPs@FA-PABA-QP was comprised the presence of gold in AuNPs core covering by the high concentration of FA-PABA-QP shells (C and O atoms), consistent with previous studies [85, 86]. Cu signals are an experimental artifact that originated from the mounting copper grid used to coating TEM-sample. Elemental mapping of EDS was used to verify the distributions of elements in the same region of AuNPs@FA-PABA-QP as shown in Figure 48b-e. The dark-field TEM-EDS images of the small white of spherical AuNPs@FA-PABA-QP were the only areas where only Au<sup>0</sup> elements was observed in Figure 48b (white spots). Similarly, the elemental composition of AuNPs@PABA-QP was characterized by EDS as shown in Figure A9. Characteristic absorption peaks of carbon, oxygen, copper and gold, which gave a strong signal from Au atoms, confirmed that the formed nanoparticles had gold in the AuNPs core covered by PABA-QP shells (C and O atoms), consistent with previous studies [85]. Moreover, ICP-OES was used to determine the amount of gold in all AuNPs@pullulan derivatives.



(f)

Element	Weight (%)	Atomic (%)
C K	82.27	97.22
O K	0.51	0.45
Cu K	7.17	1.60
Au M	10.06	0.72
<b>Total</b>	<b>100.00</b>	<b>100.00</b>

**Figure 48** (a) EDS spectrum, (b) dark-field TEM micrograph, (c-e) the elemental mapping in the same AuNPs region and (f) the elemental composition of AuNPs@FA-PABA-QP under optimal condition.

#### 4.4.5 X-ray photoelectron spectroscopy (XPS) and ATR-FTIR of AuNPs@FA-PABA-QP

X-ray photoelectron spectroscopy (XPS) was performed to characterize the surface concentration, composition, oxidation state and surface chemical state of the metallic nanostructure. XPS survey spectrum of AuNPs@FA-PABA-QP indicates the presence of Au (4f), C (1s), Au (4d), O (1s), Au (4p), and Au (4s) species in AuNPs formations as shown in Figure 49a. The high-resolution spectrum of Au (4f) core level region display a doublet peaks located at 82.76 and 86.41 eV ( $\Delta$ B.E. = 3.65 eV), which corresponded to Au (4f<sub>7/2</sub>) and Au (4f<sub>5/2</sub>), respectively as shown in Figure 49b. The obtained peak were shifted to the lower binding energy (1.24 eV) due to the electron transfer from hydroxyl groups to AuNPs compared with the peak of bulk metallic gold at 84.0 eV. These values are in agreement with the previously reported [87, 88] and the surface chemical state demonstrates in AuNPs@FA-PABA-QP film corresponds to Au<sup>0</sup>, whereas the binding energies of 88.1 and 84.9 eV of Au (4f<sub>7/2</sub>) correspond to Au(III) and Au(I), respectively [61]. To examine mechanism of AuNPs@FA-PABA-QP generations, ATR-FTIR spectrum of AuNPs@FA-PABA-QP presented new absorptions at 1595 and 1362 cm<sup>-1</sup> which corresponded to COO<sup>-</sup> asymmetric and symmetric stretching, respectively, as shown in Figure 55a. These results confirmed the intermediates after reducing Au<sup>3+</sup> to Au<sup>0</sup>, while hydroxyl groups at terminal chain of FA-PABA-QP were oxidized to carboxylate moieties resulted in spherical AuNPs@FA-PABA-QP consistent with our previous report [14]. The O-H stretching shifted from 3293 to 3284 cm<sup>-1</sup> due to FA-PABA-QP capped on AuNPs core through the hydroxyl groups by self-assembly processes [89]. These results confirmed that AuNPs@FA-PABA-QP were successfully synthesized and then served as universal nanocarriers to deliver and enhance cytotoxicity of the anticancer drugs.

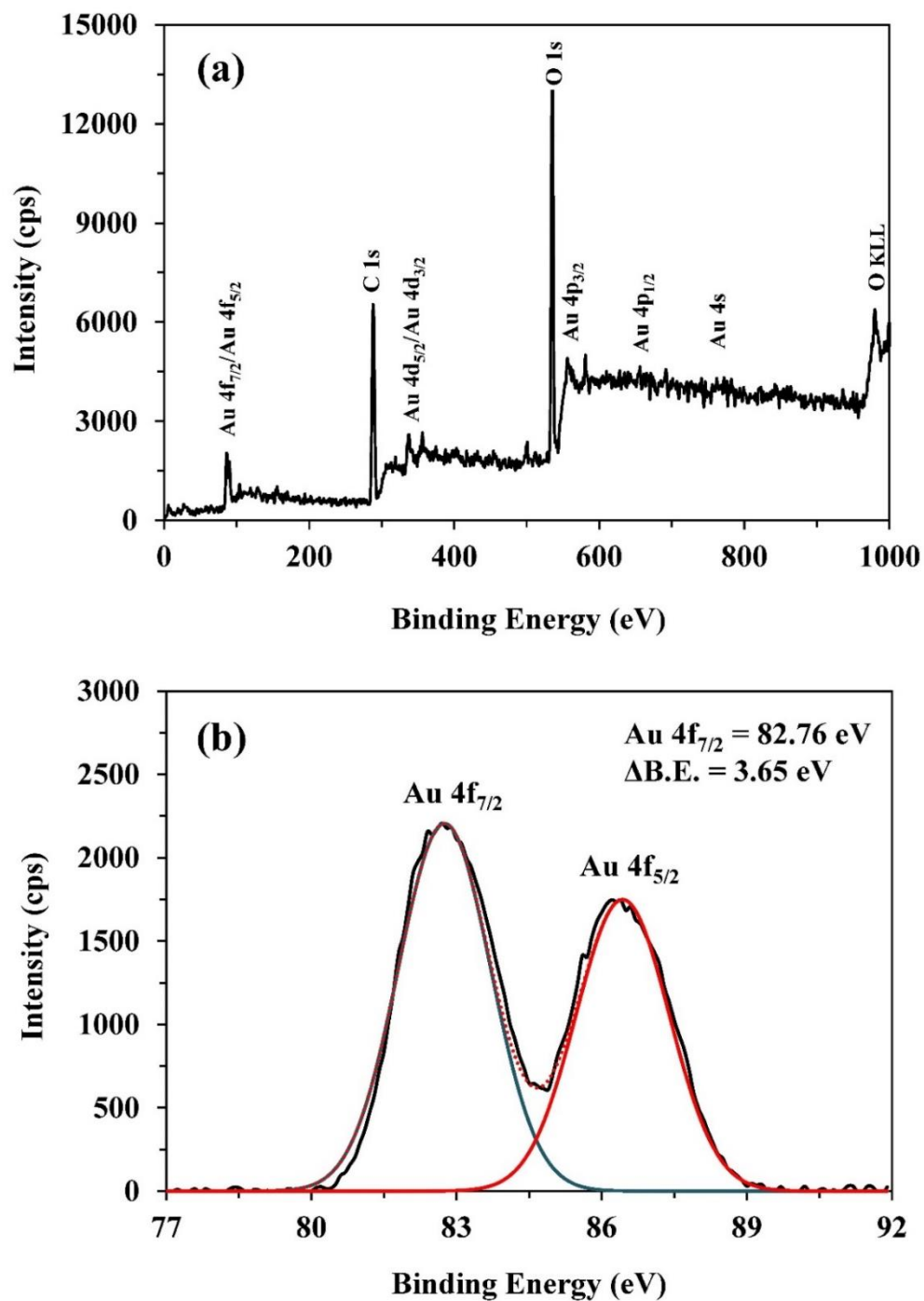


Figure 49 (a) XPS survey spectrum and (b) XPS spectrum of the Au (4f) core level region for AuNPs@FA-PABA-QP film.

Part III: Preparation and characterization of anticancer drugs loaded on AuNPs@pullulan derivatives for enhancing anticancer activities.

#### 4.5 Preparation and characterization of DOX-loaded on AuNPs@PABA-QP

In this work, DOX-AuNPs@PABA-QP was successfully prepared by combination between AuNPs@PABA-QP and DOX via intermolecular interactions and its preparation was confirmed by UV-vis, zeta-potential and ATR-FTIR analyses as shown in Figure 50-51. AuNPs have been studied that, anions self-assembled on AuNPs, it would bind with cations that coexisted in the solution to form new combination through intermolecular attractions [11].

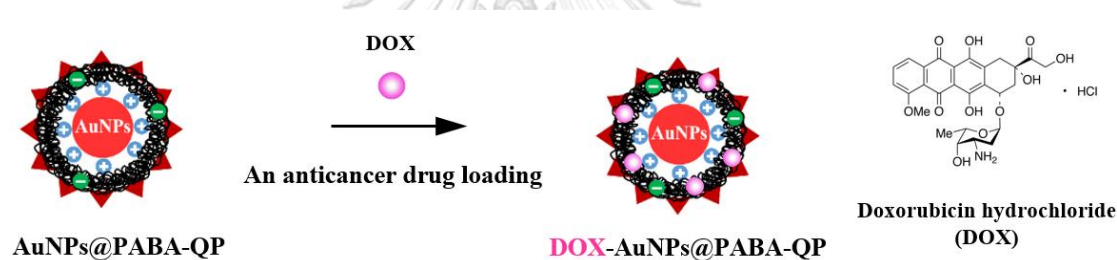
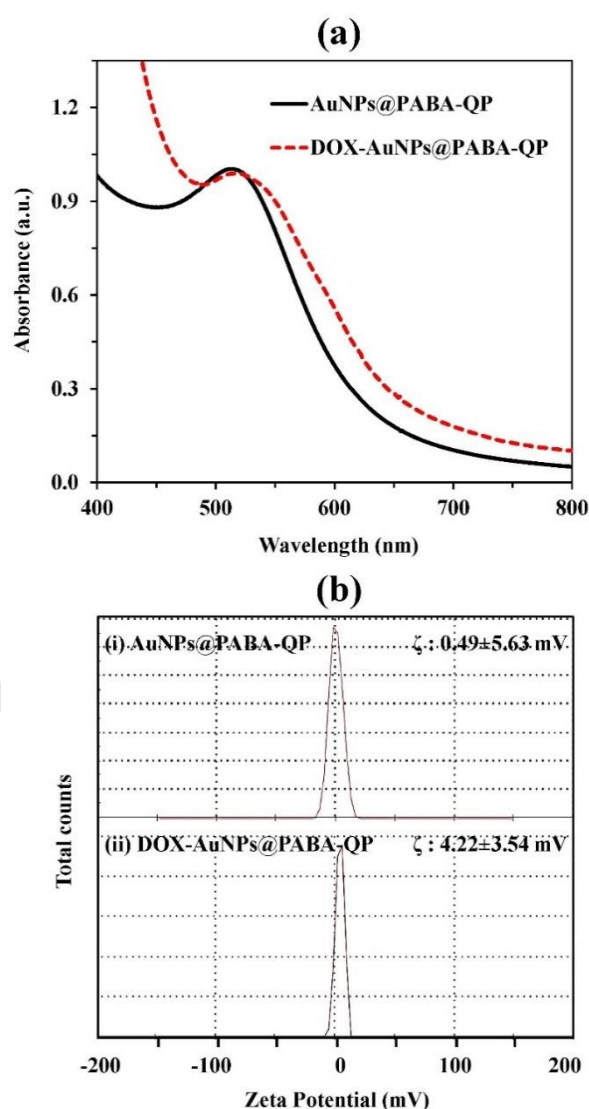


Figure 50 Preparation and chemical structure of DOX-loaded on AuNPs@PABA-QP.

##### 4.5.1 UV-Vis and zeta-potential analysis of DOX-AuNPs@PABA-QP

According to Figure 51a, the chemical structures of DOX-AuNPs@PABA-QP showed their high binding affinity through intermolecular interactions because DOX contain positively charged amino groups, carbonyl and hydroxyl groups, and aromatic rings that interact with the negatively charged AuNPs@PABA-QP containing rich hydroxyl and carboxylate groups, and aromatic rings. Doxorubicin hydrochloride bears a protonated amino group [90] and adsorption of AuNPs is strongly related to the charge states of the amino groups [91]. As expected, DOX binding on AuNPs@PABA-QP was confirmed by slight redshift in the maximum LSPR toward longer wavelengths (515

to 520 nm). The occurrence of the redshift after loading indicates that the particle size of the new complex increased due to the formation of a protective layer on the AuNPs surface upon binding with DOX. Our data are consistent with the results of previous studies [92, 93]. The zeta potential value (Figure 51b) of DOX-AuNPs@PABA-QP was  $4.22 \pm 3.54$  mV. This increase in the zeta potential was assigned to the presence of positively charged DOX and AuNPs@PABA-QP, indicating the presence of attractive forces including electrostatic interactions [13].



**Figure 51** (a) UV-vis spectra and (b) zeta-potentials of (i) AuNPs@PABA-QP and (ii) DOX-AuNPs@PABA-QP.



#### 4.5.2 ATR-FTIR and fluorescence spectroscopy of DOX-AuNPs@PABA-QP

ATR-FTIR spectrum (Figure 52) of DOX-AuNPs@PABA-QP showed characteristic peaks at 1709, 1642 and 1609-1514  $\text{cm}^{-1}$  that correspond to the C=O, N-H and C=C (phenyl ring) stretching of DOX, respectively. In addition, the symmetric COO- stretching of AuNPs@PABA-QP shifted slightly from 1364 to 1375  $\text{cm}^{-1}$  due to intermolecular interactions. In addition, fluorescence spectroscopy with excitation and emission wavelengths of 480 and 594 nm, respectively, was used to quantify the loading amount of DOX onto AuNPs. The efficiency of AuNPs@PABA-QP for loading DOX after 12 h was 93.9%, which was a factor of 1.3 higher than the fraction of the DOX-loaded AuNPs@P (72.2%) using an equal concentration of AuNPs due to higher intermolecular interactions (Figure A11a-c). The dominant factor of high drug loading of DOX onto AuNPs@PABA-QP suggested that carboxylate groups of AuNPs@PABA-QP were associated with the ammonium group of DOX through electrostatic interactions, hydrophobic interactions, hydrogen bonding and diffusion of DOX into AuNPs which could play a major role in facilitating the drug-loading process. These results confirmed that attractive forces including electrostatic,  $\pi$ - $\pi$  stacking and hydrogen bonding intermolecular-interactions could be playing a main role in supporting AuNPs@PABA-QP containing DOX, indicating that DOX was successfully loaded onto AuNPs@PABA-QP to form new DOX-AuNPs@PABA-QP for anticancer drug delivery systems.

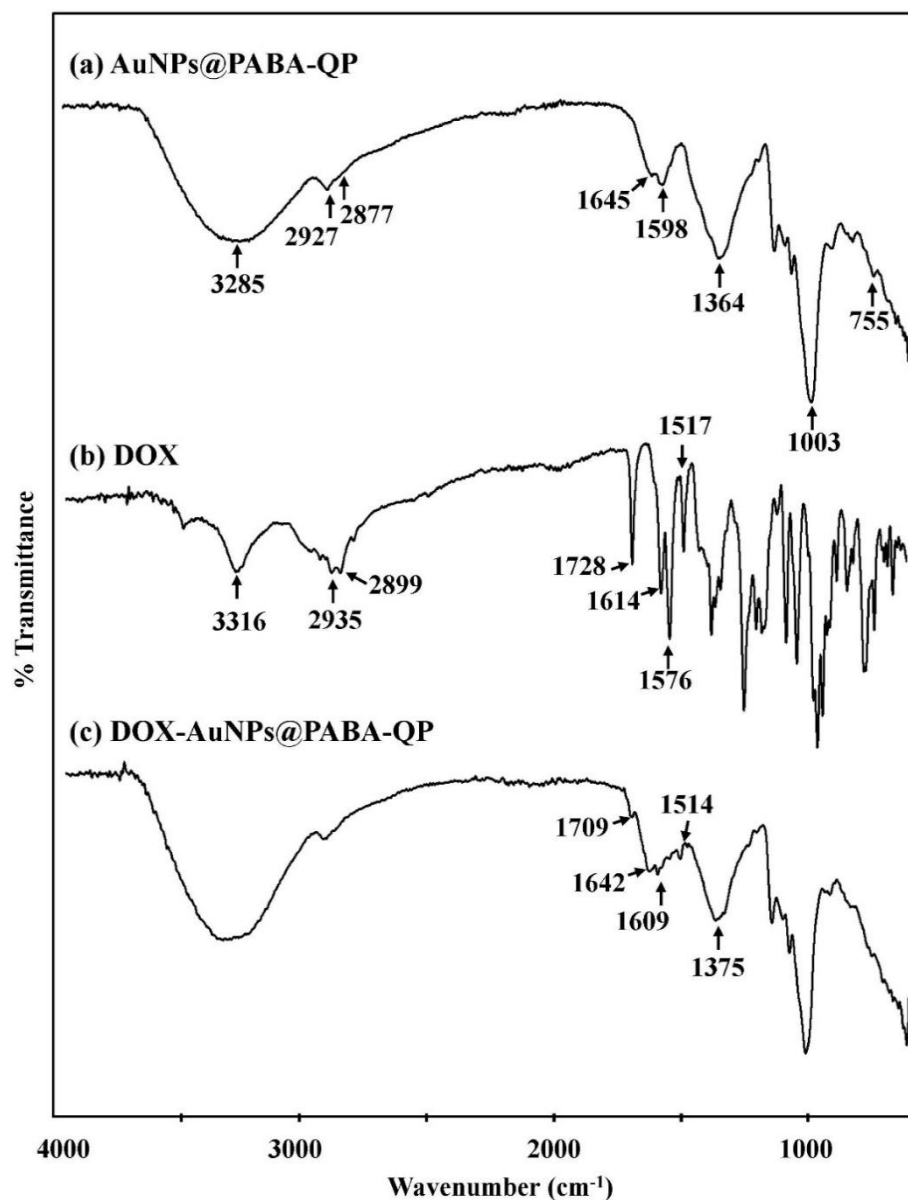


**Figure 52** ATR-FTIR spectra of (a) AuNPs@PABA-QP, (b) DOX and (c) DOX-AuNPs@PABA-QP.

#### 4.6 Preparation and characterization of DOX-loaded and CPT-loaded on AuNPs@FA-PABA-QP

After biosynthesis of AuNPs@FA-PABA-QP, Drug-AuNPs@FA-PABA-QP was prepared by the subsequent loading of an anticancer drugs into AuNPs@FA-PABA-QP

(Figure 53), and then characterized by ATR-FTIR, UV-vis and zeta-potentials. In this work, using these delivery system with non-covalently loaded drug is considered more rational method to from new combinations that avoids any potential issues associated with a prodrug strategy [7]. The adsorption of AuNPs@biopolymers has strong relation to the charging states of amino and hydroxyl groups which DOX has a protonated amino groups [90]. Moreover, we used camptothecin (CPT) as model hydrophobic drugs and doxorubicin hydrochloride (DOX) as model hydrophilic drugs by loading them into amphiphilic AuNPs@FA-PABA-QP as universal nanocarriers to facilitate the use of CPT and DOX in the human body.

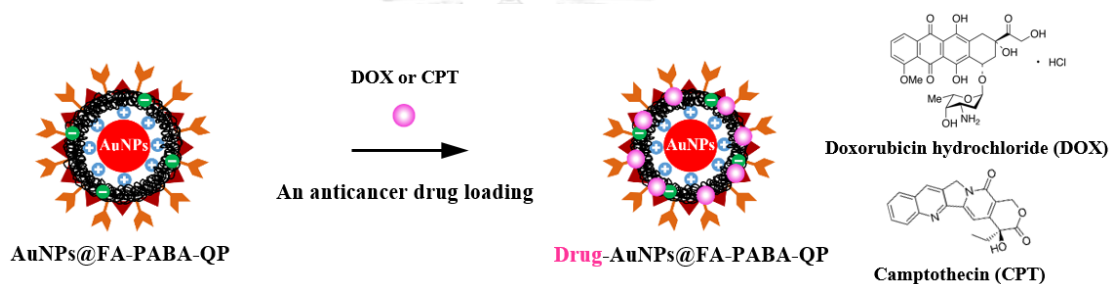


**Figure 53** Preparation and chemical structure of DOX-loaded and CPT-loaded on AuNPs@FA-PABA-QP.

#### 4.6.1 UV-Vis and zeta-potential analysis of DOX-AuNPs@FA-PABA-QP and CPT-AuNPs@FA-PABA-QP

After loading drugs, UV-vis spectra (Figure 54a) of DOX-AuNPs@FA-PABA-QP and CPT-AuNPs@FA-PABA-QP were occurred slightly red-shifts from 519 to 525 and 528 nm, respectively, which confirmed the new bigger nanoparticles and a protective layer on AuNPs surface upon binding with DOX and CPT. Our data are consistent with a previous study [93]. The zeta potential values (Figure 54b) of DOX-AuNPs@FA-PABA-QP and CPT-AuNPs@FA-PABA-QP was 6.56 and 5.73 mV, respectively. This increase in zeta potentials was approved to the presence of positively charged DOX and CPT loading and binding on AuNPs@FA-PABA-QP, indicated that attractive forces including

electrostatic interactions [13]. Moreover, the structures of DOX-AuNPs@FA-PABA-QP and CPT-AuNPs@FA-PABA-QP showed their high binding affinity via non-covalent interactions, as DOX and CPT contain many functional groups that can interact with AuNPs@FA-PABA-QP containing rich hydroxyl and carboxylate groups. FA-PABA-QP covered on AuNPs creating attractive forces including electrostatic,  $\pi$ - $\pi$  stacking and hydrogen bonding interaction could be playing a main role supporting AuNPs@FA-PABA-QP binding with DOX and CPT [94].

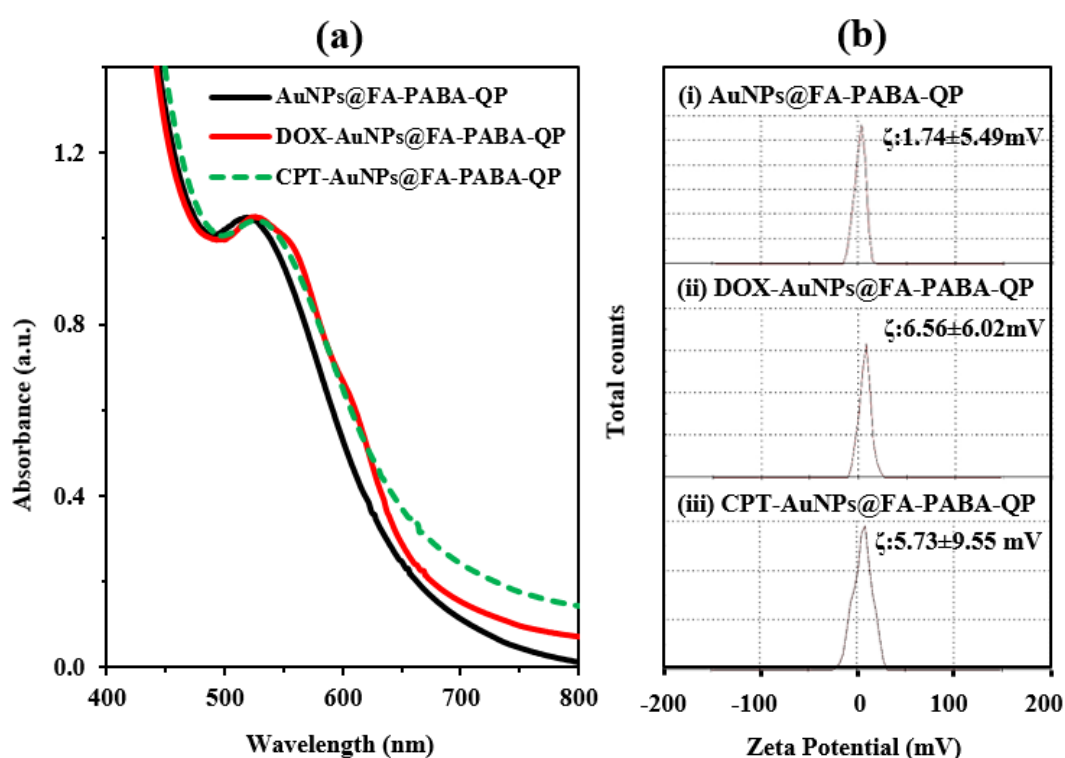


**Figure 54** (a) UV-vis spectra and (b) zeta-potentials of (i) AuNPs@FA-PABA-QP, (ii) DOX-AuNPs@FA-PABA-QP and (iii) CPT-AuNPs@FA-PABA-QP.

#### 4.6.2 ATR-FTIR and fluorescence spectroscopy of DOX-AuNPs@FA-PABA-QP and CPT-AuNPs@FA-PABA-QP

After loading drugs, ATR-FTIR spectra (Figure 55) of DOX-AuNPs@FA-PABA-QP were showed characteristic peaks at 1702 (C=O), 1605 (N-H) and 1557-1516 (C=C of aromatic rings)  $\text{cm}^{-1}$  of DOX, while CPT-AuNPs@FA-PABA-QP was observed new peaks

at 2931, 1730, 1598  $\text{cm}^{-1}$  that corresponded to quinoline (Ar-H), ketone (C=O), and C=C of CPT, respectively. Moreover, the high loading of DOX and CPT onto AuNPs@FA-PABA-QP after 12 h was used fluorescence spectroscopy to quantify the drug content in the obtained pellets which was found to be  $93.5 \pm 0.7$  and  $91.4 \pm 1.3\%$  (Figure A12), respectively. According to our findings, we propose a possible growth mechanism for the formation of the DOX-AuNPs@FA-PABA-QP and CPT-AuNPs@FA-PABA-QP complex as follows. First, primary AuNPs@FA-PABA-QP form through the reduction of  $\text{HAuCl}_4$  by FA-PABA-QP, where the hydroxyl groups of the FA-PABA-QP covering the AuNPs and the carboxylate groups and other conjugations are directed toward the outside of the shell of the structure; here, hydrophobic FA, hydrophobic PABA, and positively charged quat188 on AuNPs could help binding to the drug and enhance the uptake into the cells. After the addition of DOX and CPT, AuNPs@FA-PABA-QP and anticancer drugs (DOX and CPT) move independently in their surrounding space when shaken at room temperature for 12 h, performing a random walk and resulting in the carboxylate moieties on the surface of AuNPs becoming associated with the ammonium group on the DOX and CPT structures through electrostatic and  $\pi$ - $\pi$  stacking interactions in the new composites, respectively [14]. Furthermore, the aromatic substituents (FA-PABA-QP) which create  $\pi$ - $\pi$  stacking interactions and the hydroxyl and amino groups which govern hydrogen bonding are exposed to more active functional groups on the AuNPs surface by associating with active functional groups of DOX and CPT [94]. Finally, the DOX-AuNPs@FA-PABA-QP and CPT-AuNPs@FA-PABA-QP complexes are assembled to form larger spherical particles as a final structure. These results confirmed that DOX-AuNPs@FA-PABA-QP and CPT-AuNPs@FA-PABA-QP were successfully prepared using a delivery system with the non-covalently loaded drugs and then studied the anticancer activities and mechanism of these systems.

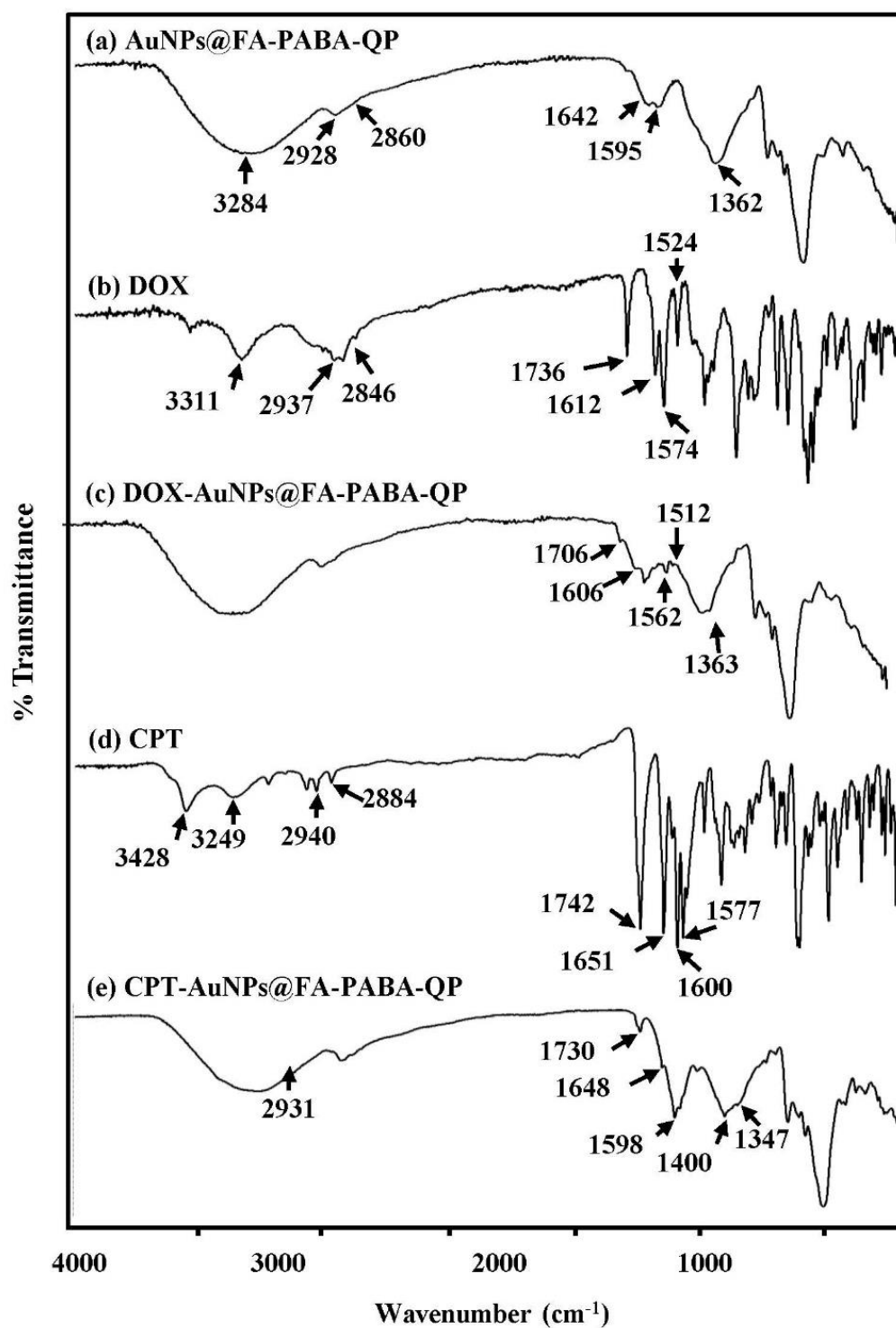


**Figure 55** ATR-FTIR spectra of (a) AuNPs@FA-PABA-QP, (b) DOX, (c) DOX-AuNPs@FA-PABA-QP, (d) CPT and (e) CPT-AuNPs@FA-PABA-QP.

Part IV: Evaluation of their cytotoxicity against human cancer and normal cells, intracellular uptake, drug release, and anticancer mechanism (cell cycle and apoptosis assay) of AuNPs@pullulan derivatives.

#### 4.7 Biological activities of DOX-AuNPs@PABA-QP

To study gold nanoparticles as a passive targeted drug delivery nanocarriers for enhancing cytotoxicity and intracellular uptake of commercial drugs against tested cancer cells (Figure 56).

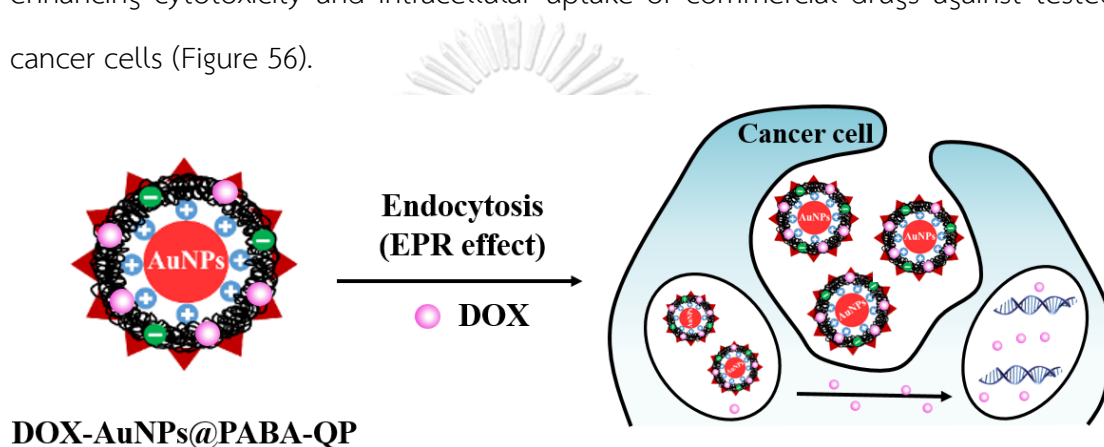


**Figure 56** Schematic representation showing intracellular releasing of DOX on AuNPs@PABA-QP as a passive targeted nanocarriers in Chago-k1 cells.

จุฬาลงกรณ์มหาวิทยาลัย  
CHULALONGKORN UNIVERSITY

##### 4.7.1 Cytotoxicity study of DOX-AuNPs@PABA-QP

To study AuNPs@PABA-QP as a passive targeted nanocarriers for enhancing cytotoxicity and intracellular uptake of commercial drugs against cancer cells. In this work, we investigated the cytotoxicity of PABA-QP, AuNPs@P, AuNPs@QP, AuNPs@PABA-QP and DOX-AuNPs@PABA-QP compared to free DOX against KATO-III and Chago-k1 cancer cells. To study the role of cationic AuNPs@pullulan derivatives, the cytotoxicity against both cancer cells was evaluated using  $IC_{50}$  of PABA-QP > AuNPs@P > AuNPs@QP > AuNPs@PABA-QP, as shown in Table 3, A1 and A5, suggesting

the dependence of bioactivity on the surface modification of AuNPs [45]. The unexpectedly enhanced anticancer activity of AuNPs@PABA-QP was explained as follows (Figure A13-19). The surface charges showed charge density and charge polarity playing a role in the cytotoxic action of AuNPs@PABA-QP. Additionally, the intracellular uptake and localizations of AuNPs@PABA-QP in cells were characterized by TEM and CLSM. After treatment, AuNPs@PABA-QP showed highly enhanced anticancer activity and accumulated in the vesicles of the cells via endocytosis. After modification of pullulan by positive charges (Quat188), a significantly enhancement of cytotoxicity compared to unmodified pullulan was observed in MTT assay. Additionally, positively charged Quat188 and hydrophobic PABA conjugated to the pullulan backbone (PABA-QP) can help increase intracellular uptake and cell permeability in biological processes, which for Quat188 and PABA may be due to the enhanced electrostatic interactions with the negative charge of the cell membrane, and increased hydrophobic interactions with the hydrophobic parts of the cell membrane, respectively [16]. Similarly, Fröhlich et al. reported that cationic NPs cause a more pronounced disruption of the plasma-membrane integrity, stronger mitochondrial and lysosomal damage, and a higher number of autophagosomes than anionic NPs and neutral NPs to enhance cytotoxicity and inhibit cancer cells [44], which was consistent with the results of our MTT assay. Consequently, modified AuNPs not only play the role of a model drug delivery carriers but also help to increase cell inhibition to open pathways for cationic AuNPs as a new effect. Moreover,  $IC_{50}$  of free DOX against KATO-III cells was approximately  $0.91 \pm 0.35 \mu\text{M}$ . After loading DOX onto AuNPs,  $IC_{50}$  of DOX-AuNPs@PABA-QP against KATO-III cells was lowered to  $0.55 \pm 0.14 \mu\text{M}$ . A similar trend was also observed for the  $IC_{50}$  of DOX loaded AuNPs@PABA-QP against Chago-k1 cells which decreased by a factor of two-fold compared to the nonloaded AuNPs@PABA-QP (DOX= $0.82 \pm 0.16$  and DOX-AuNPs@PABA-QP= $0.39 \pm 0.18 \mu\text{M}$ ). The greater difference in the  $IC_{50}$  between DOX and DOX-AuNPs@PABA-QP found for both cancer cell, suggested



that AuNPs@PABA-QP are excellent nanocarriers, and the surface-modified AuNPs by cationic PABA-QP could enhance the anticancer activity of DOX. Therefore, the high efficacy of nanocarriers themselves supported the improvement of  $IC_{50}$  of DOX-AuNPs@PABA-QP, which was enhanced by intracellular uptake of AuNPs@PABA-QP to deliver cellular internalization of DOX by EPR effects. Overall, the results suggest that DOX-AuNPs@PABA-QP shows more potent activity in cancer cells, while it exhibits less toxicity toward normal cells.

To reduce the toxicity of DOX against normal lung cells (Wi-38), AuNPs@PABA-QP are used as a model drug nanocarrier. According to Figure 57, PABA-QP, AuNPs@P, AuNPs@PABA-QP and DOX-AuNPs@PABA-QP (DOX loaded at 0.1 and 1  $\mu$ M) showed relatively less toxicity to normal cells with cell viability higher than 80%, whereas the high dose of free DOX at 1  $\mu$ M was quite toxic toward normal cells. This improvement may be due to the effect of the surface-modified AuNPs, which is expected to provide protection of payload drug from the biological environment outside the cells and which are taken up by endocytosis so that the DOX drug is specifically released in cancer cells by the enhanced permeability and retention (EPR) effect [10]. This also shows that AuNPs@PABA-QP are nanocarriers that are suitable for drug delivery applications. Therefore, AuNPs@PABA-QP as nanocarriers are suitable for cancer treatments due to the increased efficacy and safety of these systems. Furthermore, the cytotoxicity of DOX-AuNPs@PABA-QP at 72 h showed the best cell inhibitory activities against Chago-k1 which was more than that obtained for KATO-III cells compared to DOX. Therefore, lung carcinoma (Chago-k1) cell lines were chosen for subsequent studies.

**Table 3** Cytotoxicity (IC<sub>50</sub>) of each compound against Chago-k1 and KATO-III cells.

Compound	Cytotoxicity <sup>a</sup> (IC <sub>50</sub> , μM)	
	Chago-k1	KATO-III
PABA-QP	>100	>100
AuNPs@P	>100	>100
AuNPs@QP	36.98±2.09	51.76±4.43
AuNPs@PABA-QP	35.44±2.13	44.88±2.68
DOX	0.82±0.16	0.91±0.35
DOX-AuNPs@PABA-QP	0.39±0.18	0.55±0.14

<sup>a</sup> Cytotoxicity was derived after 72h exposure to the compound by MTT assay.

Data are shown as mean ±1SD, derived from three independent trials.

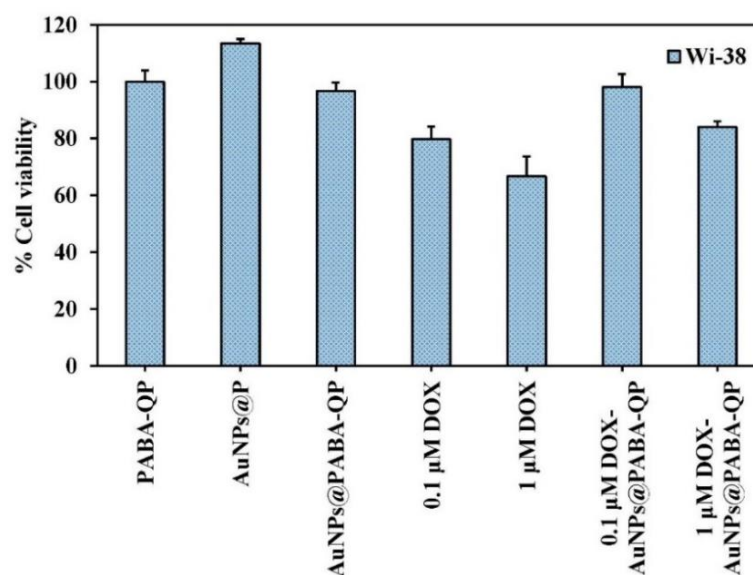


**Figure 57** Cytotoxicity of DOX and DOX-AuNPs@PABA-QP against normal cells (Wi-38) compared with PABA-QP, AuNPs@P and AuNPs@PABA-QP.

#### 4.7.2 Intracellular uptake study by TEM of AuNPs@PABA-QP

To study whether AuNPs@PABA-QP was taken up in cancer cells by endocytosis, TEM images of Chago-k1 cells treated with 40 μM AuNPs@PABA-QP for 72 h were compared with untreated Chago-k1 cells. After treatment with AuNPs@PABA-QP (Figure 56 and 58), AuNPs@PABA-QP and other AuNPs were endocytosed and accumulated within vacuole of cells, resulting in cell disruption and discontinuous nuclear membrane. In untreated Chago-k1 cells, the nuclear membrane and cell membrane were intact and continuous. The intracellular uptake of AuNPs is facilitated by PABA as hydrophobic molecules and positive charges on the surface of AuNPs. The TEM results strongly indicated that AuNPs@PABA-QP as nanocarriers could induce intracellular uptake by endocytosis, enhancing cytotoxicity of DOX-AuNPs@PABA-QP.

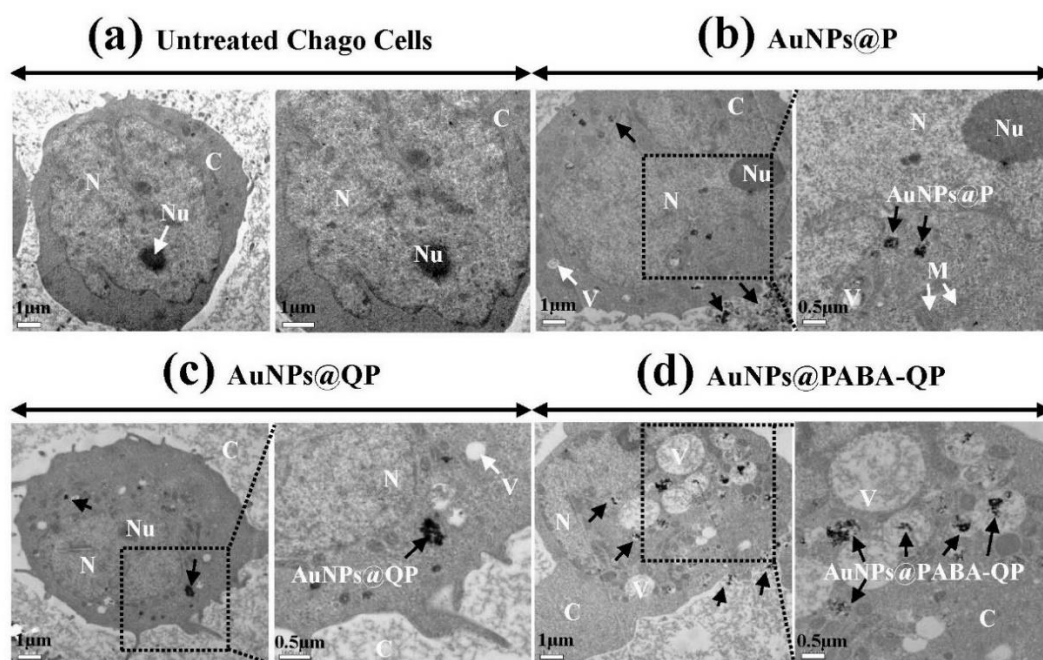


**Figure 58** Intracellular uptake by TEM images of (a) untreated and treated Chago-k1 cells with 40  $\mu\text{M}$  (b) AuNPs@P, (c) AuNPs@QP and (d) AuNPs@PABA-QP after 72 h (N=nucleus; Nu=nucleolus; C=cytoplasm; V=vacuole).

#### 4.7.3 Confocal study of DOX-AuNPs@PABA-QP

CLSM was used to study the intracellular uptake of DOX-loaded AuNPs@PABA-QP (Figure 59). DOX-AuNPs@PABA-QP could be effectively internalized in Chago-k1 cells for 12 h. Moreover, all samples presented greenish-blue fluorescence in nucleus (DAPI). DOX alone showed weakly red fluorescence in both cytoplasm and nucleus. The cells incubated with DOX-AuNPs@PABA-QP exhibited strong DOX fluorescence in both the cytoplasm and nucleus due to the greater amount of DOX released from DOX-AuNPs@PABA-QP under the reducing environment of the cells. The CLSM images showed a dependence on the time-dependent cellular uptake of DOX-AuNPs@PABA-QP and fast DOX releasing from reduction-sensitive AuNPs@PABA-QP under reductive intracellular uptake conditions due to the reductive cleavage of the interactions and disassembly of PABA-QP stabilized AuNPs. This result showed that DOX-AuNPs@PABA-

QP enter cancer cells by endocytosis and the loaded drug is subsequently released because DOX is a small molecule and can rapidly diffuse into the cancer cells and enter the nucleus by passive diffusion [95]. Therefore, the reductive-sensitive AuNPs@PABA-QP can be used as suitable drug nanocarriers.

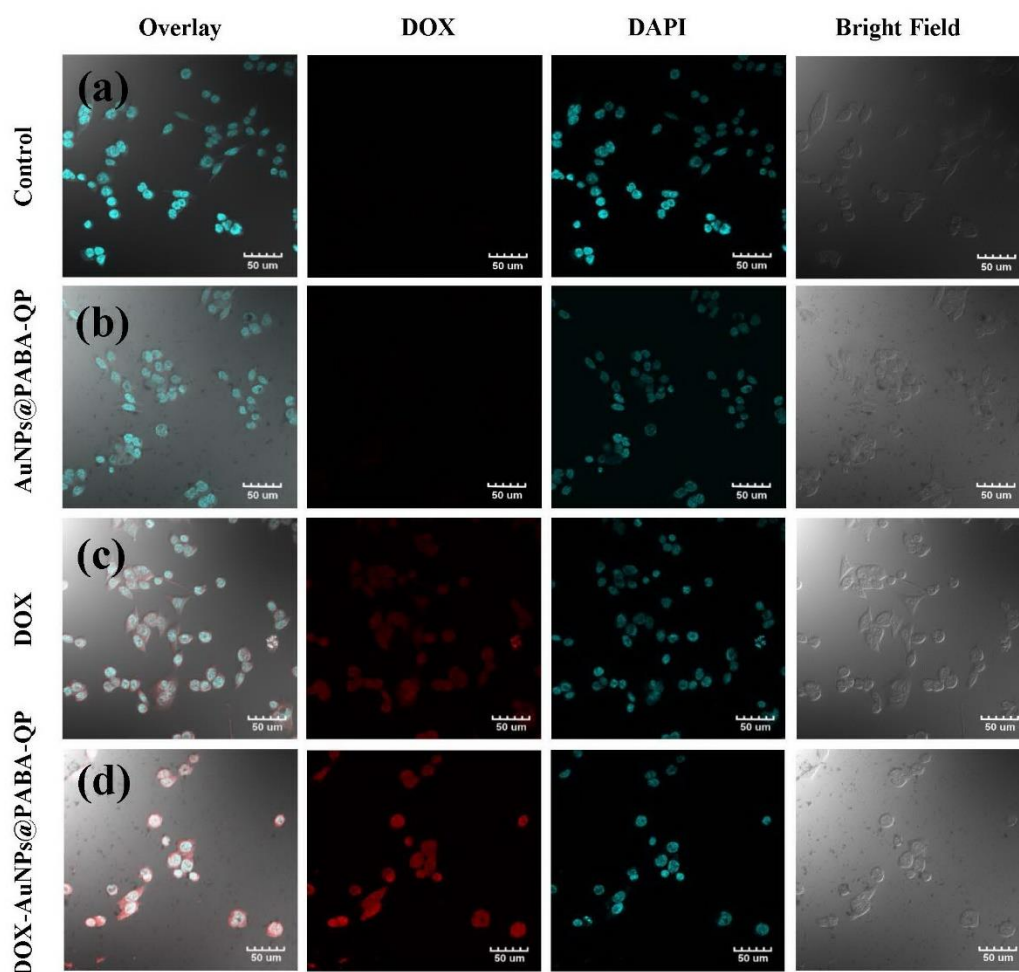


**Figure 59** Confocal microscopy images showing intracellular uptake of (a) control group and Chago-k1 cells incubated with (b) AuNPs@PABA-QP, (c) DOX and (d) DOX-AuNPs@PABA-QP at 37°C for 12 h (DOX and AuNPs@PABA-QP at 0.3 and 40 μM, respectively).

#### 4.7.4 Cell cycle assay of DOX-AuNPs@PABA-QP

The cells were treated with DOX-AuNPs@PABA-QP for 24 h, and it was found that a significant number of cells were arrested at the S and G2-M phases of the cell cycle (Figure 60). In 0.3  $\mu\text{M}$  DOX-treated cells, the fractions of Chago-k1 cells in cell cycle consisting of sub-gap 1 phase (sub-G1), gap 0-gap 1 phases (G0-G1), synthesis phase (S) and gap 2-mitosis phases (G2-M) were 4.03, 44.4, 18.0 and 27.1%, respectively. However, the fractions of the cells in the S and G2-M phases of 0.3  $\mu\text{M}$  DOX-AuNPs@PABA-QP were increased to 13.5 and 4.5% (a total S/G2-M increased to 18.0%), respectively, and the G0-G1 phase was decreased to 11.3%, compared to the use of DOX alone. Similar results were obtained when the cells were treated with the dose of DOX-AuNPs@PABA-QP increased from 0.15 to 0.5  $\mu\text{M}$ , showing an increase of the cells in synthesis/gap 2-mitosis phases (S/G2-M). These data provide strong evidence for the cell cycle arrest induced by DOX-AuNPs@PABA-QP, which could be related to the DOX interaction with DNA to inhibit the DNA replication of the cells. Moreover, the inhibited cell growth could also be attributed to enhanced apoptotic cell death, consistent with previous reports [96]. We therefore also studied whether DOX-AuNPs@PABA-QP could induce apoptotic cells.

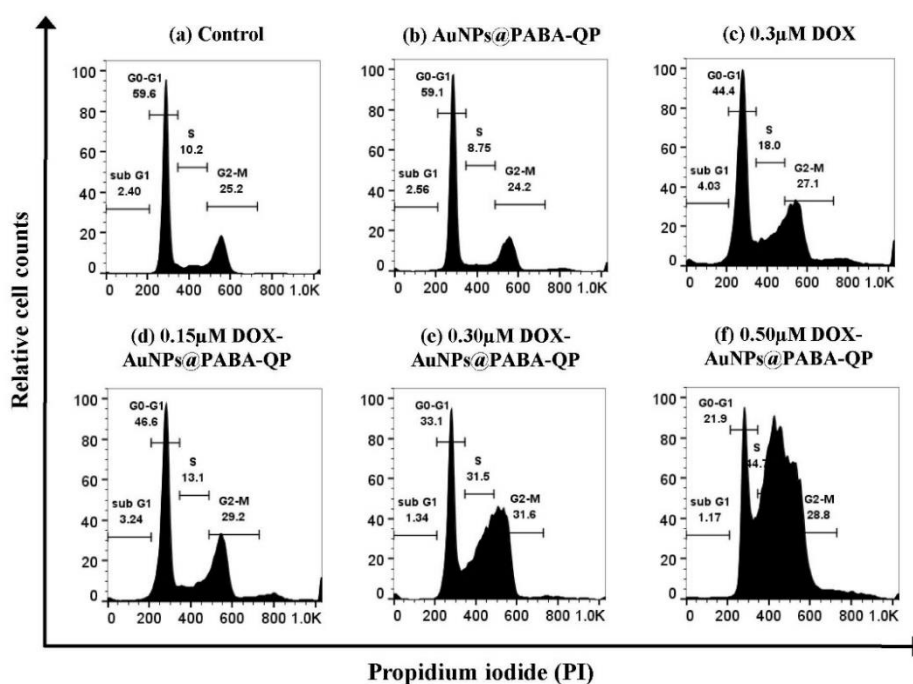


**Figure 60** Cell cycle analysis of Chago-k1 cells after 24 h treatment with (a) control, (b) AuNPs@PABA-QP, (c) DOX and (d-f) DOX-AuNPs@PABA-QP as detected by Annexin V-FITC/PI dual staining method.

#### 4.7.5 Apoptosis assay of DOX-AuNPs@PABA-QP

To study apoptosis/necrosis using a flow cytometer, Chago-k1 cells were treated with DOX, AuNPs@PABA-QP, and DOX-AuNPs@PABA-QP (DOX and AuNPs@PABA-QP at 0.3 and 40 μM) for 12 h (Figure 61). For the majority of untreated and treated Chago-k1 cells with AuNPs@PABA-QP, 98.4% and 96.5% of viable cells were observed. In contrast, for the cells were treated with DOX and DOX-AuNPs@PABA-QP, 0.003% and 0.01% of viable cells were observed, demonstrating complete cell death. These results indicate that DOX-AuNPs@PABA-QP showed apoptosis (25.0%) and necrosis (75.0%), whereas doxorubicin alone demonstrated apoptosis (6.4%) and necrosis (93.6%). DOX-AuNPs@PABA-QP exhibited increasing apoptosis and decreasing necrosis for the pathways of cell death at approximately 18.6% showing better cell death pathway than that for DOX. A slight increase in late apoptosis (Annexin V<sup>+</sup>/PI<sup>+</sup>)

and a decrease in necrosis (Annexin V<sup>-</sup>/PI<sup>+</sup>) were also observed, indicating both apoptotic/necrotic cell death mechanisms, which is consistent with the previous reports [97] and our cytotoxicity results. Therefore, DOX-loaded AuNPs@PABA-QP as bio-nanocarriers exhibit greater ability to induce apoptosis cells and reduced side effect than doxorubicin alone. Consequently, these results suggested that the novel combination of DOX-AuNPs@PABA-QP has the potential to be developed for human cancer treatments.

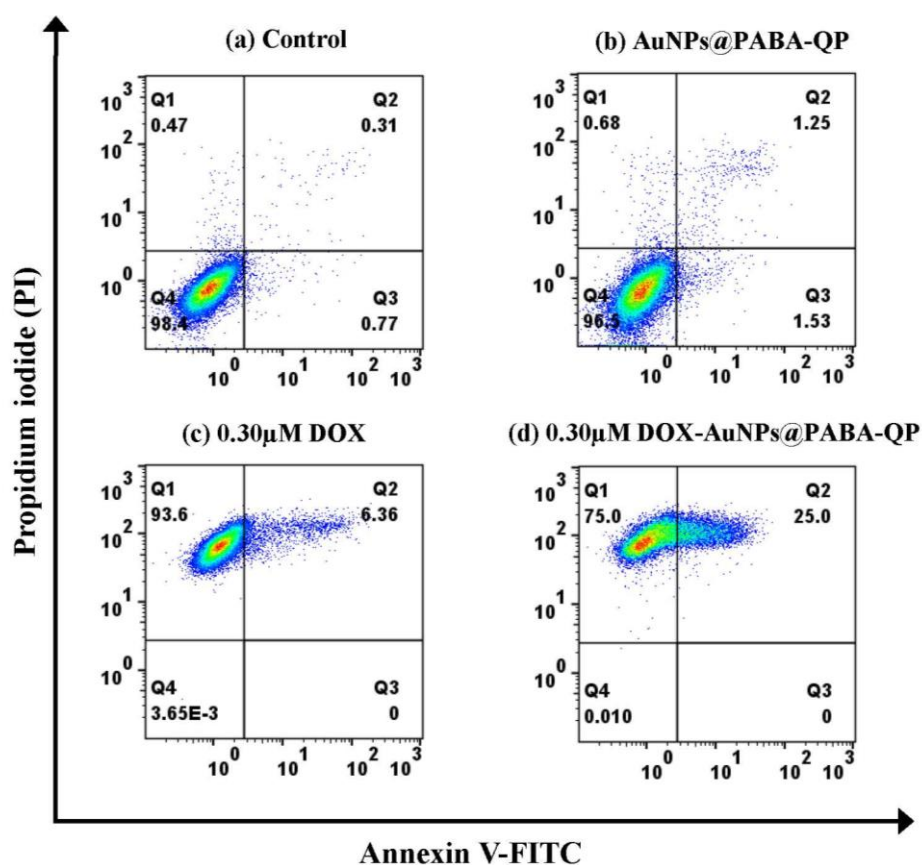


**Figure 61** Flow cytometric analysis of Chago-k1 cells after 12 h treatment with (a) control, (b) AuNPs@PABA-QP, (c) DOX and (d) DOX-AuNPs@PABA-QP as detected by Annexin V-FITC/PI dual staining method.



## 4.8 Biological activities of DOX-AuNPs@FA-PABA-QP and CPT-AuNPs@FA-PABA-QP

### 4.8.1 Cytotoxicity study of Drug-AuNPs@FA-PABA-QP

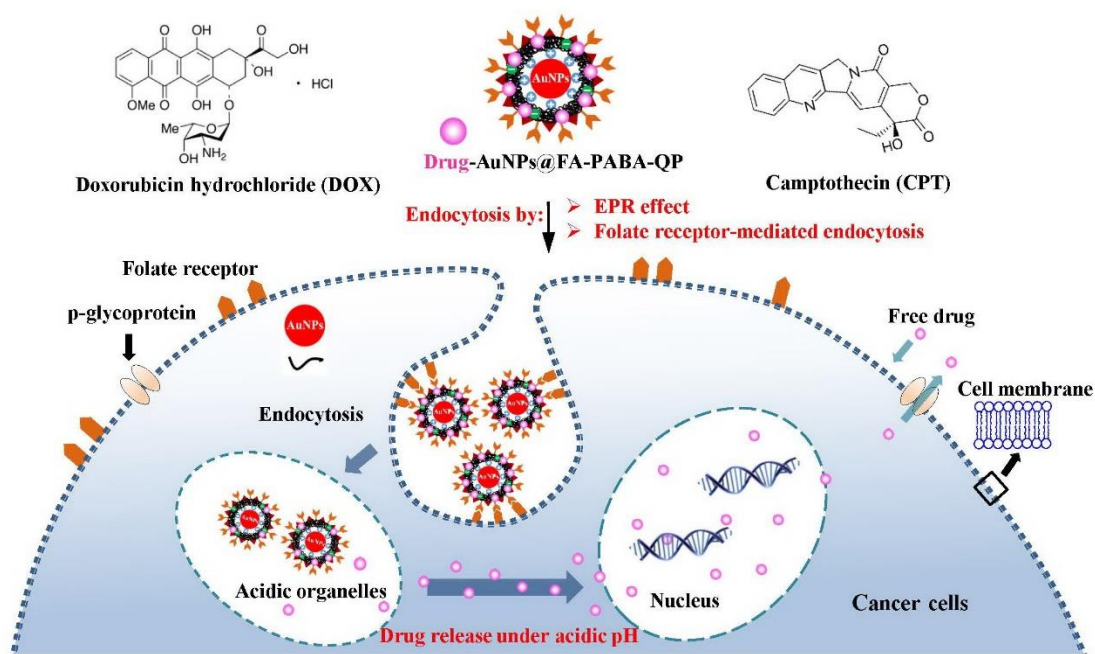


**Figure 62** Schematic representation showing intracellular releasing of DOX and CPT on AuNPs@FA-PABA-QP as an active targeted nanocarriers in Chago-k1 cells.

To study enhanced cytotoxicity and intracellular uptake, we studied anticancer activities of folate-receptor-targeted amphiphilic AuNPs@FA-PABA-QP as universal bio-nanocarriers and as an active targeted nanocarriers and combining with various concentrations of DOX and CPT as loaded anticancer drugs (Figure 62). This is firstly study to evaluate and report their cytotoxicity of our newly synthesized DOX-AuNPs@FA-PABA-QP and CPT-AuNPs@FA-PABA-QP using MTT assay against five human cancer cells including BT474 (breast-carcinoma), A549 (adenocarcinoma), KATO-III (gastric-carcinoma), Hep-G2 (liver-carcinoma) and Chago-k1 (lung bronchogenic-

carcinoma), and human lung normal cells (Wi-38). The ability to interfere with their colony formation were also investigated.

New combinative platforms of DOX-AuNPs@FA-PABA-QP and CPT-AuNPs@FA-PABA-QP showed different cytotoxic activities in each cancer cells. Among these cells, DOX-AuNPs@FA-PABA-QP and CPT-AuNPs@FA-PABA-QP exhibited strongly cytotoxic activity against Chago-k1 cells with  $IC_{50}$  of  $0.17 \pm 0.12$  and  $2.21 \pm 1.01 \mu\text{M}$  and more sensitive than DOX-alone and CPT-alone with  $IC_{50}$  of  $0.82 \pm 0.16$  and  $6.19 \pm 1.21 \mu\text{M}$ , respectively, while AuNPs@FA-PABA-QP was similarly high cytotoxicity to Chago-k1 cells (Table 4 and Table A2-A4). When time incubations increased from 24 to 72h, cytotoxicity of AuNPs@FA-PABA-QP increased due to higher cell inhibition against both cancer cells (Table A6) [98]. The cytotoxicity of AuNPs@FA-PABA-QP at 72h showed the best cell inhibition against Chago-k1 cells compared with Hep-G2 cells (Figure 63a). In our case the calculated  $IC_{50}$  of DOX-AuNPs@FA-PABA-QP was 1.16-fold, 1.68-fold, 1.72-fold, 1.65-fold, and 4.82-fold lower than  $IC_{50}$  of DOX-alone against BT474, A549, KATO-III, Hep-G2, and Chago-k1 cells, respectively, due to increasing the anticancer activity. Similarly, the activity of CPT increased in KATO-III, Hep-G2, and Chago-k1 cells when loaded on AuNPs@FA-PABA-QP by approximately 1.30-fold, 1.34-fold, and 2.80-fold, respectively, decreasing the  $IC_{50}$  values. More importantly, the highest difference of  $IC_{50}$  between both Drug-AuNPs@FA-PABA-QP and both drug-alone found for lung carcinoma cells, which showed the highest efficacy to enhance the antiproliferative activity and intracellular internalization of DOX and CPT using AuNPs@FA-PABA-QP [99]. This selectivity is due to the folate-targeting ligand on AuNPs@FA-PABA-QP, which targets the folate-receptor that is overexpress in Chago-k1 cells through folate-receptor-mediated endocytosis pathway and results in the stronger cytotoxic effects [80]. Therefore, the lung carcinoma (Chago-k1) cell line was chosen for subsequent studies. In addition, DOX-AuNPs@FA-PABA-QP and CPT-AuNPs@FA-PABA-QP were relatively less toxic to lung normal cells (Wi-38) with cell viability > 70%, whereas DOX-

alone and CPT-alone was more toxicity (DOX and CPT at 1 and 5  $\mu\text{M}$ , respectively) (Figure 63b). Hence, drug loaded on AuNPs@FA-PABA-QP showed more potential against lung cancer cells, while it exhibited less toxicity to lung normal cells.

**Table 4** *In vitro* cytotoxicity of each compound against five cancer cells.

Compound	Cytotoxicity <sup>a</sup> (IC <sub>50</sub> , $\mu\text{M}$ )				
	BT474	A549	KATO-III	Hep-G2	Chago-k1
FA-PABA-QP	>100	>100	>100	>100	>100
AuNPs@FA-PABA-QP	49.32±4.10	83.22±4.76	44.68±2.55	34.72±3.07	34.10±1.78
DOX	0.50±0.13	0.64±0.10	0.91±0.11	0.61±0.14	0.82±0.16
DOX-AuNPs@FA-PABA-QP	0.43±0.11	0.38±0.12	0.53±0.22	0.37±0.15	0.17±0.12
CPT	ND <sup>b</sup>	16.06±1.96	9.84±1.56	13.29±1.25	6.19±1.21
CPT-AuNPs@FA-PABA-QP	ND	ND	7.56±2.12	9.95±1.99	2.21±1.01

<sup>a</sup>Cytotoxicity was derived after 72h exposure to each compound using MTT assay.

<sup>b</sup>ND=not determined.

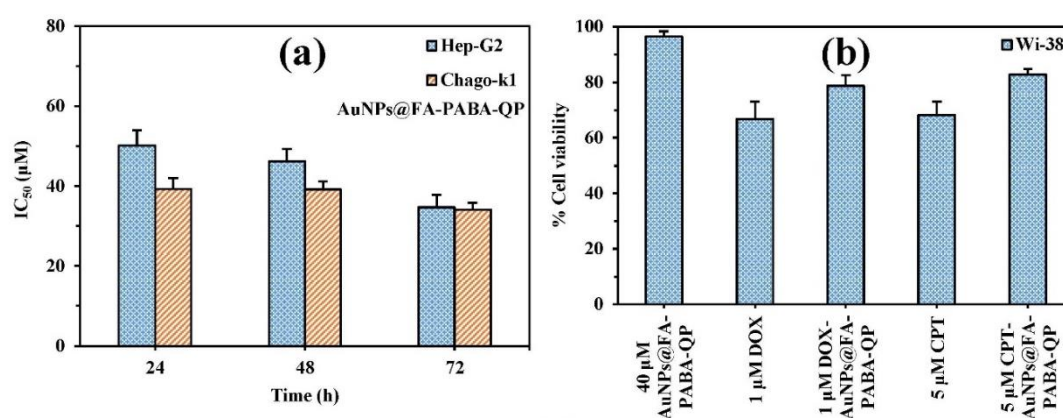


**Figure 63** Cytotoxicity of AuNPs@FA-PABA-QP against (a) cancer (Hep-G2 and Chago-k1), and (b) normal cells (Wi-38) for 72 h.

#### 4.8.2 Colony formation assay of Drug-AuNPs@FA-PABA-QP

Colony formation assay was performed to verify long-term antiproliferation efficacy of DOX-AuNPs@FA-PABA-QP and CPT-AuNPs@FA-PABA-QP in Chago-k1 cells. After treatment, the reduction in colony formation ability was observed significantly when the concentration of drug loaded on AuNPs@FA-PABA-QP was increased. A less number of colonies were observed in cells treated with DOX-AuNPs@FA-PABA-QP and CPT-AuNPs@FA-PABA-QP than DOX-alone, CPT-alone, cisplatin treated cells and untreated cells (Figure 64). Specifically, DOX-AuNPs@FA-PABA-QP was more sensitive than CPT-AuNPs@FA-PABA-QP which was consistent with MTT assay. Therefore, new opportunities of DOX-AuNPs@FA-PABA-QP and CPT-AuNPs@FA-PABA-QP as novel platforms have new potential to be developed and used for lung cancer treatments

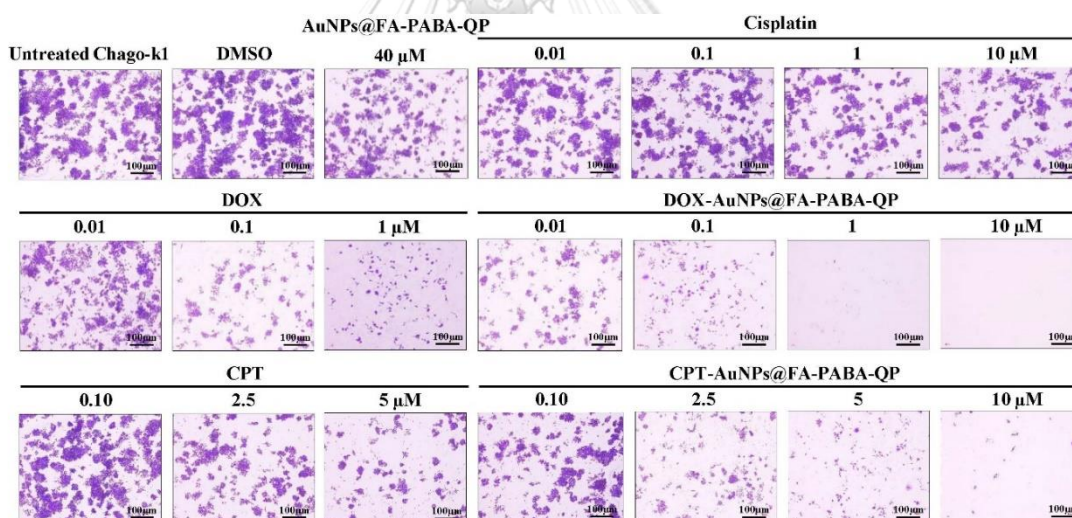


**Figure 64** Colony formation assay in Chago-k1 cells treated with DOX-AuNPs@FA-PABA-QP, CPT-AuNPs@FA-PABA-QP and compared with other groups.

#### 4.8.3 Cell morphology study of Drug-AuNPs@FA-PABA-QP

To investigate whether the DOX, AuNPs@pullulan derivatives, or the combination of DOX-AuNPs@FA-PABA-QP and CPT-AuNPs@FA-PABA-QP could influence cell morphology. Untreated Chago-k1 cancer cells were homogeneously distributed in the culture plate demonstrating a polygonal shape (flat or fusiform) and homogenous cellular contents (Figure 65). Unlike DOX and CPT, the morphology of the treated cells with DMSO, AuNPs@P, AuNPs@QP and AuNPs@PABA-QP showed the cell morphology similar to the un-treatment group. In addition, the morphology of the treated cells with AuNPs@FA-PABA-QP at 40  $\mu\text{M}$  caused cell morphological changes such as a round shape and decreased cell density at a dose-dependent manner. After treatment of the cells with DOX and CPT alone caused marginal cell morphological changes such as a round shape, while the combination of DOX-AuNPs@FA-PABA-QP and CPT-AuNPs@FA-PABA-QP caused strong morphological changes (abnormal morphology) such as rounder, fewer, and deader compared to the single treatment group. Similarly, Chago-k1 cells treated with DOX and CPT alone and DOX-AuNPs@FA-PABA-QP and CPT-AuNPs@FA-PABA-QP at 0.1, 1, and 10  $\mu\text{M}$ , cells density was decreased at a dose-dependent manner. Moreover, DOX-AuNPs@FA-PABA-QP showed better cytotoxic activity than CPT-AuNPs@FA-PABA-QP due to different cell death mechanism to kill cancer cells. Therefore, these results suggest that the combination of DOX-AuNPs@FA-PABA-QP and CPT-AuNPs@FA-PABA-QP induces morphological changes (cellular shrinkage and detachment) and cell death in Chago-k1 cells and these results were consistent with that of MTT assay. Overall, the preliminary data that the combination alter cellular morphology provide evidence for their toxicity.

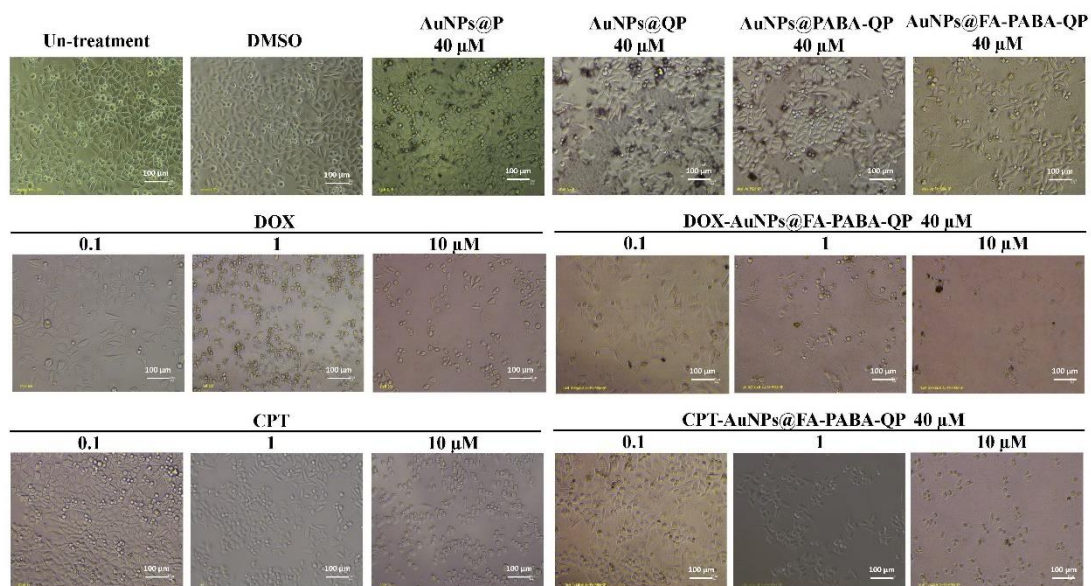


**Figure 65** Phase contrast micrographs showed cytotoxic effect exerted by DMSO, AuNPs@P, AuNPs@QP, AuNPs@PABA-QP, AuNPs@FA-PABA-QP, DOX, CPT, and the combination of DOX-AuNPs@FA-PABA-QP and CPT-AuNPs@FA-PABA-QP against Chago-k1 after 72 h. Treated cells were photographed under a light microscope at a magnification of 20x (scale bare: 100 μm).

#### 4.8.4 Intracellular uptake study by TEM of AuNPs@FA-PABA-QP

To study whether endocytosis of targeted-AuNPs@FA-PABA-QP were entered into cells, Chago-k1 cells were incubated with 40  $\mu$ M AuNPs@FA-PABA-QP for 72 h and fixed for TEM compared with untreated cells (Figure 62 and 66). TEM image in untreated cells showed continuously cell membranes, while cells culturing with AuNPs@FA-PABA-QP which many of AuNPs@FA-PABA-QP were found and accumulated in vesicles of cells such as endosomes or lysosomes. Moreover, AuNPs@FA-PABA-QP showed the intracellular uptake more than AuNPs@PABA-QP > AuNPs@QP > AuNPs@P by ICP-OES at 40  $\mu$ M (Figure A10). Also, TEM images and intracellular uptake by ICP-OES confirmed that AuNPs@FA-PABA-QP as universal nanocarriers were taken and accumulated into the cancer cells via folate receptor-mediated endocytosis process, hydrophobic-mediated endocytosis, positive charge-mediated endocytosis, and EPR effect, which likely delivered, and enhanced biocompatibility and cytotoxicity of the drugs [100].

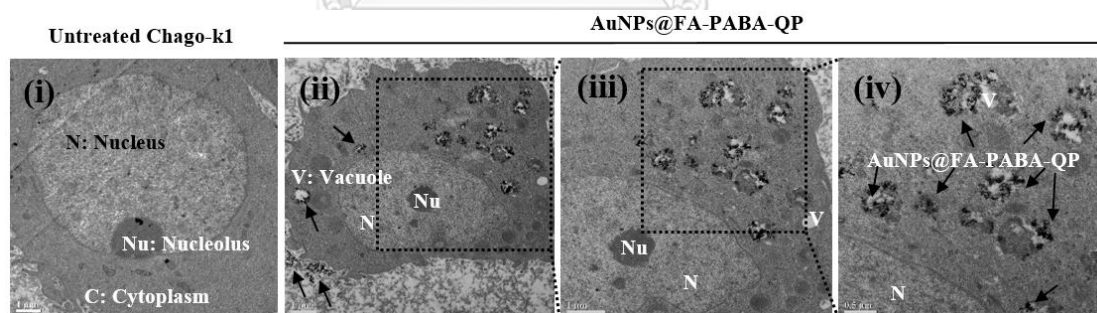


**Figure 66** Intracellular uptake by TEM images of Chago-k1 cells after culturing with or without AuNPs@FA-PABA-QP as an active targeted nanocarriers for 72h (N=nucleus; Nu=nucleolus; C=cytoplasm; V=vacuole).

#### 4.8.5 Confocal study of Drug-AuNPs@FA-PABA-QP

Confocal laser scanning microscopy (CLSM) was used to study the intracellular uptake and localizations of CPT and DOX loaded onto AuNPs@FA-PABA-QP in Chago-k1 cells for 12 h (Figure 67). CLSM was based on the red and blue autofluorescence of DOX and CPT and the greenish-blue fluorescence from DAPI bind to nucleus of cells, respectively. After treatments, cells cultured with 0.3  $\mu\text{M}$  DOX-AuNPs@FA-PABA-QP and 5.0  $\mu\text{M}$  CPT-AuNPs@FA-PABA-QP produced very strong red- and blue-fluorescence from DOX and CPT inside the cytoplasm and nucleus of cells. This result confirmed that DOX and CPT were effectively internalized, escaped, and highly released into the cells from DOX-AuNPs@FA-PABA-QP and CPT-AuNPs@FA-PABA-QP with pH-sensitive, which can rapidly diffuse into the cells, enter nucleus by passive diffusion and inhibit cancerous cells [95]. Moreover, fluoresces signals in cells incubated with DOX-AuNPs@FA-PABA-QP and CPT-AuNPs@FA-PABA-QP were much stronger than those incubated with DOX and CPT-alone. These result indicated that the specific uptake of DOX-AuNPs@FA-PABA-QP and CPT-AuNPs@FA-PABA-QP in targeted cells to nanocarriers, which improved the solubility of hydrophobic drug and conjugation of cancer-targeting FA via receptor mediated endocytosis and EPR effects as shown in Figure 62. Therefore, the enhanced cytotoxicity of Drug-AuNPs@FA-PABA-QP may also be due to the improved intracellular uptake and localization characteristics of a pH-sensitive AuNPs@FA-PABA-QP as universal nanocarriers.



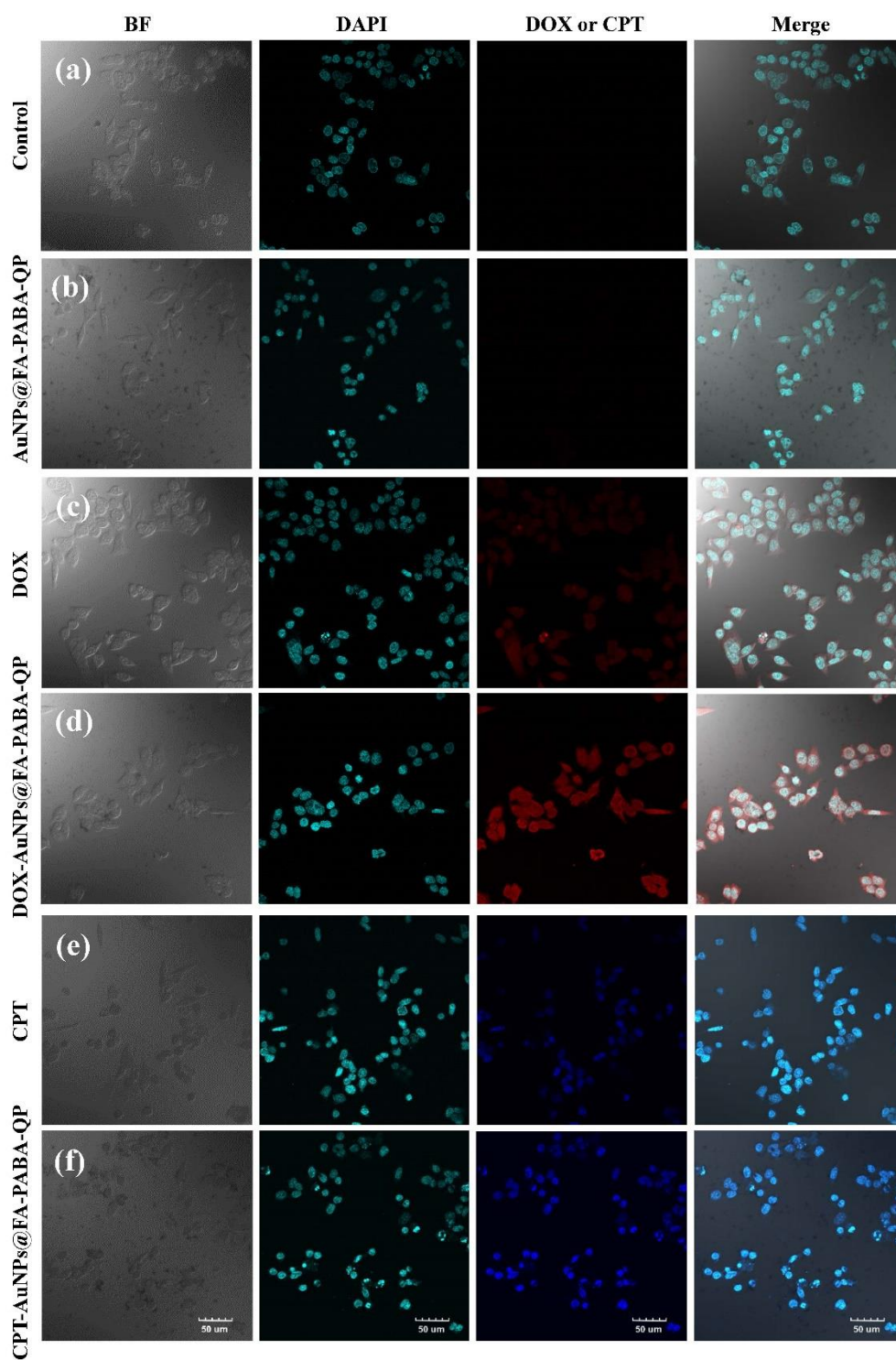


**Figure 67** Confocal laser scanning microscope images of (a) control and Chago-k1 cells incubated with (b) 40  $\mu\text{M}$  AuNPs@FA-PABA-QP, (c) DOX, (d) DOX-AuNPs@FA-PABA-QP, (e) CPT, (d) CPT-AuNPs@FA-PABA-QP at 37°C for 12 h.

#### 4.8.6 *In vitro* release profiles of Drug-AuNPs@FA-PABA-QP

The ability of AuNPs@FA-PABA-QP as universal bio-nanocarriers to deliver and release anticancer drugs at desired site into targeted cancer cells is important features for drug delivery. The *in vitro* release profiles of drugs (DOX or CPT) from Drug-AuNPs@FA-PABA-QP was studied in acetate (pH=5.0) and PBS buffer (pH=7.4), which represent the pH of vesicles in endosome or lysosomes and the pH of physiological blood and normal tissues in the human body, respectively [101]. The cumulative amounts of CPT and DOX from Drug-AuNPs@FA-PABA-QP formations at pH=5.0 were reached 30% and 51% at 6h, while the release at pH=7.4 was 9% and 22% at 6h, respectively. At the end of 72h, 66% and 30% release of CPT from CPT-AuNPs@FA-PABA-QP (Figure 68a), and 85% and 46% release of DOX from DOX-AuNPs@FA-PABA-QP (Figure 68b) were released in acetate and PBS buffer, respectively. These results showed that the release of both drugs from Drug-AuNPs@FA-PABA-QP in acidic pH was greater than in neutral pH, which more acidic environment is helpful of swelling of AuNPs@FA-PABA-QP and controlled release of drugs. The pH-dependent release of CPT-AuNPs@FA-PABA-QP and DOX-AuNPs@FA-PABA-QP can help improve anticancer efficacy of drugs under acidic environment lead to rapid release after uptake and internalization into cancer cells via folate-receptor-mediated endocytosis pathway [102]. Moreover, the half release of anticancer drugs in neutral pH will help to reduce toxicity of DOX and CPT to normal tissues which was consistent with MTT assay.

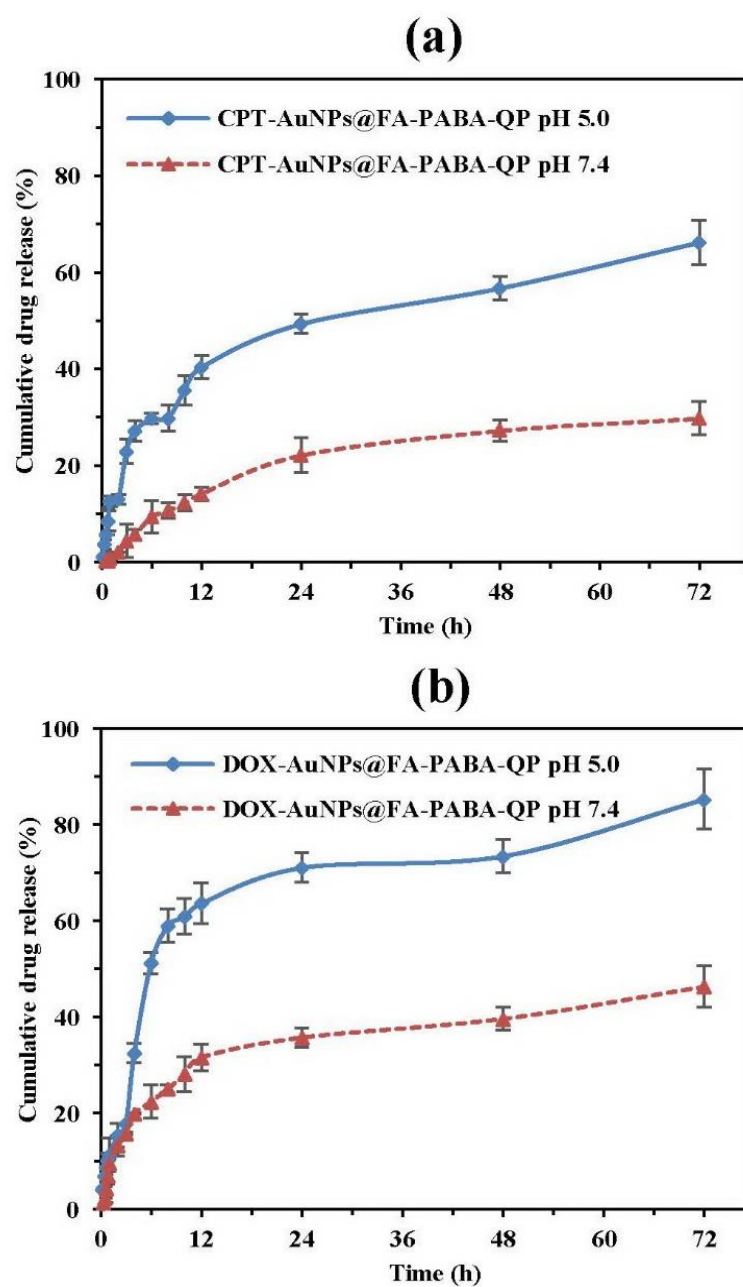


**Figure 68** Release profiles of (a) CPT-AuNPs@FA-PABA-QP and (b) DOX-AuNPs@FA-PABA-QP in PBS (pH 7.4) and acetate buffer (pH 5.0).

#### 4.8.7 Cell cycle assay of Drug-AuNPs@FA-PABA-QP

To investigate whether CPT-AuNPs@FA-PABA-QP and DOX-AuNPs@FA-PABA-QP for 24h affect regulation of cell cycle in Chago-k1 cells using flow cytometer. The observed differences of CPT-AuNPs@FA-PABA-QP and DOX-AuNPs@FA-PABA-QP treatments on cell proliferation suggested different mechanisms of action of these two drugs due to drugs inhibit cells by averting cell division at different checkpoints. After cells were treated with CPT-AuNPs@FA-PABA-QP, we found a significant number of cells that were dramatically arrested and increased the cell cycle and population at G0-G1 phases as compared to AuNPs@FA-PABA-QP and control groups (Figure 69a,c). The percent of cells in G0-G1 was 67.8% and 72.9% at 2.5 and 5.0 $\mu$ M CPT-AuNPs@FA-PABA-QP, respectively, while control group showed 57.7% accumulation of cells in G0-G1. Interestingly, CPT-AuNPs@FA-PABA-QP producing around 10-11% increase in G0-G1 population as comparing with 2.5 and 5.0  $\mu$ M CPT-alone. On the other hand, the cells in S and G2-M phases of 0.3 $\mu$ M DOX-AuNPs@FA-PABA-QP were increased to 36.1% and 34.7% cells (total S/G2-M=70.8%), respectively, and G0-G1 was decreased to 23.9% as compared with a control sample (Figure 69b,d). Similarly, cells were treated with reducing dose of 0.15  $\mu$ M DOX-AuNPs@FA-PABA-QP. Observably, DOX-AuNPs@FA-PABA-QP showed significantly at 26-31% increasing in S/G2-M populations compared with both DOX-alone concentrations. These data provide strong evidence for cell cycle arrest induced by CPT-AuNPs@FA-PABA-QP and DOX-AuNPs@FA-PABA-QP, which the unique mode of action for DOX and CPT was found to act via interacting DNA to inhibit DNA replications [103] and inhibition of topoisomerase I enzyme [104], respectively. Therefore, our study proves that CPT-AuNPs@FA-PABA-QP and DOX-AuNPs@FA-PABA-QP induce cell cycle arrest significantly at G0-G1 and S/G2-M phase in Chago-k1 cells, respectively.

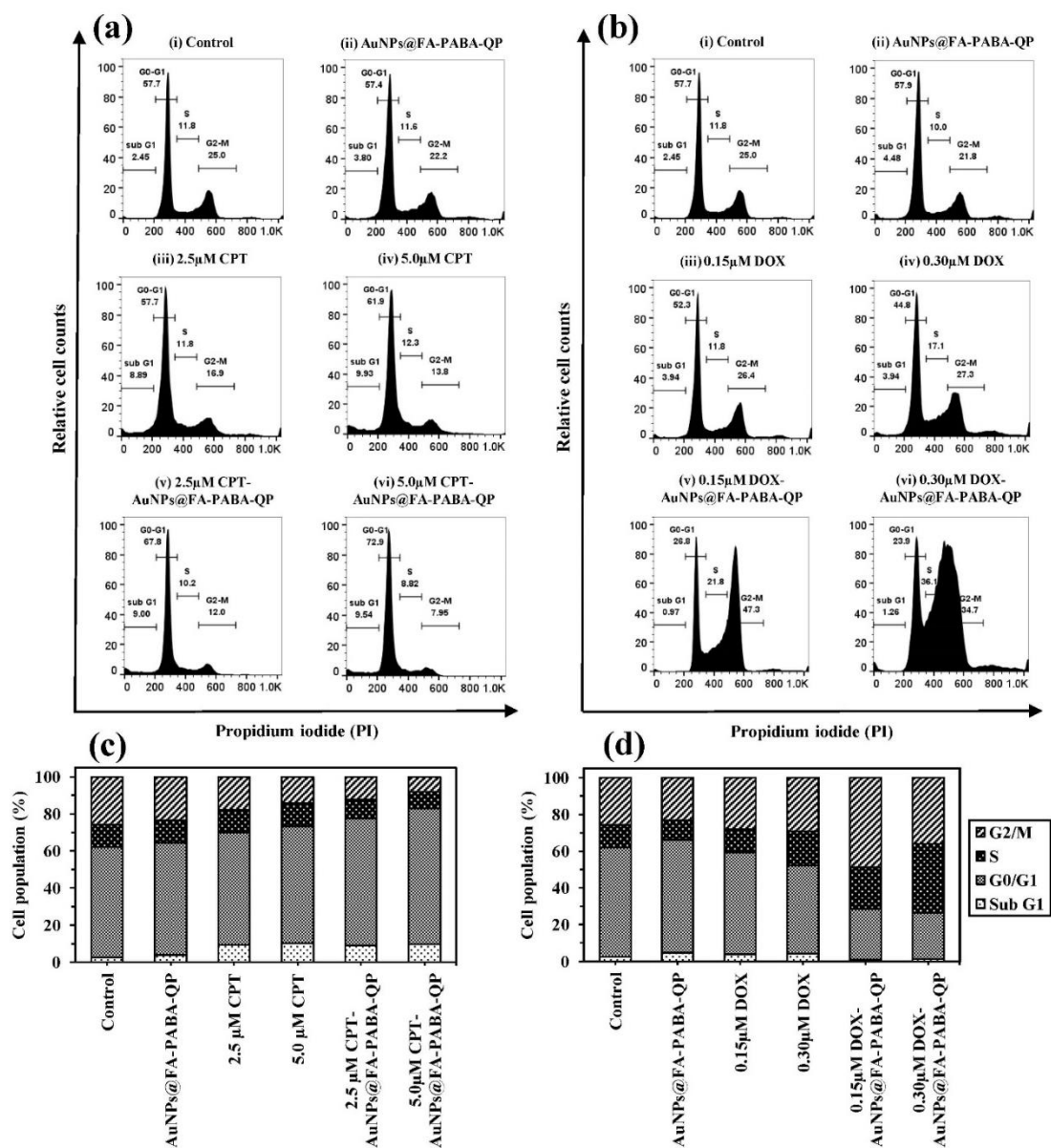


**Figure 69** (a-b) Cell cycle analysis and (c-d) cell populations of Chago-k1 cells after 24h treatment with (i) control, (ii) AuNPs@FA-PABA-QP, (iii-iv) CPT or DOX, and (v-vi) CPT-AuNPs@FA-PABA-QP or DOX-AuNPs@FA-PABA-QP as detected by PI.

#### 4.8.8 Apoptosis assay of Drug-AuNPs@FA-PABA-QP

To study whether the reduction in viable Chago-k1 cells treated with CPT-AuNPs@FA-PABA-QP and DOX-AuNPs@FA-PABA-QP for 12 h was caused by induction of apoptosis or necrosis, we detected cells after treatments using Annexin V-FITC/PI double staining. The stimulation of apoptosis has been considered as a standard and best strategy in anticancer therapy [105]. After treatment, Annexin-positively in Chago-k1 cells increased from 8.39% and 23.12% in CPT-alone treatment to 16.59% and 37.09% of early-apoptotic cells (Annexin V<sup>+</sup>/PI<sup>-</sup>), when cells were treated with 2.5 and 5.0 μM CPT-AuNPs@FA-PABA-QP, respectively (Figure 70a). Our results showed that both CPT-AuNPs@FA-PABA-QP exhibited higher levels of early-apoptosis (8.20-13.97% increase) compared to CPT-alone, while a control and 40 μM AuNPs@FA-PABA-QP demonstrated mainly 98.1% and 95.3% of viable cells. Moreover, to treat cells with DOX and DOX-AuNPs@FA-PABA-QP at 0.15 μM, 75.2% and 61.4% of viable cells were observed, respectively (Figure 70b). Moreover, the percent of apoptosis of cells was increased with increasing dosage of DOX-AuNPs@FA-PABA-QP. The late-apoptosis (Annexin V<sup>+</sup>/PI<sup>+</sup>) was 37% in cells treated with 0.3 μM DOX-AuNPs@FA-PABA-QP compared to 10.6% treated with DOX-alone, which increased significantly late-apoptosis to 26.4% (0.3 μM DOX-AuNPs@FA-PABA-QP) and also decreased necrosis compared to free-DOX. This suggested that CPT-AuNPs@FA-PABA-QP and DOX-AuNPs@FA-PABA-QP induced early and late-apoptotic cells, respectively, which showed cell death pathway better than both Drug-alone as consistent with previously report [97] and our cytotoxic study. Hence, these results approved that amphiphilic AuNPs@FA-PABA-QP as universal nanocarriers to deliver CPT and DOX showed better efficacy to induce, enhance apoptotic Chago-k1 cells, and reduce side effects than CPT and DOX-alone after treatment with new delivery systems of CPT-AuNPs@FA-PABA-QP and DOX-AuNPs@FA-PABA-QP.

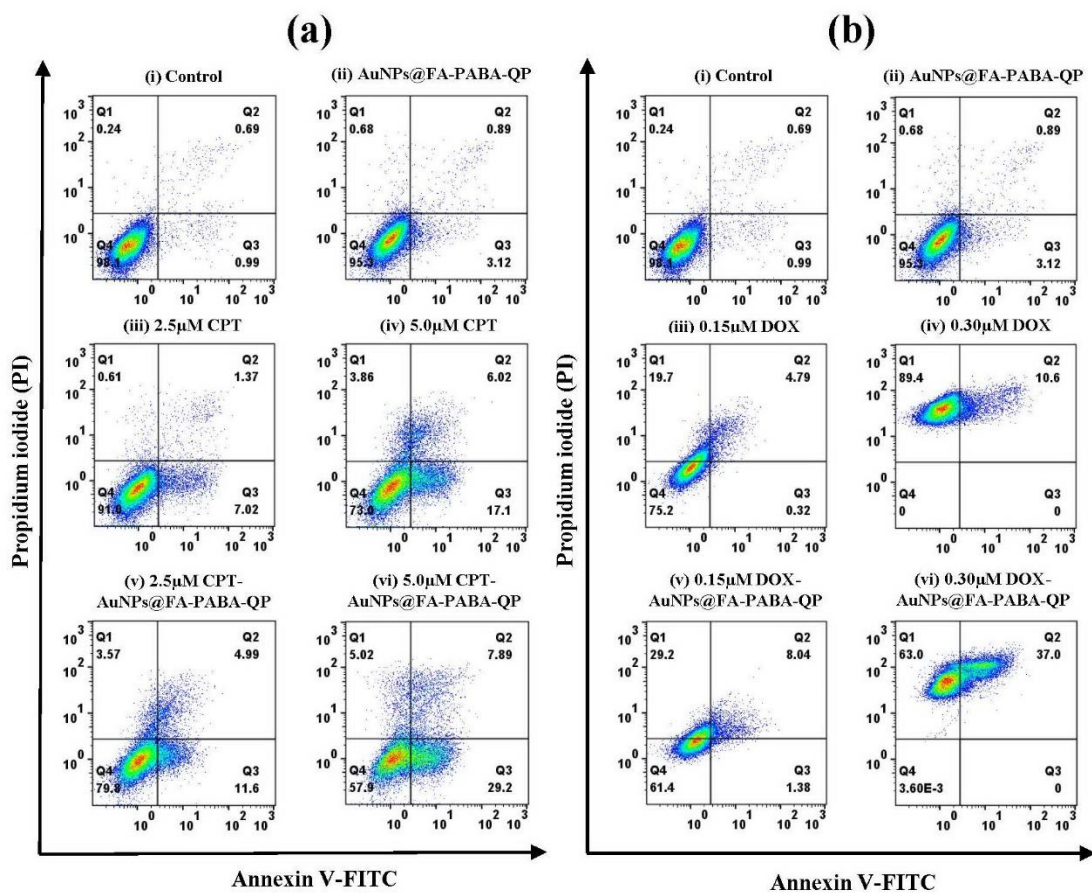


**Figure 70** (a-b) Flow cytometric analysis of Chago-k1 cells after 12h treatment with (i) control, (ii) AuNPs@FA-PABA-QP, (iii-iv) CPT or DOX, and (v-vi) CPT-AuNPs@FA-PABA-QP or DOX-AuNPs@FA-PABA-QP as detected by Annexin V-FITC/PI staining.

## CHAPTER V

### CONCLUSION

In summary, a nanoparticle-based drug carriers have been developed to improve performance of chemotherapeutic drugs. This study firstly report multifunctional gold nanoparticles reduced/stabilized/capped with folic acid-*para*-aminobenzoic acid-quat188-pullulan (FA-PABA-QP) as folate-amphiphilic nanocarriers for the active targeted delivery of camptothecin (CPT) or doxorubicin (DOX) to enhance anticancer efficacy of these systems. Spherical AuNPs@FA-PABA-QP as universal nanocarriers were synthesized under the optimal condition by facile and green reduction and characterized by UV-VIS, TEM, EDS, SAED, XRD, ATR-FTIR, XPS and zeta-potential analyses, and showed a narrow size distribution of  $12.6\pm 1.5$  nm. For drug delivery systems, DOX and CPT as a commercial anticancer drug were successfully loaded onto AuNPs@FA-PABA-QP via intermolecular interactions. In addition, Enhanced anticancer activities of CPT-AuNPs@FA-PABA-QP and DOX-AuNPs@FA-PABA-QP against Chago-k1 cells were found to decrease  $IC_{50}$  of DOX and CPT by approximately 4.8-time and 2.8-time, compared with Drug-alone, respectively, while exhibiting less cytotoxicity against normal cells. When compared between an active and a passive targeted nanocarrier, DOX-AuNPs@FA-PABA-QP as an active targeted nanocarriers ( $IC_{50}=0.17$   $\mu$ M) showed higher cytotoxicity against Chago-k1 cancer cells than DOX-AuNPs@PABA-QP as a passive targeted nanocarriers ( $IC_{50}=0.82$   $\mu$ M), which intracellular uptake of DOX-AuNPs@FA-PABA-QP showed better than DOX-AuNPs@PABA-QP through both folate receptor-mediated endocytosis and EPR effects. The pH-dependent cumulative release of both chemodrugs from Drug-AuNPs@FA-PABA-QP in acidic pH (pH 5.0) was greater than in neutral pH (pH 7.4) by approximately 2-time after internalization into cancer cells via folate receptor-mediated endocytosis, which more acidic environment



is helpful of swelling of AuNPs@FA-PABA-QP and controlled release of chemodrugs. Moreover, the new combinations of CPT-AuNPs@FA-PABA-QP and DOX-AuNPs@FA-PABA-QP induced better cell death by increasing total-apoptosis about 14% and 26%, respectively. Then, CPT-AuNPs@FA-PABA-QP and DOX-AuNPs@FA-PABA-QP also arrested increasing in G0-G1 and S/G2-M phases of the Chago-k1 cell cycle by approximately 11% and 31%, respectively, and exhibited excellent cytotoxicity when compared with drugs alone. Therefore, the novel combinations of Drug-AuNPs@FA-PABA-QP as new platforms have the potential to be developed for targeted lung cancer treatments.



## REFERENCES

- [1] Khutale, G.V. and Casey, A. Synthesis and characterization of a multifunctional gold-doxorubicin nanoparticle system for pH triggered intracellular anticancer drug release. European Journal of Pharmaceutics and Biopharmaceutics 119 (2017): 372-380.
- [2] Max, P.D., Freddie, B., J., F., and Paola, P. Global Cancer Statistics, 2002. CA: A Cancer Journal for Clinicians 55(2) (2005): 74-108.
- [3] A., T.L., Freddie, B., L., S.R., Jacques, F., Joannie, L.T., and Ahmedin, J. Global cancer statistics, 2012. CA: A Cancer Journal for Clinicians 65(2) (2015): 87-108.
- [4] Madhusudhan, A., et al. Efficient pH Dependent Drug Delivery to Target Cancer Cells by Gold Nanoparticles Capped with Carboxymethyl Chitosan. International Journal of Molecular Sciences 15(5) (2014): 8216.
- [5] Afzal, O., et al. A review on anticancer potential of bioactive heterocycle quinoline. European Journal of Medicinal Chemistry 97 (2015): 871-910.
- [6] Tajani, B., Tahvilian, R., Khazaei, S., Javadi, K., and Fattahi, A. Preparation and characterization of camptothecin grafted chitosan oligosaccharide nanomicelles. Journal of Reports in Pharmaceutical Sciences 4(1) (2015): 1-11.
- [7] Manivasagan, P., et al. Doxorubicin-loaded fucoidan capped gold nanoparticles for drug delivery and photoacoustic imaging. International Journal of Biological Macromolecules 91 (2016): 578-588.
- [8] Bonifácio, B.V., da Silva, P.B., Ramos, M.A.d.S., Negri, K.M.S., Bauab, T.M., and Chorilli, M. Nanotechnology-based drug delivery systems and herbal medicines: a review. International Journal of Nanomedicine 9 (2014): 1-15.
- [9] Gao, Y., et al. Nanotechnology-based intelligent drug design for cancer metastasis treatment. Biotechnology Advances 32(4) (2014): 761-777.

- [10] Rana, S., Bajaj, A., Mout, R., and Rotello, V.M. Monolayer coated gold nanoparticles for delivery applications. Advanced Drug Delivery Reviews 64(2) (2012): 200-216.
- [11] Mirza, A.Z. and Shamshad, H. Preparation and characterization of doxorubicin functionalized gold nanoparticles. European Journal of Medicinal Chemistry 46(5) (2011): 1857-60.
- [12] Ahmed, K.B.A., Kalla, D., Uppuluri, K.B., and Anbazhagan, V. Green synthesis of silver and gold nanoparticles employing levan, a biopolymer from *Acetobacter xylinum* NCIM 2526, as a reducing agent and capping agent. Carbohydrate Polymers 112 (2014): 539-545.
- [13] Kumar, C.S., Raja, M.D., Sundar, D.S., Gover Antoniraj, M., and Ruckmani, K. Hyaluronic acid co-functionalized gold nanoparticle complex for the targeted delivery of metformin in the treatment of liver cancer (HepG2 cells). Carbohydrate Polymers 128 (2015): 63-74.
- [14] Laksee, S., Puthong, S., Teerawatananond, T., Palaga, T., and Muangsin, N. Highly efficient and facile fabrication of monodispersed Au nanoparticles using pullulan and their application as anticancer drug carriers. Carbohydrate Polymers 173 (2017): 178-191.
- [15] Singh, R.S., Kaur, N., Rana, V., and Kennedy, J.F. Pullulan: A novel molecule for biomedical applications. Carbohydrate Polymers 171 (2017): 102-121.
- [16] Muddineti, O.S., Ghosh, B., and Biswas, S. Current trends in using polymer coated gold nanoparticles for cancer therapy. International Journal of Pharmaceutics 484(1) (2015): 252-267.
- [17] Torre, L.A., Bray, F., Siegel, R.L., Ferlay, J., Lortet-Tieulent, J., and Jemal, A. Global cancer statistics, 2012. CA: A Cancer Journal for Clinicians 65(2) (2015): 87-108.

- [18] Siegel, R.L., Miller, K.D., and Jemal, A. Cancer statistics, 2016. CA: A Cancer Journal for Clinicians 66(1) (2016): 7-30.
- [19] Ferlay, J., et al. Cancer incidence and mortality patterns in Europe: Estimates for 40 countries in 2012. European Journal of Cancer 49(6) (2013): 1374-1403.
- [20] DeSantis, C.E., et al. Cancer treatment and survivorship statistics, 2014. CA: A Cancer Journal for Clinicians 64(4) (2014): 252-271.
- [21] Jaividhya, P., Dhivya, R., Akbarsha, M.A., and Palaniandavar, M. Efficient DNA cleavage mediated by mononuclear mixed ligand copper(II) phenolate complexes: The role of co-ligand planarity on DNA binding and cleavage and anticancer activity. Journal of Inorganic Biochemistry 114 (2012): 94-105.
- [22] Yang, F., Teves, S.S., Kemp, C.J., and Henikoff, S. Doxorubicin, DNA torsion, and chromatin dynamics. Biochimica et Biophysica Acta (BBA) - Reviews on Cancer 1845(1) (2014): 84-89.
- [23] Karimi, M., Zangabad, P.S., Ghasemi, A., and Hamblin, M.R. Introduction. in Smart Internal Stimulus-Responsive Nanocarriers for Drug and Gene Delivery, pp. 1-1-1-6: Morgan & Claypool Publishers, 2015.
- [24] Arora, D. and Jaglan, S. Nanocarriers based delivery of nutraceuticals for cancer prevention and treatment: A review of recent research developments. Trends in Food Science & Technology 54 (2016): 114-126.
- [25] Connot, J., et al. Cancer immunotherapy: nanodelivery approaches for immune cell targeting and tracking. Frontiers in Chemistry 2(105) (2014).
- [26] Jia, X., Xu, X., and Zhang, L. Synthesis and stabilization of gold nanoparticles induced by denaturation and renaturation of triple helical beta-glucan in water. Biomacromolecules 14(6) (2013): 1787-94.
- [27] Khan, M.S., Vishakante, G.D., and Siddaramaiah, H. Gold nanoparticles: a paradigm shift in biomedical applications. Advances in Colloid and Interface Science 199-200 (2013): 44-58.

- [28] Moubasher, H. and Wahsh, S. Pullulan production from *Aureobasidium pullulans* by continuous culture. Basic Research Journal of Microbiology 1 (2014): 11-15.
- [29] Singh, R.S., Saini, G.K., and Kennedy, J.F. Pullulan: Microbial sources, production and applications. Carbohydrate Polymers 73(4) (2008): 515-31.
- [30] Leathers, T.D. Biotechnological production and applications of pullulan. Applied Microbiology and Biotechnology 62(5-6) (2003): 468-73.
- [31] Kanmani, P. and Lim, S.T. Synthesis and characterization of pullulan-mediated silver nanoparticles and its antimicrobial activities. Carbohydr Polym 97(2) (2013): 421-8.
- [32] Vigderman, L. and Zubarev, E.R. Therapeutic platforms based on gold nanoparticles and their covalent conjugates with drug molecules. Advanced Drug Delivery Reviews 65(5) (2013): 663-676.
- [33] Wang, F., Wang, Y.-C., Dou, S., Xiong, M.-H., Sun, T.-M., and Wang, J. Doxorubicin-Tethered Responsive Gold Nanoparticles Facilitate Intracellular Drug Delivery for Overcoming Multidrug Resistance in Cancer Cells. ACS Nano 5(5) (2011): 3679-3692.
- [34] Brown, S.D., et al. Gold Nanoparticles for the Improved Anticancer Drug Delivery of the Active Component of Oxaliplatin. Journal of the American Chemical Society 132(13) (2010): 4678-4684.
- [35] Leonid Vigderman, E.R.Z. Therapeutic platforms based on gold nanoparticles and their covalent conjugates with drug molecules. Advanced Drug Delivery Reviews 66 (2013): 663-676.
- [36] Dreaden, E.C., Mwakwari, S.C., Sodji, Q.H., Oyelere, A.K., and El-Sayed, M.A. Tamoxifen-Poly(ethylene glycol)-Thiol Gold Nanoparticle Conjugates: Enhanced Potency and Selective Delivery for Breast Cancer Treatment. Bioconjugate Chemistry 20(12) (2009): 2247-2253.

- [37] Gu, Y.-J., Cheng, J., Man, C.W.-Y., Wong, W.-T., and Cheng, S.H. Gold-doxorubicin nanoconjugates for overcoming multidrug resistance. Nanomedicine: Nanotechnology, Biology and Medicine 8(2) (2012): 204-211.
- [38] Ghosh, P., Han, G., De, M., Kim, C.K., and Rotello, V.M. Gold nanoparticles in delivery applications. Advanced Drug Delivery Reviews 60(11) (2008): 1307-1315.
- [39] Adnan, N.N.M., et al. Effect of gold nanoparticle shapes for phototherapy and drug delivery. Polymer Chemistry 7(16) (2016): 2888-2903.
- [40] Freese, C., Gibson, M.I., Klok, H.-A., Unger, R.E., and Kirkpatrick, C.J. Size- and Coating-Dependent Uptake of Polymer-Coated Gold Nanoparticles in Primary Human Dermal Microvascular Endothelial Cells. Biomacromolecules 13(5) (2012): 1533-1543.
- [41] Yao, M., He, L., McClements, D.J., and Xiao, H. Uptake of Gold Nanoparticles by Intestinal Epithelial Cells: Impact of Particle Size on Their Absorption, Accumulation, and Toxicity. Journal of Agricultural and Food Chemistry 63(36) (2015): 8044-8049.
- [42] Singh, R.S., Kaur, N., and Kennedy, J.F. Pullulan and pullulan derivatives as promising biomolecules for drug and gene targeting. Carbohydrate Polymers 123 (2015): 190-207.
- [43] Noh, S.M., Kim, W.-K., Kim, S.J., Kim, J.M., Baek, K.-H., and Oh, Y.-K. Enhanced cellular delivery and transfection efficiency of plasmid DNA using positively charged biocompatible colloidal gold nanoparticles. Biochimica et Biophysica Acta (BBA) - General Subjects 1770(5) (2007): 747-752.
- [44] Fröhlich, E. The role of surface charge in cellular uptake and cytotoxicity of medical nanoparticles. International Journal of Nanomedicine 7 (2012): 5577-5591.
- [45] Komenek, S., et al. Nanogold-Gallate Chitosan-Targeted Pulmonary Delivery for Treatment of Lung Cancer. AAPS PharmSciTech (2016): 1-12.

- [46] Asadishad, B., Vossoughi, M., and Alemzadeh, I. Folate-Receptor-Targeted Delivery of Doxorubicin Using Polyethylene Glycol-Functionalized Gold Nanoparticles. Industrial & Engineering Chemistry Research 49(4) (2010): 1958-1963.
- [47] Ganeshkumar, M., Ponrasu, T., Raja, M.D., Subamekala, M.K., and Suguna, L. Green synthesis of pullulan stabilized gold nanoparticles for cancer targeted drug delivery. Spectrochimica Acta Part A: Molecular and Biomolecular Spectroscopy 130 (2014): 64-71.
- [48] Kelly, K.L., Coronado, E., Zhao, L.L., Schatz, G.C. The Optical Properties of Metal Nanoparticles: The Influence of Size, Shape, and Dielectric Environment. J. Phys. Chem. B 107 (2003): 668-677.
- [49] Ghosh, S.K., Pal, T. Interparticle Coupling Effect on the Surface Plasmon Resonance of Gold Nanoparticles: From Theory to Applications. Chem. Rev. 107(11) (2007): 4797-4862.
- [50] Mosmann, T. Rapid colorimetric assay for cellular growth and survival: Application to proliferation and cytotoxicity assays. J. Immunol. Methods 65(1-2) (1983): 55-63.
- [51] Kerr, J.F., Wyllie, A.H., and Currie, A.R. Apoptosis: a basic biological phenomenon with wide-ranging implications in tissue kinetics. Br J Cancer 26(4) (1972): 239-57.
- [52] Fink, S.L. and Cookson, B.T. Apoptosis, Pyroptosis, and Necrosis: Mechanistic Description of Dead and Dying Eukaryotic Cells. Infection and Immunity 73(4) (2005): 1907-1916.
- [53] van Engeland, M., Ramaekers, F.C., Schutte, B., and Reutelingsperger, C.P. A novel assay to measure loss of plasma membrane asymmetry during apoptosis of adherent cells in culture. Cytometry 24(2) (1996): 131-9.

- [54] Vermes, I., Haanen, C., Steffens-Nakken, H., and Reutelingsperger, C. A novel assay for apoptosis. Flow cytometric detection of phosphatidylserine expression on early apoptotic cells using fluorescein labelled Annexin V. J Immunol Methods 184(1) (1995): 39-51.
- [55] Casciola-Rosen, L., Rosen, A., Petri, M., and Schlissel, M. Surface blebs on apoptotic cells are sites of enhanced procoagulant activity: implications for coagulation events and antigenic spread in systemic lupus erythematosus. Proceedings of the National Academy of Sciences of the United States of America 93(4) (1996): 1624-1629.
- [56] Vermes, I., Haanen, C., Steffens-Nakken, H., and Reutellingsperger, C. A novel assay for apoptosis Flow cytometric detection of phosphatidylserine expression on early apoptotic cells using fluorescein labelled Annexin V. Journal of Immunological Methods 184(1) (1995): 39-51.
- [57] Edinger, A.L. and Thompson, C.B. Death by design: apoptosis, necrosis and autophagy. Current Opinion in Cell Biology 16(6) (2004): 663-669.
- [58] Blagosklonny, M.V. and Pardee, A.B. The Restriction Point of the Cell Cycle. Cell Cycle 1(2) (2002): 102-109.
- [59] Bae, B.-c. and Na, K. Self-quenching polysaccharide-based nanogels of pullulan/folate-photosensitizer conjugates for photodynamic therapy. Biomaterials 31(24) (2010): 6325-6335.
- [60] Nonsuwan, P., Puthong, S., Palaga, T., and Muangsin, N. Novel organic/inorganic hybrid flower-like structure of selenium nanoparticles stabilized by pullulan derivatives. Carbohydrate Polymers 184 (2018): 9-19.
- [61] Varshosaz, J., Hassanzadeh, F., Sadeghi Aliabadi, H., Nayeb Sadrian, M., Banitalebi, M., and Rostami, M. Synthesis and Characterization of Folate-Targeted Dextran/Retinoic Acid Micelles for Doxorubicin Delivery in Acute Leukemia. BioMed Research International 2014 (2014): 14.



- [62] Du, Y.Q., Yang, X.X., Li, W.L., Wang, J., and Huang, C.Z. A cancer-targeted drug delivery system developed with gold nanoparticle mediated DNA-doxorubicin conjugates. RSC Advances 4(66) (2014): 34830-34835.
- [63] Sangthong, S., et al. Anthracene-9, 10-dione derivatives induced apoptosis in human cervical cancer cell line (CaSki) by interfering with HPV E6 expression. European Journal of Medicinal Chemistry 77 (2014): 334-342.
- [64] Wang, X., Wang, J., Bao, Y., Wang, B., Wang, X., and Chen, L. Novel reduction-sensitive pullulan-based micelles with good hemocompatibility for efficient intracellular doxorubicin delivery. RSC Advances 4(104) (2014): 60064-60074.
- [65] Luesakul, U., Puthong, S., Neamati, N., and Muangsin, N. pH-responsive selenium nanoparticles stabilized by folate-chitosan delivering doxorubicin for overcoming drug-resistant cancer cells. Carbohydrate Polymers 181 (2018): 841-850.
- [66] Yu, B., Li, X., Zheng, W., Feng, Y., Wong, Y.-S., and Chen, T. pH-responsive cancer-targeted selenium nanoparticles: a transformable drug carrier with enhanced theranostic effects. Journal of Materials Chemistry B 2(33) (2014): 5409-5418.
- [67] Benke, B.P. and Madhavan, N. Aminobenzoic acid incorporated octapeptides for cation transport. Bioorganic & Medicinal Chemistry 23(7) (2015): 1413-1420.
- [68] Fiege, K., Lünsdorf, H., Atarjazarzadeh, S., and Mischnick, P. Cyanoethylation of the glucans dextran and pullulan: Substitution pattern and formation of nanostructures and entrapment of magnetic nanoparticles. Beilstein Journal of Organic Chemistry 8 (2012): 551-566.
- [69] Nichifor, M., Stanciu, M.C., and Simionescu, B.C. New cationic hydrophilic and amphiphilic polysaccharides synthesized by one pot procedure. Carbohydrate Polymers 82(3) (2010): 965-975.
- [70] Saber-Samandari, S. and Gazi, M. Pullulan based porous semi-IPN hydrogel: Synthesis, characterization and its application in the removal of mercury from

- aqueous solution. Journal of the Taiwan Institute of Chemical Engineers 51 (2015): 143-151.
- [71] Trovatti, E., Fernandes, S.C.M., Rubatat, L., Freire, C.S.R., Silvestre, A.J.D., and Neto, C.P. Sustainable nanocomposite films based on bacterial cellulose and pullulan. Cellulose 19(3) (2012): 729-737.
- [72] Sun, L., Li, J., Cai, J., Zhong, L., Ren, G., and Ma, Q. One pot synthesis of gold nanoparticles using chitosan with varying degree of deacetylation and molecular weight. Carbohydrate Polymers 178 (2017): 105-114.
- [73] Noruzi, M., Zare, D., Khoshnevisan, K., and Davoodi, D. Rapid green synthesis of gold nanoparticles using Rosa hybrida petal extract at room temperature. Spectrochimica Acta Part A: Molecular and Biomolecular Spectroscopy 79(5) (2011): 1461-5.
- [74] Pienpinijtham, P., Thammacharoen, C., and Ekgasit, S. Green synthesis of size controllable and uniform gold nanospheres using alkaline degradation intermediates of soluble starch as reducing agent and stabilizer. Macromolecular Research 20(12) (2012): 1281-1288.
- [75] Ghosh, S.K. and Pal, T. Interparticle Coupling Effect on the Surface Plasmon Resonance of Gold Nanoparticles: From Theory to Applications. Chemical Reviews 107(11) (2007): 4797-4862.
- [76] Choudhury, A.R., Malhotra, A., Bhattacharjee, P., and Prasad, G.S. Facile and rapid thermo-regulated biomineralization of gold by pullulan and study of its thermodynamic parameters. Carbohydrate Polymers 106 (2014): 154-159.
- [77] Jin, Y., Li, Z., Hu, L., Shi, X., Guan, W., and Du, Y. Synthesis of chitosan-stabilized gold nanoparticles by atmospheric plasma. Carbohydrate Polymers 91(1) (2013): 152-156.

- [78] Uthaman, S., et al. Green synthesis of bioactive polysaccharide-capped gold nanoparticles for lymph node CT imaging. Carbohydrate Polymers 181 (2018): 27-33.
- [79] Yan, J.-K., Liu, J.-L., Sun, Y.-J., Tang, S., Mo, Z.-Y., and Liu, Y.-S. Green synthesis of biocompatible carboxylic curdlan-capped gold nanoparticles and its interaction with protein. Carbohydrate Polymers 117 (2015): 771-777.
- [80] Yen, H.-j., et al. Positively charged gold nanoparticles capped with folate quaternary chitosan: Synthesis, cytotoxicity, and uptake by cancer cells. Carbohydrate Polymers 183 (2018): 140-150.
- [81] Barman, S.R., Nain, A., Jain, S., Punjabi, N., Mukherji, S., and Satija, J. Dendrimer as a multifunctional capping agent for metal nanoparticles for use in bioimaging, drug delivery and sensor applications. Journal of Materials Chemistry B 6(16) (2018): 2368-2384.
- [82] Reddy, K.R., Sin, B.C., Ryu, K.S., Kim, J.-C., Chung, H., and Lee, Y. Conducting polymer functionalized multi-walled carbon nanotubes with noble metal nanoparticles: Synthesis, morphological characteristics and electrical properties. Synthetic Metals 159(7-8) (2009): 595-603.
- [83] Pyell, U., Jalil, A.H., Pfeiffer, C., Pelaz, B., and Parak, W.J. Characterization of gold nanoparticles with different hydrophilic coatings via capillary electrophoresis and Taylor dispersion analysis. Part I: Determination of the zeta potential employing a modified analytic approximation. Journal of Colloid and Interface Science 450 (2015): 288-300.
- [84] Pyell, U., Jalil, A.H., Urban, D.A., Pfeiffer, C., Pelaz, B., and Parak, W.J. Characterization of hydrophilic coated gold nanoparticles via capillary electrophoresis and Taylor dispersion analysis. Part II: Determination of the hydrodynamic radius distribution – Comparison with asymmetric flow field-flow fractionation. Journal of Colloid and Interface Science 457 (2015): 131-140.

- [85] Dananjaya, S.H.S., Udayangani, R.M.C., Oh, C., Nikapitiya, C., Lee, J., and De Zoysa, M. Green synthesis, physio-chemical characterization and anti-candidal function of a biocompatible chitosan gold nanocomposite as a promising antifungal therapeutic agent. RSC Advances 7(15) (2017): 9182-9193.
- [86] Dichello, G.A., et al. Preparation of liposomes containing small gold nanoparticles using electrostatic interactions. European Journal of Pharmaceutical Sciences 105 (2017): 55-63.
- [87] Movahed, S.K., Fakharian, M., Dabiri, M., and Bazgir, A. Gold nanoparticle decorated reduced graphene oxide sheets with high catalytic activity for Ullmann homocoupling. RSC Advances 4(10) (2014): 5243-5247.
- [88] Luo, Y., Shen, Z., Liu, P., Zhao, L., and Wang, X. Facile fabrication and selective detection for cysteine of xylan/Au nanoparticles composite. Carbohydrate Polymers 140 (2016): 122-128.
- [89] Ganeshkumar, M., Sathishkumar, M., Ponrasu, T., Dinesh, M.G., and Suguna, L. Spontaneous ultra fast synthesis of gold nanoparticles using Punica granatum for cancer targeted drug delivery. Colloids and Surfaces B: Biointerfaces 106 (2013): 208-216.
- [90] Bhattacharjee, J., Verma, G., Aswal, V.K., and Hassan, P.A. Small angle neutron scattering study of doxorubicin-surfactant complexes encapsulated in block copolymer micelles. Pramana 71(5) (2008): 991-995.
- [91] Zhu, T., Fu, X., Mu, T., Wang, J., and Liu, Z. pH-Dependent Adsorption of Gold Nanoparticles on p-Aminothiophenol-Modified Gold Substrates. Langmuir 15(16) (1999): 5197-5199.
- [92] Hsiao, P.F., Peng, S., Tang, T.-C., Lin, S.-Y., and Tsai, H.-C. Enhancing the in vivo transdermal delivery of gold nanoparticles using poly(ethylene glycol) and its oleylamine conjugate. International Journal of Nanomedicine 11 (2016): 1867-1878.

- [93] Mohanty, R.K., Thennarasu, S., and Mandal, A.B. Resveratrol stabilized gold nanoparticles enable surface loading of doxorubicin and anticancer activity. Colloids and Surfaces B: Biointerfaces 114 (2014): 138-143.
- [94] Asprion, N., Hasse, H., and Maurer, G. FT-IR spectroscopic investigations of hydrogen bonding in alcohol–hydrocarbon solutions. Fluid Phase Equilibria 186(1) (2001): 1-25.
- [95] Wang, Y., et al. pH-sensitive pullulan-based nanoparticles for intracellular drug delivery. Polymer Chemistry 5(2) (2014): 423-432.
- [96] Aranha, O., Wood, D.P., and Sarkar, F.H. Ciprofloxacin Mediated Cell Growth Inhibition, S/G<sup>2</sup>-M Cell Cycle Arrest, and Apoptosis in a Human Transitional Cell Carcinoma of the Bladder Cell Line. Clinical Cancer Research 6(3) (2000): 891-900.
- [97] Pan, Y., et al. Gold Nanoparticles of Diameter 1.4 nm Trigger Necrosis by Oxidative Stress and Mitochondrial Damage. Small 5(18) (2009): 2067-2076.
- [98] Lankoff, A., et al. The effect of agglomeration state of silver and titanium dioxide nanoparticles on cellular response of HepG2, A549 and THP-1 cells. Toxicology Letters 208(3) (2012): 197-213.
- [99] Wójcik, M., et al. Enhancing Anti-Tumor Efficacy of Doxorubicin by Non-Covalent Conjugation to Gold Nanoparticles – In Vitro Studies on Feline Fibrosarcoma Cell Lines. PLOS ONE 10(4) (2015): e0124955.
- [100] Zhao, L., Kim, T.-H., Kim, H.-W., Ahn, J.-C., and Kim, S.Y. Enhanced cellular uptake and phototoxicity of Verteporfin-conjugated gold nanoparticles as theranostic nanocarriers for targeted photodynamic therapy and imaging of cancers. Materials Science and Engineering: C 67 (2016): 611-622.
- [101] Kim, E.Y., Kumar, D., Khang, G., and Lim, D.-K. Recent advances in gold nanoparticle-based bioengineering applications. Journal of Materials Chemistry B 3(43) (2015): 8433-8444.

- [102] Banu, H., et al. Doxorubicin loaded polymeric gold nanoparticles targeted to human folate receptor upon laser photothermal therapy potentiates chemotherapy in breast cancer cell lines. Journal of Photochemistry and Photobiology B: Biology 149 (2015): 116-128.
- [103] Oktay, T., Pornsak, S., and R., D.C. Doxorubicin: an update on anticancer molecular action, toxicity and novel drug delivery systems. Journal of Pharmacy and Pharmacology 65(2) (2013): 157-170.
- [104] F., L.L., D., D.S., TSAI-KUN, L., YONG, M., MEI, S., and SAI-PENG, S. Mechanism of Action of Camptothecin. Annals of the New York Academy of Sciences 922(1) (2000): 1-10.
- [105] Ramalingam, V., Varunkumar, K., Ravikumar, V., and Rajaram, R. Target delivery of doxorubicin tethered with PVP stabilized gold nanoparticles for effective treatment of lung cancer. Scientific Reports 8(1) (2018): 3815.



APPENDICES

จุฬาลงกรณ์มหาวิทยาลัย  
**CHULALONGKORN UNIVERSITY**





Part I: Design, synthesis and characterization of pullulan and its derivatives as a trifunctional reducing, stabilizing and capping agent for synthesis of gold nanoparticles (AuNPs).

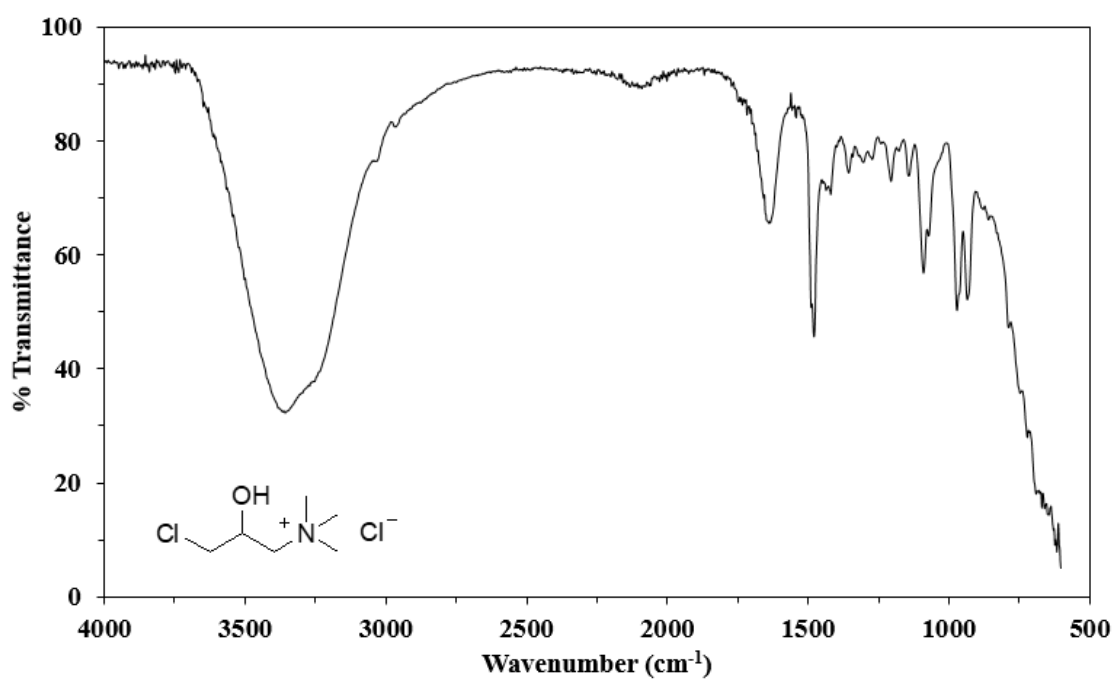


Figure A1 ATR-FTIR spectrum of Quat188.

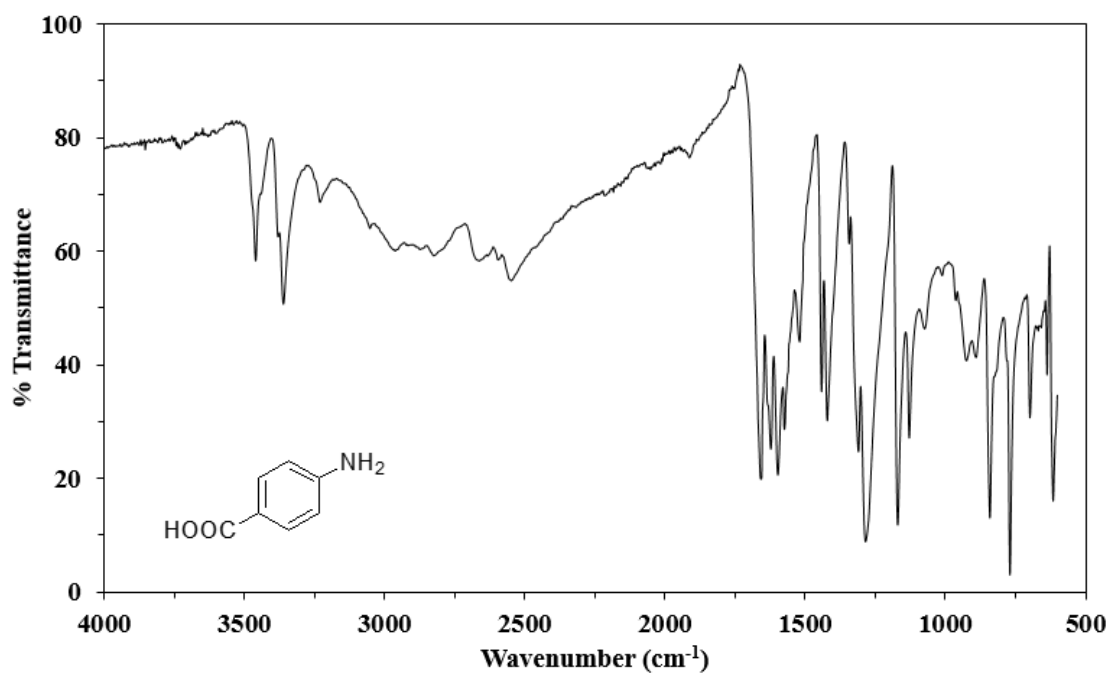


Figure A2 ATR-FTIR spectrum of PABA.

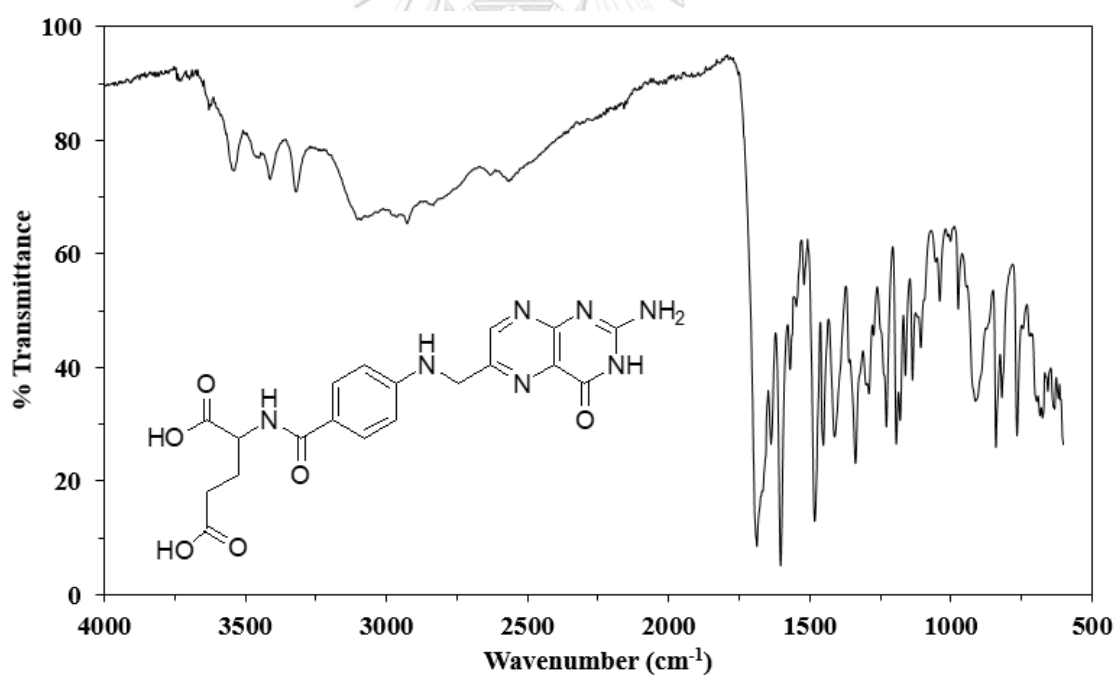


Figure A3 ATR-FTIR spectrum of FA.

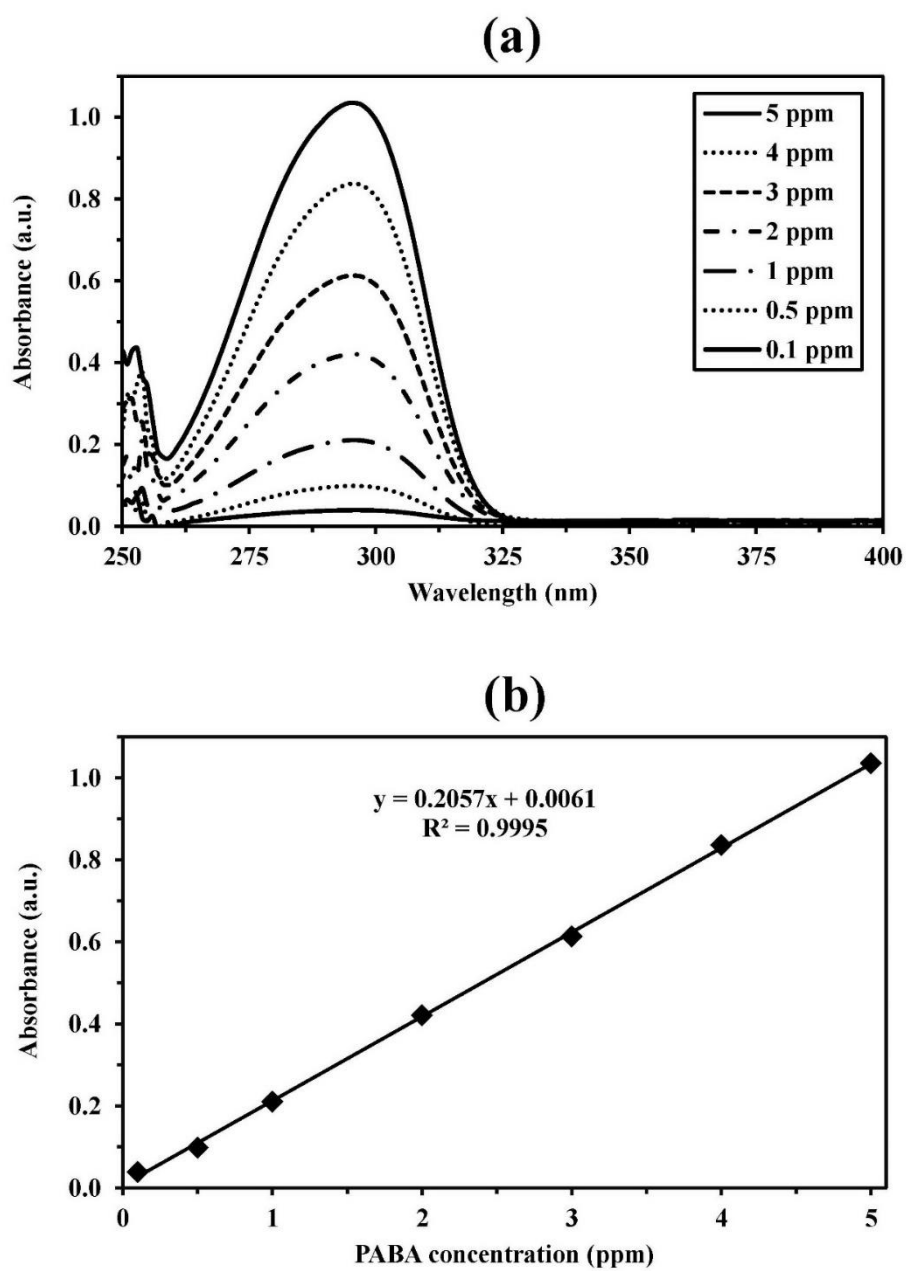


Figure A4 (a) The UV-vis spectra and (b) the calibration curve of PABA in the range of 0.1-5.0 ppm.

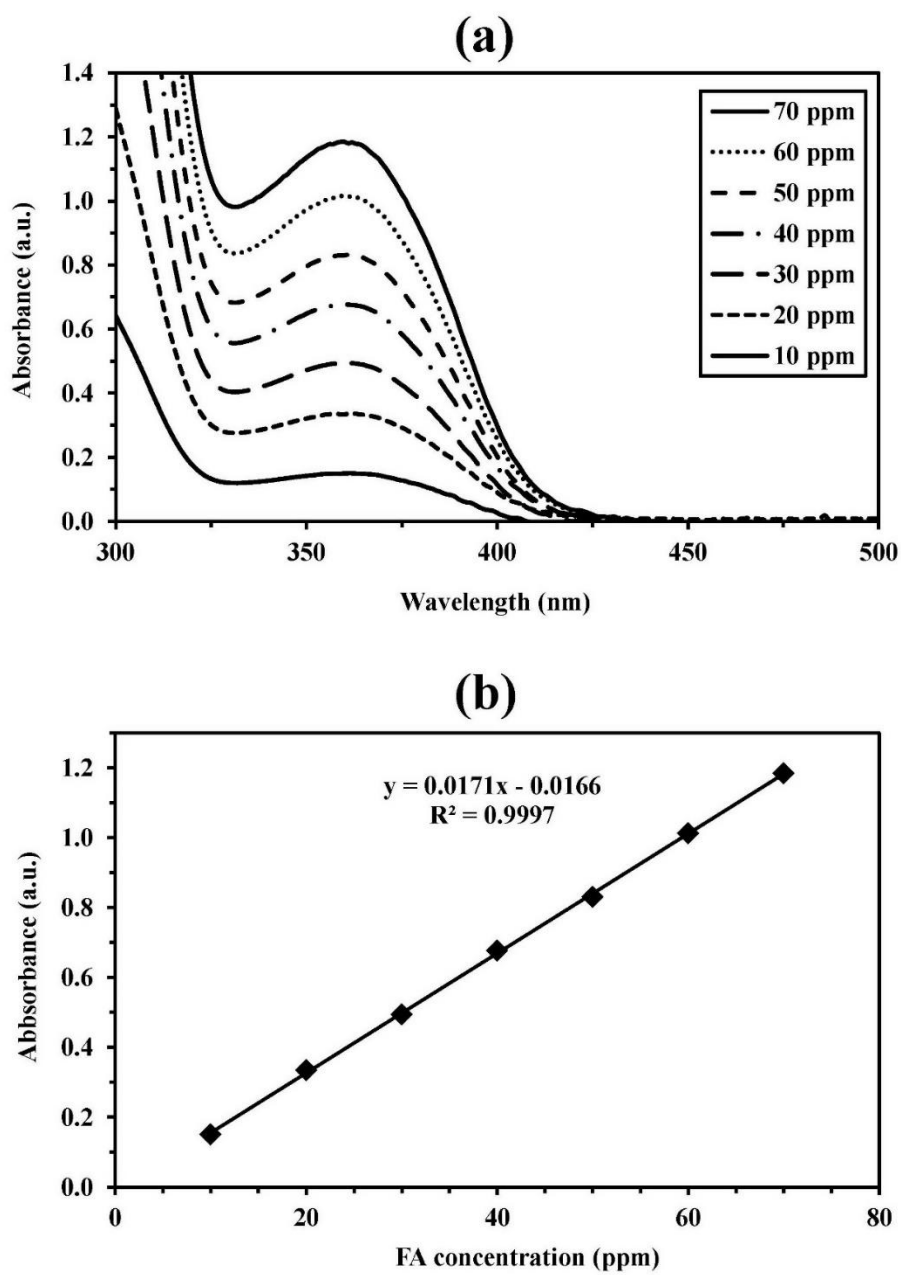
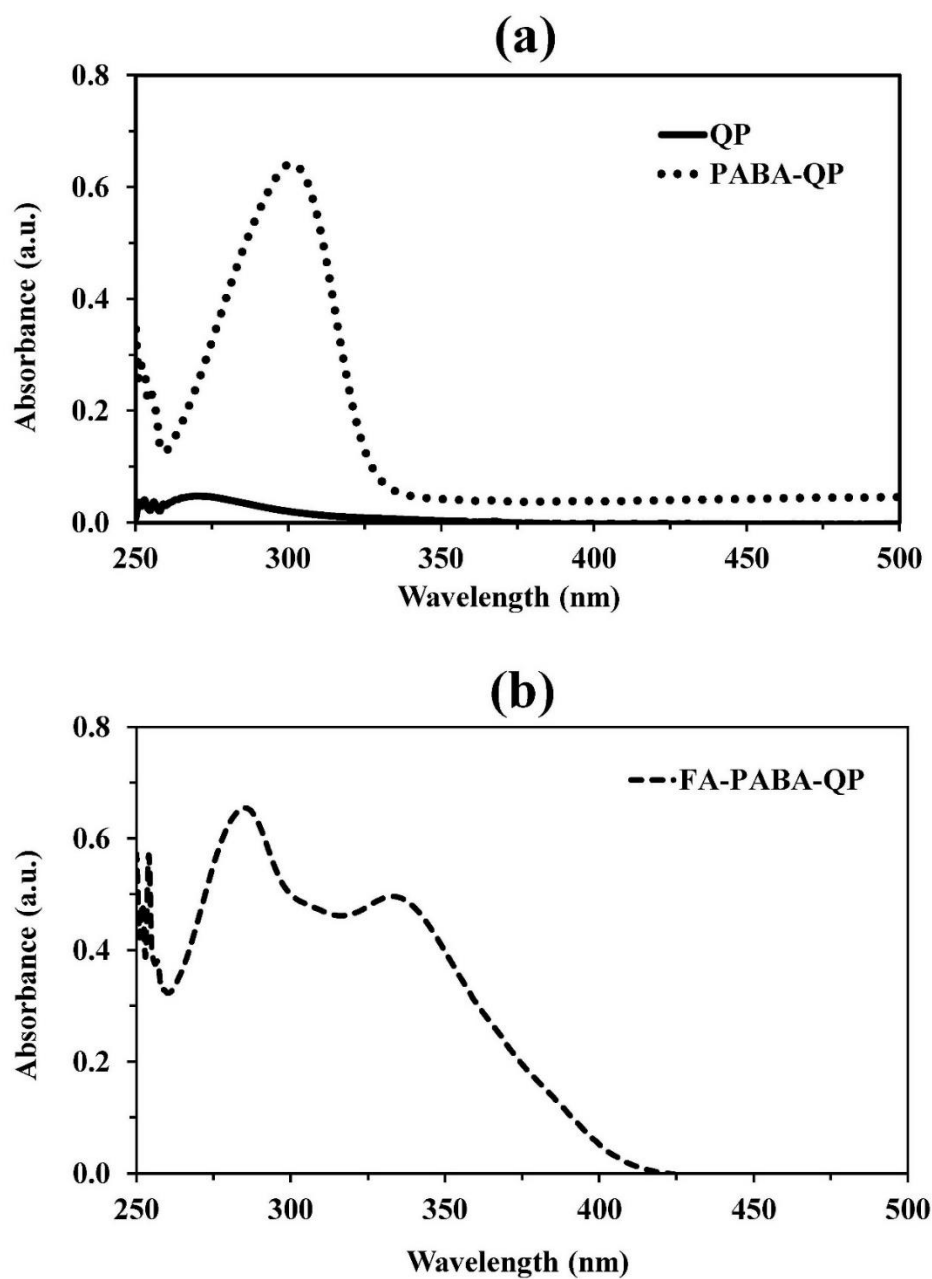


Figure A5 (a) The UV-vis spectra and (b) the calibration curve of FA in the range of 10-70 ppm.



**Figure A6** UV-vis spectra of (a) QP and PABA-QP (a dilution of 36-fold), and (c) FA-PABA-QP (a dilution of 40-fold).

Part II: Synthesis and characterization of pullulan derivatives reduced/stabilized/capped gold nanoparticles (AuNPs@pullulan derivatives) as targeted nanocarriers for anticancer drug delivery systems.

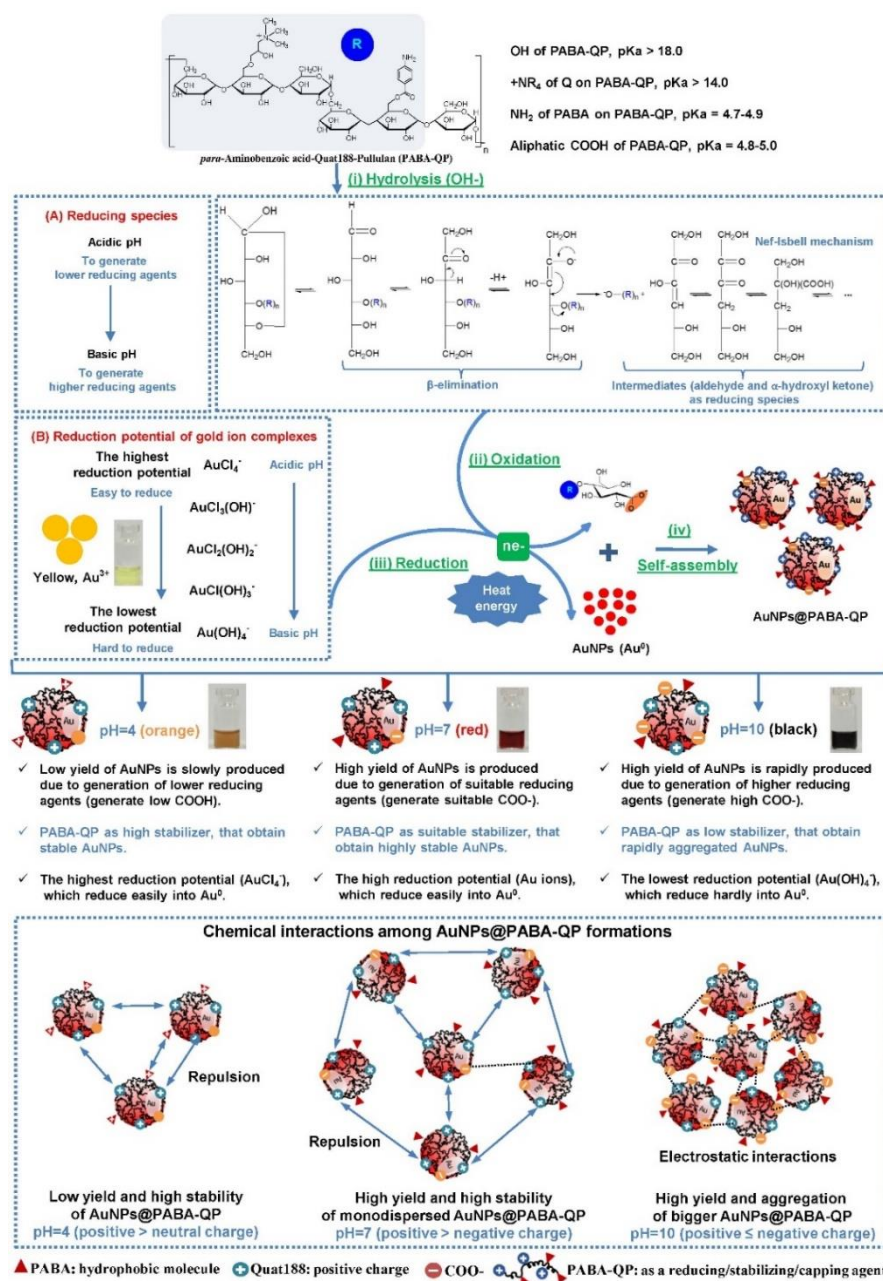
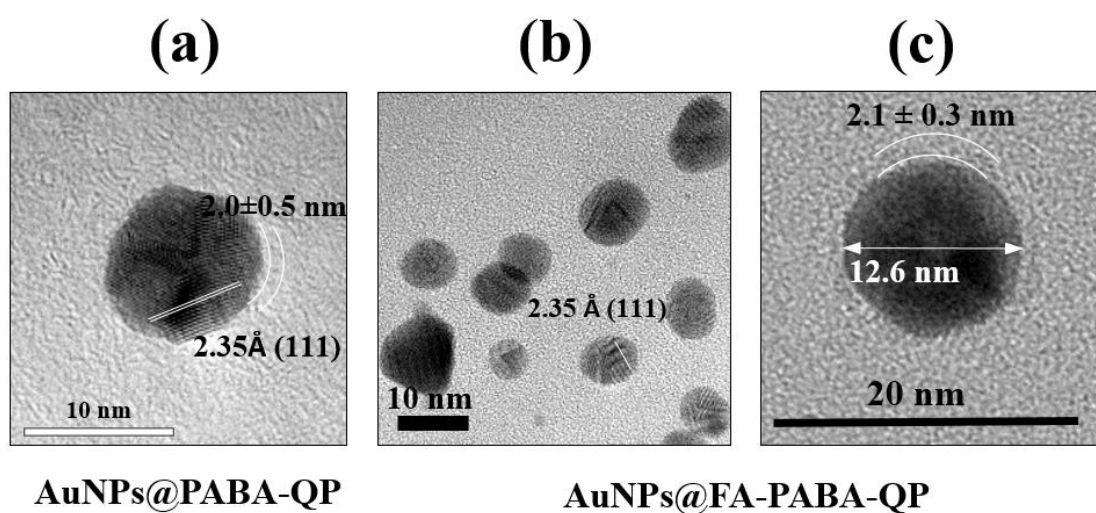
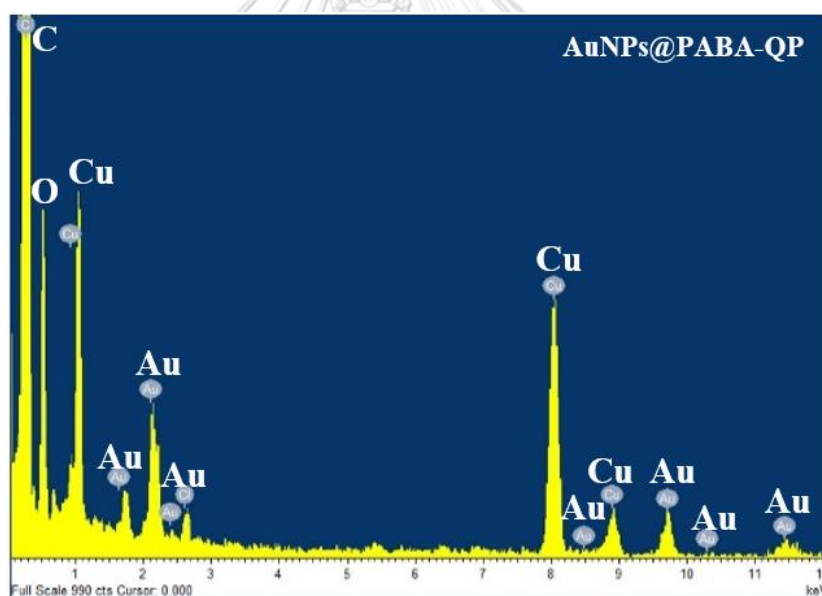


Figure A7. The proposed mechanism pathway of gold ion complex (Au<sup>3+</sup>) reduction by PABA-QP and chemical interactions among AuNPs@PABA-QP formations under various pH conditions.



**Figure A8** Characterizations of AuNPs formation: TEM images of (a) AuNPs@PABA-QP and (b-c) AuNPs@FA-PABA-QP under optimal conditions.



**Figure A9** EDS-TEM image of AuNPs@PABA-QP under optimal conditions.

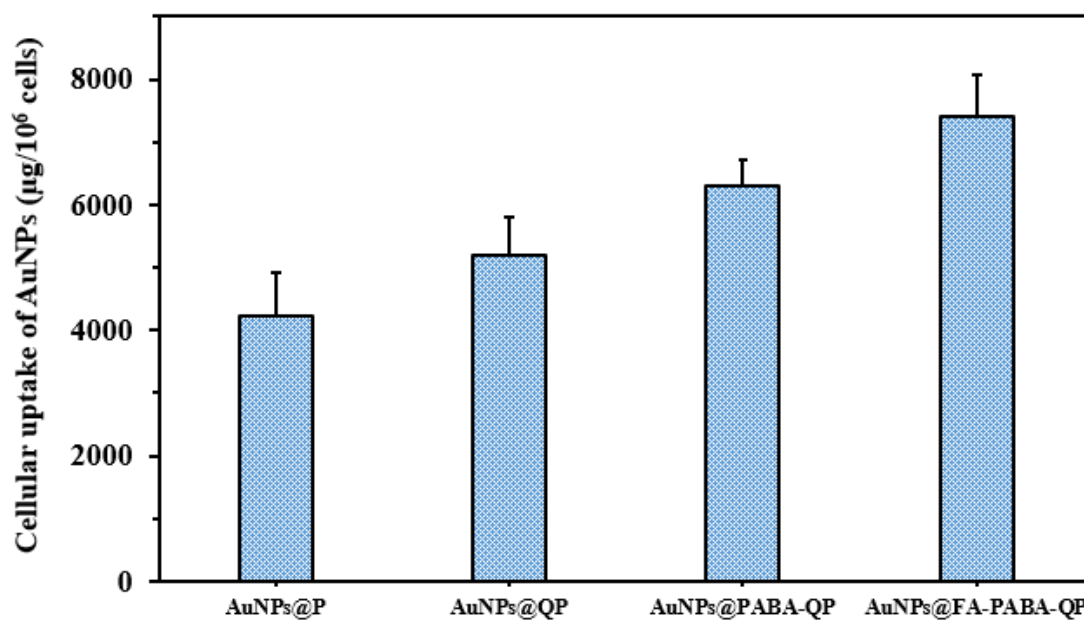


Figure A10 Intracellular uptake of AuNPs@P, AuNPs@QP, AuNPs@PABA-QP and AuNPs@FA-PABA-QP at 40 µM by ICP-OES.



Part III: Preparation and characterization of anticancer drugs loaded on AuNPs@pullulan derivatives for enhancing anticancer activities.

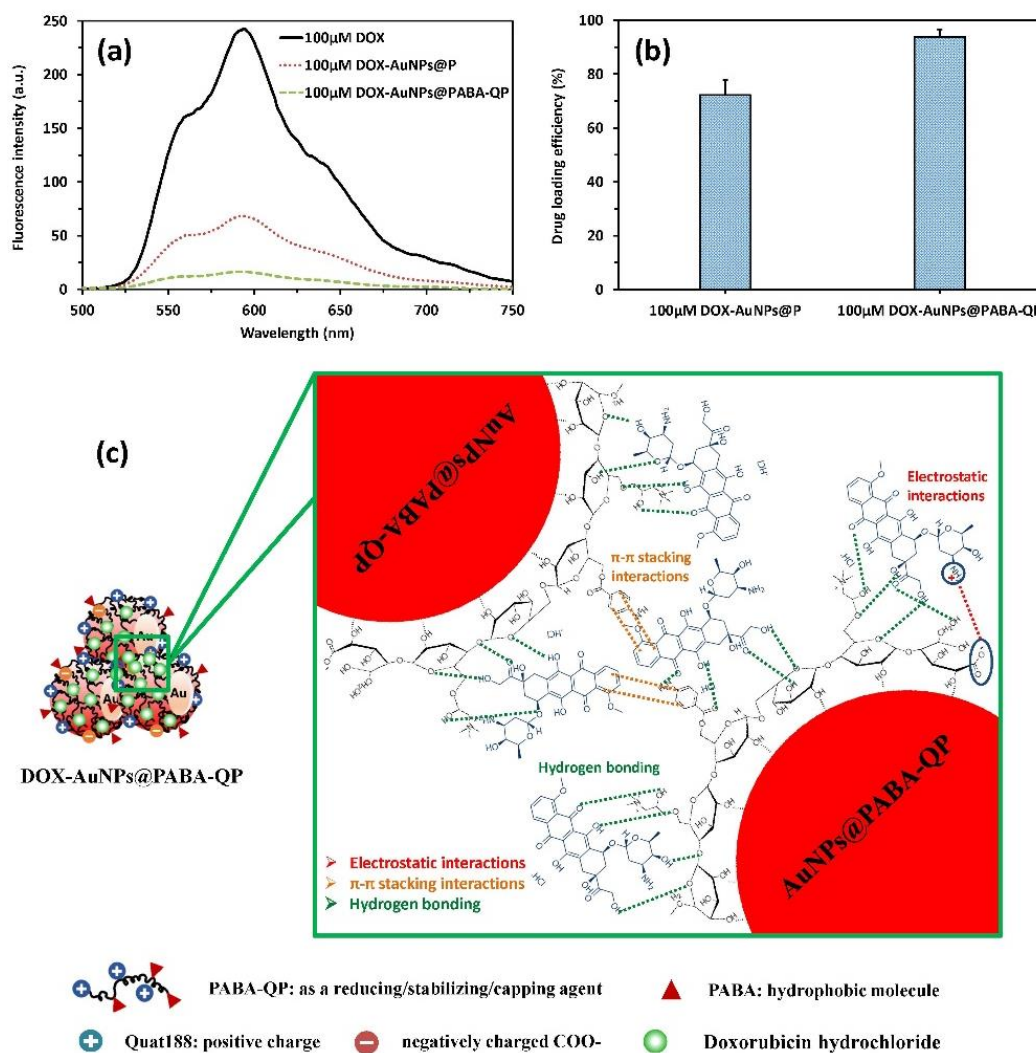
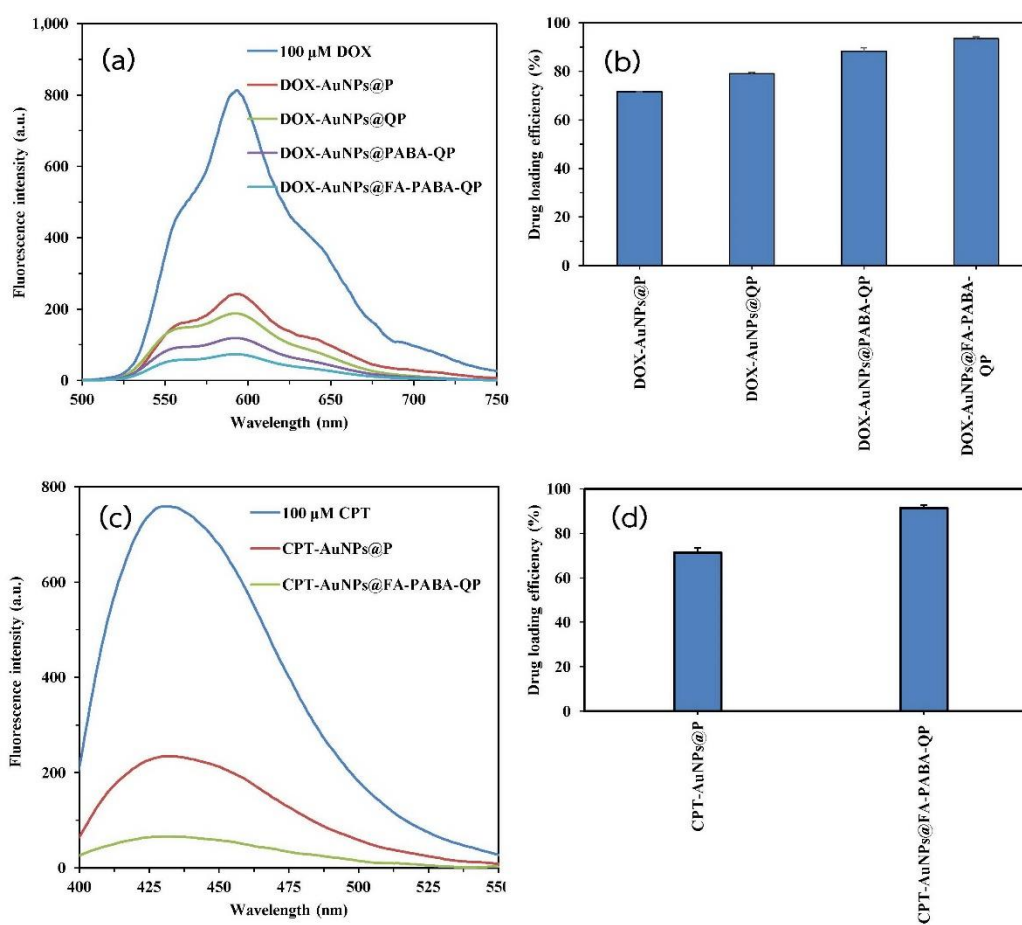


Figure A11 (a) Fluorescence spectra, (b) percent drug loading and (c) intermolecular interactions of 100  $\mu$ M DOX loaded on AuNPs@PABA-QP, compared with AuNPs@P.



**Figure A12** (a-c) Fluorescence spectra, (b-d) percent drug loading of 100  $\mu$ M DOX and CPT loaded on AuNPs@FA-PABA-QP, compared with AuNPs@pullulan derivatives.

Part IV: Evaluation of their cytotoxicity against human cancer and normal cells, intracellular uptake, drug release, and anticancer mechanism (cell cycle and apoptosis assay) of AuNPs@pullulan derivatives.

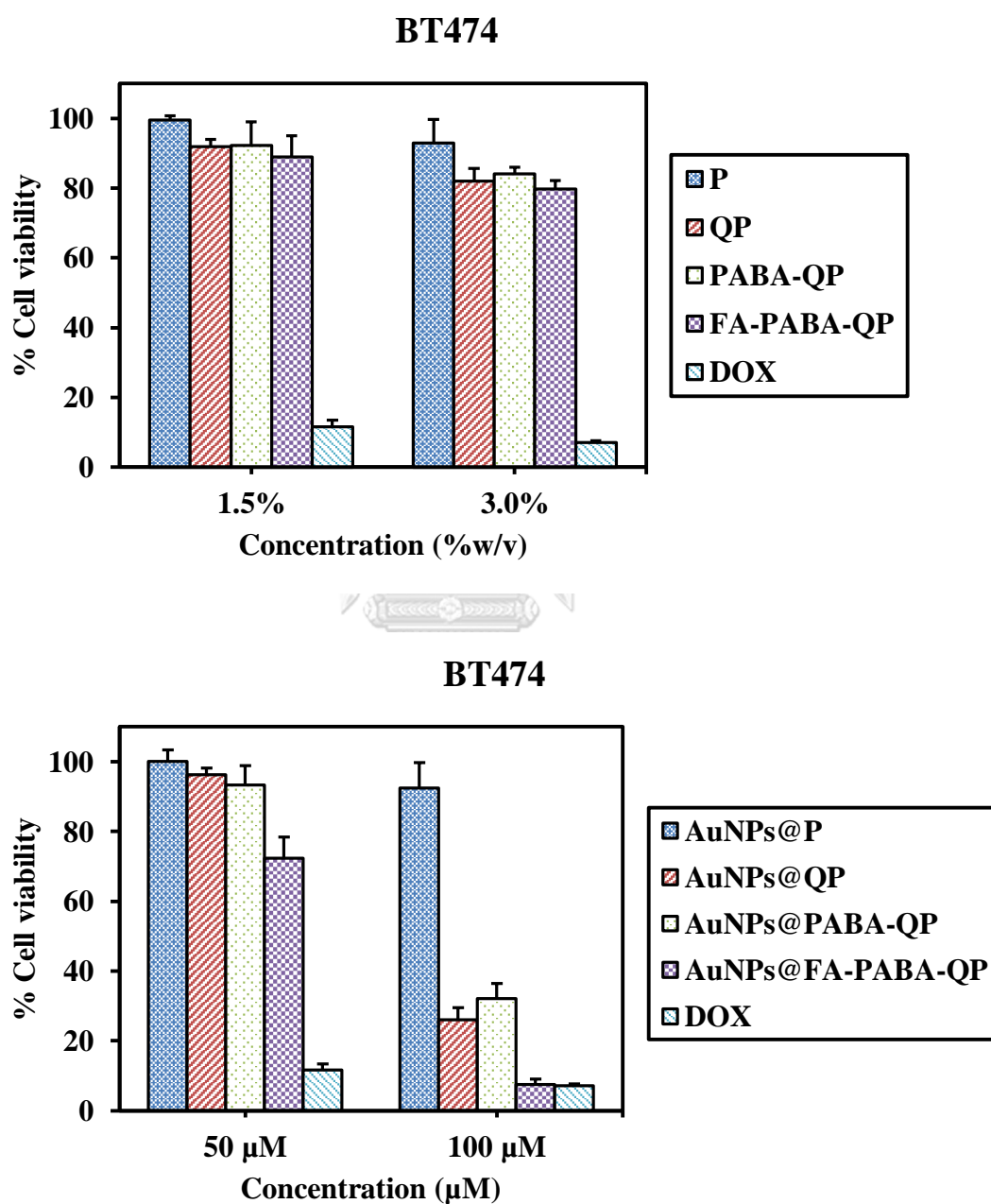


Figure A13 Preliminary screening of cytotoxicity of each sample against BT474 cells.

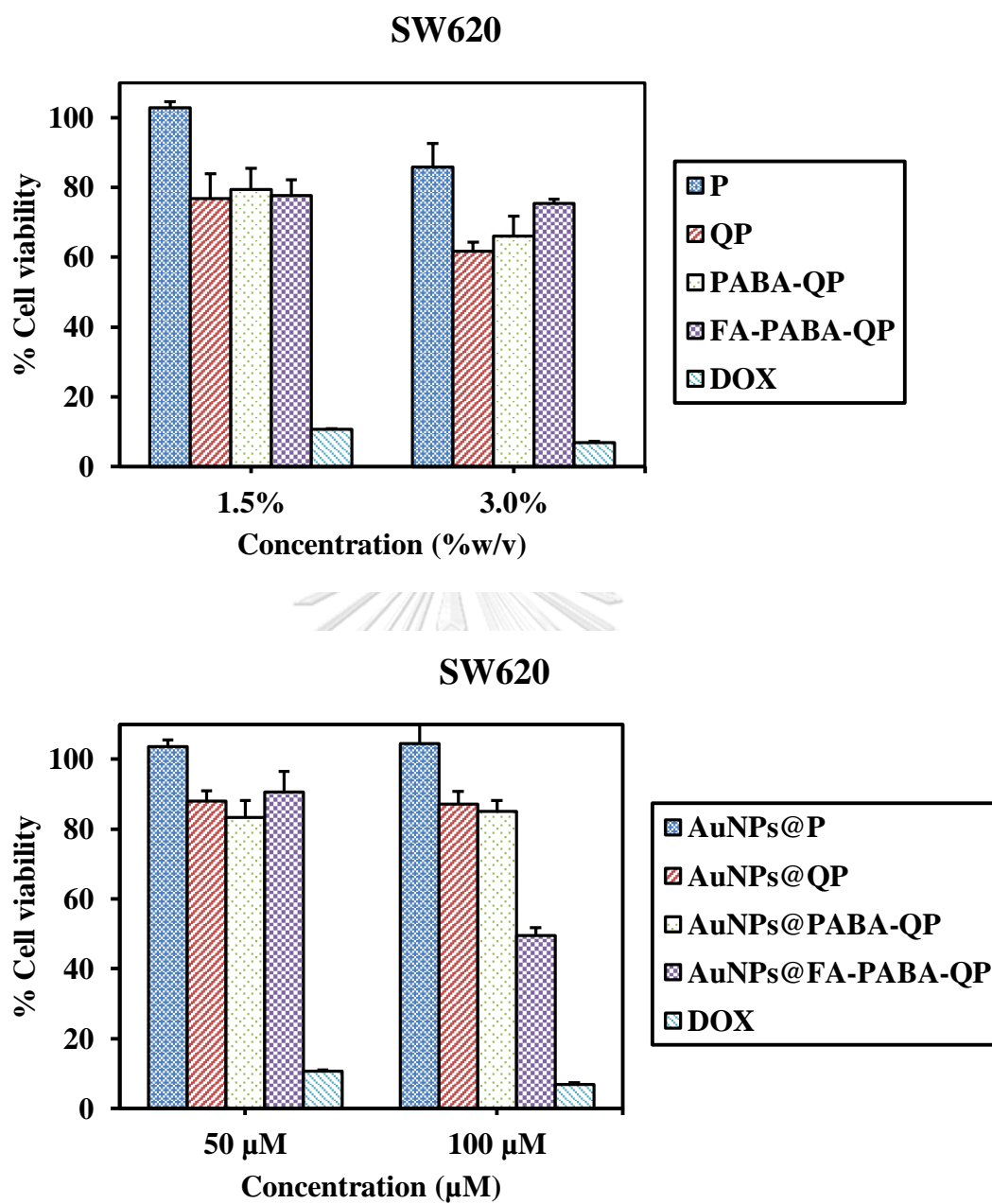


Figure A14 Preliminary screening of cytotoxicity of each sample against SW620 cells.

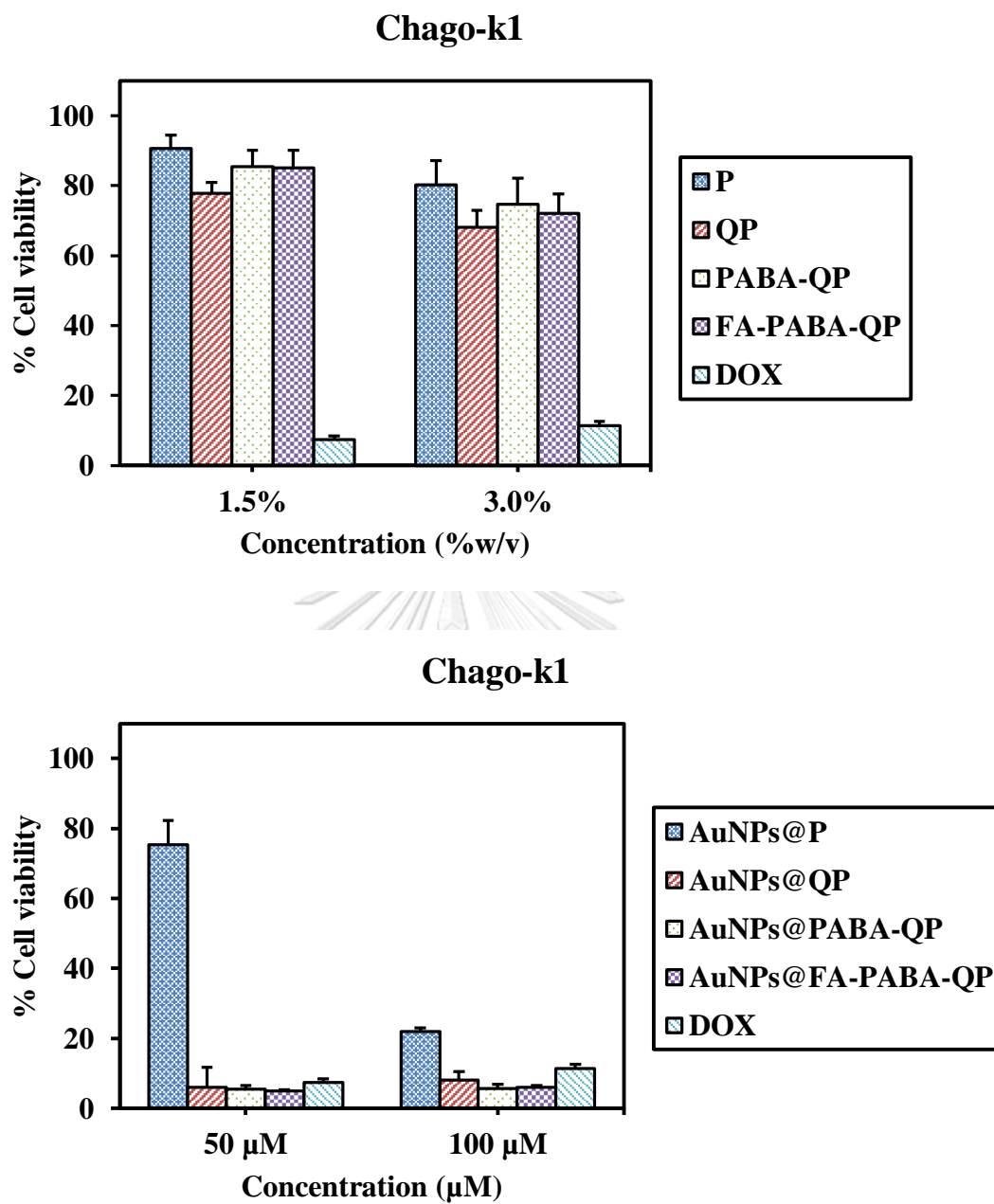


Figure A15 Preliminary screening of cytotoxicity of each sample against Chago-k1 cells.

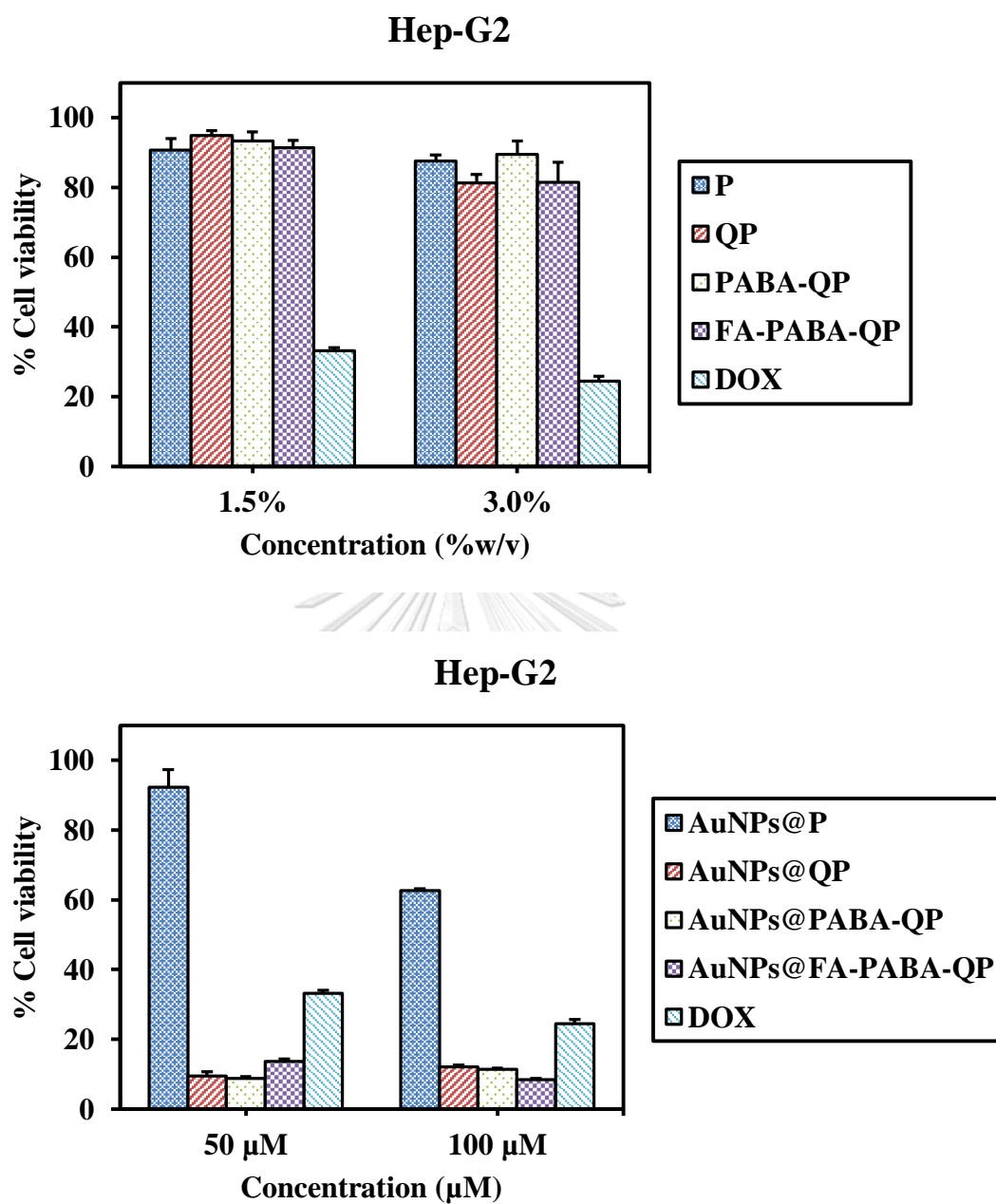


Figure A16 Preliminary screening of cytotoxicity of each sample against Hep-G2 cells.

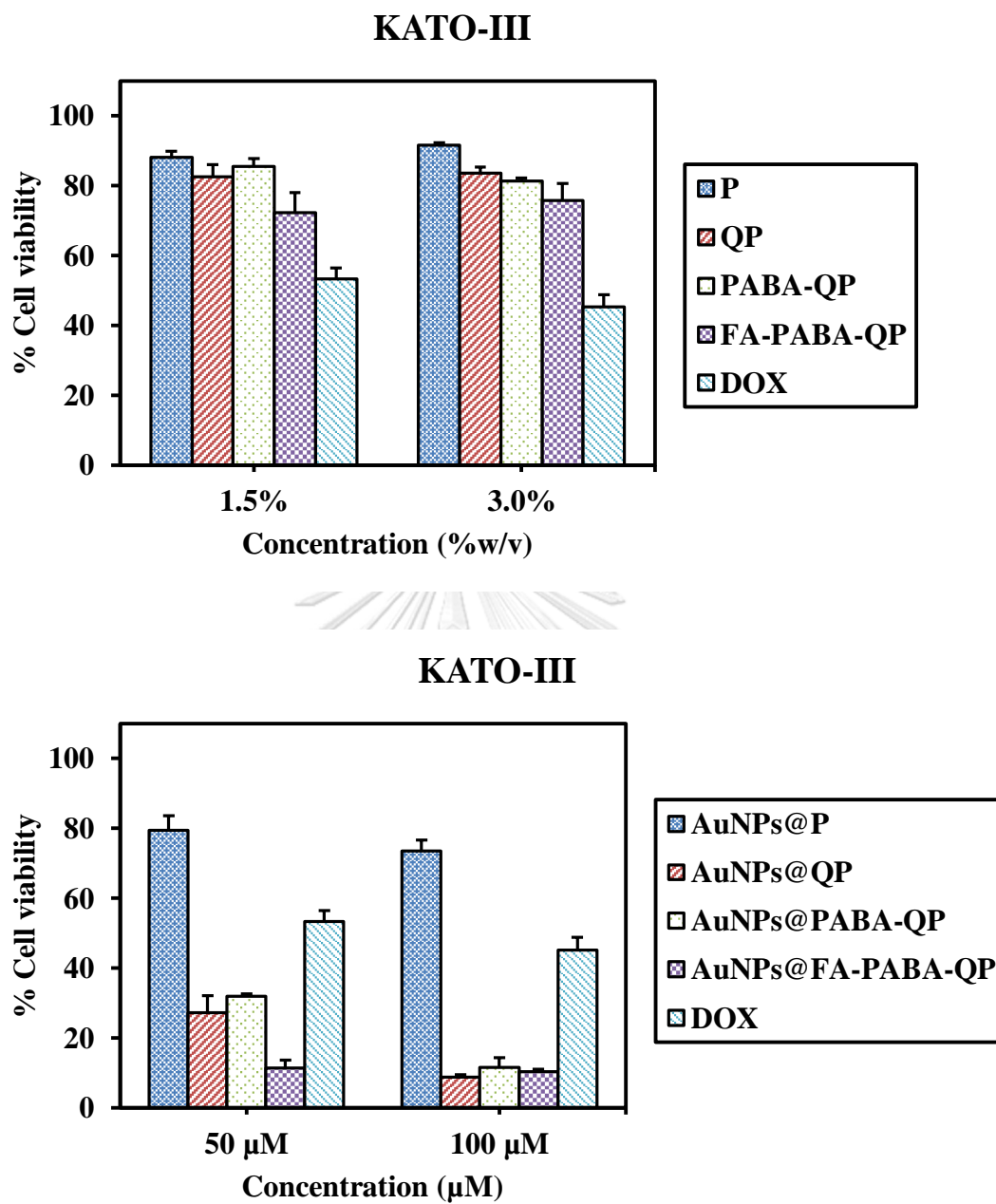


Figure A17 Preliminary screening of cytotoxicity of each sample against KATO-III cells.

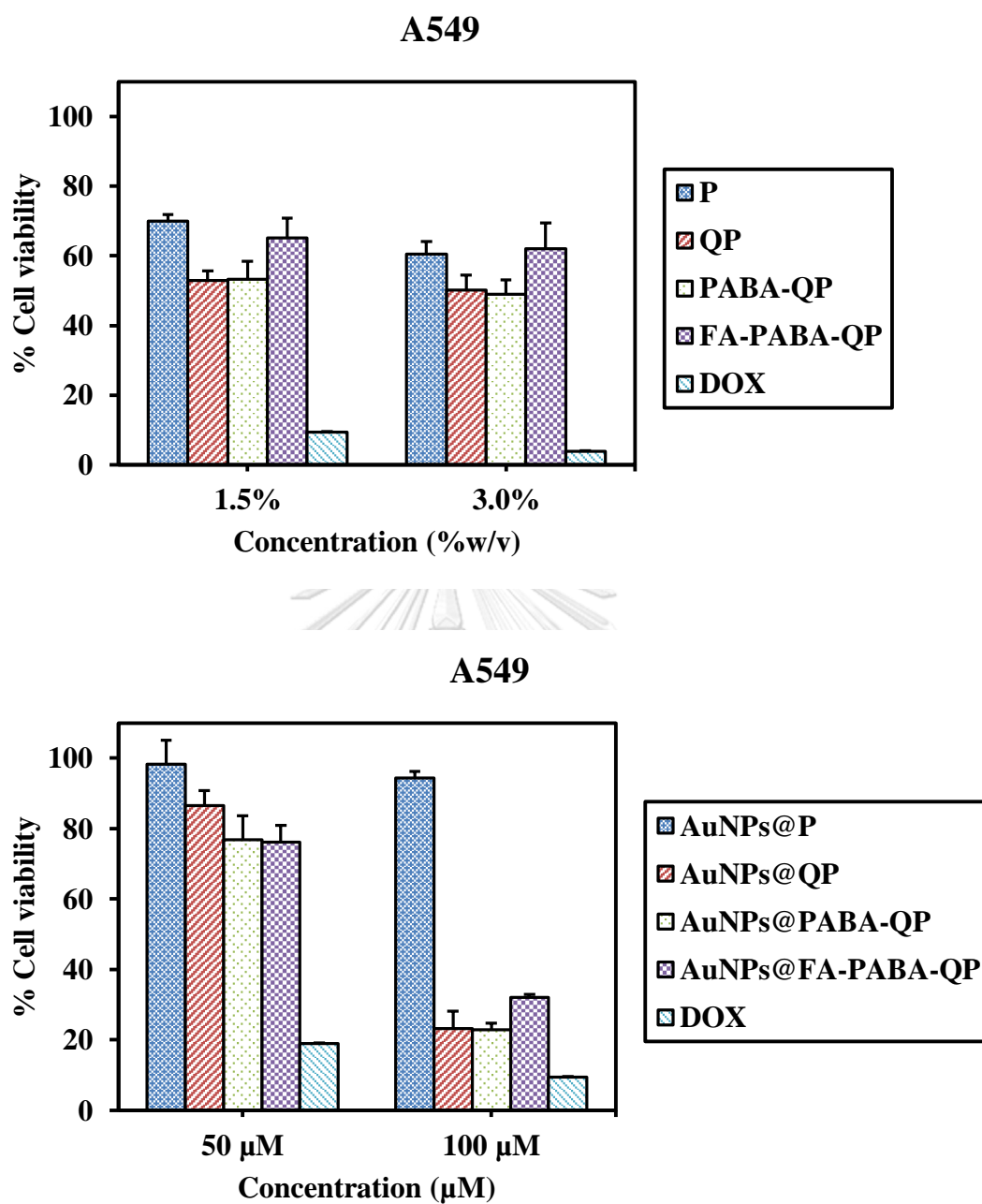


Figure A18 Preliminary screening of cytotoxicity of each sample against A549 cells.



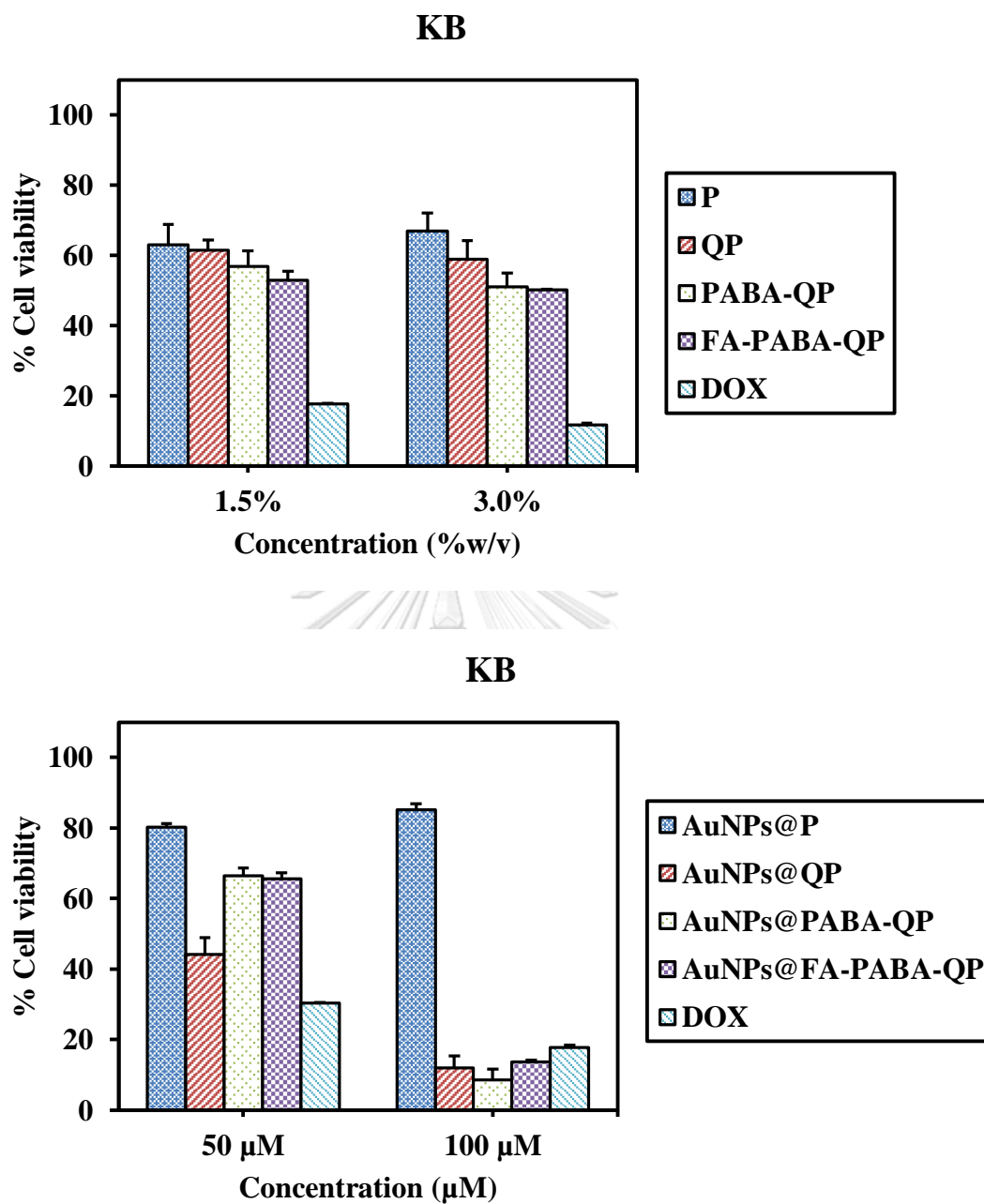
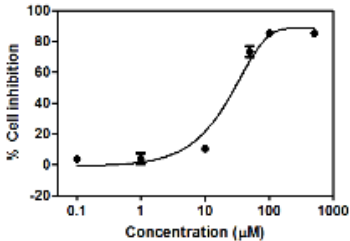
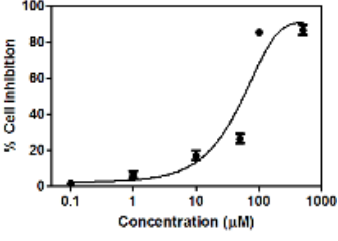
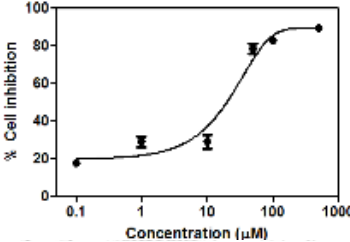
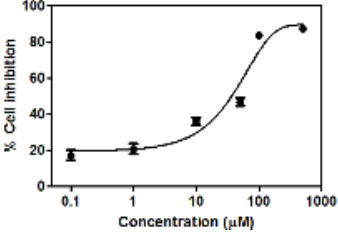
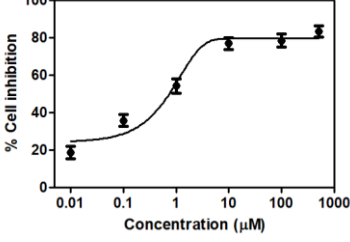
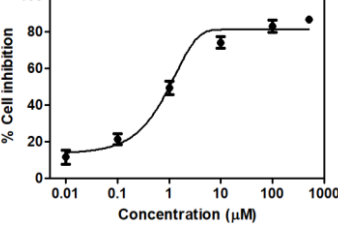
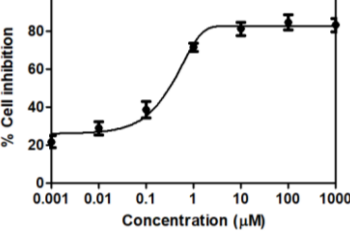
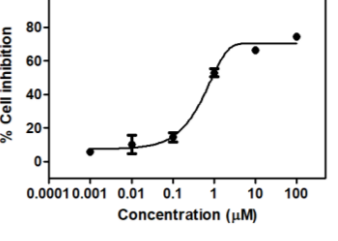
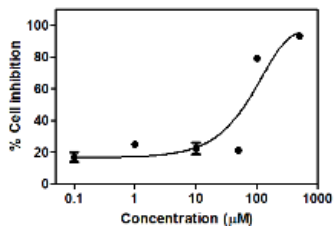
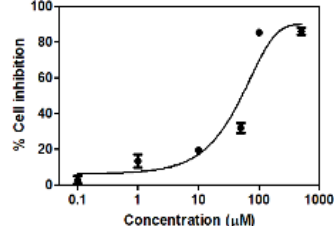
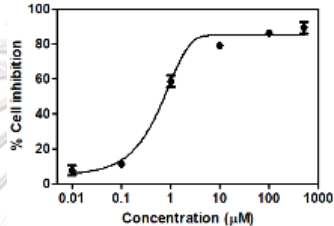
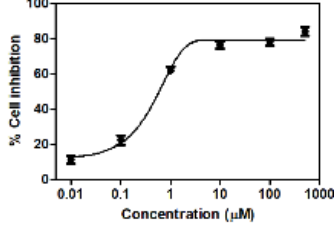
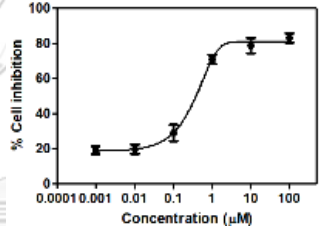
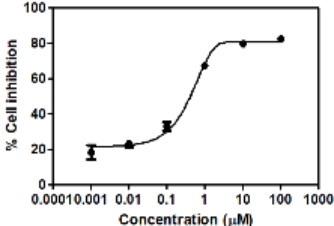
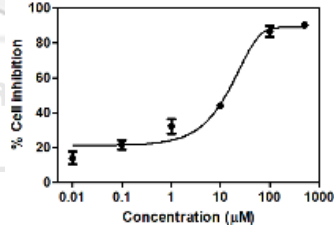


Figure A19 Preliminary screening of cytotoxicity of each sample against KB cells.

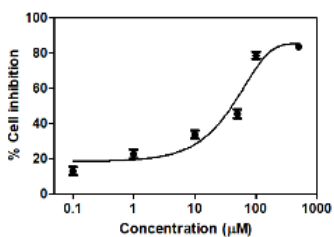
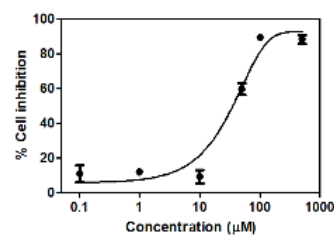
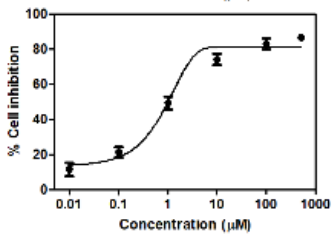
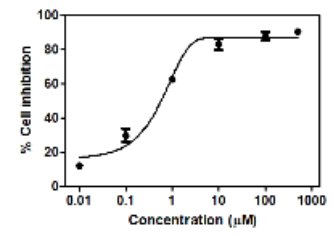
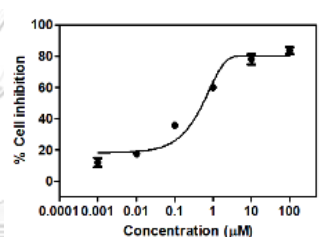
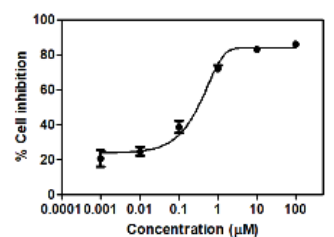
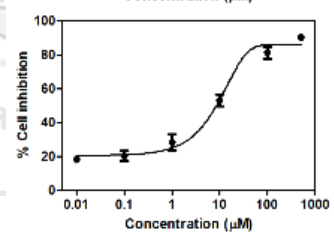
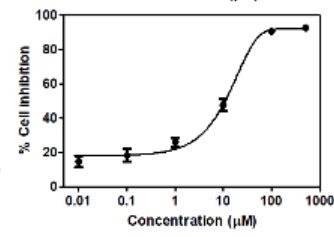
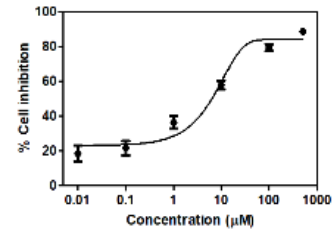
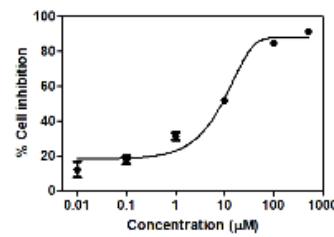
**Table A1** Cytotoxicity ( $IC_{50}$ ) of each compound against Chago-k1 and KATO-III cells.

Compound	Cytotoxicity <sup>a</sup> ( $IC_{50}$ , $\mu$ M)	
	Chago-k1	KATO-III
PABA-QP	>100	>100
AuNPs@P	>100	>100
AuNPs@QP		
AuNPs@PABA-QP		
DOX		
DOX-AuNPs@PABA-QP		

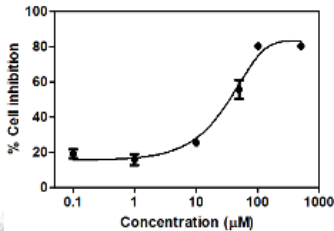
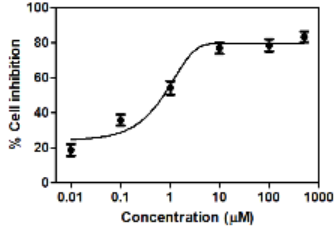
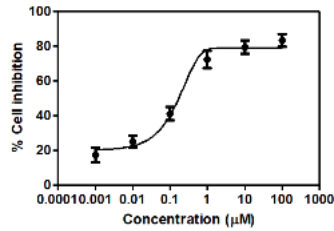
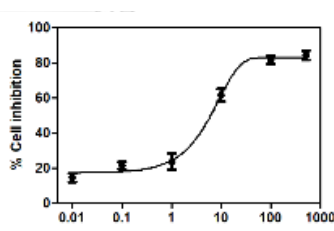
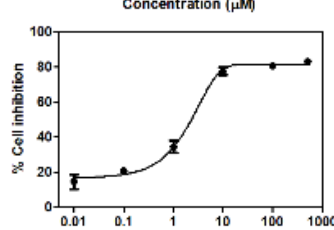
**Table A2** Cytotoxicity ( $IC_{50}$ ) of each compound against BT474 and A549 cancer cells.

Compound	Cytotoxicity <sup>a</sup> ( $IC_{50}$ , $\mu\text{M}$ )	
	A549	BT474
FA-PABA-QP	>100	>100
AuNPs@FA-PABA-QP		
DOX		
DOX-AuNPs@FA-PABA-QP		
CPT		ND
CPT-AuNPs@FA-PABA-QP	ND=not determined	ND

**Table A3** Cytotoxicity ( $IC_{50}$ ) of each compound against BT474 and A549 cancer cells.

Compound	Cytotoxicity <sup>a</sup> ( $IC_{50}$ , $\mu\text{M}$ )	
	KATO-III	Hep-G2
FA-PABA-QP	>100	>100
AuNPs@FA-PABA-QP		
DOX		
DOX-AuNPs@FA-PABA-QP		
CPT		
CPT-AuNPs@FA-PABA-QP		

**Table A4** Cytotoxicity (IC<sub>50</sub>) of each compound against Chago-k1 cancer cells.

Compound	Cytotoxicity <sup>a</sup> (IC <sub>50</sub> , μM)
	Chago-k1
FA-PABA-QP	>100
AuNPs@FA-PABA-QP	
DOX	
DOX-AuNPs@FA-PABA-QP	
CPT	
CPT-AuNPs@FA-PABA-QP	

**Table A5.** IC<sub>50</sub> value of each compound against seven cancer cell lines

Compound	Cytotoxicity (IC <sub>50</sub> , $\mu$ M) of each compound						
	BT474	SW620	Hep-G2	Chago-k1	KATO-III	A549	KB
AuNPs@P	>100	>100	77.1 $\pm$ 4.0	>100	>100	>100	>100
AuNPs@QP	65.9 $\pm$ 3.9	>100	46.7 $\pm$ 3.6	37.0 $\pm$ 2.1	51.8 $\pm$ 4.4	58.9 $\pm$ 5.3	65.6 $\pm$ 6.2
AuNPs@PABA-QP	55.5 $\pm$ 3.5	>100	36.1 $\pm$ 2.3	35.4 $\pm$ 2.1	44.9 $\pm$ 2.7	83.9 $\pm$ 3.9	>100
AuNPs@FA-PABA-QP	49.3 $\pm$ 4.1	>100	34.7 $\pm$ 3.1	34.1 $\pm$ 1.8	44.7 $\pm$ 2.6	83.2 $\pm$ 4.8	>100
DOX	0.5 $\pm$ 0.1	0.9 $\pm$ 0.1	0.6 $\pm$ 0.1	0.8 $\pm$ 0.2	0.9 $\pm$ 0.1	0.6 $\pm$ 0.1	1.0 $\pm$ 0.1

Cytotoxicity was derived after 72 h exposure to the compound using the MTT assay. Data are shown as the mean  $\pm$ 1SD, derived from three independent trials.



**Table A6.** IC<sub>50</sub> value of each compound at various time incubations against Hep-G2 and Chago-k1 cancer cell lines

Compound	Cytotoxicity (IC <sub>50</sub> , μM) of each compound					
	Hep-G2			Chago-k1		
	24 h	48 h	72 h	24 h	48 h	72 h
AuNPs@P	<sup>a</sup> ND	ND	77.1±4.0	>100	>100	>100
AuNPs@QP	53.5±4.1	48.3±3.3	46.7±3.6	52.5±3.8	48.5±4.1	36.9±2.1
AuNPs@PABA-QP	51.7±4.1	50.4±2.7	36.1±2.3	47.4±3.4	43.0±3.1	35.4±2.1
AuNPs@FA-PABA-QP	50.2±3.8	46.3±3.1	34.7±3.1	39.3±2.7	39.2±1.9	34.1±1.8
DOX	14.6±2.3	7.6±1.2	0.6±0.1	1.2±0.2	0.8±0.2	0.8±0.2

Cytotoxicity was derived after 24, 48 and 72 h exposure to the compound using the MTT assay. Data are shown as the mean ±1SD, derived from three independent trials.

<sup>a</sup>ND = not determined.





**A: Conferences (Poster Presentations):**

1. Kasem Payuhadechapiwat, **Sakchai Laksee**, Thapong Teerawatananon, Chupun Gowanit, Nongnuj Muangsin “Innovation whitening cream containing kojic-acid/gold nanoparticles” Proceeding of The 23<sup>rd</sup> PPC Symposium on Petroleum, Petrochemicals, and Polymers and The 8<sup>th</sup> Research Symposium on Petrochemical and Materials Technology (PPC&PETROMAT SYMPOSIUM 2017), Pathumwan Princess Hotel, Bangkok, Thailand, May 23, **2017**, pp 1-6.
2. Kasem Payuhadechapiwat, **Sakchai Laksee**, Thapong Teerawatananon, Chupun Gowanit, Nongnuj Muangsin “Synthesis the combination of gold nanoparticles-kojic acid for antimelanin activity” The 2017 Pure and Applied Chemistry International Conference (PACCON 2017), Centra Government Complex Hotel & Convention Centre Chaeng Watthana, Bangkok, Thailand, February 2-3, **2017**.
3. **Sakchai Laksee**, Songchan Puthong, Nongnuj Muangsin “Design and synthesis of PABA-QP stabilized gold nanoparticles as drug delivery carrier” The 2016 Pure and Applied Chemistry International Conference (PACCON 2016), Bangkok International Trade & Exhibition Centre (BITEC), Bangkok, Thailand, February 9-11, **2016**.
4. **Sakchai Laksee**, Urarika Luesakul, Nongnuj Muangsin “Design and synthesis of folic acid-trimethyl chitosan (FA-TMC) for drug delivery applications” 12<sup>th</sup> International Conference of the European Chitin Society 13<sup>th</sup> International Conference on Chitin and Chitosan (ICCC/EUCHIS 2015), Juridicum Münster Universitätsstraße, Münster, Germany, August 30-September 2, **2015**.
5. **Sakchai Laksee**, Thapong Teerawatananon, Songchan Puthong, Nongnuj Muangsin “Synthesis and cytotoxicity of cassiarin A chloride derivatives as anticancer agents” The 9<sup>th</sup> Conference on Science and Technology for Youths,

Bangkok International Trade & Exhibition Centre (BITEC), Bangkok, Thailand, May 30-June 1, **2014**.

**B: Conference (Oral Presentation):**

1. **Sakchai Laksee**, Sanong Ekgasit, Songchan Puthong, Nongnuj Muangsin “Green synthesis of pullulan stabilized gold nanoparticles for drug delivery” The 40<sup>th</sup> Congress on Science and Technology of Thailand (STT 40), Hotel Pullman Khon Kaen Raja Orchid, Khon Kaen, Thailand, December 2-4, **2014**.

**C: Scholarships and Awards:**

1. **2012-2016**, Graduate scholarship, *Science Achievement Scholarship of Thailand (SAST)* (Grant No: 6/2555 and 2/2557), Chulalongkorn University, Bangkok, 10330 Thailand.
2. **2018**, Nongnuj Muangsin, Urarika Luesakul, **Sakchai Laksee**, *Special Award of Space Research Institute of RAS: “BioGreenoTech”* from 46<sup>th</sup> International Exhibition of Inventions Geneva, Palexpo, Geneva, Switzerland, April 11-15, 2018.
3. **2018**, Nongnuj Muangsin, Urarika Luesakul, **Sakchai Laksee**, *Silver Medal Award: “BioGreenoTech”* from 46<sup>th</sup> International Exhibition of Inventions Geneva, Palexpo, Geneva, Switzerland, April 11-15, 2018.
4. **2017**, Nongnuj Muangsin, Tanat Tubtimtong, **Sakchai Laksee**, *Gold Prize: “ArtWood”* from Seoul International Invention Fair 2017 (SIIF2017), COEX Hall 1, Seoul, South Korea, November 30 - December 3, 2017
5. **2017**, Nongnuj Muangsin, Urarika Luesakul, **Sakchai Laksee**, *Gold Medal Award: “GarlicUp”* from 13<sup>th</sup> Taipei Int'l Invention Show & Technomart (INST2017), TWTC Hall 1, Taipei, Taiwan, September 28-30, 2017.

6. **2017**, Nongnuj Muangsin, Urarika Luesakul, **Sakchai Laksee**, *Special Prize of Korea Invention Promotion Association for Excellent Efforts in Creating Invention: “GarlicUp”* from 13<sup>th</sup> Taipei Int'l Invention Show & Technomart (INST2017), TWTC Hall 1, Taipei, Taiwan, September 28-30, 2017.
7. **2017**, Nongnuj Muangsin, Urarika Luesakul, **Sakchai Laksee**, *Silver Medal Award: “GrandGold”* from 13<sup>th</sup> Taipei Int'l Invention Show & Technomart (INST2017), TWTC Hall 1, Taipei, Taiwan, September 28-30, 2017.

#### D: Thai Patent:

1. Nongnuj Muangsin, Urarika Luesakul, **Sakchai Laksee** “Process for preparation of gold nanoparticles/carboxylated polysaccharide and its applications” *Applied*.
2. Nongnuj Muangsin, Urarika Luesakul, **Sakchai Laksee** “Bio-efficacy enhancement process for garlic” *Application No. 1803001114*, May 11, 2018.

#### E: Publications and Proceedings:

1. **Laksee, S.**, Puthong, S., Teerawatananond, T., Palaga, T., and Muangsin, N. Highly efficient and facile fabrication of monodispersed Au nanoparticles using pullulan and their application as anticancer drug carriers. *Carbohydrate Polymers* 173 (2017): 178-191.
2. Payuhadechapipat, K., **Laksee, S.**, Teerawatananond, T., Gowanit, C., Muangsin, N. Innovation whitening cream containing kojic-acid/gold nanoparticles. *Proceeding of the 23<sup>rd</sup> PPC Symposium on Petroleum, Petrochemicals, and Polymers and the 8<sup>th</sup> Research Symposium on*

Petrochemical and Materials Technology (PPC&PETROMAT SYMPOSIUM 2017), Pathumwan Princess Hotel, Bangkok, Thailand, May 23, (2017): 1-6.

3. **Laksee, S.**, Puthong, S., Kongkavitoon, P., Palaga, T., and Muangsin, N. Facile and green synthesis of pullulan derivatives stabilized Au nanoparticles as drug carriers for enhancing anticancer activity. Carbohydrate Polymers *Revised*.



## VITA

Name: Mr. Sakchai Laksee Date of Birth: October 02, 1989

Telephone: 086-1654347 E-mail: Sakchai197@hotmail.com

Address: 38 Moo 6, Wang Manao, Pak Tho, Ratchaburi, 70140 Thailand

### Educations:

2014-2017 Ph.D. (Inorganic Chemistry, Chulalongkorn University)

2012-2013 M.Sc. (Inorganic Chemistry, Chulalongkorn University)

2008-2011 B.Sc. (Second Class Honor in Chemistry, Silpakorn University)

### Scholarships:

2012-2016 Science Achievement Scholarship of Thailand (SAST)

### Publications:

1. Laksee, S., Puthong, S., Teerawatananond, T., Palaga, T., and Muangsin, N. Highly efficient and facile fabrication of monodispersed Au nanoparticles using pullulan and their application as anticancer drug carriers. *Carbohydrate Polymers* 173 (2017): 178-191.

2. Laksee, S., Puthong, S., Kongkavitoon, P., Palaga, T., and Muangsin, N. Facile and green synthesis of pullulan derivatives stabilized Au nanoparticles as drug carriers for enhancing anticancer activity. *Carbohydrate Polymers Revised*.